Study of Vortex Stability in Swept Wing Configurations

Alexander J. Cavanagh
MEng

James Watt School of Engineering
College of Science and Engineering
University of Glasgow

Submitted in fulfilment of the requirements for the degree of *Doctor of Philosophy*

February 2026

Declaration

I hereby certify that the work presented in this thesis for examination for a PhD degree at the University of Glasgow is solely my own work except where specific reference is made to the work of others and that the thesis has not been edited by a third party beyond what is permitted by the University's PGR Code of Practice.

The copyright of this thesis rests with the author. No quotation from it is permitted without full acknowledgement.

I declare that the thesis does not include work forming part of a thesis presented successfully for another degree.

I declare that this thesis has been produced in accordance with the University of Glasgow's Code of Good Practice in Research.

I acknowledge that if any issues are raised regarding good research practice based on review of the thesis, the examination may be postponed pending the outcome of any investigation of the issues.

Alex Cavanagh
February 2026

Dedicated to my ever-loving Grandparents
Jill and Trevor Compson

Abstract

The aerodynamic performance of small flapping and plunging wings operating at low Reynolds numbers is strongly influenced by the formation and evolution of leading-edge vortices (LEVs). While the role of LEVs in lift enhancement is well established for unswept wings, the combined effects of sweep angle and unsteady kinematics on LEV stability and force production remain less well understood, particularly in the Reynolds number regime relevant to micro air vehicles (MAVs).

This thesis investigates the influence of wing sweep angle and reduced frequency on LEV dynamics for finite wings undergoing prescribed plunging motions at Reynolds number 2×10^4. High-fidelity improved delayed detached eddy simulations (IDDES) are performed for wings with sweep angles of $\Lambda = 0°, 30°$, and $60°$, spanning quasi-steady to highly unsteady motion regimes. The resulting flow fields are analysed to characterise LEV formation, growth, convection, and breakdown across the wing span.

Two distinct LEV breakdown modes are identified and characterised: burst-type breakdown at low reduced frequency, involving abrupt collapse of a coherent LEV, and spiral-type breakdown at higher reduced frequency, in which three-dimensional helical instabilities lead to progressive deformation and downstream convection of the vortex. These modes correspond to established breakdown behaviours in the literature and are shown here to be robustly distinguished by reduced frequency for the present finite-wing configurations, with each breakdown mode associated with a distinct aerodynamic response.

The leading-edge suction parameter (LESP) is assessed as a predictive metric for LEV initiation on swept wings and is shown to remain qualitatively applicable, with important modifications arising from three-dimensional effects and spanwise transport. Force and moment partitioning methods are employed to quantify the spanwise distribution of vorticity-induced lift and thrust contributions, enabling direct links between flow structure and aerodynamic loading.

The results demonstrate that increasing reduced frequency promotes earlier LEV detachment and more rapid downstream convection, leading to pronounced transient lift peaks associated

with impulsive acceleration effects. Wing sweep fundamentally alters LEV stability by enhancing spanwise vorticity transport, promoting sustained LEV attachment near the wing root whilst modifying the spanwise distribution of aerodynamic loading. These findings regarding wing sweep provide new insight into the coupled roles of unsteadiness and sweep in LEV-dominated flows and offer guidance for the aerodynamic design of bio-inspired MAVs operating in gust-sensitive environments.

Publications

Journal articles

A. Cavanagh, C. Bose and K. Ramesh, "Effect of sweep angle on three-dimensional vortex dynamics over plunging wings," *Physics of Fluids*, vol. 36, no. 11, p. 117115, 2024.

Conference papers

A. Cavanagh, C. Bose and K. Ramesh, "Effect of sweep on leading edge vortex dynamics of plunging wings," *DisCoVor 2023*, 16-19 May 2023, Breckenridge, USA.

A. Cavanagh, C. Bose and K. Ramesh, "LEADING-EDGE VORTEX DYNAMICS OF HIGH-AMPLITUDE PITCHING SWEPT WINGS," *The 18th OpenFOAM Workshop (OFW18)*, 11-14 July 2023, Genoa, Italy.

A. Cavanagh, C. Bose and K. Ramesh, "Leading-edge vortex dynamics of plunging swept wings," *UK Fluids Conference*, 17-19 October 2023, Glasgow, UK.

A. Cavanagh, C. Bose and K. Ramesh, "Insights from force partitioning on vortex dynamics around plunging swept wings," *DisCoVor 2024*, 16-19 April 2024, Delft, Netherlands.

Acknowledgements

Firstly, I would like to thank my supervisor Kiran Ramesh for his insight and support throughout this PhD process. Your knowledge and experience have been a huge help and I appreciate your supervision approach allowing me to pursue alternative research avenues of my own choosing.

I also want to express my deepest gratitude to Chandan Bose for supervising this project. Without your expertise in CFD methods, completing this work would not have been possible. Many thanks for agreeing to become part of this process and adding your invaluable insight.

To members of our research group, past and present, Hugh Bird, Alfonso Martínez and Pedro Hernandez Gelado, thanks firstly for making our research group a great environment to work in and explore the world of unsteady aerodynamics. Thanks again for your support and assistance in proofreading thesis chapters and providing suggestions and advice in meetings.

I would also like to thank other staff from the University of Glasgow; Julia Deans and Maisie Mullings for handling untold administrative queries and Raymond Brasas for his persistence in ensuring that *Turing* remained online to enable post-processing of the CFD simulations present in this thesis. Thanks to Wrik Mallik for taking over supervision of this project in the latter stages and for assistance with signing the necessary paperwork. Thanks to Hossein Zare-Behtash for being my second supervisor and especially for your help signing my leave of absence form in a time of need. Thanks to Ian Taylor and Kostas Kontis as my Annual Progress Review Convener and Examiner respectively for your guidance and remarks.

Thanks to Shūji Ōtomo for performing experiments to complement the simulations in this thesis. I hope we can publish these results together soon. Thanks to Yuanhang Zhu for your help on the FMPM and for providing open-source access to your three-dimensional code.

I must also thank my family for your support throughout these last 4 years and the whole of my life beforehand. I can always count on you all to provide some much-needed laughs when things aren't quite going to plan!

To my partner Anya, we met at the start of this PhD and I couldn't and wouldn't have made it to this point without all your support and guidance. I think you normally know how to help me

better than I know how to myself. Thank you for everything. A last personal thanks goes to the newest addition to the family, our cat Luna.

No acknowledgements section would be complete without thanking my examiners, Juan Li and Ian Taylor for their detailed, constructive and insightful feedback. Your comments have ensured that the final version of this thesis has improved significantly from the initial version. It would also be remiss of me not to thank Rene Steijl for acting as the Viva convener and attending to the administrative duties associated with organising the meeting.

During the preparation of the revised version of this thesis, generative artificial intelligence tools (ChatGPT, OpenAI) were used in a limited and transparent manner to support editing, structural refinement, and improvement of clarity in response to examiner feedback. The use of generative AI was undertaken in accordance with the University of Glasgow's guidance on the responsible use of artificial intelligence in research and assessment, and with UK Research and Innovation (UKRI) principles on research integrity, transparency, and author responsibility. No generative AI tools were used at any stage in the preparation of the original thesis submitted for examination.

Finally, I gratefully acknowledge the support of the UK Engineering and Physical Sciences Research Council (EPSRC) through a DTA scholarship, grant EP/T517896/1. This work used the Cirrus UK National Tier-2 HPC Service at EPCC (http://www.cirrus.ac.uk) funded by the University of Edinburgh and EPSRC (EP/P020267/1). This work used the ARCHER2 UK National Supercomputing Service (https://www.archer2.ac.uk).

Contents

List of Figures

List of Tables

Nomenclature

Acronyms

AR	Aspect ratio, $AR = b/c$
CFD	Computational Fluid Dynamics
DDES	Delayed Detached Eddy Simulation
DES	Detached Eddy Simulation
DNS	Direct Numerical Simulation
FMPM	Force and moment partitioning method
IDDES	Improved Delayed Detached Eddy Simulation
LAULLT	Large-amplitude unsteady lifting-line theory
LES	Large Eddy Simulation
LESP	Leading-edge suction parameter
LEV	Leading-edge vortex
LOM	Low-order model
MAV	Micro air vehicle
RANS	Reynolds-averaged Navier–Stokes
UAV	Unmanned aerial vehicle

Greek Symbols

$\Gamma(s)$	Spanwise distribution of bound circulation
Λ	Wing sweep angle
μ	Dynamic viscosity
ν	Kinematic viscosity

ω	Angular frequency of oscillation
ρ	Fluid density

Latin Symbols

$\dot{h}$	Plunge velocity
ν_t	Turbulent (eddy) viscosity
b	Wing span
c	Wing chord
C_D	Drag coefficient
C_L	Lift coefficient
C_L^ω	Vorticity-induced lift coefficient
C_T	Thrust coefficient
C_T^ω	Vorticity-induced thrust coefficient
D	Drag force
h	Plunge displacement
$h(t)$	Plunge displacement as a function of time
h_0	Plunge amplitude
k	Reduced frequency
L	Lift force
Re	Reynolds number
S	Wing planform area
T	Oscillation period
T	Thrust force
t	Time
t^*	Convective non-dimensional time, $t^* = tU_\infty/c$
U	Velocity vector
U_∞	Free-stream velocity
w	Downwash velocity
LESP(s,t)	Spanwise and time-dependent leading-edge suction parameter
$\text{LESP}_{\text{crit}}$	Critical leading-edge suction parameter

Subscripts and Superscripts

$(\cdot)_0$	Reference or amplitude value
$(\cdot)_\infty$	Free-stream (far-field) value
$(\cdot)_{2D}$	Two-dimensional quantity
$(\cdot)_{3D}$	Three-dimensional quantity
$(\cdot)_{\text{crit}}$	Critical value
$(\cdot)_{\text{out}}$	Outer solution
$(\cdot)_{\text{wi}}$	Wake-induced (inner) solution
$(\cdot)_{\text{max}}$	Maximum value
$(\cdot)_{\text{min}}$	Minimum value

1

Introduction

> *I share my name with an aerobatic bird that can whiz across a whole summer sky in seconds. A swift is so equipped for speed that it can scarcely cope with being stationary.*
>
> **— Graham Swift**
> (Writer)

According to traditional aerodynamic theories insects cannot fly. However, it is common knowledge that insects can not only fly, but demonstrate extraordinary agility and control in doing so. For example, the housefly (*Musca domestica*) can land upside down and perform evasive manoeuvres. This phenomenon highlights a gap in classical fluid dynamics when applied to nature, as such high-lift flight dynamics remain difficult to replicate in engineered systems.

The aerodynamic mechanisms behind these capabilities offer inspiration for the development of more manoeuvrable and efficient flight platforms. The formation and control of leading-edge vortices (LEVs), first identified by Ellington *et al.* [1] during studies of flapping insect flight, is the key flow structure in unsteady biological flight. LEVs represent coherent vortical structures that form at the leading edge, enhancing lift far beyond predictions made by steady-state theories. The delay in stall caused by LEV formation, referred to as dynamic stall [2], allows insects to maintain lift even under highly unsteady kinematic conditions. It was found that, in insect flight, vortex stability is aided by LEV convection in the spanwise direction towards the tip, as shown in Figure 1.1.

The LEV is formed through shear layer roll-up at the leading edge of a wing, which sheds and convects downstream. As the LEV grows in strength and re-attaches to the wing surface, flow travels towards the leading edge between the LEV and wing, causing secondary separation. This process leads to a counter-rotating secondary vortex under the primary vortex [5]. LEV formation also occurs in numerous other lifting wing applications, such as over helicopter rotor blades [6],

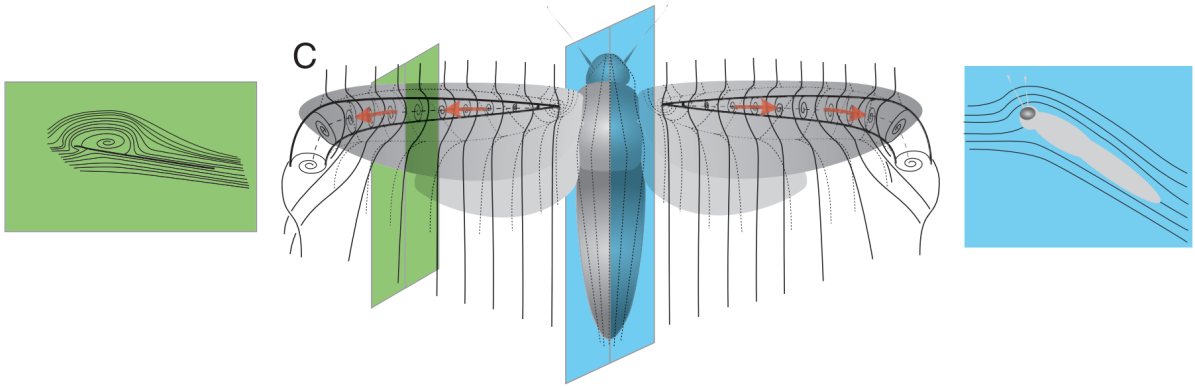

Figure 1.1: Hawkmoth (*Manduca sexta*) LEV structure described by Van den Berg and Ellington [1, 3] where the LEV is similar to that found on a delta wing. Spanwise (axial) flow is marked by orange arrows. Vertical planes show the simplified flow topology at the centreline (blue) and mid-span (green) positions. Adapted from Bomphrey *et al.* [4], with permission.

in wind energy systems and micro air vehicles (MAVs). While initial studies aimed to suppress LEV formation in engineering contexts [7], more recent work in bio-inspired design seeks to harness the lift-enhancing potential of the LEV [8]. Accordingly, engineers attempt to stabilise the LEV near the wing surface to benefit from its improved transient lift. Crucially, natural flyers achieve enhanced LEV stability not only through kinematics, but also through wing morphology, particularly wing sweep.

Biological flyers utilise various wing planforms to enable agile flight dynamics. Swept wings are ubiquitous in nature, from the common swift (*Apus apus*) to the hawk moth (*Manduca sexta*). The common swift is known to adapt its wing sweep and aspect ratio dynamically, achieving improved aerodynamic efficiency across different flight regimes [9–12]. Biological flyers frequently operate in low-Reynolds-number ($Re = \mathcal{O}(10^4)$) regimes, where unsteady flow features dominate, and traditional aerodynamic models lose predictive power. Understanding and modelling these regimes is key to enhancing flight envelopes of small-scale aerial vehicles, especially under gusty or transient conditions. Inspired by insect flight, recent studies have considered the low Reynolds numbers and high reduced frequencies typical of biological flight [13].

Figure 1.2 situates biological flapping flight and conventional man-made flight within a combined Reynolds number–mass parameter space, highlighting the fundamentally different aerodynamic regimes in which they operate. Biological flyers, particularly insects and small vertebrates, inhabit a low-Reynolds-number regime where unsteady aerodynamic mechanisms, including LEV formation and persistence, play a dominant role in force generation. In contrast, conventional fixed-wing aircraft operate at much higher Reynolds numbers, where quasi-steady aerodynamic assumptions are generally valid.

The present work intentionally targets the low-Reynolds-number, unsteady regime relevant to biological flight and micro air vehicle scales. Although wing sweep is traditionally associated with

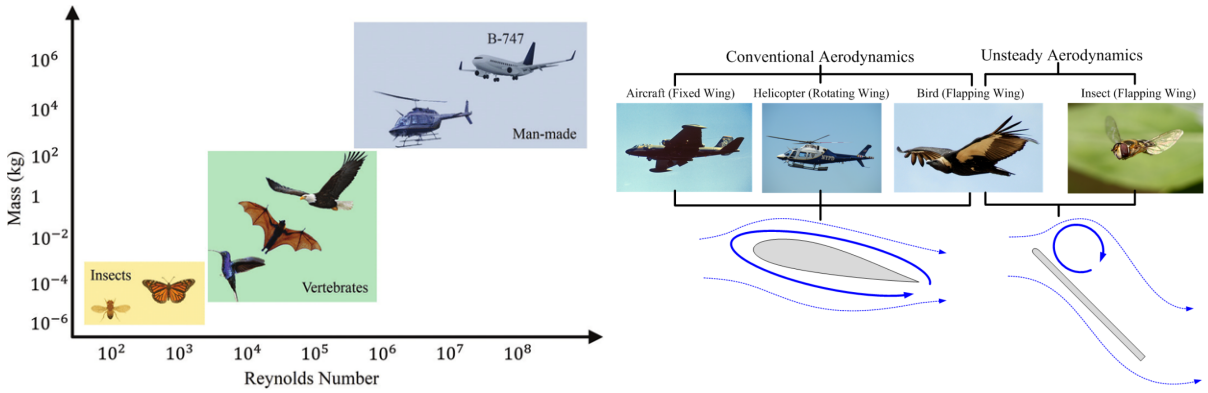

Figure 1.2: *Left:* Characteristics of biological flapping flight and conventional man-made flight based on the Reynolds number and body mass, illustrating the transition between unsteady and conventional aerodynamic regimes. Picture courtesy of Science & Society Picture Library. *Right:* Illustration of different aerodynamic flight regimes, reproduced from Frank [14], with permission.

high-speed aerodynamics, swept or highly three-dimensional planforms also arise naturally in biological flyers operating far outside the assumptions of conventional aerodynamics. This motivates the present focus on understanding how sweep angle influences LEV formation, stability, and breakdown in low-Reynolds-number, unsteady flows. This is a regime that remains comparatively under-explored. Moreover, the dominance of unsteady aerodynamics in this regime suggests that sweep may play an important role in modulating transient force responses to gust-like disturbances, further motivating its investigation in the context of micro air vehicle (MAV) stability and control.

Despite these observations, there remains a notable gap in the literature. While unswept or purely pitching wings have been studied extensively, the combined effects of wing sweep, plunging motion and three-dimensional unsteady flow at biologically relevant Reynolds numbers remain under-explored. Additionally, the predictive accuracy of low-order models (LOMs) in these regimes is poorly understood.

This work addresses these gaps by investigating swept plunging wings using a combination of high-fidelity numerical simulations and LOM development. Specifically:

- Improved delayed detached eddy simulation (IDDES) is used to capture complex LEV dynamics and spanwise interactions at $Re = 2 \times 10^4$, a regime typical of MAV-scale wings.
- The role of sweep angle, aspect ratio and aerofoil thickness in LEV formation and breakdown is examined.
- The suitability of LOMs, including the large-amplitude unsteady lifting line theory (LAULLT) and Leading-edge suction parameter (LESP), is evaluated for swept wing geometries.
- A force and moment partitioning method (FMPM) is used to interpret vortex-induced lift and thrust across the span.

The central question guiding this research is:

How do sweep angle and unsteady plunging motion affect LEV dynamics and spanwise lift distribution at low Reynolds numbers, and can these effects be accurately captured using low-order models?

Firstly, the practical relevance of this work is outlined in Section 1.1, before relevant research is critically analysed in Section 1.2. Following this, the remaining gaps in the literature addressed by this thesis are discussed in Section 1.3, including the objectives and original contributions of this work, along with an overview of the thesis structure.

1.1 Motivation and applications

One of the most high-profile use cases of unmanned aerial vehicles (UAVs), or drones, has been their deployment in modern military conflicts. Most notably, the Russo-Ukrainian War has seen extensive and successful drone strikes conducted by both sides against military targets [15, 16]. UAVs also have the potential for profound humanitarian action, with *Nature* [17] reporting deliveries of numerous types of vaccines in Malawi since 2019 and Ebola vaccines in the Democratic Republic of the Congo. The UK's National Health Service launched a preliminary programme of a drone delivery system for COVID-19 tests, personal protective equipment and medicines in Argyll and Bute, Scotland. This allowed vital supplies to be sent and received quickly to some of the UK's most remote communities [18]. Postal services and courier companies are also looking to benefit from drone delivery, with Royal Mail trialling postal deliveries in Orkney between the mainland and smaller islands [19]. Search and rescue in remote or otherwise inaccessible locations is another application of UAVs. In the UK this is primarily of concern for mountain rescue teams, where adverse weather conditions can also hamper efforts [20]. International applications include operation within disaster zones, exemplified by drone use for aerial photography and explosion risk detection in Turkey and Syria after the 2023 Turkey-Syria earthquakes [21].

In these applications, unmanned aerial vehicle (UAV) performance depends heavily on aerodynamic efficiency and manoeuvrability. While most UAVs currently rely on propellers and fixed, unswept wings based on steady aerodynamic principles, recent studies suggest that unsteady aerodynamic phenomena, such as the formation and stability of LEVs, can be leveraged to enhance lift, agility, and energy efficiency, particularly in low-speed flight [8, 22]. For example, swept wings, although traditionally associated with transonic aircraft to delay drag divergence [5], have been shown to stabilise LEVs in low-speed flapping or manoeuvring scenarios [1], providing additional lift and control benefits that could directly improve UAV performance.

Unsteady aerodynamic effects are also relevant in other fields, such as renewable energy. Flapping foils inspired by fish propulsion can extract significant energy from incident fluid flows due to LEV formation [23–25]. However, most studies focus on two-dimensional aerofoils, and the influence of three-dimensional geometries, including swept wings, remains poorly understood [26],

limiting real-world deployment. Similarly, the aerodynamic efficiency of large wind turbines can be affected by unsteady flow, and vertical-axis wind turbines have been proposed as an alternative to mitigate these effects [27–31]. Understanding LEV dynamics in three dimensions is therefore critical for optimising such energy-harvesting devices.

Therefore, this thesis aims to investigate LEV dynamics over swept wing platforms for the application of low-speed UAVs and MAVs. The effects that geometric and kinematic changes have on LEV characteristics are studied to this end. The three-dimensionality of the LEV is of particular focus due to the inherent three-dimensional nature of swept wings. This is achieved computationally using the IDDES methodology. Throughout the thesis, the performance of LOMs is studied to determine model suitability as a fast calculation method in place of computational fluid dynamics (CFD) simulations as a first analysis stage. By linking the fundamental understanding of LEV behaviour to practical UAV and energy applications, this work aims to inform design strategies that enhance performance, efficiency, and manoeuvrability in low-speed flight.

1.2 Review of relevant literature

To position this research within the context of prior work, this section surveys the principal developments in LEV theory and modelling, emphasising phenomena and methods relevant to low-Reynolds-number, unsteady flows over swept wings. The review is structured to recall the discovery and early modelling of the LEV in Section 1.2.1, examine LEV dynamics in low-Reynolds-number and bio-inspired flows in Section 1.2.2, and review analytical and low-order methods in Section 1.2.3. Then, LEV initiation is discussed with emphasis on LESP in Section 1.2.4, and lifting-line (in Section 1.2.5) and unsteady lifting-line (in Section 1.2.6) frameworks used to generalise two-dimensional theories to finite wings. Vorticity-based FMPM is described in Section 1.2.7, flow-control strategies used to stabilise or manage LEVs are surveyed in Section 1.2.8, and experimental and computational approaches for LEV analysis are summarised in Section 1.2.9.

1.2.1 Discovery and early modelling of the LEV

The relation between circulation and lift was established early in aerodynamic theory and formalised through Lanchester and Prandtl's work [32, 33]. Subsequent investigations into highly swept and delta wings, driven by the need to delay drag divergence and maintain lift at high angles of attack, revealed that leading-edge separation may form a coherent vortex that produces significant additional suction over the wing surface. Seminal experimental and theoretical studies showed that vortex lift is a physically distinct mechanism from classical attached-flow lift and must be represented through models that capture separation, the vortex core, and downstream interactions [34, 35].

Early analytical representations of the LEV treated the problem using vortex-sheet or point-vortex approximations [36, 37]. Such models gradually matured to include vortex-core structure (convective outer solution and diffusive inner solution) [38, 39] and viscous corrections [40]. The leading-edge suction analogy proposed by Polhamus [41] provided a practical semi-empirical way to calculate the LEV contribution to lift by partitioning potential and vortex-induced forces. Subsequent refinements extended the leading-edge suction analogy to finite planforms and included panel-method corrections to lessen over-prediction issues for high-aspect-ratio wings [42, 43].

Concurrently, experimental observations of vortex breakdown and complex three-dimensional vortex topologies highlighted limitations of purely steady, inviscid models [44, 45]. These phenomena underscored the role of Reynolds-number-dependent viscous diffusion, pressure gradients, and wake interactions in determining LEV evolution and its contribution to aerodynamic loads. Collectively, early work established the LEV as a robust, geometry-dependent lift mechanism, but left unresolved how unsteady and three-dimensional effects modify this lift-generation process at the lower Reynolds numbers typical of MAVs and small UAVs.

The early literature provides both the conceptual model of vortex lift and the mathematical tools (vortex sheets, panel methods, leading-edge suction analogy) that form the basis of later unsteady and three-dimensional extensions. However, these models are primarily steady and inviscid and therefore cannot predict unsteady LEV formation, breakdown, and their impact on instantaneous aerodynamic loads in low-Reynolds-number situations.

1.2.2 LEV dynamics in low-Reynolds-number, unsteady flight

At Reynolds numbers of $\mathcal{O}(10^4)$, characteristic of MAVs and insects, flow fields become highly sensitive to unsteady kinematics and three-dimensional effects. The LEV is recognised as a dominant lift-generating feature under such conditions. Kinematic parameters such as reduced frequency and stroke amplitude strongly influence LEV attachment and detachment. Eldredge and Jones [13] demonstrated analytically that LEV stability depends on a delicate balance between vorticity convection and viscous diffusion, which is more readily disrupted in low-Reynolds-number, three-dimensional flows.

Scaling effects play a central role in this regime. As size and velocity decrease, viscous diffusion and convective timescales become comparable, allowing vortices to persist longer but reducing their stability margins. This means that LEVs over low-Reynolds-number wings often remain attached for longer than expected, but are far more sensitive to small disturbances, structural vibrations, or unsteady inflow [6, 46]. Such characteristics are fundamental to understanding the aerodynamic efficiency of insects and the challenges of designing MAVs.

While swept wings are often associated with supersonic or high-speed applications, they are also relevant at low Reynolds numbers and low Mach numbers. Sweep modifies the spanwise flow over the wing, affecting the three-dimensional structure of the LEV and its stability, even at these small scales. For small flyers and bio-inspired MAVs, controlling this spanwise flow can

improve vortex attachment, lift generation, and manoeuvrability, providing a mechanism similar to natural fliers to manage aerodynamic performance.

In swept-wing configurations, the interaction between spanwise flow and vortex stability becomes critical. Han and Breitsamter [47] experimentally investigated sweep-angle effects across a range of angles of attack and identified an optimal aspect ratio near 3, consistent with insect-like planforms, that provides a favourable compromise between LEV stability and lift generation. This result suggests that vortex coherence, rather than wing loading alone, governs the aerodynamic benefit of sweep at low Reynolds numbers.

Chiereghin *et al.* [48, 49] observed that increasing sweep enhances spanwise transport of vorticity, but may also promote three-dimensional instabilities that deform the LEV core. In their studies, sweep was introduced through geometric shear of the wing planform relative to the freestream, generating a sustained spanwise velocity component along the leading edge. Son *et al.* [50] numerically extended this analysis to higher reduced frequencies and identified spanwise wave-like instabilities and LEV deformation, but restricted their investigation to unswept aerofoils and wings, leaving the applicability of these findings to swept configurations unresolved. By contrast, Beem *et al.* [51] considered nominally unswept wings inclined to the oncoming flow, as shown in Figure 1.3, such that spanwise flow arose primarily due to kinematics rather than geometric shear. Under these conditions, stronger spanwise flow did not necessarily stabilise the LEV. Collectively, these studies indicate that the influence of spanwise transport on LEV stability depends not only on its magnitude, but also on how it is generated and coupled to the three-dimensional vortex structure. Consequently, LEV behaviour in swept configurations cannot be directly extrapolated from unswept cases, and sweep may be both beneficial and destabilising depending on the precise geometry and kinematics.

A further complication arises from the external flow environment. For small flyers, atmospheric disturbances such as gusts or turbulence are large relative to body size and can strongly perturb the delicate LEV structure. Extensive studies have characterised gust encounters for conventional aerofoils and unswept finite wings [52–62], showing rapid changes in lift and moment under unsteady inflow. However, comparable studies for swept wings remain limited, leaving the combined effects of sweep, unsteady kinematics, and atmospheric forcing poorly understood. Watkins *et al.* [63] and Jones *et al.* [64, 65] showed that gusts with characteristic scales similar to the wing chord can rapidly convect or dissipate the LEV, causing abrupt changes in lift and moment. The limited number of studies addressing gust encounters on finite, swept geometries indicates that there is still no systematic characterisation of LEV behaviour under these conditions

In summary, while the LEV has been extensively characterised for wings undergoing transient low-Reynolds-number kinematics, LEV dynamics over swept geometries and under unsteady atmospheric forcing remain insufficiently understood. Quantitative prediction of LEV onset, stability, and breakdown under such combined effects represents a major challenge and forms one motivation for this work.

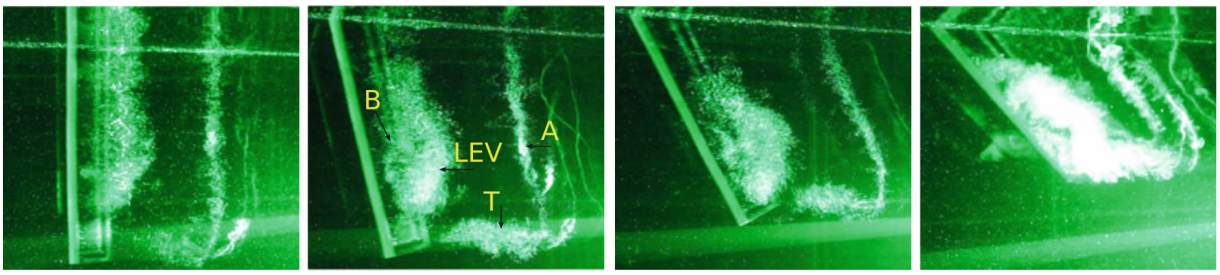

(a) Suction side

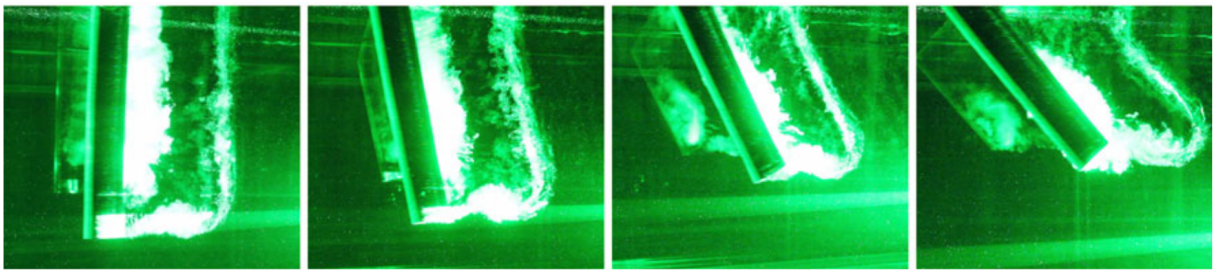

(b) Pressure side

Figure 1.3: Vortex topology visualisations (A = starting, B = stopping, T = tip and LEV) at sweep angles of $\Lambda = 0°, 15°, 30°$ and 45° from left to right. As the sweep angle increases, the connection between vortex structures increases. Adapted from Beem *et al.* [51], with permission.

1.2.3 Analytical and low-order modelling approaches

Classical unsteady aerofoil theories such as Wagner's indicial response [66] and Theodorsen's frequency-domain formulation [67] remain foundational in unsteady aerodynamics. These models decompose unsteady lift into circulatory and non-circulatory components, identify the role of wake-induced vorticity, and introduce reduced frequency, k, as a key non-dimensional quantity governing unsteadiness [68]. Wagner's theory is based on a linearised, planar, inviscid unsteady flow assumption, with small perturbations imposed on a uniformly translating aerofoil. The resulting indicial lift response represents the gradual build-up of circulation following an impulsive change in angle of attack.

Theodorsen [67] developed a complementary frequency-domain theory for harmonic motions. The model is based on thin aerofoil theory under small perturbations, assumes attached flow with a planar wake, and is formulated for small-amplitude harmonic oscillations at constant forward velocity. Theodorsen's function,

$$C(k) = \frac{H_1^{(2)}(k)}{H_1^{(2)}(k) + iH_0^{(2)}(k)}, \tag{1.1}$$

expresses the reduction of the circulatory lift due to unsteady wake convection. The numerator $H_1^{(2)}$ represents the induced velocity contribution at the trailing edge, while the denominator combines this with the added phase lag from the shed wake via $H_0^{(2)}$. Thus $C(k)$ modulates the classical quasi-steady lift, reducing its magnitude and introducing a phase delay as reduced

frequency increases.

Although derived under small-amplitude and attached-flow assumptions, Wagner's and Theodorsen's theories perform better than anticipated in several separated-flow cases due to the dominance of added-mass effects or the continuing relevance of the trailing-edge Kutta condition, which specifies zero pressure jump at the trailing edge [69, 70]. Their limitations arise not only from the assumption of uniform forward velocity, but also from the requirement of a planar, non-deforming wake, the absence of leading-edge separation or LEV formation, and linearity constraints that preclude modelling large-amplitude or strongly non-linear kinematics.

To extend predictive capability into larger amplitude motions and moderate separation, Ramesh *et al.* [71] developed large-angle unsteady thin-aerofoil theory (LAUTAT), which removes small-angle approximations and explicitly accounts for leading-edge suction contributions to both lift and drag [71]. LAUTAT remains inviscid, but it forms a powerful basis for coupled models where discrete-vortex shedding is introduced by an explicit criterion (such as LESP) to represent leading-edge separation.

Vortex-based low-order methods, such as discrete vortex methods (DVM) and unsteady vortex lattice methods (UVLM), model wake roll-up and shed vorticity efficiently and have been widely used to examine flapping and revolving wing problems [72–75]. Classical discrete-vortex approaches [76] represent the wake as a collection of point vortices convected by the local velocity field. More recent formulations, such as the Xia–Mohseni [77] vortex sheet method and the Li and Wu [78] discrete-vortex model, improve fidelity by incorporating vortex-blob regularisation, non-planar wake geometry, and more accurate enforcement of the Kutta condition. These methods calculate the velocity field induced by vortex filaments, known as the Biot–Savart law, and track vortex elements in a Lagrangian fashion, enabling efficient modelling of wake roll-up, unsteady circulation changes, and vortex–wing interaction. Their key limitation is the need for a robust separation criterion. This motivates hybrid approaches that combine low-order wake convection with LESP-like initiation rules.

Low-order models remain essential for rapid parametric studies. Their continued development hinges on reliable, physically grounded criteria for LEV initiation and for representing spanwise processes in finite wings.

1.2.4 LEV initiation and the leading-edge suction parameter

Building on LAUTAT, Ramesh *et al.* [79] introduced LESP as a physically meaningful metric linking unsteady circulation growth to LEV initiation. LESP represents the instantaneous suction force at the leading edge, proportional to local vorticity accumulation. Formally, LESP is defined as a non-dimensional measure of leading-edge suction derived from the first Fourier coefficient of the bound vorticity distribution, A_0. In the unsteady thin-aerofoil formulation of Ramesh *et al.* [71], the bound vorticity is expressed as a Fourier series, with the leading coefficient A_0 directly proportional to the instantaneous leading-edge suction force. Thus,

$$LESP(t) = A_0(t), \tag{1.2}$$

providing a compact scalar measure of the instantaneous circulation loading at the leading edge.

When this parameter exceeds a critical value, $LESP_{crit}$, the flow can no longer remain attached, and a vortex of strength proportional to the excess LESP is shed, reducing the suction to the critical level.

$LESP_{crit}$ is determined empirically by matching the thin-aerofoil prediction of leading-edge suction to either CFD or experimental pressure distributions. Because A_0 is the leading-order coefficient governing the singular growth of suction at the sharp leading edge, the condition $A_0(t) = LESP_{crit}(t)$ provides a well-defined onset criterion for LEV formation across arbitrary pitch–plunge kinematics.

The conceptual importance of LESP lies in its unification of several prior ideas, namely the correlation between circulation growth rate, leading-edge pressure gradient, and the onset of flow separation. Whereas earlier thin-aerofoil theories captured only smooth variations in lift due to attached flow, LESP provides a quantitative threshold criterion for LEV initiation [79, 80]. LESP is derived directly from the unsteady Bernoulli equation, linking local velocity at the leading edge to the effective suction distribution. In practice, LESP acts as a surrogate for the bound-circulation gradient, and its critical value effectively marks the transition from attached flow to LEV-dominated lift generation.

The LESP framework was implemented through the LESP-modulated discrete vortex method (LDVM) [79], allowing the discrete shedding of LEVs to be predicted dynamically. This model captures intermittent vortex shedding observed in experiments, features that traditional unsteady aerofoil theories cannot reproduce. Subsequent work [80, 81] generalised LESP to include time-varying and zero free-stream conditions, expanding applicability to perching and hovering manoeuvres.

However, the thin-aerofoil assumptions underlying LDVM impose an inviscid, slender-body framework in which separation effects are represented indirectly through discrete vortex shedding rather than by resolving boundary-layer dynamics. Model accuracy deteriorates when boundary-layer growth becomes sufficiently large to invalidate the Kutta condition and thin-sheet approximation, for example under strong adverse pressure gradients or in the presence of laminar separation bubbles upstream of LEV roll-up. In such regimes, the inviscid potential-flow foundation of LDVM can no longer represent the dominant viscous effects.

Compared with purely kinematic models, LDVM uniquely couples the vorticity-field evolution to the instantaneous suction constraint. LDVM can therefore represent the formation, advection, and reattachment of the LEV without explicit viscous modelling, a considerable computational advantage for low-order analysis [82]. Nonetheless, because the method assumes a potential background flow and neglects boundary-layer development, its accuracy decreases once large-scale separation or vortex interaction dominates the near field.

Several validation efforts have confirmed the physical relevance of the LESP framework. Ramesh *et al.* [71] first demonstrated agreement between LESP-based predictions and experiments for pitching aerofoils, supported by complementary CFD studies across different pivot locations, pitch amplitudes, and Reynolds numbers. Their results showed that flow separation and vortex roll-up consistently begin once $LESP_{crit}$ is exceeded, which is insensitive to motion history. Subsequent work by Ramesh *et al.* [79] validated the LESP criterion against a broader set of literature data, including the sinusoidal pitch-plunge motions of Kinsey and Dumas [83] and the unsteady pitch results of Wang and Eldredge [84], further demonstrating that the onset of LEV formation correlates closely with a critical LESP across diverse kinematics and aerofoil geometries. Bird *et al.* [85] subsequently showed, using low-order unsteady lifting-line models, that this critical suction threshold is also reflected in finite-wing behaviour for unswept configurations. In their study, LESP was evaluated at the wing centreline as a time-resolved indicator, with a spanwise distribution considered at a single time instant, reinforcing its interpretation as a locally defined onset criterion governed primarily by geometry and Reynolds number.

Attempts to extend LESP to three-dimensional flows using unsteady vortex lattice methods (UVLM) [73–75] have typically relied on empirical scaling to match the two-dimensional critical LESP, while neglecting spanwise pressure gradients and flow curvature. In particular, Hirato *et al.* [73, 74] incorporated LESP into UVLM by computing the first Fourier coefficient of bound vorticity, A_0, locally along the span from the UVLM-induced velocity field. A discrete LEV was shed from each spanwise panel once the local A_0 exceeded the prescribed $LESP_{crit}$, effectively applying two-dimensional LDVM onset criterion to a three-dimensional lifting surface. While this approach enables a spanwise prediction of LEV initiation, the influence of sweep, tip effects, and three-dimensional vortex dynamics on the interpretation and applicability of LESP remains unresolved.

More recently, numerical studies have attempted to relate the variation of LESP across the span to the onset of LEV asymmetry. For example, unsteady vortex lattice implementations have shown that the local effective angle of attack and downwash gradient modify the local $LESP_{crit}$ [74], implying that sweep could either delay or advance LEV onset depending on geometry. However, these remain unverified hypotheses due to the absence of direct experimental or high-fidelity CFD simulations for swept wing configurations.

In summary, LESP provides a bridge between theoretical and empirical descriptions of LEV onset. However, its predictive capability for finite, swept wings, where spanwise advection modifies the effective suction distribution, has not been rigorously established. This thesis, therefore, explores its applicability in such configurations.

1.2.5 Lifting-line theory

Lifting-line theory (LLT) represents the cornerstone of three-dimensional aerodynamic modelling. Prandtl's original formulation [33] idealised a finite wing as a bound vortex filament connected to

trailing vortices, as shown in Figure 1.4, relating local circulation to downwash via the Biot–Savart law. The model is formulated for a straight, planar leading edge in an unswept, high-aspect-ratio wing configuration, with linear aerodynamic behaviour assumed throughout. These restrictions permit closed-form expressions for the spanwise lift distribution and induced drag.

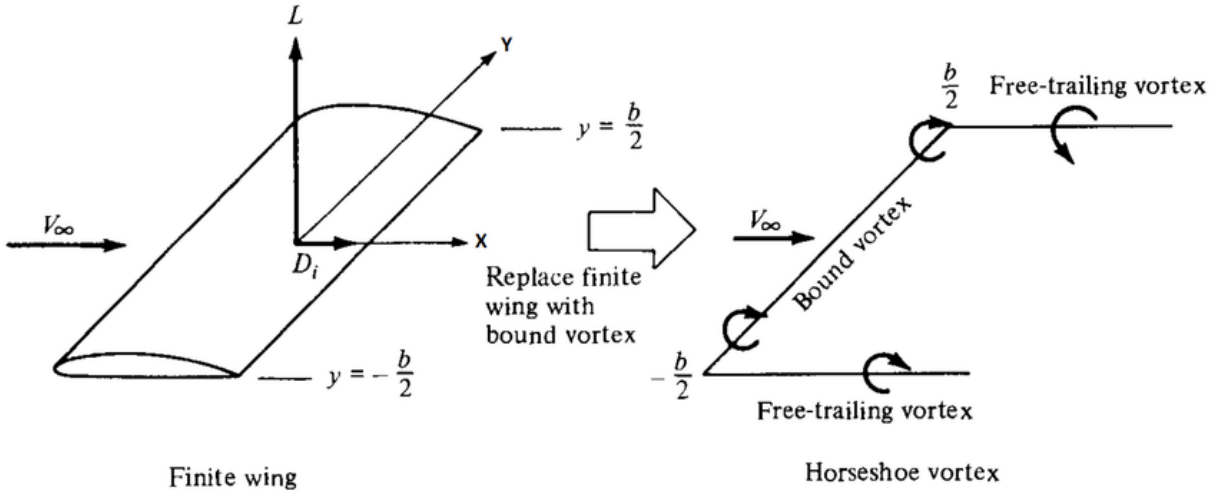

Figure 1.4: Illustration of Prandtl's method for replacing a finite wing with a horseshoe vortex. Reproduced from Anderson [5], with permission.

Prandtl's theory reduces the full three-dimensional aerodynamic field to a one-dimensional problem by introducing a spanwise circulation distribution. The linear-lift assumption restricts the model to regimes in which the flow remains attached and lift varies approximately proportionally with angle of attack. Once non-linear or viscous effects become significant, the idealised formulation breaks down.

More systematic refinements were introduced through the method of matched asymptotic expansions (MAE), which couples the two-dimensional inner flow (chord-scale) with the three-dimensional outer flow (span-scale). Van Dyke [86] standardised this procedure for straight, unswept, planar wings of high aspect ratio by matching the chord-scale inner solution with the span-scale outer solution to recover the bound circulation distribution, as illustrated in Figure 1.5.

Cheng [88] extended MAE to swept wings using separate coordinate systems for the inner and outer regions, while Guermond [89] generalised the formulation to curved and non-planar wings using Hadamard's finite-part integrals [90]. These developments provided a formal mathematical framework for correcting the original linear theory.

Together, these analytical models show that classical LLT captures the leading-order behaviour of finite-wing aerodynamics but is fundamentally steady, inviscid, and limited to attached flow [86]. LLT cannot predict vortex shedding, leading-edge separation, or the formation and evolution of a LEV.

Panel methods, such as the Hess and Smith [91] formulation, relaxed geometric limitations by discretising the surface potential field, but they also rely on inviscid and attached-flow assumptions

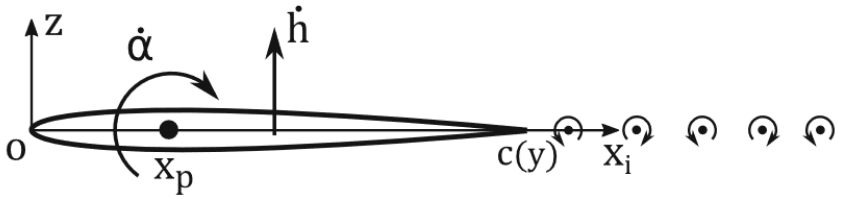

(a) Schematic diagram of the inner domain, showing the velocities of the aerofoil, pitch-axis location, chord length and spanwise shed vorticity.

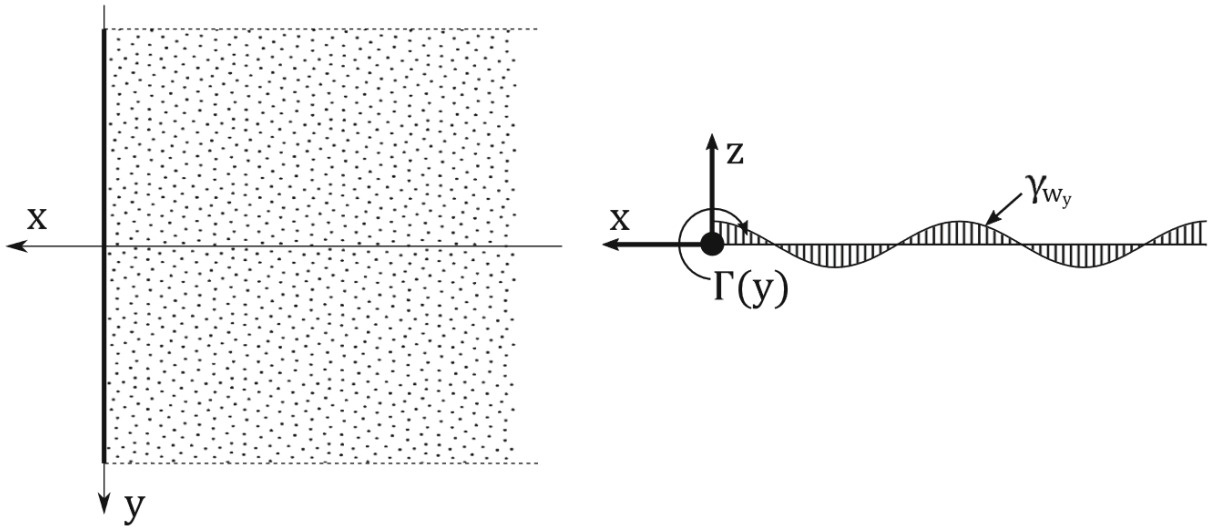

(b) *Left:* Plan view of the outer domain consisting of the lifting line and its wake. *Right:* View of the two-dimensional problem in the outer domain.

Figure 1.5: Schematic diagrams showing the inner and outer domains to be matched, based on the methodology developed by Van Dyke [86]. Adapted from Bird and Ramesh [87], with permission.

and therefore cannot capture vortex breakdown or LEV-driven lift augmentation.

Unsteady lifting-line theory extends these ideas towards time-dependent aerodynamics, but classical LLT itself serves primarily as a foundation for understanding how chord-scale and span-scale flow structures interact. This motivates the development of fully time-dependent variants described in the next section.

1.2.6 Unsteady lifting-line theory

Unsteady lifting-line theory (ULLT) extends classical LLT to wings undergoing time-dependent motion. Early developments, motivated primarily by rotorcraft aerodynamics, assumed a chordwise-uniform induced downwash and were therefore restricted to low reduced frequencies, where the wake remains approximately planar and chordwise vorticity convection is weak [92, 93]. These limitations were later clarified by Ahmadi and Widnall [94], who demonstrated that such formulations become inconsistent as reduced frequency increases due to the harmonic variation of induced downwash associated with both chordwise and spanwise wake vorticity.

Cheng and Murillo [95] extended steady asymptotic lifting-line methods to unsteady flow

over curved wings at low reduced frequency. Their formulation applied to thin, planar wings undergoing small-amplitude plunging motion with a planar wake, and provided an early attempt to account for geometric curvature within an unsteady lifting-line framework. However, the coordinate system adopted for the inner solution imposed strict limitations on allowable curvature, which was required to scale as $\mathcal{O}(b^{-1})$, where b is the wing semi-span. As a result, the theory is restricted to weakly curved geometries and low reduced frequencies, highlighting the sensitivity of unsteady lifting-line formulations to inner–outer matching assumptions and motivating the development of more systematic MAE-based approaches.

A major advance was provided by Sclavounos [96], who formulated a ULLT using Van Dyke's method of MAE. In this framework, the inner solution is governed by Theodorsen's two-dimensional unsteady aerofoil theory, while the outer solution introduces an interaction kernel that accounts for harmonic variation of both chordwise and spanwise wake vorticity. The resulting formulation is uniformly valid across a broad range of frequencies, with exceptions occurring only at very high frequencies where the MAE assumptions no longer apply. Subsequent numerical studies confirmed both the validity of these assumptions and their sensitivity to wake modelling [97]. Comparative studies by Bird and Ramesh [87] showed that the full MAE-based formulation provides the closest agreement with CFD for thin, high-aspect-ratio wings undergoing harmonic motion at low reduced frequency, while simplified or pseudosteady lifting-line models can perform comparably at higher reduced frequencies.

Extensions of ULLT have sought to relax geometric restrictions by generalising the outer solution. Guermond and Sellier [98] developed a unified ULLT applicable to curved and swept wings and valid across all reduced frequencies, noting that many earlier limitations arose from coordinate choices rather than from the lifting-line assumption itself. As with earlier MAE-based models, the formulation is asymptotically invalid near rectangular wing-tips. However, in practice, LLT is nevertheless often applied successfully even when these idealised geometric conditions are not met [97]. Guermond and Sellier's method relies on the dominance of effectively two-dimensional chordwise flow physics; otherwise, spanwise variation becomes too strong for a lifting-line approximation. Devinant [99] later introduced a first-order unsteady correction to the outer solution, enabling prediction of transient spanwise circulation while retaining a quasi-steady downwash approximation. Although initially formulated for unswept wings, this restriction was subsequently removed [100]. In practice, however, the simplified outer-flow modelling confines these approaches to low reduced frequencies.

More recent developments have introduced non-linear extensions of ULLT to address large-amplitude motion and aeroelastic deformation. Ramesh *et al.* [101] incorporated a geometrically non-linear inner solution derived from the LDVM framework, coupled to a quasi-steady lifting-line correction, enabling representation of non-planar wakes and aspects of vortex-dominated unsteady response at higher reduced frequencies. Building on Devinant's outer formulation, Bird *et al.* [102] developed the large-amplitude unsteady lifting-line theory (LAULLT), which

applies over a broader frequency range and introduces physically realistic phase behaviour. These non-linear formulations nevertheless remain restricted to straight, high-aspect-ratio wings and tend to over-predict lift amplitudes as oscillation amplitude and frequency increase.

Overall, ULLT represents a hierarchy of LOMs for unsteady high-aspect-ratio wings, unified by the assumption that chordwise and spanwise flow physics remain weakly coupled. While extensions exist for curved and nominally swept geometries [98, 100], the lifting-line assumption fundamentally limits applicability to swept wings, where spanwise pressure gradients, streamwise vorticity, and non-planar wake development introduce strong three-dimensional coupling. These effects invalidate the separability of chordwise and spanwise dynamics even in attached-flow regimes, placing swept-wing unsteady aerodynamics outside the reliable scope of lifting-line-based predictive models. Consequently, alternative diagnostic approaches are required to analyse unsteady force production mechanisms in swept wings at low Reynolds numbers.

1.2.7 Force and moment partitioning

To quantify the aerodynamic influence of vortical flow features, Zhang *et al.* [103] proposed the force and moment partitioning method (FMPM). FMPM provides a diagnostic framework for decomposing the instantaneous aerodynamic force on a lifting surface into physically interpretable components. This is achieved by expressing the aerodynamic force balance using a vorticity-based formulation of the unsteady momentum equations and evaluating the resulting volume-integral expressions over prescribed regions of the flow field. This enables contributions associated with vorticity-induced loading to be distinguished from kinematic and viscous effects, allowing a direct connection to be drawn between vortex dynamics and unsteady force production in fully three-dimensional, time-dependent flows.

Several alternative approaches have been proposed for attributing aerodynamic forces to flow structures, including impulse-based methods [104] and vortex force mapping techniques [105]. While these approaches have been applied successfully to a wide range of unsteady flows, their practical implementation often involves additional modelling or interpretive choices, such as the identification of coherent vortex systems, the selection of control volumes, or the definition of regions over which forces are evaluated. While FMPM likewise requires the specification of integration regions, the method does not rely on explicit definitions of vortex strength or topology, instead emphasising a direct partitioning of instantaneous aerodynamic forces by physical mechanism.

Subsequent studies have used FMPM to analyse unsteady and three-dimensional effects. Zhu and Breuer [106] found that sweep angle has only a modest influence on overall force generation but significantly affects the spanwise moment distribution, which becomes increasingly asymmetric due to variation in the effective pitch axis [107]. Menon *et al.* [108] demonstrated that spanwise and cross-span vortices contribute differently to lift, while applications to swept wings at fixed angle of attack [109] and delta wings [110] further highlighted the method's ability

to distinguish the roles of multiple vortex systems. Despite these advances, most studies consider either static or periodic motion, omitting fully transient manoeuvres or gust encounters.

The collective insight from these studies highlights that FMPM provides a useful framework for connecting vortex topology to aerodynamic loading, but its application to low-Reynolds-number, swept-wing flows remains relatively limited. Although FMPM has been applied successfully to a range of unsteady flow problems, systematic use of locally partitioned force contributions in fully three-dimensional swept-wing configurations is less common. In this work, FMPM is therefore employed as a diagnostic framework to aid interpretation of the relationship between flow features and unsteady lift and thrust forces.

Specifically, the FMPM framework has not previously been applied to systematically quantify spanwise lift and thrust distributions for low-Reynolds-number swept wings undergoing unsteady motion. Addressing this gap, the present thesis uses FMPM as an analytical tool to link three-dimensional vortex topology to aerodynamic performance in swept-wing configurations.

1.2.8 Flow control and LEV stabilisation strategies

Flow control studies seek to manipulate LEV stability through either passive or active means. Passive techniques such as leading-edge protuberances, vortilons [111–113] and leading-edge roughness modify separation onset by introducing streamwise vorticity. Active control via synthetic jets [114] or distributed blowing has been shown to delay LEV detachment and reduce unsteady loading. For swept wings, Garmann and Visbal [115] demonstrated that high-frequency forcing can inhibit laminar separation bubble bursting and delay dynamic tip stall.

Flow control represents a logical extension of LEV research into practical applications. Passive devices such as vortilons stabilise the leading-edge shear layer, while active methods including pulsed jets or plasma actuators enable dynamic modification of vortex formation [116]. Despite extensive study, however, the scalability and robustness of these approaches across varying sweep angles, reduced frequencies, and Reynolds numbers remain uncertain.

A prerequisite to effective control is therefore a clear understanding of the intrinsic stability of the LEV itself. Accordingly, this thesis focuses on characterising natural LEV stability rather than implementing specific control strategies, while recognising their potential as future extensions.

1.2.9 Computational and experimental approaches for LEV analysis

Modern investigations of LEV behaviour increasingly rely on a combined computational–experimental approach, reflecting the inherently unsteady, three-dimensional nature of LEV-dominated flows on finite wings. Classical Reynolds-averaged approaches, while computationally efficient, are fundamentally limited by their reliance on time-averaged closures, which obscure the transient shear-layer roll-up, vortex deformation, and breakdown processes that govern LEV formation and stability at low Reynolds numbers. As a result, high-fidelity numerical methods such as

large eddy simulation (LES), direct numerical simulation (DNS), and hybrid Reynolds-averaged Navier–Stokes (RANS)–LES formulations have become essential tools for resolving the flow physics relevant to LEV dynamics.

DNS and LES explicitly capture the unsteady separation and three-dimensional vortex evolution associated with LEV-dominated flows, but their computational cost limits their applicability for parametric studies involving multiple planform geometries or kinematic conditions. Hybrid approaches such as IDDES [117] offer a pragmatic compromise, resolving the dominant large-scale unsteady structures while modelling near-wall boundary layer behaviour using RANS-based closures. Hence, hybrid methods enable systematic investigation of LEV formation, breakdown, and spanwise transport while remaining computationally tractable. Accordingly, IDDES is adopted in the present thesis as the primary numerical framework for resolving the unsteady three-dimensional flow structures governing LEV behaviour.

High-fidelity simulations across a range of finite-wing planforms demonstrate that LEV dynamics are strongly influenced by sweep angle, aspect ratio, and associated three-dimensional transport mechanisms. Sweep has been shown to promote spanwise convection, alter breakdown pathways, and attenuate unsteady wake fluctuations, while sufficiently high aspect ratio introduces additional mid-span effects such as periodic vortex shedding, arch-vortex formation, and shear-layer instabilities [118–122]. These studies collectively indicate that LEV breakdown on finite wings arises from the interaction of multiple three-dimensional mechanisms whose relative importance depends on geometry and kinematics.

While additional geometric features such as taper further influence tip vortex strength and the spanwise extent of unsteady flow [123], their inclusion introduces coupled effects that complicate physical interpretation. Accordingly, the present work deliberately considers only sweep effects using rectangular planforms, enabling unambiguous interpretation of sweep-induced modifications to LEV behaviour and facilitating comparison with analytical and low-order modelling frameworks.

LES studies of dynamically forced swept and unswept wings further demonstrate that sweep fundamentally reorganises the three-dimensional vortex system, introducing additional breakdown pathways that are not captured by quasi-two-dimensional interpretations. In particular, multiple arch-vortex structures with chord-scale wavelengths have been observed, with their breakdown mediated by wall-induced instabilities and interactions with the trailing-edge vortex (TEV) [119, 124, 125].

LES simulations by Visbal and Garmann [125] show that increasing sweep angle promotes outboard migration of the LEV legs and the emergence of secondary stall regions at high aspect ratio. A representative example from their study, reproduced in Figure 1.6, illustrates the simultaneous presence of the LEV, tip vortex, and arch-vortex structures, emphasising the multi-mechanism nature of vortex breakdown in dynamically forced swept wings.

Experimental measurements remain essential for validating high-fidelity numerical simulations

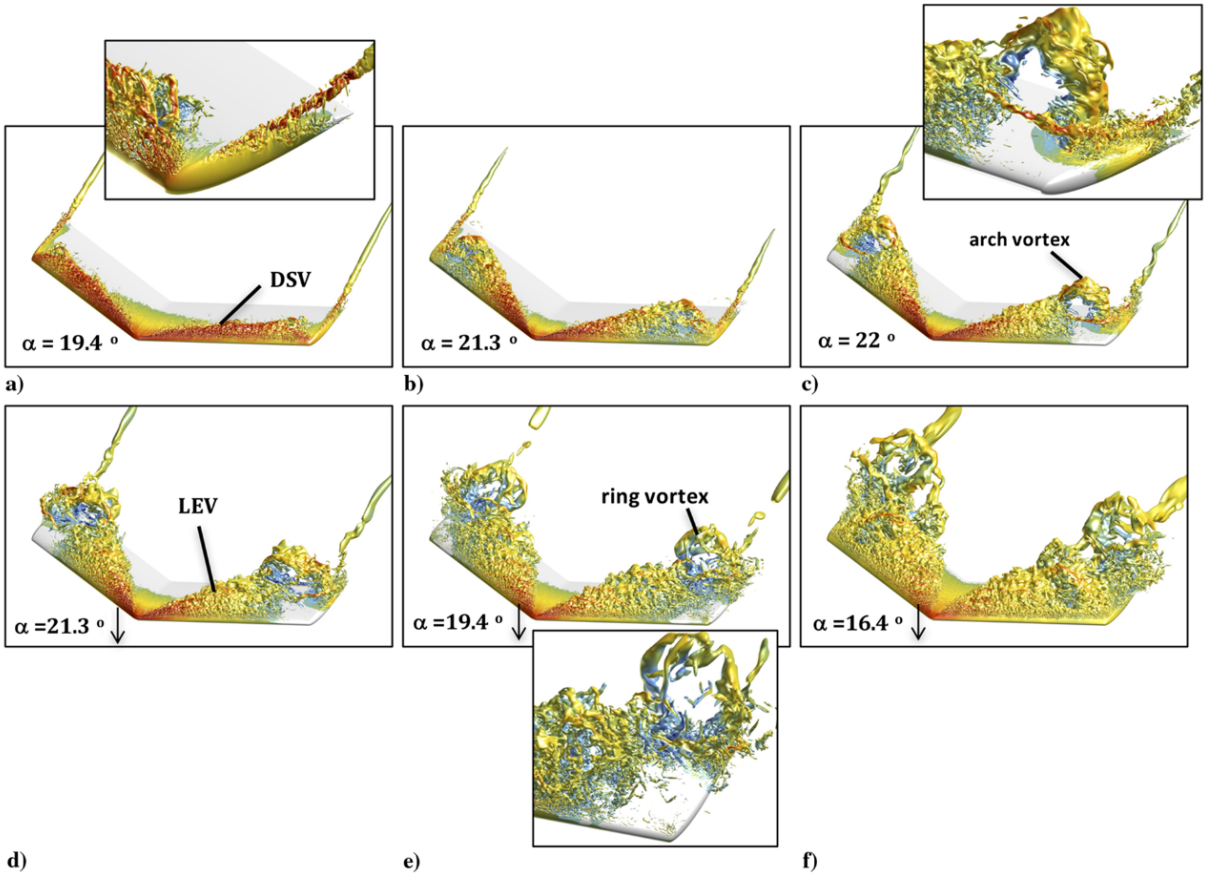

Figure 1.6: Instantaneous three-dimensional flow structure for a pitching $\Lambda = 30°$ wing using an iso-surface of normalised stagnation density. Reproduced from Visbal and Garmann [125], with permission.

of LEV-dominated flows. Time-resolved stereo particle image velocimetry (PIV), in particular, provides direct evidence of three-dimensional vortex interactions and breakdown processes, despite inherent limitations in spatial resolution and optical access [126]. Such measurements play a critical role in establishing confidence in advanced CFD approaches, but they also highlight the challenge of extracting force-generation mechanisms directly from complex flow-field data.

Consequently, analytical and diagnostic frameworks are required to interpret the large volumes of information produced by high-fidelity simulations. In the present thesis, this need is addressed by combining IDDES with FMPM. While IDDES resolves the unsteady three-dimensional flow topology, FMPM is employed as a diagnostic tool to quantify vortex-induced force contributions and relate them systematically to the underlying flow structures. This complementary approach enables physical interpretation of LEV-driven force production that would not be accessible through CFD or experimental measurements alone.

1.2.10 Summary and research gaps

The LEV is a central mechanism for lift enhancement in natural and engineered flyers, yet its behaviour depends sensitively on wing geometry, Reynolds number, and unsteady kinematics. Existing analytical and low-order models (LOMs) capture aspects of LEV-driven lift in either steady or quasi-steady regimes, but they cannot predict the formation, evolution, and breakdown of fully three-dimensional, unsteady LEVs that dominate flight at low Reynolds numbers. At $Re = \mathcal{O}(10^4)$, vortex behaviour is strongly influenced by spanwise convection, shear-layer instability, and vortex–tip interactions, effects that are amplified on swept wings.

While the leading-edge suction parameter (LESP) provides a robust criterion for LEV onset in two-dimensional flows, its applicability to finite wings, and particularly to swept configurations where spanwise pressure gradients redistribute leading-edge suction, remains largely untested. Similarly, large-amplitude unsteady lifting-line formulations offer an attractive low-order framework, but their inner solutions assume a dominance of two-dimensional chordwise flow and uniform downwash, which are assumptions that may be violated when sweep-driven spanwise transport becomes dynamically significant. The predictive capability of these models, therefore, requires systematic evaluation under controlled, three-dimensional, low-Reynolds-number conditions.

Force and moment partitioning methods (FMPM) have demonstrated potential for quantifying the contributions of individual vortical structures to aerodynamic loading. However, their application has so far been limited mainly to static or periodic flows, with few studies examining transient plunging motion on swept, low-Reynolds-number wings.

Separately, flow-control studies indicate that LEV stability can be manipulated, but such efforts depend on a detailed baseline understanding of natural vortex behaviour. In particular, the combined influence of sweep, aspect ratio, and unsteady motion on the emergence and persistence of coherent LEV structures remains insufficiently understood.

Consequently, a significant gap exists in understanding how wing sweep, unsteady plunging motion, and three-dimensional flow mechanisms interact to govern LEV formation, breakdown, and force production at low Reynolds numbers.

While LOMs such as LAULLT and LESP offer attractive frameworks for interpreting unsteady aerodynamics, their applicability to finite, swept wings, where spanwise flow is intrinsic rather than a perturbation, remains uncertain. In particular, the extent to which these tools can meaningfully diagnose LEV initiation and spanwise aerodynamic loading under strongly three-dimensional, transient conditions has not been systematically assessed.

Although vortex-based force partitioning provides a powerful framework for relating flow structure to aerodynamic forces, its application to transient, low-Reynolds-number swept wings remains limited. In particular, existing studies have focused predominantly on unswept or two-dimensional configurations, leaving the influence of sweep on unsteady force generation mechanisms poorly understood. Addressing this gap requires a combined approach that leverages high-fidelity simula-

tions to resolve the three-dimensional flow physics, while using LOMs selectively as interpretive tools rather than for predictive capability.

1.3 Research objectives and original contributions

This thesis investigates how wing sweep and unsteady plunging motion influence the formation, three-dimensional development, and breakdown of leading-edge vortices (LEVs) on finite wings at low Reynolds numbers, representative of small-scale UAV and MAV applications. While previous studies have examined unswept configurations or isolated kinematic modes, the coupled effects of sweep-driven spanwise flow, chord-reduced frequency (herein abbreviated to reduced frequency), and aspect ratio on LEV behaviour remain insufficiently explored under controlled, transient conditions. In particular, the interaction between spanwise vorticity transport induced by sweep and the impulsive unsteadiness associated with plunging motion has not been characterised systematically at biologically relevant Reynolds numbers.

1.3.1 Research objectives

To address these gaps, this research implements high-fidelity simulations, low-order modelling and vorticity-based force partitioning. The specific objectives are to:

1. Characterise LEV dynamics on finite swept wings undergoing plunging motion at low Reynolds number, with particular emphasis on LEV initiation, three-dimensional development, and breakdown mechanisms.

2. Assess the applicability of low-order modelling tools, including LAULLT and LESP, for interpreting unsteady aerodynamic behaviour on swept wings, identifying both their capabilities and limitations.

3. Examine the influence of reduced frequency, sweep angle, and aspect ratio on LEV structure and stability during plunge ramp motions.

4. Quantify the contributions of vortical structures to lift and thrust using FMPM, and assess how these contributions are modified by wing sweep and unsteady kinematics.

1.3.2 Original contributions

This thesis makes the following original contributions:

- A systematic characterisation of LEV dynamics on plunging swept wings at low Reynolds number, isolating the roles of reduced frequency, sweep angle, and aspect ratio.

- A first-order sweep correction to large-amplitude unsteady lifting-line theory, with a critical assessment of its applicability and limitations for finite wings.
- A verification of variable LESP as a physically meaningful diagnostic for identifying LEV initiation on finite and swept wings using high-fidelity CFD data.
- Identification of distinct LEV breakdown modes and their dependence on reduced frequency and three-dimensional transport mechanisms.
- Application of the FMPM method to quantify lift and thrust contributions from vortical structures on transient, low-Reynolds-number swept wings.
- Design-relevant insights into the trade-off between peak aerodynamic performance and robustness in swept-wing MAV configurations operating in gust-prone environments.

Together, these contributions establish a coherent and physically grounded framework that links high-fidelity numerical simulations with carefully interpreted low-order aerodynamic models. Rather than seeking direct prediction, the thesis uses these tools in a complementary manner to diagnose, interpret, and rationalise LEV behaviour in three-dimensional, unsteady, low-Reynolds-number flows.

The remainder of the thesis is structured as follows:

- Chapter 2 presents the numerical methodology, including CFD solver setup, mesh methodology, validation against available experimental data, and verification of numerical parameters such as the Courant number and mesh resolution.
- Chapter 3 introduces the low-order modelling framework, including a first-order sweep angle correction to large-amplitude unsteady lifting-line theory and a verification of variable LESP as a useful diagnostic indicator of LEV initiation on finite swept wings.
- Chapter 4 investigates LEV breakdown mechanisms, identifying distinct breakdown modes and their dependence on reduced frequency.
- Chapter 5 examines the influence of reduced frequency on LEV formation, evolution, and stability, highlighting how kinematics govern vortex strength and breakdown behaviour.
- Chapter 6 isolates the effects of wing sweep on LEV dynamics, demonstrating how spanwise vorticity transport fundamentally alters vortex topology and stability.
- Chapter 7 applies the FMPM method to quantify the contributions of vortical structures to lift and thrust, and discusses the implications of sweep-induced trade-offs between peak aerodynamic performance and robustness for MAV design.
- Chapter 8 summarises the key findings of the thesis and outlines directions for future research.

2

Computational Methodology

> *Who owns the mesh, owns the solution.*
>
> **— Hrvoje Jasak**
> (Mechanical Engineer)

THE aerodynamic phenomena investigated in this thesis are characterised by strongly unsteady, three-dimensional flow behaviour dominated by the formation, evolution, and breakdown of leading-edge vortices (LEVs). Although the Reynolds number considered is relatively low ($Re = 2 \times 10^4$), the prescribed kinematics induce large-scale flow separation, vortex roll-up, and significant spanwise transport, resulting in complex, time-dependent flow structures that cannot be adequately represented by steady or time-averaged modelling approaches. Accurately capturing these mechanisms is essential, as the subsequent analysis focuses explicitly on vortex dynamics, LEV stability, and their sensitivity to sweep angle and reduced frequency.

Conventional RANS approaches are attractive from a computational standpoint but are fundamentally limited in this context, as they model unsteady flow features through time-averaged turbulence closures. While RANS methods may provide reasonable predictions of integrated aerodynamic loads under some conditions, they are unable to resolve the transient vortex structures and breakdown processes that underpin the physical interpretation developed in later chapters. Higher fidelity models, such as LES, offer the ability to resolve the dominant unsteady structures directly, but at prohibitive computational cost for the three-dimensional, parametric study undertaken here, particularly given the need for fine near-wall resolution and long physical time integrations.

To balance physical fidelity and computational efficiency, this study employs an IDDES framework based on the Spalart–Allmaras (SA) turbulence model. IDDES combines RANS modelling in attached near-wall regions with LES in separated regions of the flow, allowing large-scale unsteady vortical structures to be resolved explicitly while maintaining tractable computational cost. This hybrid approach is well-suited to the present problem, where separation and vortex dynamics play a central role, but full wall-resolved LES would be impractical across the wide parameter space considered.

This chapter describes the numerical methodology adopted throughout the thesis. Section 2.1 introduces the governing equations for incompressible flow, followed in Section 2.2 by a discussion of turbulence modelling approaches and the motivation for the IDDES framework. Sections 2.3-2.5 describe the spatial and temporal discretisation strategies, numerical algorithms, and iterative solution methods employed. The problem definition, including geometry, kinematics, and flow conditions, is presented in Section 2.6, followed by details of the mesh generation strategy in Section 2.7. Finally, Section 2.8 establishes the credibility of the numerical approach through validation against experimental data and verification studies assessing grid and time-step sensitivity.

2.1 Governing equations

CFD is a branch of fluid mechanics that uses computing systems to numerically solve the conservation laws governing fluid motion to provide a quantitative prediction of fluid flow phenomena and forces. The three conservation laws are conservation of mass, conservation of momentum (Newton's second law) and conservation of energy. From the conservation of mass law, we arrive at the continuity equation. The continuity equation says that the rate of mass increase is equal to the difference between the rate of mass entering and leaving a control volume [127]. For an incompressible fluid, this is described by Equation 2.1,

$$\nabla \cdot \mathbf{u} = 0, \tag{2.1}$$

where ∇ represents the divergence of a vector field, and $\mathbf{u}$ is the velocity vector field. By applying the principle of conservation of momentum, we arrive at the Navier-Stokes equation. Considering the same control volume, the Navier-Stokes equation states that the rate of momentum increase is equal to the difference between the rate of momentum entering and leaving the control volume, plus the sum of forces acting on that control volume [127]. The Navier-Stokes momentum equation for an incompressible Newtonian fluid is given by Equation 2.2,

$$\frac{D\mathbf{u}}{Dt} = \frac{\partial \mathbf{u}}{\partial t} + (\mathbf{u} \cdot \nabla)\mathbf{u} = \nu \nabla^2 \mathbf{u} - \frac{\nabla p}{\rho_0} + \mathbf{g}, \tag{2.2}$$

where D/Dt is the material derivative representing how a vector changes in Lagrangian coordinates and $\partial/\partial t + (\mathbf{u} \cdot \nabla)$ is the equivalent Eulerian representation. $\partial/\partial t$ is the transient term, $\mathbf{u} \cdot \nabla$ represents the convection terms, $\nu \nabla^2$ are the diffusion terms, $\nabla p/\rho_0$ is the source term and $\mathbf{g}$ is the body force term. For our application, the body force is zero as this typically represents gravitational, magnetic and centripetal forces, which are not considered in this study.

The energy equation is concerned with thermal and kinetic energy; hence, due to our assumptions of incompressibility and an isothermal fluid, no energy equation is required.

2.2 Turbulence modelling

In most scenarios, the Navier-Stokes equations cannot be solved analytically, due to the non-linear form of the equations. Most practical flows, even at low Reynolds numbers, require numerical solutions. The Reynolds number is defined as the ratio between inertial and viscous forces in a flow and therefore indicates the relative importance of these effects. This can be used to assess whether a flow is likely to remain laminar or transition to turbulence. In this thesis, the simulations are conducted at $Re = 2 \times 10^4$, which under steady conditions would produce a predominantly laminar boundary layer over the wing. However, the wing motion is prescribed with unsteady kinematics that induce local flow separation and generate time-dependent vortical structures in the near-wall region and wake. These effects can trigger early transition in the boundary layer, producing complex, unsteady flow behaviour even at this relatively low Reynolds number.

Capturing these features accurately requires a numerical approach capable of resolving time-dependent behaviour and large-scale flow separation. Accordingly, this study employs an IDDES framework, which allows the resolution of coherent unsteady vortical structures while maintaining computational efficiency. Although the Reynolds number considered, $Re = 2 \times 10^4$, lies in a regime where transition and near-wall modelling can influence boundary-layer development, the primary focus of the present work is on the formation, evolution, and breakdown of large-scale separated shear layers and LEVs. These features are not captured reliably by steady or URANS approaches, whereas IDDES is able to resolve the dominant unsteady structures governing the force response. Crucially, the suitability of this approach for the present problem is established through direct validation against experimental measurements in Section 2.8, demonstrating good agreement in LEV topology, breakdown timing, and integrated force histories. On this basis, the CFD results are treated as a reliable reference dataset for the subsequent flow-physics analysis and low-order modelling.

2.2.1 Reynolds-averaged Navier-Stokes

The numerical simulations in this study are based on Reynolds-averaged formulations of the Navier–Stokes equations, which form the foundation of the turbulence modelling approaches employed. The most common technique was introduced by Reynolds [128], which separates the flow variables into mean and fluctuating components. Therefore, the technique is a time-averaging method known as Reynolds averaging, which results in the Reynolds-averaged Navier-Stokes (RANS) momentum equations, shown in Equation 2.3,

$$\frac{D\bar{u}_i}{Dt} = \frac{\partial \bar{u}_i}{\partial t} + \frac{\partial}{\partial x_j}(\bar{u}_i\bar{u}_j + \overline{u_i'u_j'}) = \frac{\partial}{\partial x_j}\left[\nu\left(\frac{\partial \bar{u}_i}{\partial x_j} + \frac{\partial \bar{u}_j}{\partial x_i}\right)\right] - \frac{1}{\rho_0}\frac{\partial \bar{p}}{\partial x_i}, \tag{2.3}$$

where ν is the kinematic viscosity, ρ_0 is the reference fluid density and p is pressure. By performing Reynolds averaging on the momentum equation an additional unsteady term $\overline{u_i'u_j'}$, known as the

specific Reynolds stress tensor, is generated [129]. Therefore, further unknowns have been produced. While transport equations can be formulated for the Reynolds stresses, doing so introduces higher-order correlations, resulting in an underdetermined system. This imbalance between the number of unknowns and available equations is referred to as the closure problem.

To resolve this, turbulence models can be derived to approximate the unknown unsteady terms. The two main techniques by which this is achieved are the eddy viscosity concept and by directly solving transport equations for the Reynolds stress tensor, which are known as Reynolds stress models (RSM) [130, 131]. RSM are significantly more complex than eddy viscosity models and are not considered in this study.

The eddy viscosity concept provides a closure for the unknown turbulent stresses by approximating them as being proportional to the mean rate of strain, analogous to viscous stresses. This approach was introduced by Boussinesq [132] who proposed that turbulent stresses could be modelled in this way. This required the introduction of the eddy viscosity parameter ν_t and results in Equation 2.4,

$$-\overline{u_i' u_j'} = \nu_t \left(\frac{\partial \bar{u}_i}{\partial x_j} + \frac{\partial \bar{u}_j}{\partial x_i} \right) - \frac{2}{3} k \delta_{ij}, \tag{2.4}$$

where δ_{ij} is the Kronecker delta tensor and $k = \frac{1}{2}\overline{u_i' u_i'}$ is turbulent kinetic energy. Hence, eddy viscosity turbulence models aim to calculate ν_t.

The Spalart-Allmaras model [133] is an empirically determined one-equation model that solves a transport equation for modified turbulence viscosity $\tilde{\nu}$. $\tilde{\nu}$ is related to ν_t by the kinematic viscosity ν. The idea behind the method is that $\tilde{\nu}$ is defined such that it varies nearly linearly in the near-wall viscous sub-layer region. This means significantly fewer cells are needed to resolve the velocity profile than ν_t, which has a quartic relationship with dimensionless wall distance y^+ in this region. y^+ is used in CFD primarily to determine the thickness of the first volume mesh cell next to the surface of the body of interest. Hence, the transport equation for $\tilde{\nu}$ is much easier to solve numerically and has much lower computational requirements than solving for ν_t. While the model performs well for a wide range of unsteady, separated external aerodynamic flows [70, 79], the Spalart-Allmaras model is known to over-predict eddy viscosity in regions of strong adverse pressure gradient or massive separation. Despite this limitation, the Spalart-Allmaras model is used in this study for turbulence closure due to its computational efficiency and demonstrated effectiveness for the type of flows considered.

2.2.2 Large eddy simulation

Large eddy simulation (LES) is a turbulence modelling approach that explicitly resolves the large, energy-containing scales of motion while modelling the smaller, subgrid-scale (SGS) motions. In turbulent flows, the large-scale eddies transport most of the mass and momentum, whereas the smaller-scale motions contribute primarily to dissipation. LES reduces computational

cost compared to DNS by filtering the velocity field to separate the resolved large scales from the unresolved small scales [134, 135]. The filtered momentum equations resemble the RANS equations, but without the Reynolds stress term. Instead, an SGS model is required to account for the effect of unresolved motions [136]. In this study, SGS models are not employed directly, as a hybrid approach combining RANS and LES methods is used, allowing the benefits of LES resolution without explicitly modelling the subgrid-scale motions.

2.2.3 Detached eddy simulation

The most common family of hybrid RANS-LES methods are detached eddy simulation (DES) methods, developed by Spalart *et al.* [137]. In detached eddy simulation, the wall-distance length scale in the Spalart–Allmaras model is replaced by a hybrid length scale defined as the minimum of the wall distance and a grid-based length proportional to the local maximum cell dimension. This modification forces a transition from RANS behaviour near the wall to LES behaviour in separated regions where the grid spacing becomes the limiting scale [137, 138]. As complex three-dimensional eddies are resolved directly, this makes DES more accurate for highly-separated flows than RANS models, while requiring significantly less computational resources than LES. The main issue with DES is modelled-stress depletion (MSD) [139]. The problem arises due to the mesh density in the near-wall boundary layer. If the LES length scale, based on maximum grid spacing, falls below the RANS length scale, based on the distance to the wall, then the flow is modelled by LES. This is an issue as the boundary layer grid is usually not sufficiently refined for wall-resolved LES when using a DES methodology. As a result, the modelled Reynolds stresses provided by the RANS formulation are prematurely reduced, while the grid is insufficiently resolved to sustain the corresponding LES turbulence, leading to a net loss of turbulent stress [140]. This MSD can lead to erroneous separation due to the grid density, which is termed grid-induced separation (GIS).

A modification to the method that aimed to resolve the MSD issue was proposed by Spalart *et al.* [141], known as delayed-DES (DDES). This was achieved by shielding the boundary layer to preserve the RANS formulation by using a derivative of the functions proposed by Menter and Kuntz [142]. The authors observed that DDES maintained LES behaviour after large-scale separation. However, others found that the model did not eliminate MSD sufficiently [143].

Improved delayed detached eddy simulation (IDDES) improves upon the DDES model by resolving an issue that was present in DES, but not addressed in the DDES formulation [141]. The issue concerns using DES where a grid is sufficiently refined to achieve wall-modelled LES (WMLES). This causes only the inner boundary layer to be modelled using RANS [144]. Hence, in this formulation there are both modelled and resolved regions of the logarithmic sublayer of the boundary layer flow. This results in a mismatch between the inner, RANS-modelled logarithmic layer and the outer, LES-resolved logarithmic layer, producing an artificial discontinuity in the mean velocity profile known as log-layer mismatch [139]. This issue is overcome in the IDDES

formulation by empirical improvements to the model that increase resolved near-wall turbulent activity, hence improving model performance in the resolved log-layer region [117]. In the IDDES formulation, the switching between RANS and LES behaviour is further modified to account for the presence of resolved turbulence. In the absence of incoming turbulence, the model retains DDES-like behaviour by shielding the attached boundary layer from premature LES activation. When sufficiently resolved turbulence is present, and the near-wall grid resolution permits wall-modelled LES, the formulation allows a gradual transition to WMLES behaviour within the boundary layer [117]. The subgrid length scale is additionally redefined to depend on the wall distance as well as the grid spacing. This is required due to the necessity of an anisotropic grid near the wall. Hence, the values for SGS model constants that work well for cubic cells in free-stream flow become too large. The use of the wall distance arises from the consideration that any wall-bounded flow becomes free away from the wall; hence, any single value would not be suitable.

Therefore, the Spalart-Allmaras IDDES model is used in this study, with the governing equation for the transport of modified turbulence viscosity $\tilde{\nu}$ given by Equation 2.5, with length scale $\tilde{d}$ given by Equation 2.6, where $SMALL$ is a numerical constant, typically $\mathcal{O}(10^{-12})$, used to prevent a singularity. All model constants and auxiliary functions take their standard values as defined in the original Spalart–Allmaras [133] and IDDES [117] formulations.

$$\frac{D}{Dt}(\rho\tilde{\nu}) = \nabla\cdot(\rho D_{\tilde{\nu}}\tilde{\nu}) + \frac{C_{b2}}{\sigma_{\nu_t}}\rho|\nabla\tilde{\nu}|^2 + C_{b1}\rho\tilde{S}\tilde{\nu}(1-f_{t2}) - (C_{w1}f_w - \frac{C_{b1}}{\kappa^2}f_{t2})\rho\frac{\tilde{\nu}^2}{\tilde{d}^2} + S_{\tilde{\nu}} \tag{2.5}$$

$$\tilde{d} = max(\tilde{f}_d(1+f_e)L_{RAS} + (1-\tilde{f}_d)L_{LES}, SMALL) \tag{2.6}$$

2.3 Finite volume method

The IDDES turbulence model described in the previous section is implemented within a finite volume framework, which is adopted here to discretise and solve the governing equations. The finite volume method (FVM) is a numerical technique to discretise the governing partial differential equations (PDEs) into algebraic equations. These equations are then applied to finite volumes, rather than the differential volumes present in PDEs, by discretising the domain into elements that form a mesh. The PDEs are integrated over each discrete element to form the algebraic equations. The system of algebraic equations is then solved to calculate the values of the variable of interest, ϕ [145].

Gaussian quadrature is used to integrate the convective, diffusive, and pressure-gradient terms, providing second-order spatial accuracy. As these fluxes are evaluated at control-volume faces, interpolation from cell centres to face centres is required. The convective term achieves this using linear interpolation, also known as central differencing. This simply states that, for an isotropic

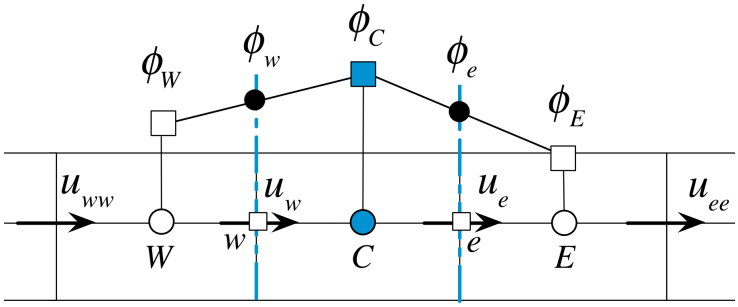

Figure 2.1: Diagram illustrating the central difference method, adapted from Moukalled [145], with permission.

mesh, the face-centre value is equal to half the difference between the neighbouring cell-centre values, as shown in Equation 2.7 and illustrated in Figure 2.1.

$$\phi_e = \frac{\phi_C + \phi_E}{2} \tag{2.7}$$

Due to the necessity of a highly non-orthogonal mesh surrounding the $\Lambda = 60°$ swept wing cell limiting is applied, for the $\Lambda = 60°$ sweep cases only, to ensure boundedness of the solution. This ensures that the interpolated face-centred value is bounded by the neighbouring cells' maximum and minimum limits [146]. However, this introduces diffusion to the solution; hence, the minimum permissible limit is sought. For $\tilde{\nu}$, a limiting coefficient of 0.5 is used to allow values to exceed the neighbouring cell centre values by up to 50%.

For the pressure-gradient terms, corrected linear interpolation is used for the unswept and moderately swept wing cases. The corrected formulation provides a second-order conservative treatment of surface-normal gradients and is required to account for mesh non-orthogonality in the swept-wing meshes, which arises from grid alignment with the wing geometry rather than the Cartesian coordinate directions. To retain second-order accuracy under these conditions, an explicit non-orthogonal correction is added to the orthogonal component [147]. This approach is valid when mesh non-orthogonality is low, defined here as a small angle between the vector joining adjacent cell centres and the corresponding face normal, such that the non-orthogonal correction remains small.

For the highly swept wing cases, mesh non-orthogonality increases sufficiently that a limited interpolation scheme is required for the pressure-gradient term. In this formulation, the explicit non-orthogonal correction is retained but limited to maintain numerical stability, with the limiter selected to maximise accuracy while preserving boundedness [146].

The convective terms are handled by linear upwind interpolation based on the gradient of the quantity of interest, with the exception of $\tilde{\nu}$ for the highly swept wing, which is based on the default gradient. The linear upwind scheme [148] is second-order accurate and is based on the cell-centre values of the cell of interest and the upwind cell. A weighting is applied such that the value of the quantity is more strongly influenced by its own cell-centre value, as shown in

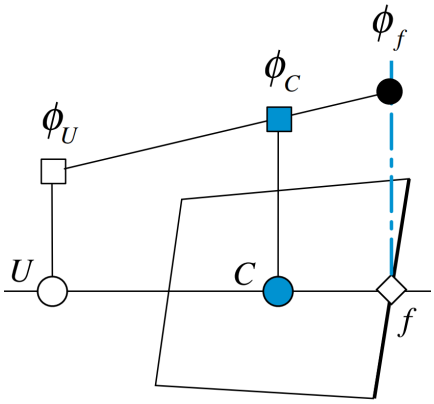

Figure 2.2: Diagram illustrating the linear upwind method, adapted from Moukalled [145], with permission.

Equation 2.8 and illustrated in Figure 2.2.

$$\phi_f = \frac{3}{2}\phi_C - \frac{1}{2}\phi_U \tag{2.8}$$

As this study deals with time-varying flows, we have a temporal term that also requires discretisation. The second-order implicit backward scheme is used to achieve this. With the assumption of a constant time step, the backward scheme is given in Equation 2.9,

$$\frac{\partial \phi}{\partial t} = \frac{1}{\Delta t}\left(\frac{3}{2}\phi - 2\phi^0 + \frac{1}{2}\phi^{00}\right), \tag{2.9}$$

where ^{0} represents the previous time step and ^{00} represents two time steps prior.

2.4 Numerical algorithms

Solving the discretised equations requires using iterative numerical techniques. As this study considers transient simulations, the PIMPLE (pressure-implicit with merged pressure-linked equations) algorithm is used. The PIMPLE algorithm is a combination of the PISO (pressure-implicit split operator) and SIMPLE (semi-implicit method for pressure-linked equations) algorithms, hence, these will be addressed first.

SIMPLE [149] is a steady-state algorithm for solving the coupled pressure-momentum equations. The momentum and pressure correction equations are solved implicitly, whereas the velocity correction is solved explicitly, hence the name semi-implicit. The velocity field is approximated by solving the momentum equation. The pressure gradient term is calculated using the previous iteration result or an initial guess. The pressure equation is constructed and solved to obtain the new pressure distribution. Velocities are corrected, and new gradients are calculated. These steps are repeated until a converged result is achieved. More specifically, the algorithm operates as follows:

1. Guess the pressure field p^*.

2. Solve the momentum equations to obtain $\mathbf{u}^*$.

3. Solve the pressure-correction equation p'.

4. Calculate p by summing p^* and p'.

5. Calculate $\mathbf{u}$ from $\mathbf{u}^*$ using the velocity-correction equations.

6. Solve the discretised momentum equation for other fields, such as the modified turbulence viscosity $\tilde{\nu}$ governing equation for IDDES.

7. Consider the corrected pressure p as a new guessed pressure p^* and repeat steps 2-6 until convergence is reached.

Here, the starred quantities (p^* and $\mathbf{u}^*$) represent fields based on guessed values. The pressure and velocity-correction equations can be found in Patankar [150].

PISO was proposed by Issa [151] to move the repeated calculations required by SIMPLE inside the solution step of the pressure-correction equation. Therefore, the momentum equation is solved explicitly in an inner loop, known as the momentum corrector step. This was necessary to reduce the computational expense associated with the transient problems for which PISO was originally formulated. Considering the above SIMPLE algorithm steps, the PISO algorithm operates by considering whether the continuity equation is satisfied after the velocity corrector step (step 5) and performs a momentum correction by returning to step 3 based on using the calculated value for $\mathbf{u}$ as a new guess for $\mathbf{u}^*$.

The PIMPLE algorithm is a combination of the PISO and SIMPLE algorithms for transient problems that uses the SIMPLE algorithm at each time step to converge to the steady-state solution. This is known as the SIMPLE loop, as illustrated in Figure 2.3. The number of SIMPLE loops performed is typically controlled by specifying convergence tolerances for the pressure p and velocity $\mathbf{u}$. In this study, the residuals of p and $\mathbf{u}$ are required to fall below 5×10^{-2} and 10^{-5} respectively, with additional convergence assessed through time histories of integral force coefficients. The momentum corrector loop is known as the PISO loop. Typically, two or three momentum corrections are performed [146], or up to four for highly transient flows. Hence, in this study, the 60° swept wings use four momentum corrections, whereas the unswept and moderately swept wings have three momentum corrections. We additionally define the non-orthogonal corrections for the pressure-gradient terms inside the PIMPLE algorithm after calculating the pressure field. Similarly, one non-orthogonal correction is defined for the unswept and 30° swept wings and three for the 60° swept wing, due to the necessity of the non-orthogonal structured mesh.

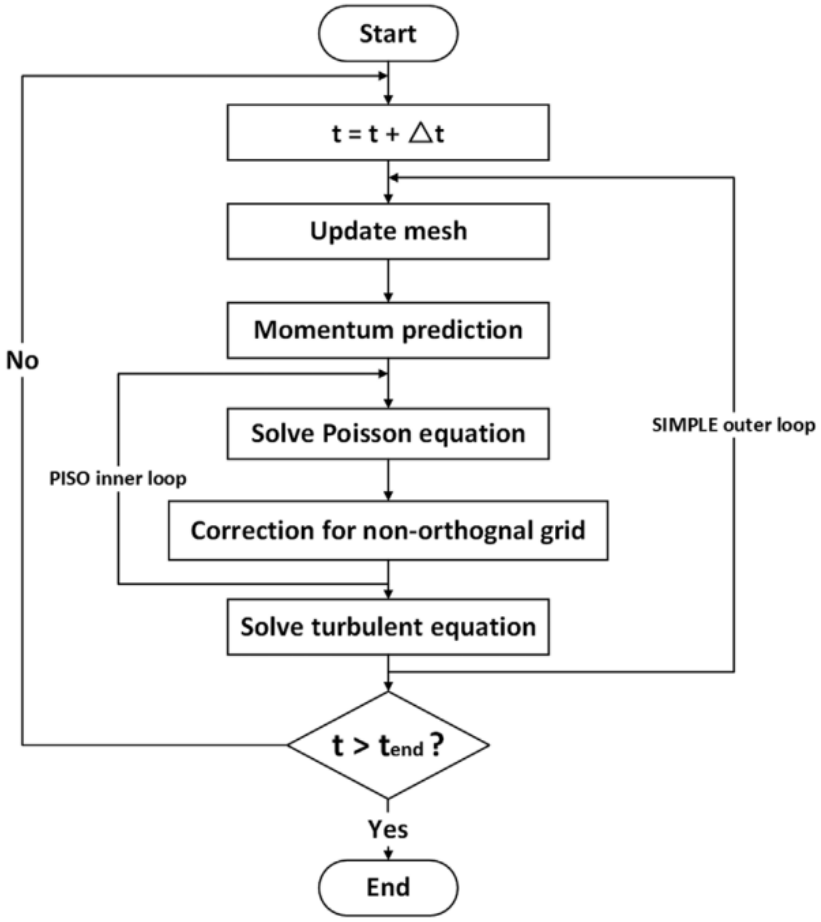

Figure 2.3: Flowchart illustrating the PIMPLE method, reproduced from Chen *et al.* [152], with permission.

2.5 Iterative methods

How to solve the system of discretised equations at each step of the solution process must now be considered. Due to the transient nature of these problems, and the sparse coefficient matrix, direct methods are not appropriate. Hence, iterative methods that require minimal computational overhead are used [145].

Before a discussion of the iterative methods used can be presented, preconditioning of the linear equations must first be considered. Preconditioning is a technique to simplify inverting the known matrix by multiplying both sides of the matrix equation by another matrix, known as the preconditioning matrix [145]. The rate of convergence of an iterative method solving a linear system is governed by the condition number of the known matrix, which governs how easy the matrix is to invert. The condition number describes how similar orthogonal gradients of the surface representing the solution to the matrix equation are. The lower the condition number, the more similar the gradients, hence the easier the matrix is to invert. The easiest matrix to invert is the identity matrix, hence preconditioning aims to modify the known matrix to be more similar to the identity matrix [146].

Different preconditioners are used for the pressure and velocity equations due to the symmetry of the pressure matrices versus the asymmetry of the velocity matrices. Faster diagonal incomplete-Cholesky (FDIC) preconditioning is used for the pressure equations, and diagonal incomplete lower-upper (DILU) preconditioning is used for the velocity equations. The modified turbulence viscosity equations are also asymmetric, hence DILU is used for these equations.

FDIC preconditioning is based on Cholesky decomposition [153], where the known matrix can be decomposed into a lower triangular matrix and its conjugate transpose. Incomplete-Cholesky (IC) decomposition maintains zero elements in the sparse matrix by approximating the original Cholesky decomposition [154]. In the original formulation, zero elements can become non-zero, which reduces efficiency. Efficiency is increased further in the diagonal incomplete-Cholesky (DIC) method by considering a lower-diagonal-lower (LDL) decomposition, where a diagonal matrix is introduced. This has the advantage of eliminating the need to compute square roots [155]. Finally, FDIC preconditioning calculates and stores upper coefficients divided by the diagonal [146]. DILU is the asymmetric version of the DIC preconditioner, where the Cholesky decomposition is replaced with a lower-upper decomposition to account for the asymmetry of the system of equations.

The iterative methods used to solve the systems of equations are based on the conjugate gradient (CG) method [156]. For the symmetric pressure equations, the preconditioned conjugate gradient (PCG) method is used, and for the asymmetric velocity equations, the preconditioned bi-conjugate gradient (PBiCG) method is used. The difference is that the asymmetric system of equations is transformed into symmetric equations by multiplying by the conjugate transpose [157]. The CG method is a descent method to find the minimum of the quadratic form of the system of equations, corresponding to the solution. The method constrains the search directions to be conjugate to the known matrix. This means that for a surface with equal principal axes gradients, the search directions are orthogonal [146].

2.6 Problem definition

To investigate sweep angle effects, 18 wing geometries, with leading-edge sweep angles of $\Lambda = 0°, 30°$ and $60°$, aspect ratios of 1, 3 and 6 and NACA 0008 and NACA 0018 aerofoil profiles are simulated in this study. Four reduced frequencies of motion ($k = 0.05, 0.1, 0.2, 0.4$) are considered to investigate geometric and kinematic effects on the LEV parametrically. The chord-reduced frequencies selected represent quasi-steady motion ($k = 0.05$), moderately unsteady ($k = 0.1$), transitional ($k = 0.2$) and highly unsteady motion ($k = 0.4$). This gives a total of 72 simulations, the parameters for which are described in Table 2.1. Unless otherwise stated, simulations employ a thin symmetric aerofoil (NACA 0008). A limited comparison with a thicker profile (NACA 0018) is presented in Chapter 5 to illustrate the influence of aerofoil thickness on reduced-frequency effects. However, aerofoil thickness is not treated as a primary study variable

Table 2.1: Case parameters.

Parameter	Values
Λ	$0°, 30°, 60°$
AR	1, 3, 6
Aerofoil	NACA 0008, NACA 0018
k	0.05, 0.1, 0.2, 0.4

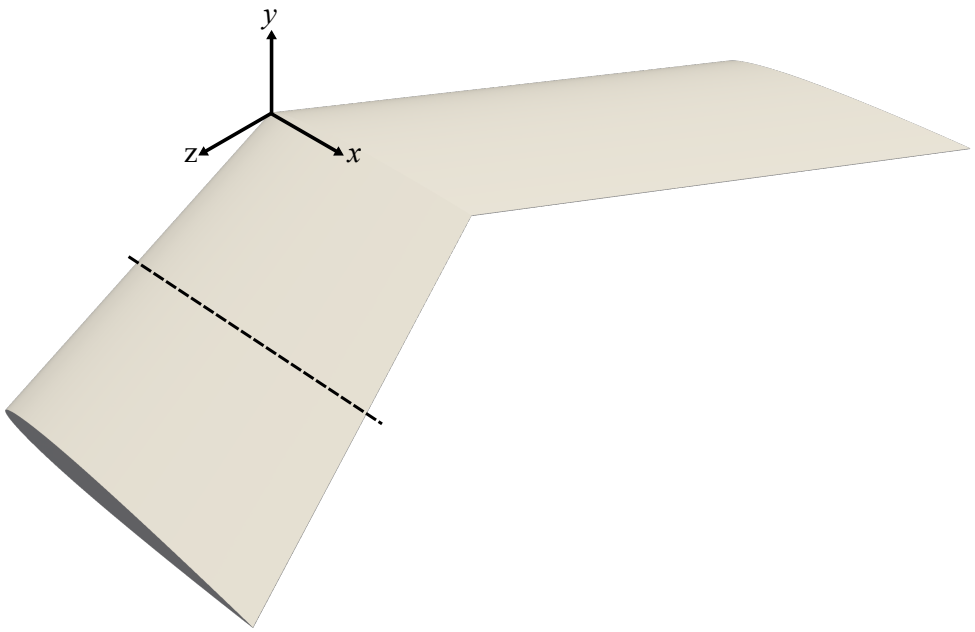

Figure 2.4: Rendered image illustrating the aspect ratio 3, $\Lambda = 30°$ wing, with the coordinate system and origin indicated. The mid-span location is indicated by the dashed line.

in this thesis.

An aspect ratio of 3 was initially chosen as it closely resembles that of biological flyers [158], before aspect ratio effects were considered. The swept wing geometries are defined by connecting two aerofoils with the same chord length at the root and tip planes, as shown in Figure 2.4. As a result, the aerofoil profile is maintained in the free-stream direction throughout the span. As square tips are studied, the planform area remains invariant under sweep angle changes.

The prescribed kinematic motion being investigated is a smoothed ramp motion [159, 160], representing a vertical gust, described in Equation 2.10 with the smoothing parameter a defined by Granlund *et al.* [161] in Equation 2.11,

$$\frac{\dot{h}}{c} = \frac{k}{a} \log \left[\frac{\cosh(a(t-t_1)}{\cosh(a(t-t_2))} \right] + \frac{(\dot{h}/c)_{amp}}{2}, \tag{2.10}$$

$$a = \frac{\pi^2}{4(t_2-t_1)(1-\sigma)}, \tag{2.11}$$

where k is the chord-reduced frequency, t_1 and t_2 represent the start and end of the plunge ramp, respectively, and the chord-reduced plunge amplitude $(\dot{h}/c)_{amp}$ is fixed as 0.25. The maximum

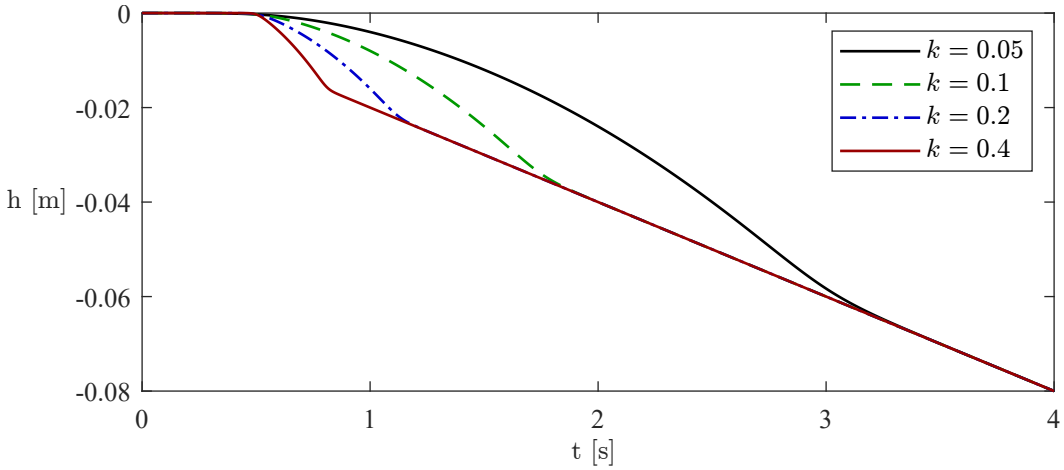

Figure 2.5: Dimensional plunge displacement for each of the 4 reduced frequencies ($k = 0.05, 0.1, 0.2, 0.4$) investigated.

plunge displacement is one chord length, $c = 0.08$m. The smoothing parameter σ is equal to 0.8. Figure 2.5 illustrates the physical plunge displacement against time.

The plunge rate $\dot{h}$ corresponds to an effective pitch angle [70], with the maximum plunge rate being equivalent to $\alpha \approx 14.5°$. This effective incidence is sufficiently large to permit LEV formation within the range of reduced frequencies examined, depending on wing geometry. The pitch angle, α, is fixed at 0°.

Time is non-dimensionalised using the convective time scale, defined as $t^* = tU_\infty/c$, where U_∞ is the free-stream velocity. This scaling is appropriate for analysing vortex formation, convection, and breakdown processes, which are governed by convective transport along the wing, and is standard practice in the study of vortex-dominated low-speed aerodynamic flows.

2.7 Mesh methodology

A body-fitted mesh is constructed around the wing with an initial wall-normal cell spacing of $1.24 \times 10^{-4}c$ and extruded up to a distance of $12c$, as shown in Figure 2.6. Up to a distance of $2c$, the growth rate and maximum cell size are limited to achieve the cubic cell requirement of DES grids within the focus region, with cell size $\Delta_0 = 0.015c$ chosen [162]. The O-mesh contains 249 chordwise cells, with increased resolution towards the leading and trailing edges, as shown in Figure 2.7. The aspect ratio 1, 3 and 6 wings to be simulated contain 127, 250 and 434 spanwise cells, respectively, with reduced spacing towards the wing-tip, as shown in Figure 2.7b. The spanwise domain extends 4 chord lengths beyond the wing-tip, with hyperbolic growth from the wing-tip, as shown in Figure 2.6c, with the first layer height being the same as in the normal direction to ensure $y^+ < 1$. The chosen domain extents are consistent with common practice in low-Reynolds-number wing simulations [85] and are sufficiently large to minimise any influence of the far-field boundaries on force generation and the region of interest. The chord length is

$c = 0.08$m, free-stream velocity $U_\infty = 0.16\text{m s}^{-1}$ and kinematic viscosity $\nu = 6.4\times10^{-6}\text{m}^2\text{s}^{-1}$ to give Reynolds number $Re = 2\times10^4$.

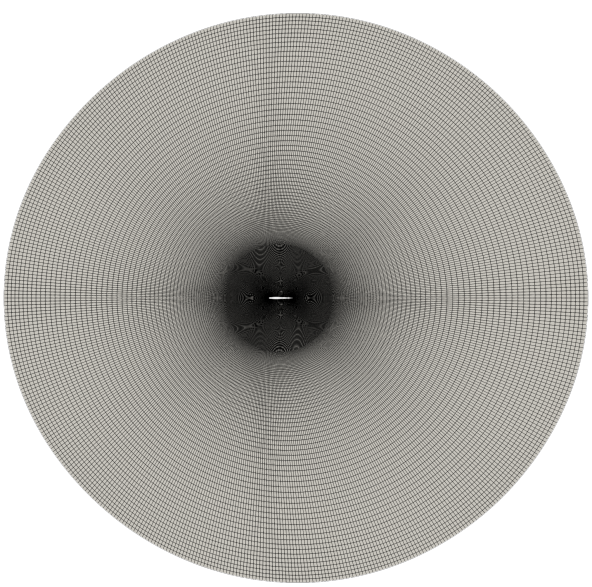

(a) Symmetry plane global mesh resolution.

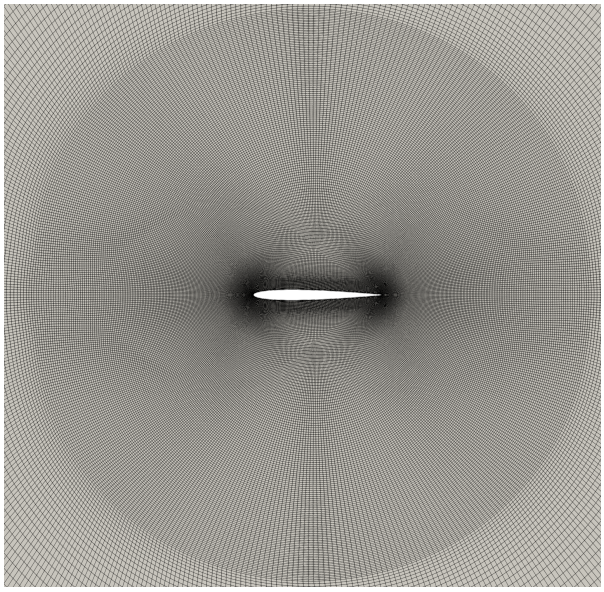

(b) Symmetry plane focus region mesh resolution.

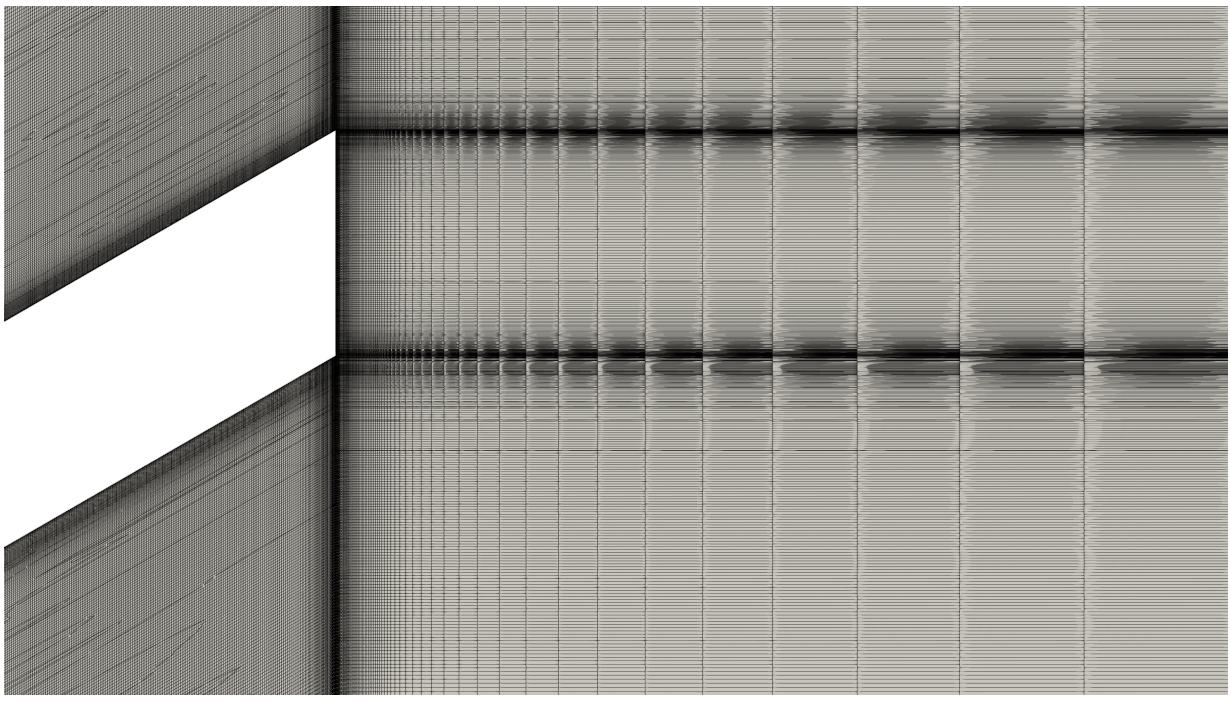

(c) Chordline mesh resolution, showing hyperbolic growth from the wing-tip.

Figure 2.6: Volume mesh images for the aspect ratio 3, NACA 0008, $\Lambda = 30°$ wing.

The open-source CFD code library OpenFOAM is used to conduct simulations. The no-slip boundary condition is applied to the wing surface. The wing rigidly moves with the prescribed motion, and the full domain moves with the wing to ensure mesh consistency. At the far-field boundary, free-stream conditions are imposed, such that the flow approaches the prescribed free-stream state. In OpenFOAM, this is implemented using a free-stream boundary condition, which

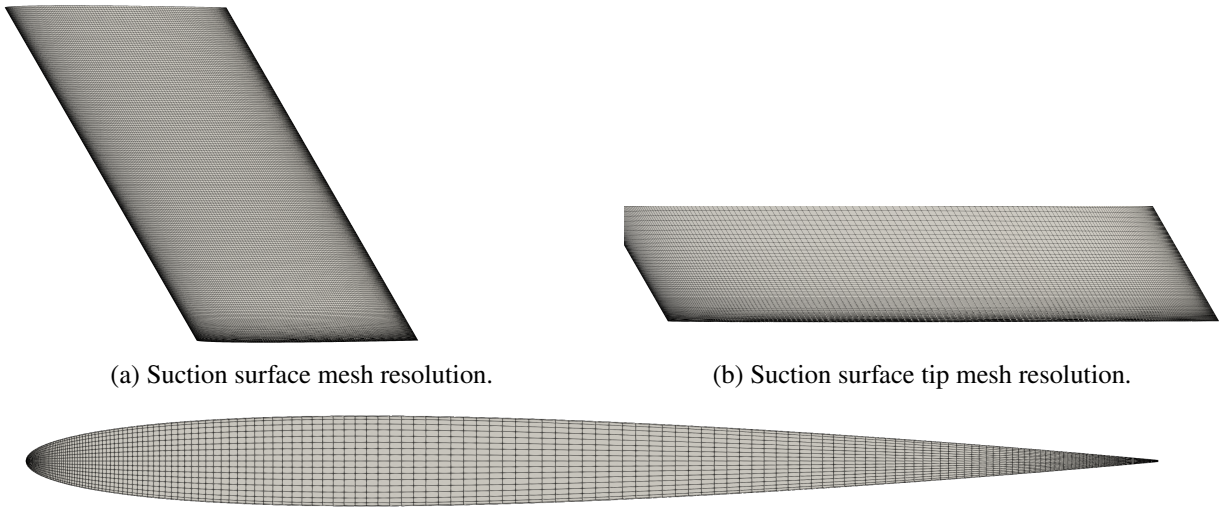

(a) Suction surface mesh resolution.

(b) Suction surface tip mesh resolution.

(c) Tip mesh resolution.

Figure 2.7: Surface mesh images for the aspect ratio 3, NACA 0008, $\Lambda = 30°$ wing.

acts as a zero-gradient condition when fluid is exiting the computational domain, meaning that the normal derivative of each flow variable is set to zero and the variable values are extrapolated from the interior. This allows the flow to leave the domain naturally, without artificial reflection or constraint, ensuring that wake and tip vortex structures are not influenced by the boundaries. When fluid enters the domain, the variables are fixed to the free-stream values, ensuring that the incoming flow matches the specified free-stream conditions. A symmetry plane is defined at the wing root plane to enable the simulation of half the symmetrical flow field. A schematic diagram of the computational domain is provided in Figure 2.8.

2.8 Validation and verification

This section establishes the accuracy and reliability of the numerical methodology employed in this thesis through validation against relevant experimental data and verification of key numerical parameters. Both force-based and flow-field comparisons are used to assess the ability of the solver to capture the unsteady, vortex-dominated aerodynamics that underpin the analyses presented in subsequent chapters.

2.8.1 Validation against experimental data

Validation was performed using a demanding two-dimensional benchmark involving high-amplitude pitching motion. The experimental study of Ōtomo *et al.* [163] considers a rigid aerofoil undergoing symmetric triangular pitching to a maximum incidence of $\alpha_0 = 64°$ at Reynolds number $Re = 3.2 \times 10^4$, consistent with the Reynolds-number regime examined in this thesis. The flow is characterised by extreme unsteadiness, large-scale separation, and dynamic stall, providing a

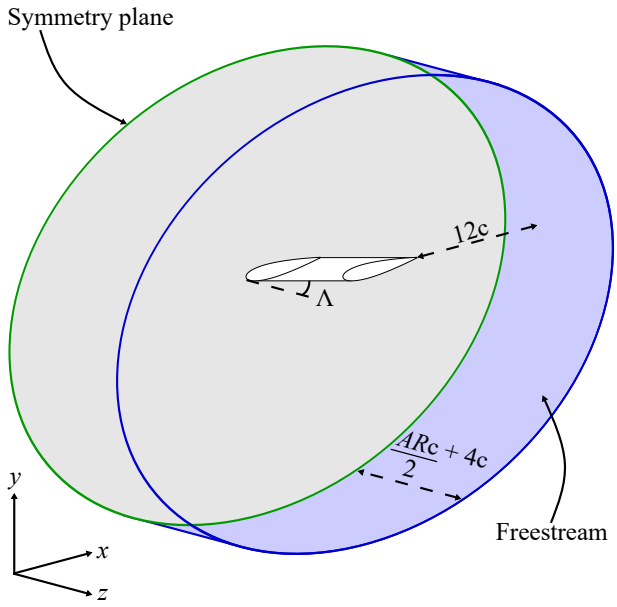

Figure 2.8: Schematic diagram of the computational domain. The symmetry boundary condition is coloured grey, and the free-stream boundary condition is coloured blue, and applied to the outer circular face and connecting curved surface. A wing of arbitrary sweep angle Λ is depicted. The free-stream flow is in the positive x direction.

stringent test of the numerical framework.

Two reduced frequencies were considered: $k = 0.88$ and $k = 0.22$. The higher reduced frequency case ($k = 0.88$) was treated as the primary validation case and was simulated over several pitching cycles to assess the repeatability and convergence of the unsteady lift response under strongly unsteady conditions. The lower reduced frequency case ($k = 0.22$) was subsequently simulated as a targeted diagnostic study, motivated by the appearance of sharp lift fluctuations in the $k = 0.88$ results, to assess whether similar behaviour persisted at lower reduced frequencies.

Given the expected complexity of the flow physics and with a view towards future applications involving large-amplitude motion and morphing configurations, an overset mesh formulation was initially considered. A systematic sensitivity study was conducted to assess the suitability of an overset mesh methodology, examining variations in overset boundary extent, interpolation strategy, background mesh refinement, near-wall resolution and growth rates, Courant number, temporal convergence over multiple pitching cycles, relaxation factors, and spanwise treatment for both strictly two-dimensional and cyclic three-dimensional formulations. This overset mesh analysis was conducted as a preliminary feasibility study; however, all results presented in this thesis are obtained using a non-overset mesh formulation.

Figure 2.9 compares the CFD-predicted and experimental lift histories. For the primary case at $k = 0.88$, the numerical results reproduce the overall waveform shape and phase of the experimental lift response. Sharp, impulsive peaks are observed in the broader lift evolution, for example, at $t/T \approx 0.25$ and 0.8. These features were found to be repeatable across cycles and insensitive to changes in overset configuration, mesh resolution, and numerical parameters,

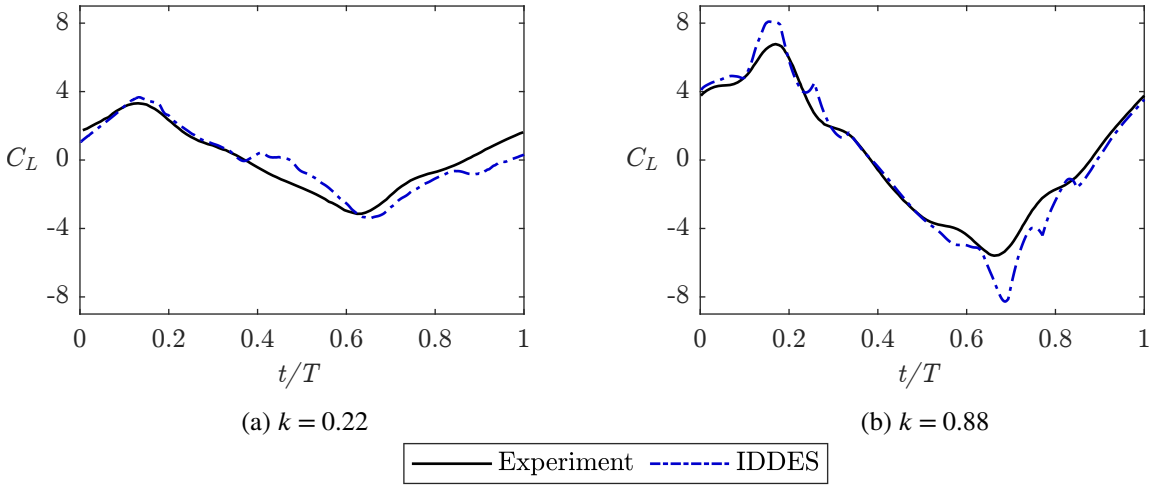

(a) $k = 0.22$ (b) $k = 0.88$

Figure 2.9: Comparison between experimental and IDDES results for a two-dimensional aerofoil undergoing triangular pitching kinematics, with pitch amplitude $\alpha_0 = 64°$ at reduced frequencies $k = 0.22$ and $k = 0.88$. Adapted from Ōtomo *et al.* [163], with permission.

indicating that they arise from the extreme unsteadiness of the imposed kinematics rather than numerical artefacts. The principal discrepancies relative to the experiment occur in the magnitude of the global extrema, which are over-predicted by the numerical solution.

The lower reduced frequency case at $k = 0.22$ was simulated specifically to assess whether the sharp lift fluctuations observed at higher reduced frequency also occur under more weakly unsteady kinematics. At $k = 0.22$, the numerical results reproduce the overall temporal evolution and amplitude of the experimental lift response, with minor deviations attributable to the single simulated cycle considered in this exploratory case. Notably, the sharp lift fluctuations observed at $k = 0.88$ are absent at $k = 0.22$, supporting the interpretation that these features are associated with the strongly unsteady kinematics of the higher reduced frequency motion.

Taken together, these comparisons indicate that the numerical methodology captures the essential structure and timing of unsteady lift generation for high-amplitude pitching aerofoils under strongly unsteady conditions, providing a sound basis for extension to three-dimensional, finite-wing configurations.

The primary three-dimensional validation case considers an unswept aspect ratio three wing undergoing sinusoidal plunging motion at Reynolds number $Re = 10^4$, corresponding to the experimental study of Bird *et al.* [102]. Bird *et al*'s work is directly relevant to the present work, as it involves low-Reynolds-number, vortex-dominated aerodynamics and finite-wing effects comparable to those investigated in later chapters.

Figure 2.10 compares the lift coefficient predicted by RANS and IDDES with experimental measurements. Both numerical approaches slightly over-predict the peak lift coefficient, by approximately 14% for RANS and 12% for IDDES. While the overall force histories predicted by both models are quantitatively similar, comparison of integrated loads alone does not reveal differences in the underlying flow physics, motivating examination of the corresponding flow-field

structures.

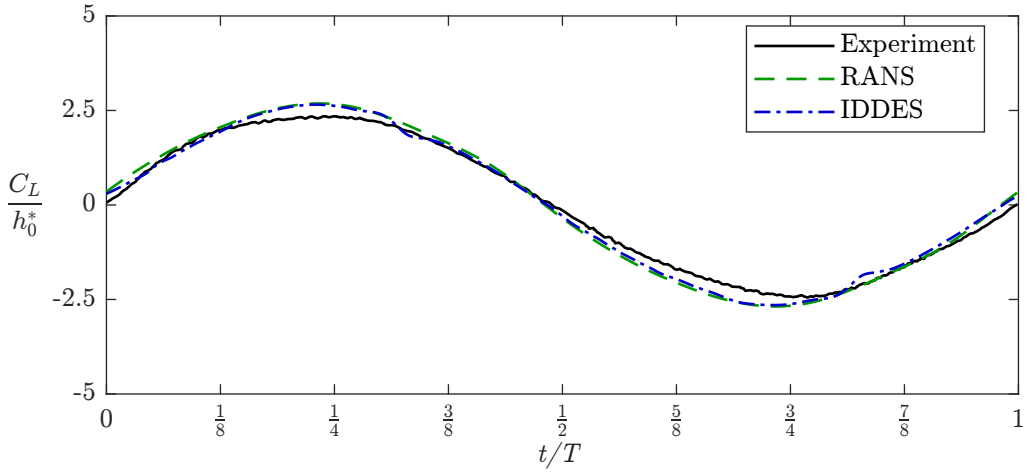

Figure 2.10: Comparison between experimental results, RANS results and IDDES results for an aspect ratio 3, unswept wing undergoing a sinusoidal plunging motion with a chord-reduced plunge amplitude $h_0^* = 0.5$ and reduced frequency $k = 0.4$. Adapted from Bird *et al.* [85], with permission.

A qualitative comparison of mid-span spanwise vorticity fields (as indicated in Figure 2.4) is shown in Figure 2.11. The IDDES results reproduce the formation, growth, and downstream convection of the LEV observed in the PIV measurements, including both the inclination of the separated shear layer and the onset of LEV breakdown at $t/T = 3/8$. The breakdown appears slightly more advanced in the IDDES results compared to PIV, consistent with the lift reduction observed in Figure 2.10.

In contrast, the RANS solution exhibits a largely smooth separated shear layer, with separation occurring at an incorrect angle relative to the wing surface and without the formation of a coherent vortex core. Although the flow is separated at $t/T = 3/8$, the absence of a resolved vortex structure and the overly diffuse vorticity field prevent an accurate representation of LEV breakdown. These observations highlight the limitations of Reynolds-averaged turbulence modelling for highly unsteady, vortex-dominated flows.

The close qualitative agreement between the IDDES results and experimental vortex topology supports the suitability of the IDDES framework for studies in which resolved vortex dynamics play a central role in unsteady force generation.

2.8.2 Verification studies

Grid independence was assessed using three systematically refined meshes for a representative configuration used directly in this thesis. The chosen configuration was a moderately swept (30°), aspect ratio 3 wing undergoing plunge ramp kinematics at reduced frequency $k = 0.4$. Grid refinement was applied primarily within the DES focus region surrounding the wing, while the boundary-layer mesh was unchanged to maintain consistent near-wall resolution.

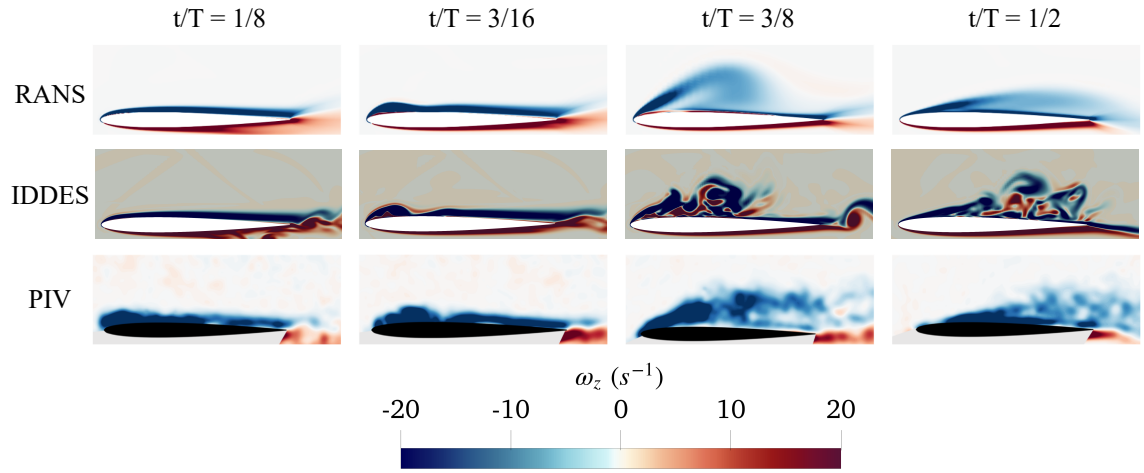

Figure 2.11: Mid-span (as indicated in Figure 2.4) spanwise vorticity distribution comparison between RANS, IDDES and experimental results for the aspect ratio 3, unswept plunging wing undergoing the same prescribed kinematics as Figure 2.10. Adapted from Bird *et al.* [85], with permission.

Table 2.2: Lift coefficient comparison between successive levels of mesh refinement at the global minimum.

Refinement level	Δ_0	C_L	Percentage error (%)
Coarse	0.018c	-2.65	0.26
Medium	0.015c	-2.66	0.01
Fine	0.010c	-2.66	–

The meshes differed principally in the target cell size within the focus region, which is key to force generation. The coarse, medium, and fine meshes employed target mesh spacings of $\Delta_0 = 0.018c, 0.015c$ and $0.010c$, respectively. While this corresponds to a factor of 1.8 variation in linear resolution, it results in an almost sixfold change in cell volume within the region responsible for resolving unsteady vortex dynamics. The spanwise grid spacing was held constant across all three meshes, following preliminary sensitivity studies used to establish an appropriate baseline resolution in the spanwise direction.

Table 2.2 reports the lift coefficient at the global minimum for each refinement level, together with the percentage difference relative to the fine mesh in the absence of experimental data for this specific case. The difference between the coarse and medium meshes is approximately an order of magnitude larger than the difference between the medium and fine meshes, while the medium and fine results are effectively indistinguishable. This behaviour is consistent with grid convergence of the integrated lift coefficient for the resolutions considered here.

To further assess convergence of the unsteady aerodynamic response, Figure 2.12 presents differences in the lift coefficient over the full plunge motion. Figure 2.12a shows the difference relative to the fine-mesh solution, illustrating that the coarse mesh begins to deviate from the fine-mesh response shortly after the onset of motion at $t^* \approx 1$, while the medium mesh remains

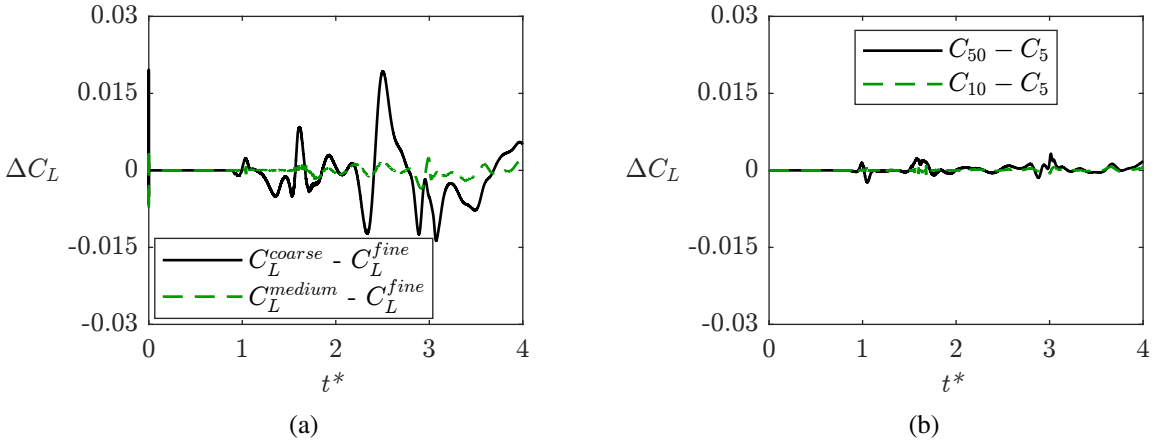

Figure 2.12: Verification of numerical sensitivity for a representative plunging wing case at $k = 0.4$. *Left:* Difference in lift coefficient relative to the fine-mesh solution, $\Delta C_L = C_L - C_L^{fine}$, illustrating convergence of the unsteady loading with mesh refinement. *Right:* Difference in lift coefficient relative to the baseline $C = 5$ case.

closely aligned until approximately $t^* \approx 1.6$, corresponding to the completion of the plunge ramp. Throughout the cycle, deviations between the medium and fine meshes remain approximately an order of magnitude smaller than those associated with the coarse mesh. The maximum deviation in ΔC_L is less than 0.02 for the coarse mesh, corresponding to approximately 1.25% of the peak lift coefficient for this case (excluding added-mass peaks).

Figure 2.12b presents the corresponding comparison for different Courant number limits on the same vertical scale. A baseline Courant number of $C = 5$ was selected as the lowest practically achievable value for the present simulations, balancing numerical accuracy and computational cost. The results show negligible sensitivity to Courant number choice, with variations that are substantially smaller than the mesh-induced differences observed in Figure 2.12a. Taken together, these results show that the selected medium mesh and baseline time-stepping strategy with $C = 5$ provide a converged and temporally robust representation of the unsteady lift response.

Additional verification checks were performed to assess sensitivity to near-wall meshing. The boundary-layer mesh specification, including first-layer height and growth rate, was refined through five successive meshing iterations to arrive at the final configuration. Differences in the resolved force histories and flow structures were observed between intermediate iterations. However, further refinement beyond the final configuration did not produce discernible changes in the quantities of interest, indicating that the near-wall resolution employed is sufficient.

Additional verification studies, including systematic variation of the spanwise domain width, were considered as part of the numerical assessment. However, their implementation was limited by practical constraints related to computational cost and the availability of specialist meshing tools. Within these constraints, the validation and verification exercises presented here provide confidence in the robustness of the numerical methodology for the parametric investigations undertaken in the subsequent chapters.

3

Low-Order Theoretical Modelling Framework

> *All models are wrong, but some are useful.*
>
> **— George Box**
> (Statistician)

3.1 Overview and purpose of the low-order modelling approach

THE aerodynamic behaviour of leading-edge vortices (LEVs) over swept wings is governed by the interaction between unsteady circulation growth, three-dimensional vortex development, and leading-edge separation. While Chapter 2 introduced the high-fidelity IDDES framework used to resolve these mechanisms directly, it is also valuable to employ simplified modelling tools that offer rapid, physically interpretable predictions of unsteady lift and LEV onset.

Therefore, this chapter establishes the low-order model (LOM) frameworks used throughout the thesis, outlining the assumptions underlying each method, their mathematical formulation, and their intended role alongside CFD analysis in later chapters.

This chapter introduces the two LOMs used throughout the thesis:

- C-LAULLT (corrected large-amplitude unsteady lifting-line theory): an extended version of LAULLT that incorporates a first-order sweep-angle correction while retaining the original model's ability to handle large-amplitude, time-dependent motions.
- Variable leading-edge suction parameter (LESP) theory for finite wings: a separate but complementary onset model that predicts the spanwise distribution of leading-edge suction and is used to infer when and where an LEV first forms.

These models serve distinct roles:

- C-LAULLT predicts the time-resolved bound circulation distribution and the corresponding unsteady lift response. The model does not include a separation or vortex-shedding model.
- Variable LESP provides an independent, physics-based criterion for the initiation of leading-edge separation and LEV formation.

Both models are presented together in this chapter because they collectively form the analytical foundation for the mechanism-based interpretations developed in Chapters 4-6, but they remain conceptually and mathematically separate.

A brief summary of the classical unsteady lifting-line and LAULLT frameworks is given in Section 3.2 for clarity before presenting the modified C-LAULLT formulation in Section 3.3. LESP theory is then introduced in Section 3.4, before being assessed against CFD trends in Section 3.5.

3.2 Classical lifting-line and LAULLT methods

This section outlines the classical lifting-line theory and its large-amplitude unsteady extension (LAULLT), which form the foundational basis for the corrected formulation (C-LAULLT) presented in Section 3.3. The lifting-line approach reduces the three-dimensional unsteady flow field around a finite wing to a one-dimensional distribution of bound circulation, with induced velocities calculated from the wake using the Biot–Savart law. The LAULLT extension enables large-angle, unsteady motions to be modelled in the time domain.

3.2.1 Classical lifting-line theory

Prandtl's [33] LLT provides a steady, inviscid framework for predicting the spanwise circulation distribution, $\Gamma(s)$, on finite wings. By relating $\Gamma(s)$ to the induced downwash through the Biot–Savart law, LLT captures essential three-dimensional aerodynamic effects, including tip vortex-driven downwash and non-uniform spanwise loading.

Despite its success for steady flows, classical lifting-line theory is inadequate for predicting unsteady aerodynamic response, vortex growth during rapid kinematic changes, interactions between impulsive motions and tip vortices, and the dynamic evolution of the wake. These limitations motivated the development of unsteady extensions.

3.2.2 Large-amplitude unsteady lifting-line theory (LAULLT)

Bird *et al.* [102] developed LAULLT, building on Devinant's unsteady lifting-line formulation [99, 100] by coupling a geometrically non-linear inner model to an unsteady outer lifting-line correction. The model considers a high-aspect-ratio straight wing, enabling a separation of the

flow into spanwise (3D) and chordwise (2D) components. In essence, each wing section is treated with a two-dimensional unsteady thin aerofoil solution (the inner problem), while the wing's trailing wake induces additional velocities across the span (the outer problem). This separation is valid for large aspect ratios, and relatively low reduced frequencies so that unsteady effects do not vary significantly over the chord. Under the large aspect ratio and low reduced frequency assumptions, the wing's surface can be collapsed to a lifting line carrying the bound circulation, and the flow is solved by matching inner and outer solutions on the lifting line.

Within LAULLT, the total downwash w at a wing section M is decomposed into the local (inner) two-dimensional contribution and the finite-wing (outer) contribution. Bird *et al.* [102] express this as Equation 3.1:

$$w(M) = w_{2D}(M) + w_{out}(M_0) - w_{wi}(M_0). \tag{3.1}$$

Here $w_{2D}(M)$ is the downwash induced by the section's bound vorticity and near wake (inner domain), while $w_{out}(M_0)$ is the additional downwash at the lifting line due to the full three-dimensional trailing wake of the wing. The term $w_{wi}(M_0)$ subtracts the portion of the near wake's influence that was counted in both domains, avoiding duplication. In other words, the inner two-dimensional solution provides the baseline corresponding to an infinite-span aerofoil section, while the outer solution applies a correction to account for finite-span induced velocities generated by neighbouring sections. This interaction is handled through the lifting line. All inner solutions communicate via the spanwise distribution of shed vorticity in the wake. Each section's effective angle of attack is thus altered by the instantaneous downwash from the rest of the wing. For example, the local relative flow velocity at section y_i becomes:

$$U_{eff}(y_i, t) = U_\infty + w_{out}(y_i, t) - w_{wi}(y_i, t), \tag{3.2}$$

which is the freestream U_∞ plus the net induced vertical velocity at the station y_i. This coupling is the key to capturing three-dimensional effects, such as lift reduction and phase lag due to tip vortices, while still using essentially two-dimensional sectional aerodynamics.

For each spanwise strip, LAULLT employs an unsteady thin-aerofoil theory capable of handling large amplitude motions. Specifically, Bird *et al.* [102] use Ramesh *et al.*'s [71] large-angle unsteady thin aerofoil theory (LAUTAT). In this framework, the bound circulation distribution along a two-dimensional section's chord is expanded in a Fourier series plus an analytical singular leading-edge term to account for the strong suction peak at the leading edge. Mathematically, the bound vorticity per unit length on the aerofoil is defined as Equation 3.3:

$$\gamma_b(y_i; t) = 2|U_\infty| \left[A_0(y_i, t) \frac{(1 + \cos\theta)}{\sin\theta} + \sum_{n=1}^{\infty} A_n(y_i, t) \sin(n\theta) \right]. \tag{3.3}$$

The aerofoil frame coordinate system used is shown in Figure 3.1, where the chord is on

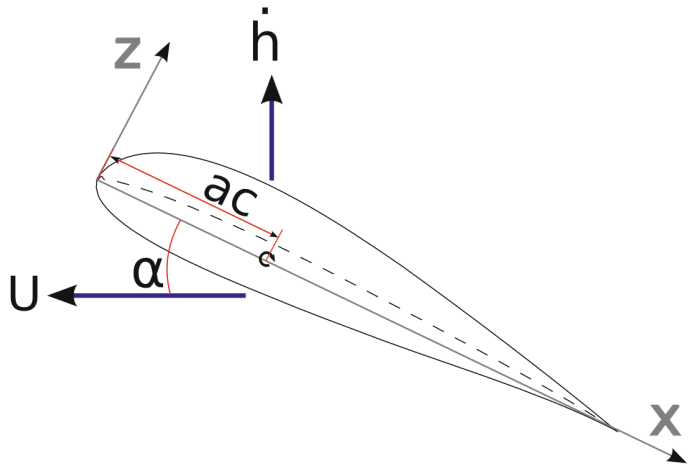

Figure 3.1: Diagram illustrating the aerofoil frame coordinate system and velocities, reproduced from Ramesh *et al.* [71], with permission.

$x \in [0, c]$. Here $x = c/2(1 - \cos\theta)$ is a coordinates substitution along the chord (with $\theta = 0$ at the leading edge), and $A_0, A_1, A_2, \ldots$ are unknown Fourier coefficients that vary with time. The $(1 + \cos\theta)/\sin\theta$ term represents a potential flow singularity at the leading edge, associated with the theoretical suction force there. Including this term allows the model to handle cases where the leading-edge suction is high or even reaches a limit, potentially signalling stall, as discussed in later in Section 3.4. In steady thin-aerofoil theory, the above expansion automatically satisfies the Kutta condition. However, in unsteady conditions, Bird *et al.* [102] do not explicitly enforce zero trailing-edge circulation at each instant. They note that deviations from the Kutta condition appear to have a small influence in unsteady flows. Instead, the shed vorticity from the trailing edge will enforce overall circulation conservation via Kelvin's theorem as the motion progresses.

To determine the coefficients $A_n(y_i, t)$, the aerofoil boundary condition of no flow penetration through the camber line is applied. This is typically done by satisfying the flow tangency condition at collocation points along the chord or by Galerkin projection. In the formulation by Ramesh *et al.* [71], the solution yields closed-form integral expressions for the coefficients, which are given by Equation 3.4:

$$A_0(y_i, t) = -\frac{1}{\pi} \int_0^{\pi} \frac{W(\theta)}{|U_\infty|} d\theta, \tag{3.4a}$$

$$A_n(y_i, t) = \frac{2}{\pi} \int_0^{\pi} \frac{W(\theta)}{|U_\infty|} \cos(n\theta) d\theta. \tag{3.4b}$$

Here $W(\theta)$ is the downwash distribution along the aerofoil chord in the section-fixed frame. $W(\theta)$ includes contributions from the wing's motion kinematics, the free-stream angle of attack, and induced velocities associated with previously shed vorticity. Enforcing the no-penetration boundary condition allows the coefficients A_0 and A_n to be solved at each time step. Once the coefficients are known, the section's bound circulation can be obtained by integrating γ_b over the chord. Performing that integration yields

$$\Gamma_b = \frac{|U_\infty| c\pi}{2}\left[A_0 + \frac{1}{2}A_1\right] \tag{3.5}$$

for each section. This shows that the lowest-order coefficients A_0 and A_1 directly relate to the total circulation on the section. Notably, A_0 governs the leading-edge suction contribution. A_1 is related to the linear loading component. In steady attached flow, A_1 adjusts to enforce the Kutta conditionby enforcing zero bound vorticity at the trailing edge. In unsteady flow, the Kutta condition is enforced in a time-dependent sense, and temporal variations in A_1 are directly linked to the shedding of a trailing-edge vortex sheet required to accommodate changes in circulation.

As the wing moves or aerofoil sections change circulation, Kelvin's theorem requires that any change in bound circulation must be shed into the wake. LAULLT enforces this by shedding discrete vortex elements from the trailing edge of each section. At the m^{th} time step t_m, a wake vortex is released such that the total circulation is conserved. In practice, Bird *et al.* [102] compute the strength of the new shed vortex $\Delta\Gamma_m$ by ensuring

$$\Gamma_b(t_m) + \sum_{p=0}^{m} \Gamma_p = 0, \tag{3.6}$$

where $\Gamma_b(t_m)$ is the bound circulation for a given section at the new time and $\sum_{p=0}^{m}\Gamma_p$ is the sum of all shed wake vortex strengths up to and including the new one indexed by $p = m$. Solving Equation 3.6 for the new Γ_m yields the shed vortex strength required to account for the bound circulation change from the previous time step. In essence, if the inner solution predicts a trailing-edge vorticity along a section, vorticity is immediately shed into the wake as a new free vortex so that the section's trailing-edge Kutta condition is physically satisfied. The shed vortex is then convected downstream in the wake domain. Figure 3.2 illustrates this process, showing the wing modelled as a lifting line with a continuous trailing wake comprised of shed vortex elements.

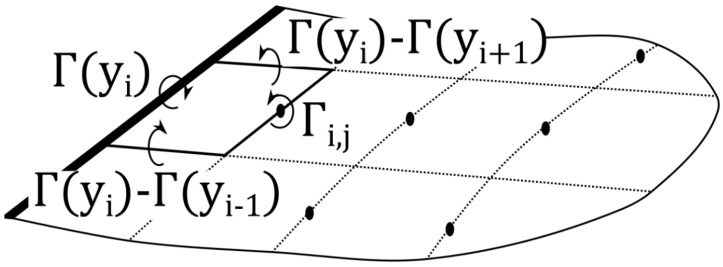

Figure 3.2: Diagram illustrating the lifting line and trailing wake vortex lattice, reproduced from Bird *et al.* [102], with permission.

The LAULLT algorithm thus proceeds by time-stepping. At each time step, the sectional coefficients A_0 and A_n, and hence the bound circulation Γ_b, are solved using the effective angle of attack, which accounts for downwash induced by the previously shed wake. New vortices are then shed in accordance with Kelvin's theorem, and the resulting wake-induced velocities are updated for use in the next time step. The outer downwash velocity, $w_{out}(y,t)$, is obtained by

summing the velocity contributions from the bound vortices and the horseshoe vortices shed into the wake. Because the wake freely convects with the flow, the induced velocities can include three-dimensional and unsteady effects such as tip vortex influence and wake distortion.

Unlike earlier ULLT formulations such as Sclavounos [96], which assume a planar wake, the LAULLT of Bird *et al.* [102] uses a fully three-dimensional discrete-vortex wake in the outer solution. Bird *et al.* [102] note that discretising the span into as few as $N = 16$ strips was sufficient to obtain accuracy within 1% relative to the asymptotically converged LAULLT solution in their test cases. In the present study, $N = 15$ strips are used per unit aspect ratio, yielding finer spanwise resolution to achieve a comparable accuracy threshold given the considered plunge-ramp kinematics.

Once the bound circulation distribution $\Gamma_b(y,t)$ is known at a given time, the lift and moments on the wing can be obtained by integrating the sectional contributions. At the sectional level, the normal-force coefficient can be expressed in terms of the A_n coefficients. For example, the theory gives an expression of the form

$$C_n(y_i,t) = \frac{(2U_\infty \cos\alpha + \dot{h}\sin\alpha)}{|U_\infty|}\left[A_0 + \frac{1}{2}A_1\right] + \frac{c}{2|U_\infty|}(3\dot{A}_0 + \dot{A}_1 + \frac{1}{2}\dot{A}_2) + \ldots, \tag{3.7}$$

where the first term represents the circulatory lift, which is proportional to instantaneous bound circulation, and the second term represents the added-mass forces. Additional induced terms from the wake are of smaller order. This shows that LAULLT retains non-linear geometric effects and unsteady terms without relying on a small-angle assumption, making it suitable for large-angle manoeuvres. In fact, Bird *et al.* [102] verified LAULLT against both small-amplitude theory and CFD and validated against experiment for wings undergoing plunge oscillations, and found the model captures the unsteady lift history well, with slight improvements over small-angle models at higher amplitudes.

In summary, LAULLT provides a framework to predict unsteady lift on a finite wing by combining two-dimensional unsteady aerofoil solutions with three-dimensional induced flow coupling through a lifting-line formulation. This theory forms the basis for the corrected large-amplitude unsteady lifting-line theory (C-LAULLT) developed in Section 3.3. C-LAULLT modifies LAULLT by incorporating a first-order sweep-angle correction, extending its applicability to swept wings. This correction follows the theoretical framework introduced by Guermond and Sellier [98], ensuring the model remains consistent with classical lifting-line behaviour, while adjusting the local effective flow direction and hence circulation strength. Notably, both LAULLT and C-LAULLT assume fully attached, inviscid flow and do not predict leading-edge separation or vortex shedding phenomena. These characteristics are addressed separately in this thesis using a variable LESP model, introduced in Section 3.4.

3.3 Correction to unsteady lifting-line theory

The large-amplitude unsteady lifting-line theory (LAULLT) introduced in Section 3.2.2 provides a time-domain framework for computing bound circulation on a finite wing undergoing arbitrary motion. However, in its original form, the model is limited to unswept, high-aspect-ratio wings and does not include flow separation modelling.

This section introduces the corrected LAULLT formulation (C-LAULLT), which extends the baseline LAULLT theory by applying a first-order sweep-angle correction to the three-dimensional interaction kernel K_1. The underlying time-domain formulation and implementation structure remain unchanged from LAULLT.

The corrected method retains the assumptions of inviscid flow and large aspect ratio, but enables lift prediction for moderately swept wings. In this thesis, C-LAULLT is applied to leading-edge sweep angles up to $\Lambda = 60°$ and serves as a supporting analytical framework in subsequent analysis.

3.3.1 Sweep-angle correction

To extend lifting-line theory to moderately swept wings, a first-order correction is sought that accounts for sweep within an inviscid, attached-flow framework. Under the classical lifting-line assumptions of high aspect ratio and slow spanwise variation of circulation, the flow over a finite wing can be treated as a perturbation from two-dimensional behaviour. These are the same conditions assumed in Bird's LAULLT [102], and they remain in effect when introducing sweep. The model assumes a thin wing with moderate leading-edge sweep angle, attached flow, and a wake aligned with the freestream. These assumptions do not hold for the CFD cases in this thesis, which feature LEV formation, tip vortices and a fully three-dimensional wake. The model is applied outside its theoretical limits to assess its usefulness under such conditions. Under the large aspect ratio, inviscid flow, and linear wake assumptions, Guermond and Sellier's ULLT [98] shows that a swept wing does not invalidate the asymptotic expansion. Rather, sweep modifies the form of the solution at leading order.

For a wing with leading-edge sweep angle Λ, as shown in Figure 3.3, only the free-stream component normal to the lifting line contributes to lift. The free-stream velocity can be decomposed into a component $U_\infty \cos\Lambda$ perpendicular to the bound vortex line and a component $U_\infty \sin\Lambda$ in the spanwise direction. The former, $U_\infty \cos\Lambda$, is the effective velocity governing sectional lift. From the Kutta–Joukowski theorem in vector form,

$$\mathbf{f'} = \rho \mathbf{U}_\infty \times (\Gamma \mathbf{t}), \tag{3.8}$$

where force per unit span **f'** is proportional to bound circulation Γ and **t** is the local tangent vector along the lifting line. When sweep is non-zero, this becomes

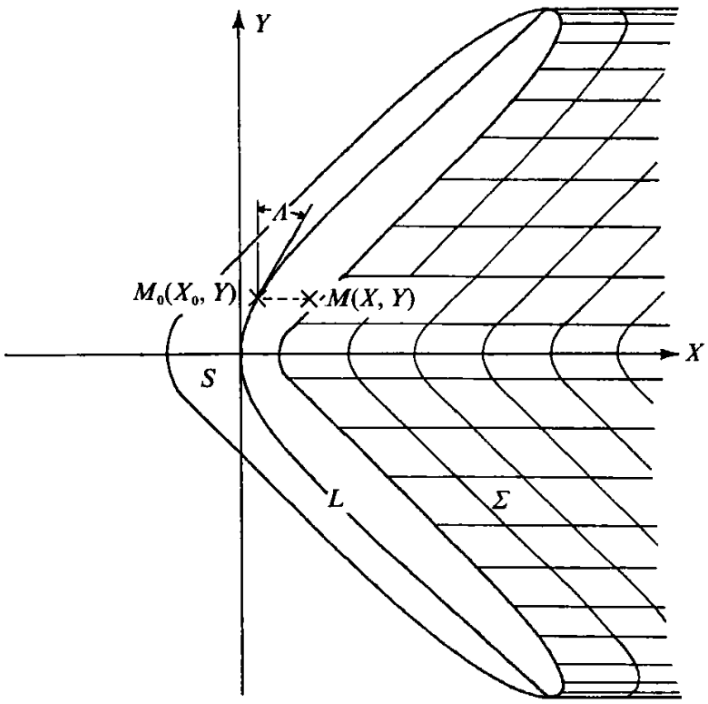

Figure 3.3: Diagram illustrating the geometry and Cartesian coordinate system, reproduced from Guermond and Sellier [98], with permission.

$$\mathbf{f}' = \rho U_\infty \Gamma \cos\Lambda. \tag{3.9}$$

Thus, the sectional lift per unit span is reduced by a factor $\cos\Lambda$, as shown in Equation 3.10.

$$L'(y) = \rho U_\infty \Gamma(y) \cos\Lambda \tag{3.10}$$

This effect can be interpreted through the induced angle of attack. In lifting-line theory, the local effective angle of attack is

$$\alpha_{eff}(y) = \alpha_{geom}(y) - \alpha_i(y). \tag{3.11}$$

With sweep, the induced angle $\alpha_i(y)$ is defined using the velocity component normal to the lifting line, as shown in Equation 3.12.

$$\alpha_i(y) \approx \frac{w(y)}{U_\infty \cos\Lambda} \tag{3.12}$$

Therefore, the same downwash $w(y)$ produces a larger induced angle α_i on a swept wing, effectively reducing α_{eff} and hence lift. In parallel, the influence of a bound vortex at y' on another spanwise location y is reduced due to the increased geometric spacing between trailing vortices, which scales as $(y - y')\cos\Lambda$. The net result is a weaker downwash field and hence a spanwise redistribution of circulation.

Guermond and Sellier's [98] ULLT provides the asymptotic basis for the sweep angle correction used in C-LAULLT. They treat the finite-wing unsteady lift problem as a singular perturbation with respect to the inverse aspect ratio, performing an expansion of the solution for a wing of large aspect ratio with moderate sweep. At each order, the three-dimensional problem decomposes into a two-dimensional-like operator capturing the local aerofoil response, coupled with a three-dimensional influence operator capturing finite-span effects. This yields a coupled operator equation for the wing's induced downwash.

In particular, Guermond and Sellier [98] show that the downwash $w(x, y)$ can be expanded as

$$w(x,y) = \frac{1}{\cos\Lambda}\mathcal{K}_0[[\psi]] + \frac{1}{AR}\mathcal{K}_1[[\psi]] + \mathcal{O}\left(\frac{1}{AR}\right). \tag{3.13}$$

Here, $[[\psi]]$ denotes the jump in acceleration potential, which is proportional to the pressure jump and hence to the bound circulation. The operators $\mathcal{K}_0$ and $\mathcal{K}_1$ represent the zeroth-order (two-dimensional) and first-order (three-dimensional) contributions to the induced downwash, respectively. Explicit expressions for these operators, along with the auxiliary quantities on which they depend, are provided in Appendix A.

Equation 3.13 shows that the downwash for an infinite aspect ratio wing is modified by a finite-span correction that enters at first order in the parameter $1/AR$. The leading-order contribution, $\mathcal{K}_0/\cos\Lambda$, corresponds to the classical two-dimensional unsteady operator, scaled by the geometric factor $1/\cos\Lambda$ arising from the chordwise projection associated with wing sweep.

The first-order correction, $(1/AR)\mathcal{K}_1$, accounts for three-dimensional finite-span effects. Importantly, as noted by Guermond and Sellier [98], sweep influences the downwash only through the leading-order geometric scaling and does not appear explicitly in the structure of the three-dimensional operator at this order. The operator $\mathcal{K}_1$ depends on auxiliary functions $G(y)$ and $H(x, y)$, which represent chordwise-integrated forms of the potential jump and geometry-dependent contributions, respectively. See Appendix A for details.

The key implication of Equation 3.13 is that swept wings exhibit a non-zero $\mathcal{O}(1/AR)$ modification to the downwash, whereas for unswept wings the first-order correction vanishes due to cancellation and higher-order terms dominate. This provides the asymptotic basis for introducing a sweep-dependent correction within the lifting-line formulation.

The next step in the asymptotic development is to invert the operator equation to obtain the potential jump $[[\psi]]$. When this is done, the solution can be written in a form that isolates the leading-order sweep dependence. In particular, Guermond and Sellier [98] show that, to first order in the parameter $1/AR$,

$$[[\psi]] = \cos\Lambda\mathcal{K}_0^{-1}\left[w(M) - \frac{1}{AR}\mathcal{K}_1[[\psi_0]]\right] + \mathcal{O}\left(\frac{1}{AR}\right). \tag{3.14}$$

Here $\mathcal{K}_0^{-1}$ denotes the inverse of the inner (2D) operator $\mathcal{K}_0$. $\mathcal{K}_0^{-1}$ recovers the potential jump

from a prescribed downwash when only the two-dimensional coupling is retained. The quantity $[[\psi_0]]$ is the zeroth-order (infinite aspect ratio) solution and is obtained by applying $\mathcal{K}_0^{-1}$ to the geometric downwash. Further details are given in Appendix A.

Guermond and Sellier identify the term $-\cos\Lambda K_1[[\psi_0]]/AR$ as the first-order induced downwash generated by finite-span effects. Physically, $-\cos\Lambda K_1[[\psi_0]]/AR$ captures the reduction in effective angle of attack caused by the wing's shed vorticity. The same structure appears in the C-LAULLT correction, where the factor $\cos\Lambda$ arises naturally from the asymptotic solution rather than from any empirical tuning. For moderately swept, high-aspect-ratio wings, sweep is accounted for at leading order, with finite-span corrections entering at first order, providing a direct theoretical justification for the correction used in this thesis. Higher-order terms in the Guermond and Sellier [98] expansion are omitted, as they are small compared with the first-order contribution.

The sweep correction developed here is intended as a leading-order extension of LAULLT within the assumptions of lifting-line theory. In particular, the correction retains the high–aspect-ratio, inviscid framework of LAULLT and introduces sweep effects through an asymptotic correction rather than a fully three-dimensional reformulation. As a result, the corrected model captures both qualitative trends and quantitative variations associated with sweep angle and unsteady kinematics, while discrepancies are primarily expected in regimes dominated by strong three-dimensional separation and vortex breakdown. In this context, the corrected formulation serves as an interpretive LOM to aid physical understanding alongside high-fidelity CFD.

With this asymptotic basis established, the corrected lifting-line formulation (C-LAULLT) is now introduced. The objective is to retain the structure of LAULLT while incorporating the sweep-dependent first-order correction identified in Equation 3.14, and to implement the correction in a form suitable for unsteady, large-amplitude wing motions.

3.3.2 Corrected LAULLT (C-LAULLT) formulation

The C-LAULLT formulation retains the structure of Bird *et al.*'s LAULLT model [102], but incorporates the first-order sweep correction identified in the Guermond and Sellier [98] asymptotics. In LAULLT, the downwash seen by a spanwise strip is given by the sum of the geometric downwash and the contribution induced by the wake. In C-LAULLT, the component of the free-stream velocity normal to the lifting line is reduced by $\cos\Lambda$, so that the effective two-dimensional problem at each strip is modified accordingly.

For a swept wing, the effective normal velocity is

$$U_\perp = U_\infty \cos\Lambda, \tag{3.15}$$

where $U_\perp$ denotes the flow component perpendicular to the lifting-line direction.

Thus, the downwash term used in Bird *et al.*'s [102] two-dimensional sectional ODE system

for the Fourier coefficients A_n is corrected by replacing the original downwash $w(y,t)$ with the sweep-corrected form

$$w_\Lambda(y,t) = w(y,t)\cos\Lambda. \tag{3.16}$$

The corresponding sectional circulation is

$$\Gamma(y,t) = U_\perp\, c(y)\left(A_0(y,t) + \frac{1}{2}A_1(y,t)\right), \tag{3.17}$$

which, substituting $U_\perp = U_\infty \cos\Lambda$, becomes

$$\Gamma_\Lambda(y,t) = \cos\Lambda\, U_\infty\, c(y)\left(A_0(y,t) + \frac{1}{2}A_1(y,t)\right). \tag{3.18}$$

Following Bird *et al.* [102], the local lift per unit span is

$$\ell_\Lambda(y,t) = \rho_\infty U_\infty \Gamma_\Lambda(y,t), \tag{3.19}$$

and the total lift is obtained by integrating along the span, as shown in Equation 3.20.

$$L_\Lambda(t) = \int_{-b/2}^{b/2} \ell_\Lambda(y,t)\,dy \tag{3.20}$$

To enable comparison with numerical and experimental datasets, the instantaneous lift coefficient is defined using the free-stream dynamic pressure and the wing planform area as

$$C_{L,\Lambda}(t) = \frac{L_\Lambda(t)}{\frac{1}{2}\rho_\infty U_\infty^2 S}. \tag{3.21}$$

This formulation therefore differs from LAULLT only in the appearance of $\cos\Lambda$ in the effective inflow velocity seen by each strip and the circulation relation, both of which reflect the first-order sweep scaling predicted by Equation 3.14. No other components of the LAULLT solution procedure are modified.

The practical implementation follows the same time-marching structure as LAULLT, with the above sweep-corrected quantities substituted into the stripwise ODEs. The method is summarised below in Section 3.3.3.

3.3.3 Implementation of C-LAULLT

The time-marching algorithm for LAULLT (and C-LAULLT) follows the structure described by Bird *et al.* [102]. At each time step:

1. **Compute the outer solution:** Evaluate the induced downwash at each spanwise station from the bound circulation and all previously shed vortex particles using the Biot-Savart law. This provides the input downwash for the inner (2D) problem.

2. **Insert new vortex particles:** At each spanwise strip, place a new vortex particle immediately downstream of the trailing edge. This particle represents the circulation that will be shed over the current time step.

3. **Solve the inner solution:** For each strip, integrate Bird *et al.*'s [102] ODE system using the sweep-corrected downwash to update the bound circulation. The change in circulation over the time step determines the strength of the newly inserted vortex particle.

4. **Convect all vortex particles:** Advect all particles in the wake using the induced velocity field. This is the dominant computational cost and scales as $\mathcal{O}(Nm^2)$, where N is the number of spanwise strips and m is the number of time steps.

5. **Advance to the next time step:** The updated particle strengths and positions determine the induced downwash for the next outer solution, closing the coupling between inner and outer solutions.

3.3.4 Limitations

While C-LAULLT provides a practical and physically grounded model for unsteady lift prediction on finite, moderately swept wings, the model carries several inherent limitations that must be acknowledged when interpreting its results.

- **Inviscid, incompressible formulation:** C-LAULLT inherits the inviscid, incompressible, and irrotational flow assumptions from classical lifting-line theory and the LAULLT extension.

- **No separation or stall modelling:** C-LAULLT assumes attached flow and hence contains no intrinsic mechanism for predicting flow separation, stall, or LEV onset. While the method captures unsteady circulation response and spanwise coupling via induced downwash, the model predicts increasing lift at high angles of attack unless supplemented with an external separation or stall model.

- **High aspect ratio requirement:** The underlying Guermond and Sellier [98] asymptotic framework is derived for wings of large aspect ratio. Although C-LAULLT is applied here to finite aspect ratio wings, its quantitative accuracy may degrade for low aspect ratios, where strong three-dimensional vortex interactions fall outside the model assumptions.

- **First-order sweep correction:** The sweep-angle correction employed here is based on a first-order asymptotic scaling with $\cos\Lambda$. This captures the leading geometric effect of sweep for moderate sweep angles but does not account for other three-dimensional effects such as spanwise pressure redistribution, spanwise flow development, or changes in leading-edge suction. Although applied up to $\Lambda = 60°$ in this study, accuracy may reduce at high sweep.

- **Limited representation of spanwise flow physics:** Spanwise coupling in C-LAULLT occurs only through the induced velocity field. Each section is treated as locally two-dimensional, with no explicit modelling of spanwise convection or vortex transport. Consequently, spanwise flow mechanisms associated with LEV growth, stability, or breakdown are not resolved directly and enter only indirectly through their influence on the downwash.

These limitations motivate the use of an additional onset model, introduced in Section 3.4, which accounts for flow separation and provides a novel shedding criterion to determine LEV formation on finite wings.

3.4 Variable LESP theory for finite wings

While C-LAULLT provides the time-resolved bound circulation on a finite wing, the model assumes attached flow and therefore cannot indicate when leading-edge separation or LEV formation will occur. To interpret these events we use LESP, originally developed for two-dimensional unsteady aerofoils [71, 79] and recently extended by Martínez *et al.* [164] through a shear-layer-based formulation.

In this thesis, LESP is used solely as a diagnostic applied to the CFD solution. At each spanwise location, the LESP value is calculated through Martínez *et al.*'s [164] formulation. The resulting spanwise LESP distribution is compared with Q-criterion visualisations in Section 3.5, to assess how effectively LESP identifies the onset and spatial variation of LEV formation on swept wings.

3.4.1 LESP and its relationship to A_0

As introduced in Section 3.2.2, unsteady thin aerofoil theory represents the bound vorticity distribution on each section using a Fourier series expansion in the transformed chordwise coordinate, defined in Equation 3.3. The instantaneous coefficients $A_0(t)$ and $A_n(t)$ are defined in Equation 3.4. Within this formulation, the leading coefficient $A_0(t)$ multiplies the singular term in the vorticity distribution associated with the leading-edge suction peak, while the higher-order coefficients describe the remaining, regular contribution to the bound circulation. The inner solution of LAULLT, therefore, admits a direct interpretation of $A_0(t)$ as a measure of the inviscid leading-edge suction at each section.

Physically, this leading-edge suction reflects the level of flow acceleration required around the rounded leading edge to maintain attachment. For a given two-dimensional aerofoil geometry and Reynolds number, this requirement is finite, as the near-wall flow cannot sustain arbitrarily large pressure gradients at the leading edge.

Following Ramesh *et al.* [71], the instantaneous LESP at a section is defined as

$$LESP(t) = A_0(t). \tag{3.22}$$

A critical value, $LESP_{crit}$, marks the onset of leading-edge separation. Ramesh *et al.* [79] demonstrated that the two-dimensional critical LESP is independent of the prescribed kinematics for a given aerofoil and Reynolds number. When LESP exceeds this value, the suction demand implied by the inviscid solution can no longer be supported by the real flow, leading to loss of attachment and roll-up of a separated shear layer to form a LEV.

Because LESP is defined in terms of the inviscid leading-edge suction predicted by thin-aerofoil theory, its evaluation requires careful treatment of the leading-edge flow. In classical unsteady thin-aerofoil theory, the velocity and vorticity fields exhibit singular behaviour at the leading edge. To obtain a physically meaningful estimate of the shear-layer velocity, this singular outer solution must be coupled to an inner solution that accounts for the finite curvature of the leading edge. Ramesh [165] related the velocity at the leading edge, u_{LE}, to A_0 via

$$u_{LE}(t) = \sqrt{\frac{2}{r_{LE}}}\, U_\infty A_0(t), \tag{3.23}$$

where r_{LE} is the radius of curvature at the leading edge. Rearranging this expression gives a direct formula for obtaining LESP from the shear-layer velocity.

$$LESP(t) = \sqrt{\frac{r_{LE}}{2}}\, \frac{u_{LE}(t)}{U_\infty} \tag{3.24}$$

This inversion is the form used in this study to compute LESP from the CFD data.

3.4.2 Constant and variable LESP shedding models

The manner in which LESP is enforced after the onset of separation has important implications for the predicted evolution of the LEV. Two related but distinct approaches exist in the literature: a constant-LESP model, in which suction is artificially constrained at its critical value, and a variable-LESP model, which allows suction to decay during vortex growth in accordance with observed shear-layer dynamics.

The original constant A_0 model of Ramesh *et al.* [71,79] assumes that leading-edge separation occurs when

$$LESP(t) > LESP_{crit}, \tag{3.25}$$

and enforces $A_0(t) = LESP_{crit}$ thereafter by shedding a discrete vortex of appropriate strength. This model predicts the timing of separation but assumes that the suction peak remains at the critical value throughout vortex growth.

While this assumption is adequate for predicting the onset of separation, experimental and

numerical studies have shown that leading-edge suction does not remain constant during LEV development; rather, it decays as the separated shear layer rolls up and feeds circulation into the vortex [166–168].

Martínez *et al.* [164] generalise this by relating the rate of circulation fed into the LEV to the shear-layer edge velocity. Starting from the classical vorticity-flux expression

$$\frac{d\Gamma_s}{dt} = \frac{1}{2}\left(V_1^2 - V_2^2\right), \tag{3.26}$$

and assuming that the shear layer is attached at the leading edge, with the LEV assumed to be the dominant flow feature, this simplifies to

$$\dot{\Gamma}_{LE}(t) = \frac{1}{2}u_{LE}^2(t). \tag{3.27}$$

Using Equation 3.23, this shedding rate can be written in terms of A_0. In this variable A_0 model, $A_0(t)$ is allowed to decrease below its initial critical value after separation begins, producing a more realistic reduction in leading-edge suction during LEV growth.

3.5 Assessment of variable LESP for finite wings using CFD

LESP correlates well with leading-edge separation onset for two-dimensional aerofoils in unsteady motion [71, 79, 164]. Its applicability to finite wings, particularly swept wings, is less certain because current LESP formulations are derived from two-dimensional theory and do not explicitly account for spanwise transport. In swept-wing flows, spanwise convection and three-dimensional redistribution of vorticity can alter both the spanwise distribution of leading-edge suction and the local relationship between suction demand and detachment.

Before using LESP as a diagnostic in the later chapters of this thesis, it is therefore necessary to assess whether LESP inferred from CFD remains a meaningful indicator of leading-edge separation on finite swept wings. The purpose of this section is not to validate LESP, but to examine whether spanwise trends in LESP correspond consistently with separation development observed in the CFD for representative finite-wing cases.

The analysis below focuses on the $k = 0.4$ plunge ramp kinematics, for which the rapid, impulsive forcing produces a compact separation onset phase, highlighting differences in spanwise distribution with sweep. LESP is inferred from the CFD shear-layer edge velocity using Equation 3.24.

3.5.1 LESP evolution across the span

Figure 3.4 shows the time histories of LESP inferred from the CFD shear-layer velocity at the root, mid-span, and tip planes for the aspect ratio 3, NACA 0008 wings at $k = 0.4$. At early

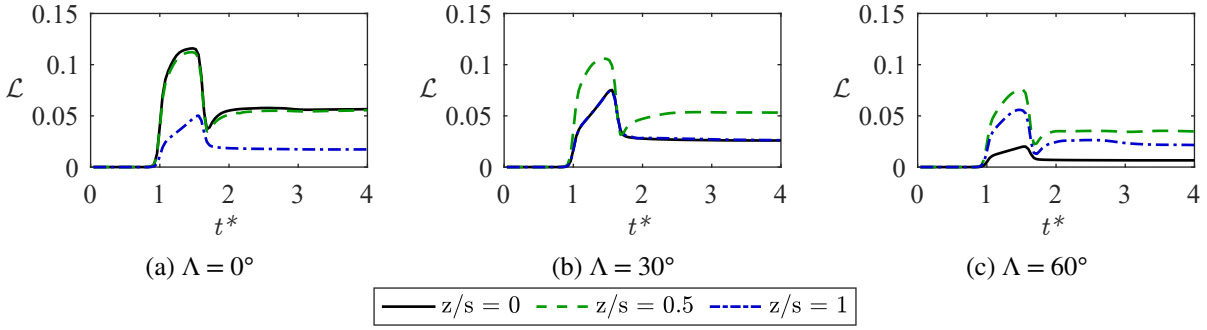

Figure 3.4: Time histories of LESP magnitude for the aspect ratio 3, NACA 0008 wings at reduced frequency $k = 0.4$ along the root, mid-span (as indicated in Figure 2.4) and tip planes of the wing.

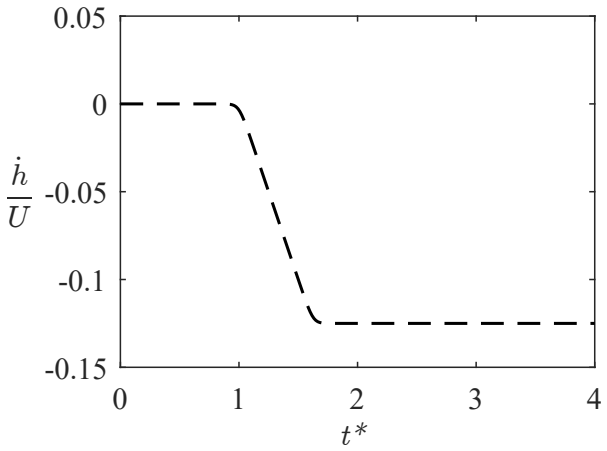

Figure 3.5: The prescribed plunge velocity kinematics at reduced frequency $k = 0.4$, used for the cases shown in Figure 3.4.

times, $t^* < 1$, LESP remains close to zero across the span, consistent with attached flow and weak leading-edge suction.

As the plunge ramp progresses, as shown in Figure 3.5, the spanwise distribution of LESP is strongly dependent on the sweep angle. For the unswept wing, LESP rises to comparable levels at the root and mid-span, with reduced values towards the tip. At $\Lambda = 30°$, a pronounced mid-span maximum develops, while the root and tip remain at lower and more comparable levels. At $\Lambda = 60°$, the mid-span remains the dominant peak, with the root becoming the weakest loaded location. Overall, increasing sweep redistributes leading-edge suction away from the root and concentrates the strongest suction demand towards mid-span.

The maximum LESP value occurs at $t^* = 1.44$ for the $\Lambda = 0°$ and 30° wings, and slightly later at $t^* = 1.48$ for the $\Lambda = 60°$ wing. To provide a quantitative reference for the subsequent comparison between LESP and CFD, first $LESP_{crit}$ is estimated directly from the CFD for a representative swept-wing section using the methodology of Ramesh *et al.* [79].

3.5.2 Calculation of $LESP_{crit}$ from CFD

In two-dimensional flows, $LESP_{crit}$ provides a well-defined threshold for separation onset for a given aerofoil and Reynolds number [79]. For finite wings, however, leading-edge separation onset is not necessarily simultaneous along the span and may not correspond to a single unique LESP value at all spanwise locations.

The calibration is performed for the $\Lambda = 30°$ wing at the mid-span plane, where leading-edge separation signatures are clearest and least affected by root and tip interactions. The tip section is excluded because strong three-dimensional and tip-vortex effects dominate the near-tip flow, and the leading-edge shear layer does not exhibit a section-like roll-up that is directly comparable to the two-dimensional onset concept.

The CFD solution is post-processed to identify the earliest convective time at which a consistent leading-edge separation signature appears in the spanwise vorticity field. Following Ramesh *et al.* [79], this is taken as the first time at which a small region of negative vorticity appears adjacent to the wall within the developing positive vorticity region, indicating incipient shear-layer roll-up. The LESP value computed from the local shear-layer velocity at this instant is then taken as $LESP_{crit}$.

It is emphasised that $LESP_{crit}$ in the present study should be interpreted as a configuration-specific calibration rather than a universal constant. Its value depends on the aerofoil geometry and the three-dimensional flow environment. For finite wings, the presence of spanwise flow and vortex transport alters the local balance between suction and separation, so leading-edge separation does not occur simultaneously along the span and cannot be described by a single two-dimensional critical value. Here, $LESP_{crit}$ is employed as a physics-based indicator to identify the onset of leading-edge separation for the present wings and operating conditions. Modest variations in the selected threshold primarily shift the predicted onset time slightly and do not alter the qualitative spanwise trends or the comparative conclusions drawn with respect to sweep angle and reduced frequency.

Figure 3.6 illustrates the evolution of the flow near the leading edge at the mid-span plane of the $\Lambda = 30°$ swept wing over a sequence of convective times. At $t^* = 1.12$ (Figure 3.6a), the flow remains attached, with a thin layer of spanwise vorticity confined to the surface and no indication of shear-layer detachment. By $t^* = 1.16$ (Figure 3.6b), a thin region of positive vorticity begins to develop close to the surface near the leading edge, indicating the onset of local flow reversal within the boundary layer but without a clearly detached shear layer.

At $t^* = 1.32$ (Figure 3.6c), a distinct region of negative vorticity emerges at the surface within the previously reversed-flow region, signalling the initiation of shear layer roll-up and the eruption of surface flow into the outer stream. This instant is taken as the onset of LEV formation, consistent with the criterion proposed by Ramesh *et al.* [79], and is used here to define $LESP_{crit}$ from the CFD.

By $t^* = 1.36$ (Figure 3.6d), the separated shear layer is fully established and feeding vorticity

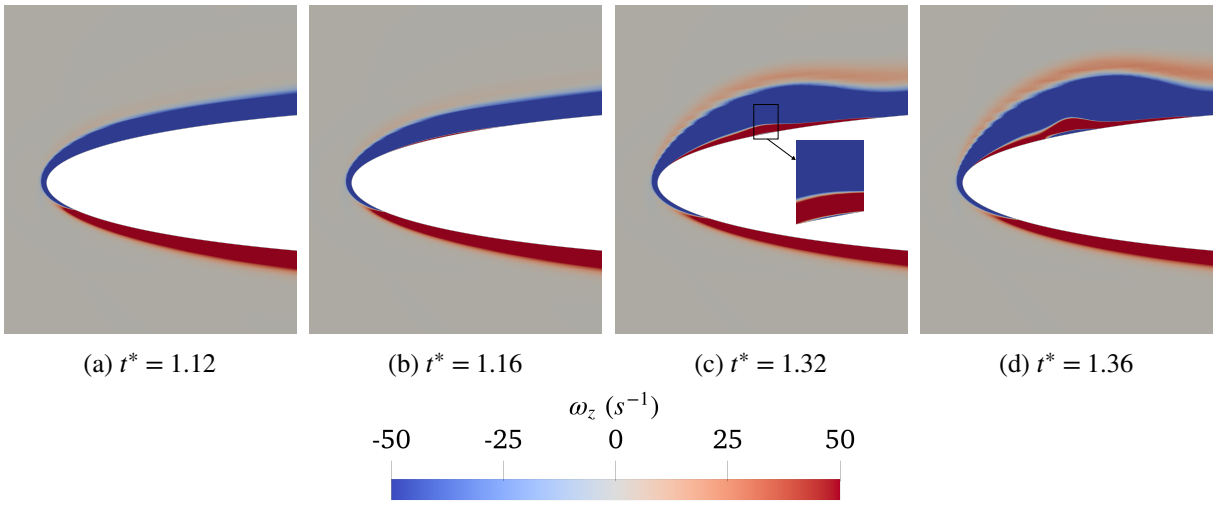

(a) $t^* = 1.12$ (b) $t^* = 1.16$ (c) $t^* = 1.32$ (d) $t^* = 1.36$

Figure 3.6: Mid-span plane spanwise vorticity (ω_z) contours at key convective times for the aspect ratio 3, NACA 0008, $\Lambda = 30°$ swept wing, at reduced frequency $k = 0.4$, focused on the leading edge.

into the developing LEV, indicating that separation is no longer incipient but has entered an early growth phase.

Hence, $LESP_{crit} = 0.10$ from Figure 3.4b. Applying the same methodology to the unswept wing suggests a comparable threshold at mid-span, with the root plane indicating $LESP_{crit} = 0.11$. Given the temporal resolution of the sampled CFD field, $LESP_{crit} = 0.10$ is adopted as a representative reference value for the NACA 0008 geometry in this study.

This procedure provides a reference threshold rather than a tuned value for each spanwise location, sweep angle, or motion. In the subsequent chapters, LESP is therefore used primarily as a diagnostic of relative LEV initiation timing and spanwise distribution, with $LESP_{crit}$ serving as a fixed reference value.

3.5.3 CFD evidence of LEV onset and development

Figures 3.7-3.9 show CFD visualisations at three representative convective times to compare LESP to the observed flow field from CFD flow visualisations: an early attached state ($t^* = 0.6$), a time near peak LESP ($t^* = 1.44$), and a later quasi-steady separated state ($t^* = 3$). Each figure includes Q-criterion isosurfaces and spanwise vorticity slices near the leading edge. While the Q-criterion provides a global view of the vortex system, the spanwise vorticity slices provide a clearer indicator of leading-edge separation onset and spanwise extent.

At $t^* = 0.6$ in Figure 3.7, the flow remains attached for all sweep angles. The vorticity slices show a thin vorticity layer aligned with the surface at the root, mid-span and tip, and no reversed flow or separation is observed. LESP is close to zero across the span, consistent with the attached-flow regime.

At $t^* = 1.44$ in Figure 3.8, separation is present but exhibits clear sweep and span-dependent

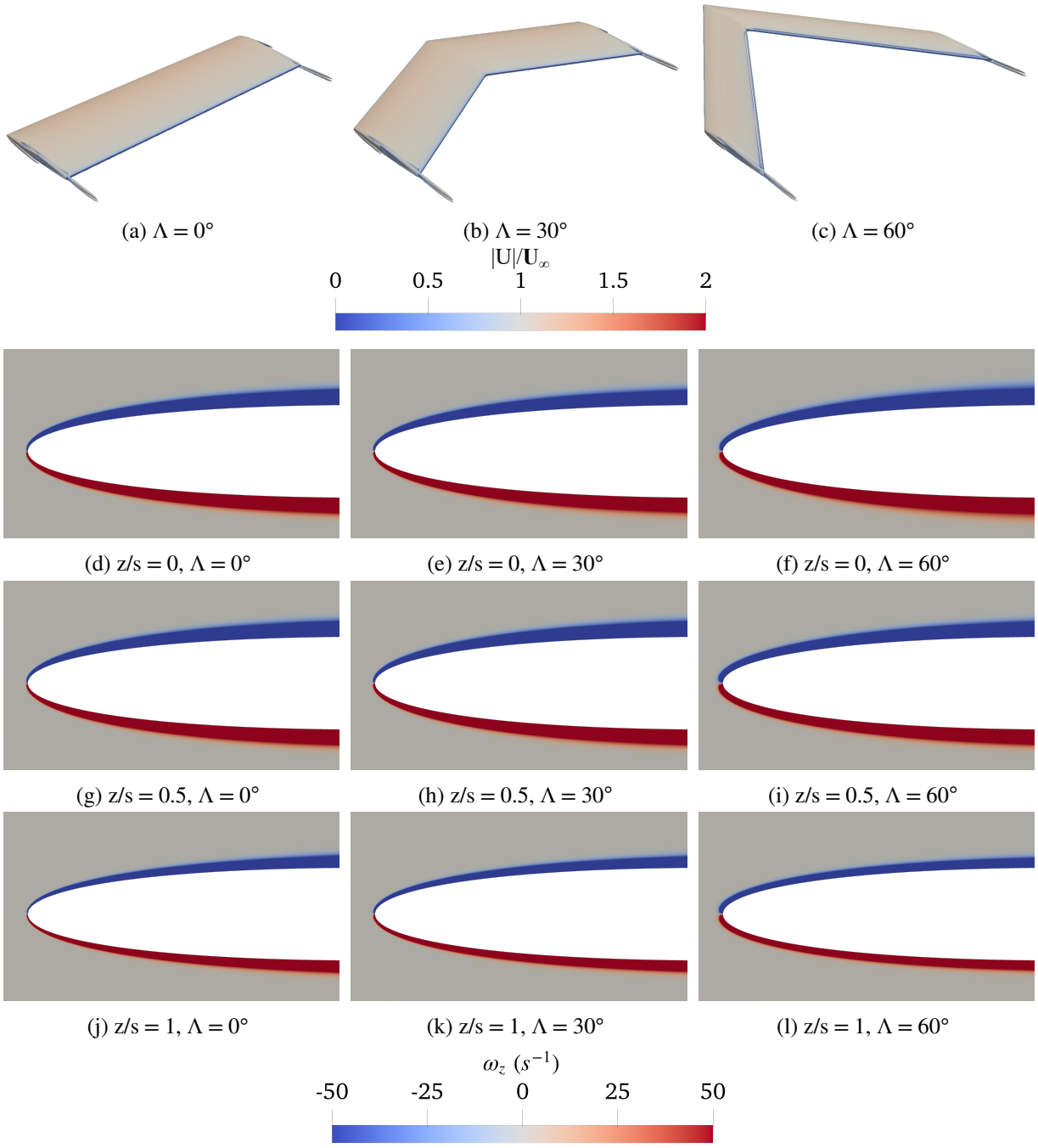

Figure 3.7: *Top:* Isosurfaces of $Q = 1$ coloured by normalised velocity magnitude and *bottom:* spanwise planes corresponding to Figure 3.4, coloured by spanwise vorticity (ω_z), focused on the leading edge. The convective time shown is $t^* = 0.6$.

structure. For the unswept wing, leading-edge separation is well established at the root (Figure 3.8d) and mid-span (Figure 3.8g), with a detached shear layer convecting downstream, while the tip (Figure 3.8j) remains largely attached. The attached tip flow is consistent with the lower LESP values observed in Figure 3.4a.

For the $\Lambda = 30°$ wing, separation extends over a significant portion of the span, but the root plane (Figure 3.8e) remains attached, consistent with outboard convection of vorticity. The

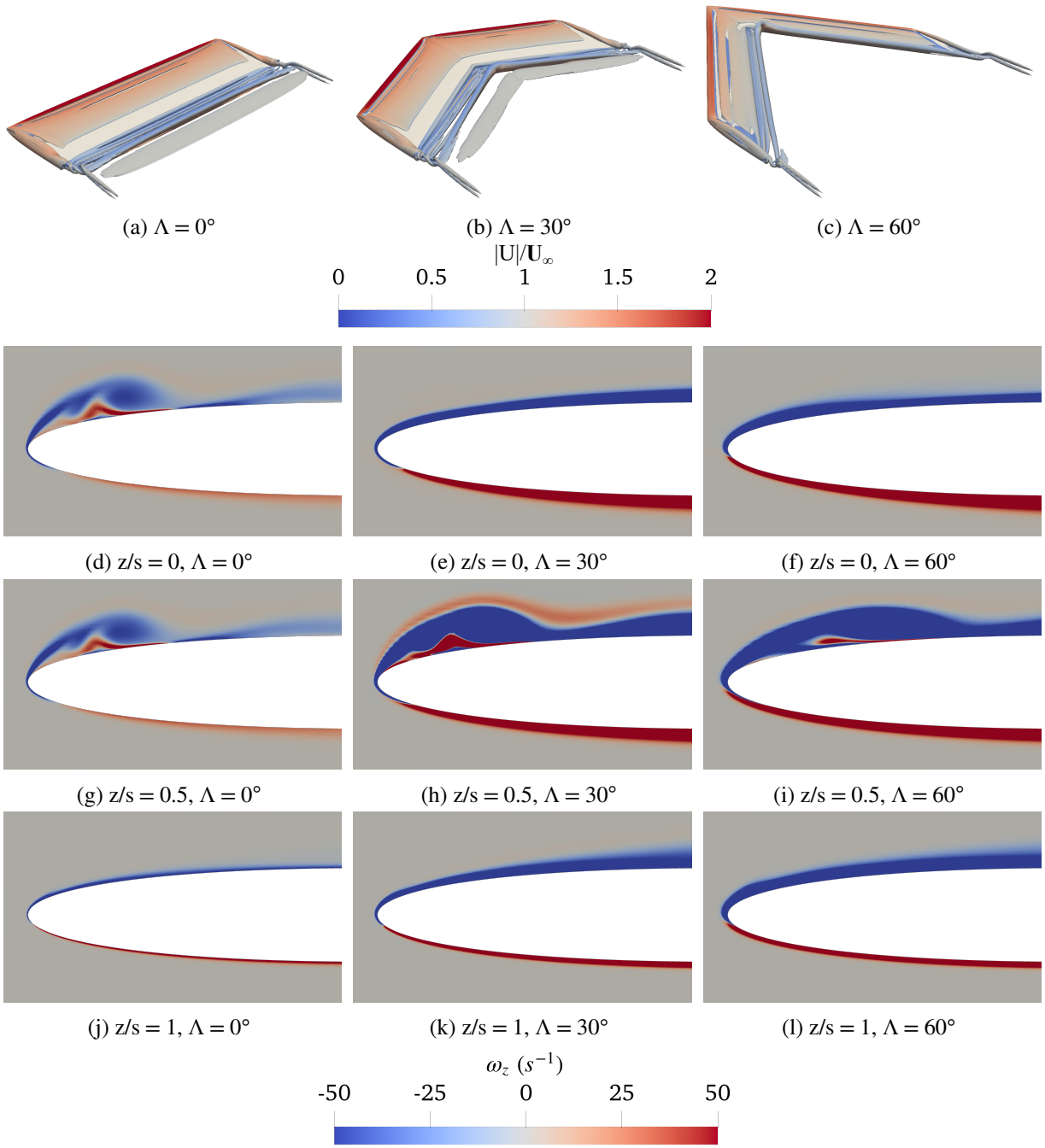

Figure 3.8: *Top:* Isosurfaces of $Q = 1$ coloured by normalised velocity magnitude and *bottom:* spanwise planes corresponding to Figure 3.4, coloured by spanwise vorticity (ω_z), focused on the leading edge. The convective time shown is $t^* = 1.44$.

mid-span plane (Figure 3.8h) exhibits stronger and more persistent detachment compared to the unswept wing, aligned with the mid-span maximum in LESP observed in Figure 3.4b.

At $\Lambda = 60°$, the separation process is more diffuse. The shear layer is detached over much of the span, but strong spanwise transport inhibits the formation of a compact, section-like roll-up. Instead, a broadened region of elevated vorticity is rapidly transported downstream, as shown in Figure 3.8i. The spanwise variation in LESP identified in Figure 3.4c, reducing from the mid-span

to the tip and root, remains qualitatively consistent with the relative strength and persistence of detachment seen in the vorticity slices.

Because the CFD-based onset time used to define $LESP_{crit}$ occurs before $t^* = 1.44$, the time of peak LESP should not be interpreted as the first occurrence of separation. Rather, peak LESP provides a consistent reference instant during the early development of separated flow across all configurations, at which differences in spanwise extent and sweep-induced redistribution are visible.

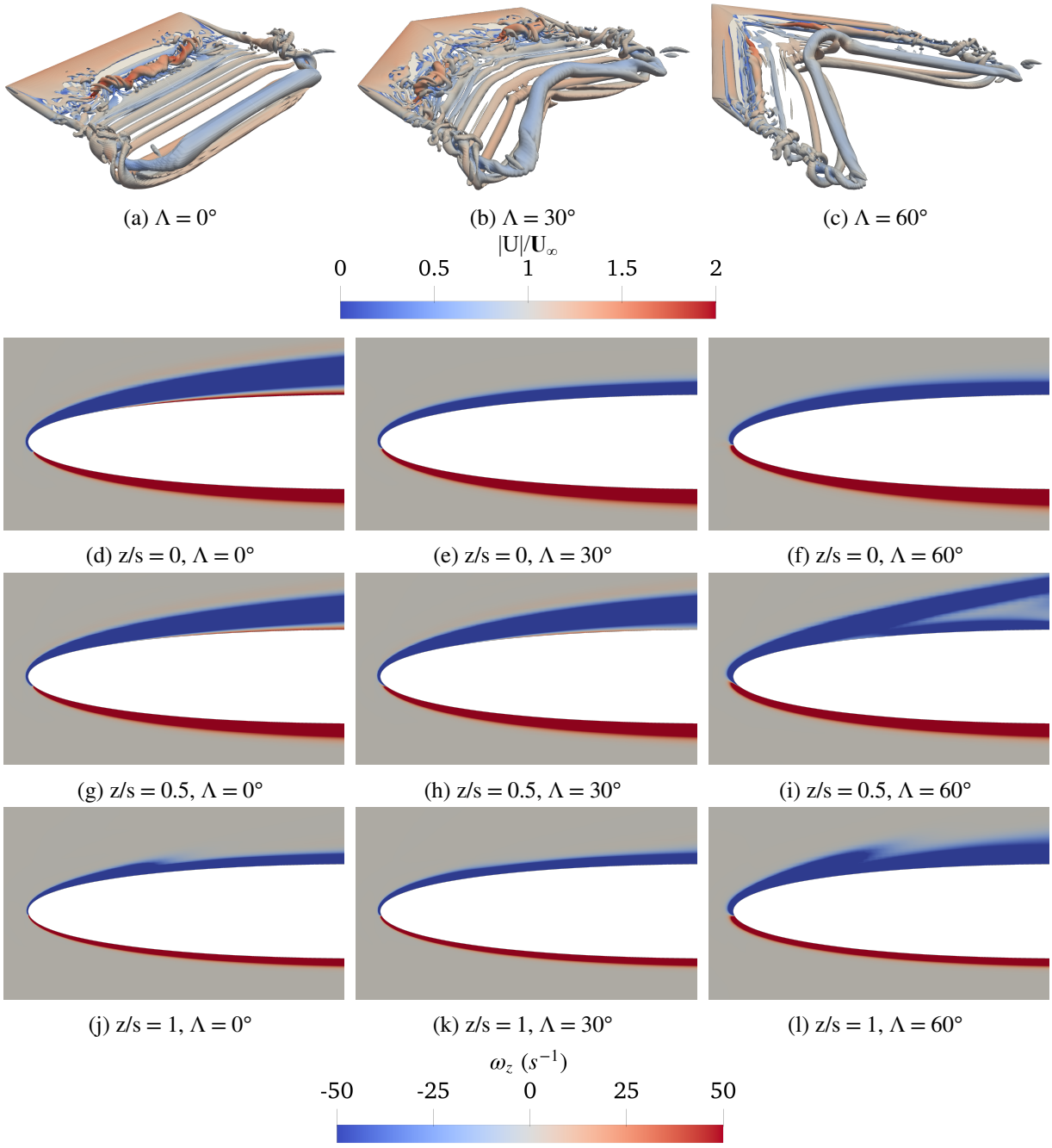

Figure 3.9: *Top:* Isosurfaces of $Q = 1$ coloured by normalised velocity magnitude and *bottom:* spanwise planes corresponding to Figure 3.4, coloured by spanwise vorticity (ω_z), focused on the leading edge. The convective time shown is $t^* = 3$.

By $t^* = 3$ in Figure 3.9, the leading-edge flow has reached a quasi-steady separated state. The Q-criterion visualisations show the downstream-convected vortex system, while the vorticity slices indicate either sustained separation or partial reattachment close to the leading edge, depending on sweep angle and spanwise location. The relative degree of detachment aligns qualitatively with the spanwise LESP distribution. For example, over the 60° swept wing, the leading-edge shear layer becomes more detached between the root (Figure 3.9f), tip (Figure 3.9l) and mid-span (Figure 3.9i) planes respectively. This agrees with the LESP distribution observed in Figure 3.4c.

3.5.4 Consistency between LESP and CFD

Taken together, the quantitative LESP time histories and qualitative CFD flow visualisations show consistent spanwise and sweep angle trends. LESP remains close to zero during attached flow, matching the absence of separation in the CFD. As the motion progresses, locations with higher LESP correspond to stronger and more persistent leading-edge detachment in the vorticity slices, even though the detailed LEV structure changes with sweep and spanwise transport.

The CFD-based calibration of $LESP_{crit}$ indicates that separation onset occurs slightly before the time of maximum LESP, due to the inherent three-dimensional nature of finite wings and spanwise vorticity transport. Nevertheless, the spanwise distribution and relative magnitude of LESP remain closely aligned with the extent of separation observed in the CFD throughout the onset and early development phases.

These results indicate that LESP, when inferred from CFD shear-layer velocity, provides a meaningful diagnostic of leading-edge separation on finite swept wings. While LESP does not identify a unique, instantaneous onset time along the entire span, because it is based on 2D theory, it captures the spanwise trends and relative strength of separation required for the analysis in this thesis.

3.5.5 Limitations

While the LESP-based diagnostic proves useful for interpreting the CFD results, several limitations should be acknowledged:

- **Inviscid origin:** LESP is defined within an inviscid potential-flow framework and does not explicitly model viscous boundary-layer development, transition, or separation-bubble dynamics. Even when evaluated using velocities extracted from viscous CFD, separation is therefore inferred indirectly through an inviscid suction parameter rather than predicted from a viscous separation model.

- **No prediction of LEV geometry or strength:** LESP identifies the onset of separation but does not provide information about the size, trajectory, circulation, or breakdown of the resulting vortex.

- **Spanwise-uniform critical threshold:** A single value of $LESP_{crit}$ is applied across the span for simplicity. In reality, the critical threshold may vary with spanwise location and sweep angle.

- **Qualitative assessment:** The comparison presented here is qualitative in nature. Although LESP shows strong consistency with CFD, no experimental data is used, and the results should not be interpreted as a formal validation.

Despite these limitations, LESP provides a computationally inexpensive and physically interpretable diagnostic that aligns closely with high-fidelity CFD evidence and offers a useful tool for analysing the onset of leading-edge separation on finite swept wings.

3.6 Summary of the low-order modelling framework

This chapter has introduced the low-order modelling tools used in this thesis to support the interpretation of high-fidelity CFD simulations of unsteady swept-wing aerodynamics. Two modelling frameworks were presented, each serving a distinct and clearly defined role:

1. Corrected large-amplitude unsteady lifting-line theory (C-LAULLT): An inviscid lifting-line formulation for finite wings undergoing unsteady motion. C-LAULLT extends the baseline LAULLT framework by incorporating a first-order sweep-angle correction derived from asymptotic theory, while retaining the original unsteady lifting-line formulation for spanwise aerodynamic coupling. The method provides time-resolved predictions of bound circulation and unsteady lift.

2. Variable leading-edge suction parameter (LESP) Theory: An inviscid, physics-based criterion for identifying the onset of leading-edge separation. LESP is evaluated here using the shear layer velocity formulation applied to CFD data, enabling a spanwise and time-resolved assessment of when the leading-edge suction demand exceeds the critical value, $LESP_{crit}$.

Importantly, these two frameworks are *not* coupled within a single predictive model in this thesis. C-LAULLT is used to analyse unsteady lift, while LESP is employed independently as a diagnostic tool to interpret the onset and progression of leading-edge separation observed in the CFD simulations.

Their complementary roles may be summarised as follows:

- C-LAULLT provides a low-order, inviscid description of the unsteady circulation response of finite swept wings, allowing interpretation of the mechanisms underlying the lift response.

- LESP provides a physically interpretable indicator of leading-edge flow separation, enabling qualitative assessment of LEV initiation timing and spanwise development directly from CFD-resolved shear-layer velocities.

Together, these tools form an interpretive framework rather than a unified solver. C-LAULLT establishes the attached-flow baseline against which deviations associated with separation can be identified, while LESP provides a compact measure of the local suction demand that signals initiation of LEV formation.

Chapter 4 applies C-LAULLT as an attached-flow reference to characterise LEV breakdown behaviour in the simulated flows. By comparing low-order predictions with high-fidelity CFD results, the observed flow evolution is interpreted in terms of established burst-type and spiral-type breakdown modes across reduced-frequency regimes. Chapters 5 and 6 then make use of both LOMs in a complementary manner. Chapter 5 examines reduced-frequency effects, using LESP diagnostics alongside CFD flow-field visualisation to interpret how changes in kinematics reorganise LEV initiation and development. Chapter 6 then focuses on sweep-angle effects, applying the same diagnostics to synthesise trends across sweep and aspect ratio and to link these changes to the resulting aerodynamic force response.

The low-order modelling tools introduced in this chapter therefore provide a conceptual bridge between inviscid aerodynamic theory and high-fidelity numerical simulation. Rather than replacing CFD, they offer physically grounded insight into the mechanisms governing unsteady lift generation and LEV formation on finite swept wings.

4

LEV Breakdown Modes – Bursting-type vs Spiral-type

> *Once you have tasted flight, you will forever walk the earth with your eyes turned skyward.*
>
> **— Leonardo da Vinci**
> (Polymath)

4.1 Introduction

VORTEX breakdown is a fundamental phenomenon in separated, vortex-dominated flows and has been widely studied in aircraft aerodynamics, rotorcraft, and delta-wing configurations. Classical literature distinguishes two primary breakdown modes: burst-type breakdown (also referred to as bubble-type) and spiral-type breakdown. Early foundational studies, such as those by Leibovich [44] and Delery [45], established the physical criteria for vortex breakdown. These include the swirl ratio, which characterises the relative strength of azimuthal and axial flow within the vortex core, the presence of an axial velocity deficit corresponding to reduced flow velocity along the vortex axis, and the transition between axisymmetric burst-type and helical spiral-type modes. Subsequent experimental and theoretical work demonstrated that breakdown behaviour is sensitive to swirl strength, pressure gradients, and three-dimensional disturbances.

In low-Reynolds-number aerodynamics, investigations by Gursul *et al.* [169], Ol and Gursul [69], and others showed that leading-edge vortices (LEVs) on finite wings can undergo breakdown in a manner that parallels classical delta-wing behaviour, but with additional modulation from tip effects and unsteady kinematics. In insect-scale and MAV flows, LEV stability and breakdown are directly linked to aerodynamic performance. Studies by Birch and Dickinson [170], Ellington *et*

al. [1], and Lentink and Dickinson [158] demonstrated that a stable LEV can sustain elevated lift, whereas breakdown is associated with a rapid degradation of lift and the onset of stall. More recent work by Jardin [171] has emphasised how breakdown modes vary with kinematics, geometry, and aspect ratio in flapping and plunging wings.

In the context of bio-inspired and low-Reynolds-number wings, vortex breakdown governs how long an LEV remains coherent, how abruptly vortex-induced lift is lost, and has important implications for the magnitude and distribution of vortex-induced lift. This chapter examines how burst-type and spiral-type breakdown manifest in finite-wing plunging simulations, and how these modes depend on reduced frequency, sweep angle, and aspect ratio. Rather than cataloguing all available flow visualisations, the analysis is structured to link the aerodynamic signature of breakdown observed in the lift histories, the extent to which the corrected large-amplitude unsteady lifting line theory (C-LAULLT) modelling approach can diagnose or represent these behaviours, and the underlying three-dimensional vortex dynamics responsible for breakdown.

While prior studies of delta wings, revolving wings, and flapping foils have noted the sensitivity of vortex breakdown to geometry and kinematics, a systematic distinction between bursting-type and spiral-type breakdown modes in oscillatory low-Reynolds-number finite wing flows has not been thoroughly documented. Figures 4.2 and 4.4 qualitatively illustrate bursting and spiral breakdown modes observed in the present simulations, respectively. Additional Q-criterion visualisations for selected baseline NACA 0008 cases are provided in Appendix B to support the discussion of the three-dimensional LEV structure. The sections that follow identify the conditions under which a classic bursting-type LEV breakdown occurs in Section 4.2 versus those that yield a spiral-type breakdown in Section 4.3, drawing on IDDES flow visualisation and the associated transient lift behaviour to establish a coherent physical interpretation.

4.2 Burst-type LEV breakdown (low reduced frequency)

4.2.1 Aerodynamic signature

The defining feature of burst-type LEV breakdown is an abrupt loss of lift following a period of steady growth. This behaviour is most clearly observed at the lowest reduced frequency examined, $k = 0.05$. Figure 4.1 compares the lift histories obtained from CFD with predictions from C-LAULLT for the NACA 0008 geometries at $k = 0.05$.

Here, time is expressed using the convective time scale $t^* = tU_\infty/c$, which is retained throughout the results to facilitate physical interpretation of LEV evolution, and is standard practice in the study of vortex-dominated low-speed aerodynamic flows.

Across unswept and 30° swept wings at aspect ratio 3 in Figure 4.1b, the lift increases approximately linearly over most of the downstroke before undergoing a sharp reduction over a narrow convective time interval near the end of the stroke. A similar behaviour is observed at aspect

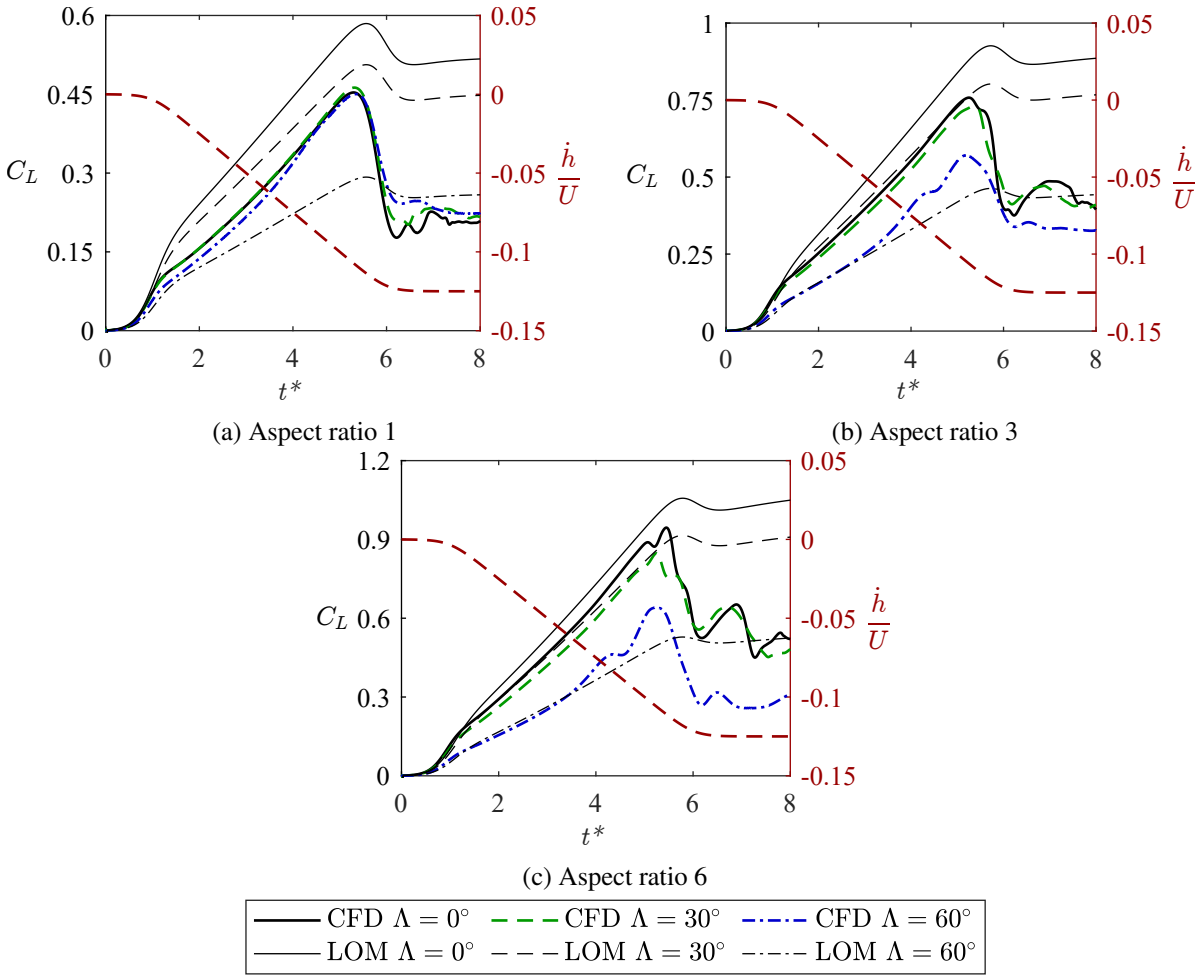

Figure 4.1: Lift coefficient time histories for the NACA 0008 wing geometries at reduced frequency $k = 0.05$, with CFD results compared against predictions from the C-LAULLT low-order model. The prescribed plunge velocity kinematics are shown on the right axis.

ratio 6 in Figure 4.1c, although the onset of the lift collapse is slightly delayed, indicating a more persistent lift-producing mechanism prior to breakdown. This abrupt late-stroke decline is not captured by C-LAULLT, which predicts only a modest reduction in lift associated with kinematic deceleration. The discrepancy indicates that the force loss is not due to a gradual reduction in bound circulation, but instead reflects the sudden loss of a significant suction-generating flow structure.

The magnitude of the lift discrepancy between CFD and C-LAULLT increases with aspect ratio, suggesting that the breakdown mechanism becomes increasingly three-dimensional and is therefore poorly represented by lifting-line assumptions. At both aspect ratios and sweep angles, the force reduction occurs over a much shorter timescale than the preceding lift growth, evidencing a sudden loss of an organised lift-producing mechanism, rather than a gradual decay.

At aspect ratio 6 in Figure 4.1c, the influence of sweep becomes more pronounced. Whereas, at aspect ratio 1 in Figure 4.1a, strong tip effects limit the development of a coherent lift-producing structure, and sweep angle effects are correspondingly reduced. While unswept and moderately

swept wings at aspect ratio 6 exhibit a sharp and well-defined lift peak followed by collapse, the highly swept configuration experiences a reduced peak lift. This difference in lift history suggests that sweep alters the coherence and persistence of the significant lift-generating flow structure, thereby limiting the maximum lift attained.

The physical origin of the abrupt loss of force observed at higher aspect ratios cannot be inferred from the lift histories alone and is therefore examined in the following section through three-dimensional flow visualisation. Following the primary force collapse near $t^* = 6$, the lift response exhibits increased unsteadiness, with more pronounced oscillations at higher aspect ratio. These post-burst fluctuations indicate the presence of secondary vortical structures or intermittent reattachment events, which are not represented in the low-order model (LOM) and motivate further examination of the underlying three-dimensional flow physics in subsequent sections.

4.2.2 Flow-physics origin of bursting

The flow-field mechanism responsible for the abrupt force loss is revealed through three-dimensional vortex visualisation. Figure 4.2 shows Q-criterion isosurfaces for representative unswept and 30° swept wings at $k = 0.05$. The convective times shown are selected to capture the fully developed post-collapse vortex structure and its subsequent evolution. All Q-criterion flow visualisations herein are geometrically symmetric about the wing centreline, and only half of each wing was simulated. The flow visualisations shown therefore represent mirrored reconstructions of the half-wing solutions, rather than independently simulated vortical structures on either side of the centreline. This approach preserves the symmetry of the flow while reducing computational cost and is applied consistently across the unswept, moderately swept, and highly swept cases.

By $t^* = 6$ the lift collapse is already largely complete, and the corresponding flow field therefore reflects the aftermath of the bursting event rather than its initiation. These later times are of primary interest, as they reveal the loss of LEV coherence and the resulting three-dimensional vortex topology that governs the post-collapse aerodynamic response.

In these low reduced frequency cases, the lift histories are consistent with early LEV formation during the downstroke, followed by progressive development of the vortex over much of the stroke before breakdown. At low reduced frequency, the smooth lift growth before collapse suggests limited spanwise convection, particularly for unswept, higher-aspect-ratio wings, allowing the vortex to remain attached over a large fraction of the span. As the stroke progresses, the increasing lift magnitude implies continued vortex growth, consistent with a thickening LEV that becomes increasingly susceptible to three-dimensional disturbances.

In the absence of strong spanwise transport, vorticity shed from the leading edge accumulates locally within the LEV core rather than being redistributed along the span. This promotes continued growth of the vortex and an increasing axial velocity deficit within the core, conditions known to favour bubble-type breakdown in canonical vortex systems. Once a critical state is reached, the vortex can no longer sustain the required pressure gradient, leading to rapid core

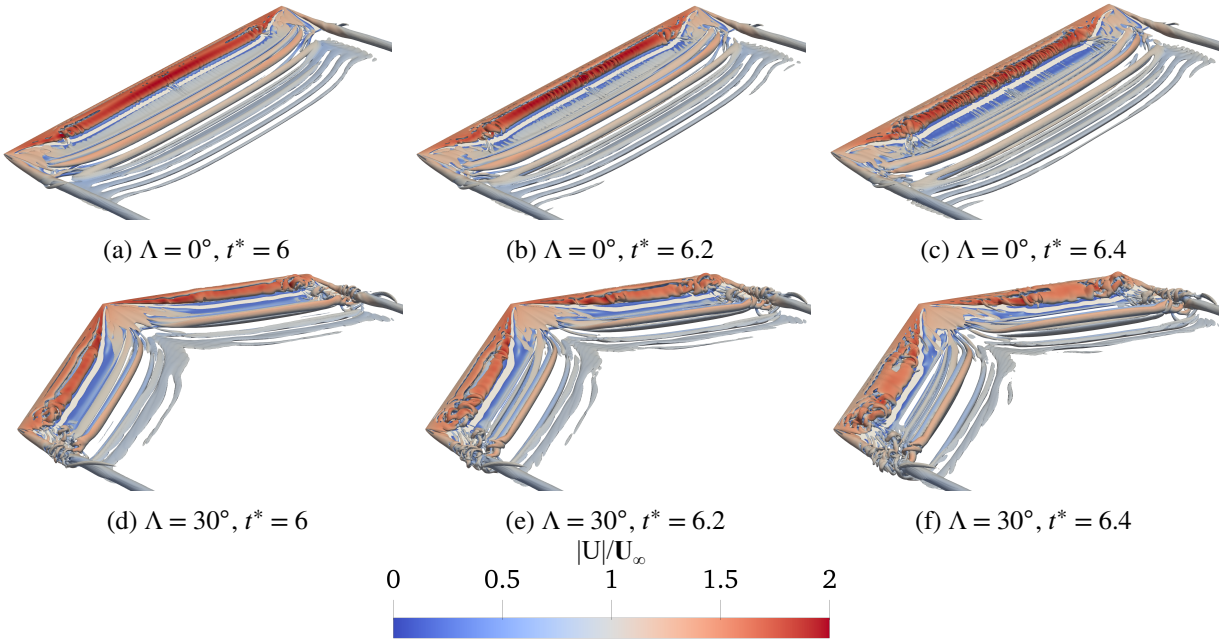

Figure 4.2: Isosurfaces of $Q = 1$ coloured by normalised velocity magnitude for the aspect ratio 6, NACA 0008, $\Lambda = 0°$ and 30° wing geometries at reduced frequency $k = 0.05$ at representative convective times where a coherent LEV exists over the wing.

expansion and loss of coherence. The post-collapse structures observed in Figures 4.2a-4.2c are consistent with this classical bursting scenario, in which breakdown occurs through sudden volumetric expansion rather than helical deformation.

Late in the downstroke, the LEV undergoes a sudden bubble-type collapse. The vortex core expands rapidly, coherence is lost, and suction on the upper surface drops abruptly. This bursting event coincides directly with the sharp reduction in lift observed in the CFD time histories. The inability of C-LAULLT to reproduce this behaviour reflects its assumption of bound circulation and its lack of any mechanism for large-scale vortex instability or detachment.

A similar bursting mechanism is observed for the 30° swept wing at low reduced frequency in Figures 4.2d-4.2f. The timing of the lift collapse is comparable to that of the unswept case, but the breakdown exhibits increased spanwise asymmetry. Moderate sweep introduces limited spanwise transport along the leading edge. However, this remains insufficient to suppress the formation of an attached inboard shear layer. Vorticity shed from this region is convected outboard into the primary LEV core, allowing the vortex to grow quasi-steadily prior to breakdown. Due to the low reduced frequency, the subsequent collapse retains the defining characteristics of burst-type behaviour rather than exhibiting spiral deformation.

Taken together, the lift histories and three-dimensional flow visualisations demonstrate that burst-type breakdown arises under quasi-steady kinematics in which leading-edge vorticity accumulates progressively until a stability limit is exceeded. The resulting breakdown is manifested as a sudden loss of vortex coherence and an abrupt global reduction in vortex-induced lift, distin-

guishing this regime from breakdown modes driven by impulsive kinematics or strong spanwise transport.

4.3 Spiral-type LEV breakdown (higher reduced frequency)

4.3.1 Aerodynamic signature

At higher reduced frequencies ($k = 0.2$ - 0.4), the aerodynamic response differs fundamentally from the burst-type regime. Figure 4.3 shows the corresponding lift histories for the NACA 0008 wings.

In Figure 4.3, the lift exhibits an initial impulsive peak at the onset of the ramp motion, coincident with rapid wing acceleration. This is followed by approximately linear lift growth for the remainder of the ramp, similar to the low reduced frequency cases. A second impulsive peak occurs at the end of the ramp motion; however, the lift does not subsequently recover, instead settling at a lower value. During the steady-state portion of the motion, the lift response exhibits oscillatory or plateaued behaviour.

C-LAULLT consistently over-predicts lift, most notably during the steady-state plunge motion. At aspect ratios 1 and 3, this over-prediction is also evident during the ramp phase, most notably for the unswept wing, where the model continues to assume an attached circulation distribution. For aspect ratio 6, the qualitative lift response is similar, but the over-prediction by C-LAULLT is reduced because the higher aspect ratio more closely satisfies the assumptions underlying lifting-line theory.

Although the lift response exhibits pronounced impulsive peaks, the subsequent loss of lift occurs rapidly rather than through a gradual decay. Within this higher reduced frequency range, the main difference between $k = 0.2$ and $k = 0.4$ is the magnitude of the impulsive lift peak. Both exhibit post-impulsive lift reduction with increased temporal variability, but the oscillations are slightly more pronounced at $k = 0.2$. The resulting force histories therefore differ qualitatively from burst-type breakdown, which is characterised by a single abrupt collapse following sustained lift growth. Instead, these spiral-type cases show post-impulsive lift reduction accompanied by variable lift response, rather than a single abrupt collapse.

4.3.2 Flow-physics origin of spiral breakdown

The flow-field origin of the aerodynamic behaviour described in Section 4.3.1 is revealed through three-dimensional vortex visualisation at high reduced frequency. Figures 4.4 and 4.5 show representative Q-criterion isosurfaces for the NACA 0008 wings at $k = 0.4$, illustrating the development of spiral-type LEV breakdown on unswept and moderately swept wings.

For the unswept wing at $k = 0.4$ at both aspect ratio 3 in Figure 4.4 and aspect ratio 6 in Figure 4.5, the LEV forms rapidly during the early phase of the downstroke as a result of the

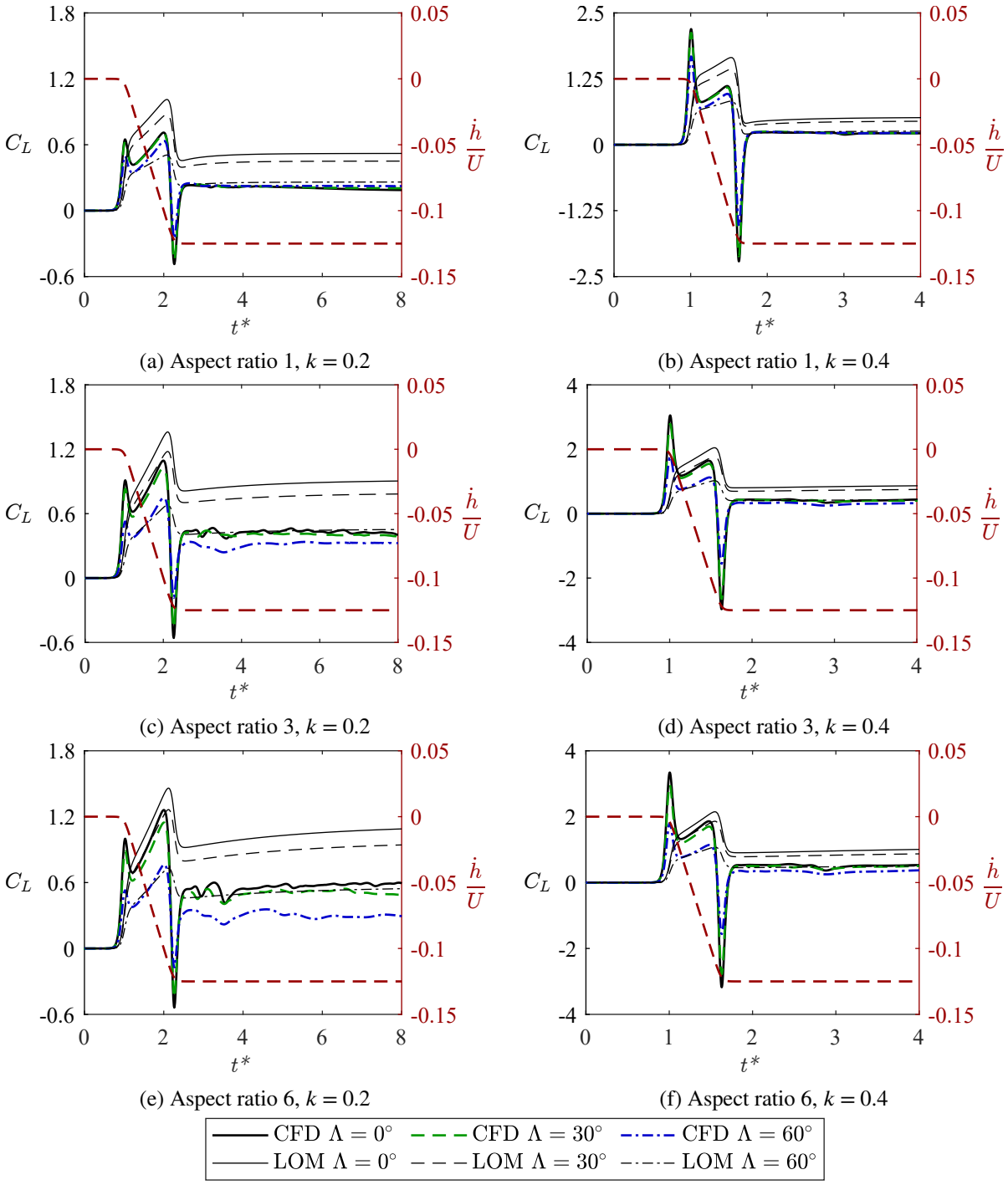

(a) Aspect ratio 1, $k = 0.2$

(b) Aspect ratio 1, $k = 0.4$

(c) Aspect ratio 3, $k = 0.2$

(d) Aspect ratio 3, $k = 0.4$

(e) Aspect ratio 6, $k = 0.2$

(f) Aspect ratio 6, $k = 0.4$

Figure 4.3: Lift coefficient time histories for the NACA 0008 wing geometries at reduced frequencies $k = 0.2$ and $k = 0.4$, with CFD results compared against predictions from the C-LAULLT low-order model. The prescribed plunge velocity kinematics are shown on the right axis.

impulsive acceleration of the wing. However, unlike the $k = 0.05$ cases discussed in Section 4.2, the vortex does not remain stably attached at the wing-tip. Instead, strong three-dimensional effects emerge shortly after formation. The outboard portion of the LEV becomes unstable first, developing helical distortions that propagate inboard along the vortex core. These spiral deformations promote progressive detachment and downstream convection of the LEV.

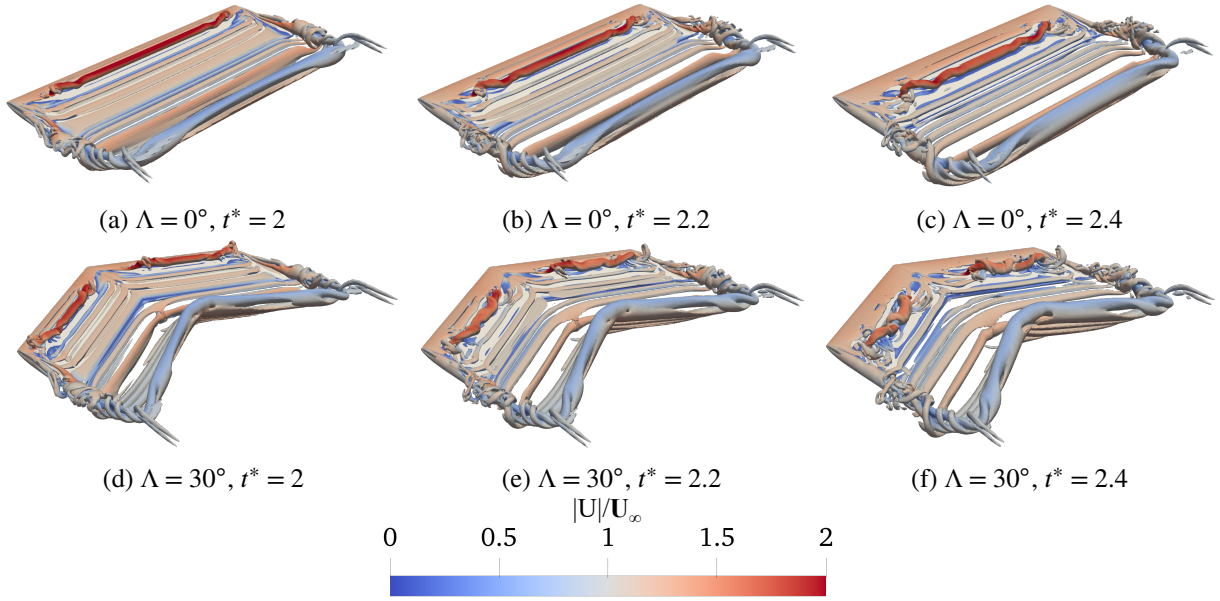

Figure 4.4: Isosurfaces of $Q = 1$ coloured by normalised velocity magnitude for the aspect ratio 3, NACA 0008, $\Lambda = 0°$ and 30° wing geometries at reduced frequency $k = 0.4$ at representative convective times where a coherent LEV exists over the wing.

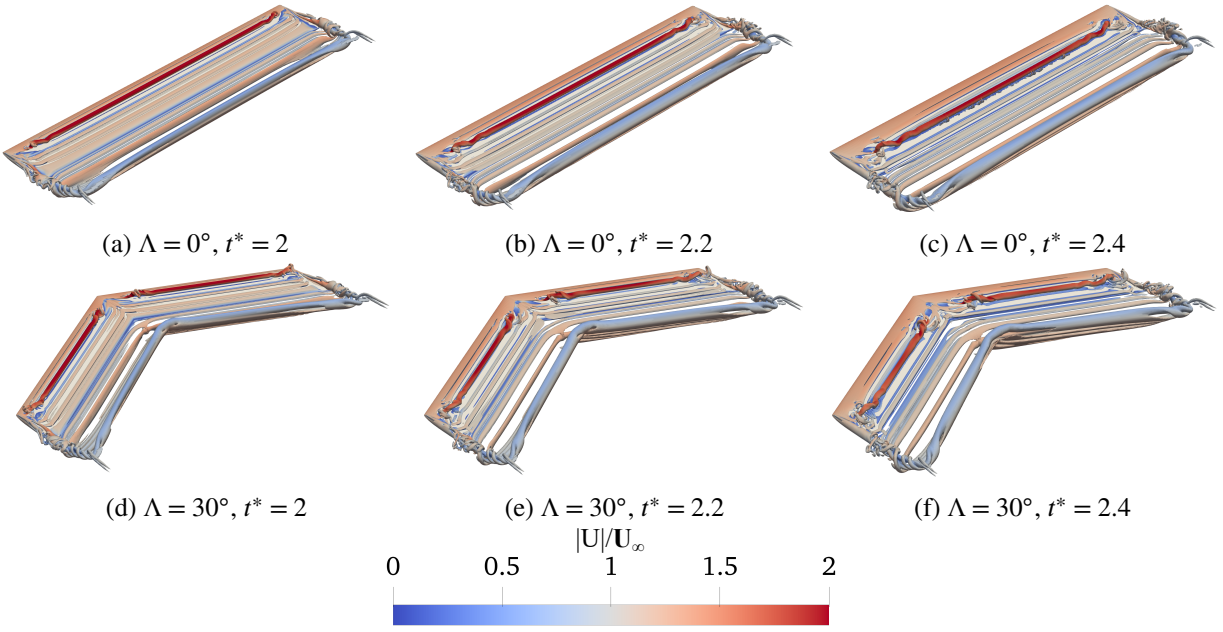

Figure 4.5: Isosurfaces of $Q = 1$ coloured by normalised velocity magnitude for the aspect ratio 6, NACA 0008, $\Lambda = 0°$ and 30° wing geometries at reduced frequency $k = 0.4$ at representative convective times where a coherent LEV exists over the wing.

A similar mechanism is observed for the 30° swept wing. At the same convective times as the unswept wing, the introduction of spanwise flow due to sweep leads to more pronounced three-dimensional deformation of the LEV at aspect ratio 3 in Figure 4.4, with spiral instabilities developing near the root and tip. The resulting breakdown proceeds through progressive three-

dimensional deformation and shedding of the LEV along the span, leading to a spatially distributed loss of coherence rather than a single abrupt collapse. This behaviour is consistent with the lift histories in Figure 4.3d, in which lift is reduced shortly after the impulsive peak at the end of the plunge ramp and subsequently exhibits plateaued behaviour during steady-state plunge. At aspect ratio 6 in Figure 4.5, the 30° swept wing exhibits a more stable central vortex core due to the longer span.

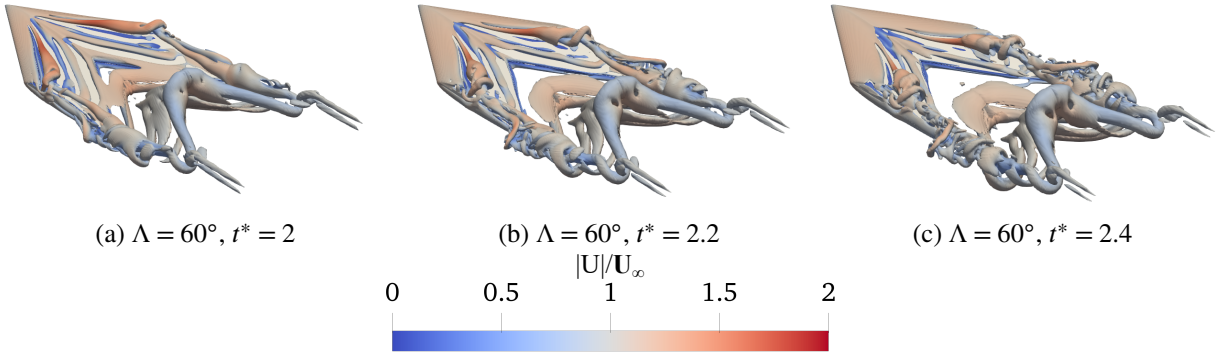

(a) $\Lambda = 60°$, $t^* = 2$ (b) $\Lambda = 60°$, $t^* = 2.2$ (c) $\Lambda = 60°$, $t^* = 2.4$

Figure 4.6: Isosurfaces of $Q = 1$ coloured by normalised velocity magnitude for the aspect ratio 1, NACA 0008, $\Lambda = 60°$ wing geometries at reduced frequency $k = 0.4$ at representative convective times where a coherent LEV exists over the wing.

The behaviour of the 60° swept wing is qualitatively distinct. Figure 4.6 shows Q-criterion isosurfaces for the aspect ratio 1 wing at $k = 0.4$, which provides a clear illustration of this regime. Strong spanwise flow rapidly convects vorticity away from the root, preventing the formation of a large, coherent LEV over the mid-span. Instead, the LEV and tip vortex merge into a single elongated structure that undergoes continuous three-dimensional deformation and downstream shedding. As a result, classical spiral breakdown of a well-defined LEV core is not observed. Instead, the vortex system remains weak, highly unsteady, and strongly coupled to tip dynamics throughout the motion.

Across all high reduced frequency cases, C-LAULLT fails to capture the observed lift response because it assumes circulation remains bound to the wing and does not account for the development or evolution of strongly three-dimensional flow structures. As a result, the model continues to predict elevated lift following the second impulsive peak, whereas the CFD results exhibit a reduction in lift accompanied by increased temporal variability. These discrepancies indicate the influence of unsteady vortical dynamics and downstream convection, which are not represented in the LOM framework.

Taken together, these flow visualisations demonstrate that spiral-type breakdown arises from instabilities of the inboard leading-edge shear layer, which deform and shed vorticity into the LEV and progressively disrupt its coherence along the span. Unlike burst-type breakdown, which results from quasi-steady growth and sudden collapse of a coherent vortex, spiral-type breakdown reflects an inherently three-dimensional, unsteady process driven by rapid kinematics and enhanced spanwise transport.

4.4 Chapter summary

This chapter has identified and characterised two fundamentally distinct LEV breakdown modes on finite plunging wings: burst-type and spiral-type breakdown. These modes are distinguished by reduced frequency and are influenced by wing geometry and three-dimensional flow dynamics. Burst-type and spiral-type breakdown are associated with distinct aerodynamic force responses.

At low reduced frequency, wings with sufficient aspect ratio exhibit force histories characterised by smooth lift growth over much of the downstroke, followed by a sharp late-stroke collapse. Flow visualisation indicates the presence of a coherent inboard LEV over much of the motion, which undergoes a sudden loss of coherence near the end of the downstroke. This behaviour is commonly described as burst-type breakdown and is associated with an abrupt reduction in lift. Low-order models such as C-LAULLT capture the general lift growth driven by the imposed kinematics but fail to reproduce the abrupt force loss, reflecting their inability to represent large-scale three-dimensional flow structures and vortex instability.

At a higher reduced frequency, the aerodynamic response differs qualitatively. The lift histories are characterised by pronounced impulsive peaks at the start and end of the ramp motion, followed by a reduction in lift and increased temporal variability during the steady-state plunge. The corresponding flow fields exhibit strong three-dimensional deformation of the dominant vortical structures, with the breakdown process evolving in a spiral-type manner, characterised by progressive deformation and downstream convection of the LEV. Unlike in burst-type cases, the force response does not collapse abruptly but instead exhibits a post-impulsive reduction, with oscillatory or plateaued behaviour. In this regime, C-LAULLT consistently over-predicts lift following the ramp motion, as the model assumes circulation remains bound to the wing and cannot represent the inherently three-dimensional flow dynamics observed in the simulations.

While these flow regimes are consistently associated with distinct lift histories, the explicit contribution of the LEV to the aerodynamic loading cannot be inferred from the force histories alone. This limitation motivates the force partitioning methodology employed in Chapter 7, which is used to separate vorticity-induced force contributions from other components of the aerodynamic loading and to more rigorously assess the role of unsteady vortical structures.

Taken together, the results demonstrate that the LEV breakdown mode is controlled primarily by reduced frequency, with sweep angle and aspect ratio modulating how each regime manifests by controlling spanwise transport and tip influence. By explicitly linking aerodynamic force histories and three-dimensional flow visualisation, this chapter establishes a coherent physical framework for interpreting LEV breakdown modes on finite wings. This framework underpins the analyses presented in Chapter 5, where reduced-frequency effects are examined in greater detail, with particular emphasis on LEV formation and attachment. Subsequently, the resulting distribution of lift along the span is analysed in Chapter 7.

5

Reduced Frequency Effects on LEV Development

> *Surely no child, and few adults, have ever watched a bird in flight without envy.*
>
> **— Isaac Asimov**
> (Writer and Professor)

5.1 Introduction

THE reduced frequency, k, is a fundamental non-dimensional parameter governing unsteady aerodynamic behaviour, comparing the oscillation rate of the wing to the characteristic time for the free-stream flow to convect over the chord. Low reduced frequencies correspond to slow, quasi-steady motions, whereas high reduced frequencies represent rapid, impulsive motions for which unsteady and inertial effects dominate. In plunging and flapping wings, variations in reduced frequency directly influence the timing of leading-edge vortex (LEV) initiation, its residence time on the wing, its breakdown mechanism, and the resulting aerodynamic force response.

This chapter examines reduced-frequency effects using four representative values, chosen to span quasi-steady to strongly unsteady flow regimes commonly reported in the unsteady aerodynamics literature:

- $k = 0.05$, corresponding to quasi-steady behaviour,
- $k = 0.1$, representing moderately unsteady conditions,
- $k = 0.2$, a transitional regime where unsteady effects become dominant, and

- $k = 0.4$, corresponding to highly unsteady motion.

These values span the range typical of low-Reynolds-number plunging and flapping wings and capture the progression from steady-like behaviour to strongly unsteady, dynamic-stall-like flow. While variations in sweep angle, aspect ratio, and aerofoil thickness are present in the dataset, the emphasis of this chapter is on reduced frequency as the primary control parameter. Geometric effects are discussed where they modulate reduced-frequency trends. Results for the thicker NACA 0018 aerofoil are included selectively in the main text to illustrate thickness sensitivity, with a more complete set of NACA 0018 cases provided in Appendix C for reference.

In Chapter 4, two distinct LEV breakdown modes were identified: burst-type breakdown associated with long residence times on the wings, and spiral-type breakdown associated with strong three-dimensional vortex leg instabilities. The results in Chapter 4 indicated that the transition between these breakdown modes occurs around $k = 0.2$. The present chapter, therefore, reorganises the results by reduced frequency to isolate this kinematic transition and to examine its consequences for LEV development and lift response.

This chapter examines how increasing reduced frequency reorganises LEV dynamics and the resulting aerodynamic forces. In particular, the analysis focuses on changes in LEV formation, coherence, breakdown, and the associated force response across the reduced-frequency range considered. Unless otherwise stated, results in this chapter are presented for aspect ratio 6. This configuration provides a representative case exhibiting strong three-dimensional LEV dynamics while minimising aspect-ratio-dependent effects, thereby allowing reduced-frequency effects to be isolated. Trends with reduced frequency were qualitatively similar across lower aspect ratios; however, these trends were less clearly resolved due to increased influence of aspect-ratio-dependent effects and their interaction with the unsteady flow. Additionally, detailed flow field visualisations at 60° sweep are omitted in this chapter, as strong sweep angle effects complicate isolation of reduced-frequency behaviour.

5.2 Low reduced frequency regime ($k = 0.05$)

At low reduced frequency ($k = 0.05$), the plunging motion is slow relative to the characteristic timescale of the flow. As a result, the aerodynamic response adjusts almost instantaneously to the imposed kinematics, with only weak unsteady phase lag and inertial effects. Although the motion is unsteady by definition, the flow response in this regime is well approximated as quasi-steady.

The lift coefficient histories at $k = 0.05$ reflect this quasi-steady flow response, exhibiting smooth, gradual variations throughout the plunge ramp, as shown in Figure 5.1. In particular, no impulsive, added-mass lift peaks are observed at the start or end of the ramp motion. Although the lift decreases significantly towards the end of the plunge ramp for both aerofoil sections, this decay occurs smoothly and does not exhibit the sharp overshoots characteristic of higher reduced frequency cases.

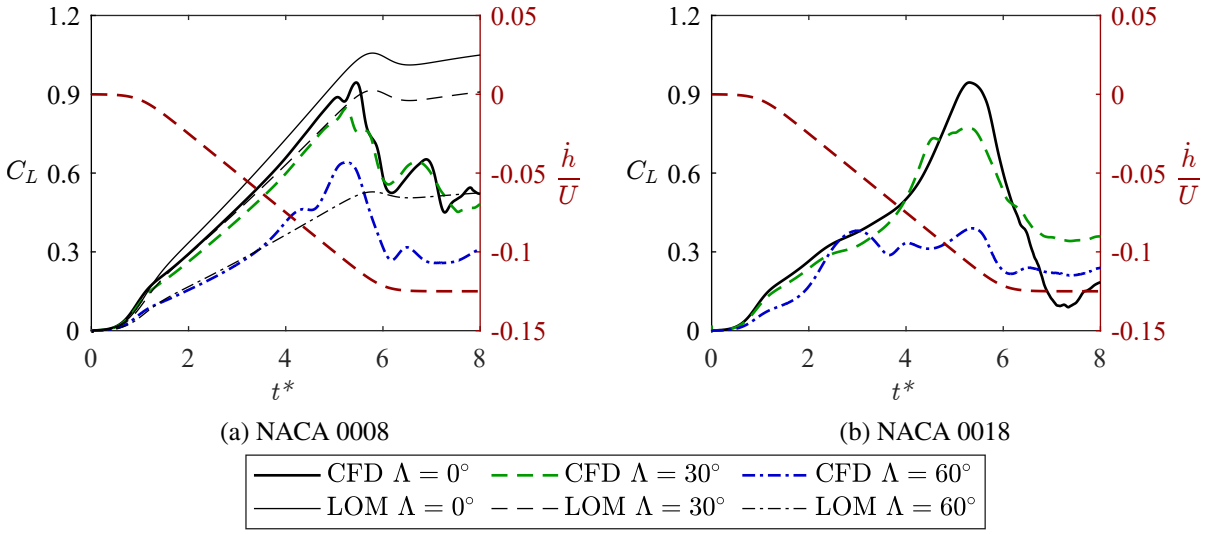

Figure 5.1: Lift coefficient time histories for the aspect ratio 6 wing geometries at reduced frequency $k = 0.05$, with CFD results compared against predictions from the C-LAULLT low-order model. The prescribed plunge velocity kinematics are shown on the right axis.

Because the wing accelerates and decelerates slowly, inertial contributions to the lift are distributed over a long time interval and do not produce impulsive force responses. Consequently, low-order unsteady models such as corrected large-amplitude unsteady lifting line theory (C-LAULLT) perform well in this regime, capturing the overall magnitude and phase of the lift response. Discrepancies arise after $t^* \approx 6$, where weak LEV bursting and viscous separation reduce lift in the CFD results (as shown in Figure 4.2).

The influence of aerofoil thickness is most apparent in this low reduced frequency regime. The thinner NACA 0008 aerofoil exhibits an approximately linear increase in lift over much of the plunge ramp, consistent with quasi-steady behaviour, whereas the thicker NACA 0018 section exhibits a non-linear lift evolution due to later leading-edge flow separation and the subsequent growth of an LEV during the ramp. In addition, at $\Lambda = 60°$ both aerofoil sections produce substantially reduced lift compared to the other wings, with the thicker NACA 0018 aerofoil producing significantly lower peak lift. These results demonstrate that sweep effects significantly effects the force response in the low reduced frequency regime, particularly with a thicker aerofoil profile.

As discussed below with reference to the corresponding flow visualisations, thickness-dependent differences at $k = 0.05$ are associated primarily with variations in leading-edge separation behaviour rather than enhanced vortex-induced lift. The thicker NACA 0018 aerofoil exhibits delayed separation and a smoother leading-edge shear layer compared with the NACA 0008 section, as demonstrated in Figures 5.1 and 5.2. The thicker aerofoil does not produce a stronger or more coherent LEV. Instead, increased thickness acts to suppress LEV formation by reducing local suction gradients at the leading edge. As a result, thickness-dependent differences in lift at low reduced frequency arise from differences in separation behaviour rather than from enhanced

vortex-induced lift.

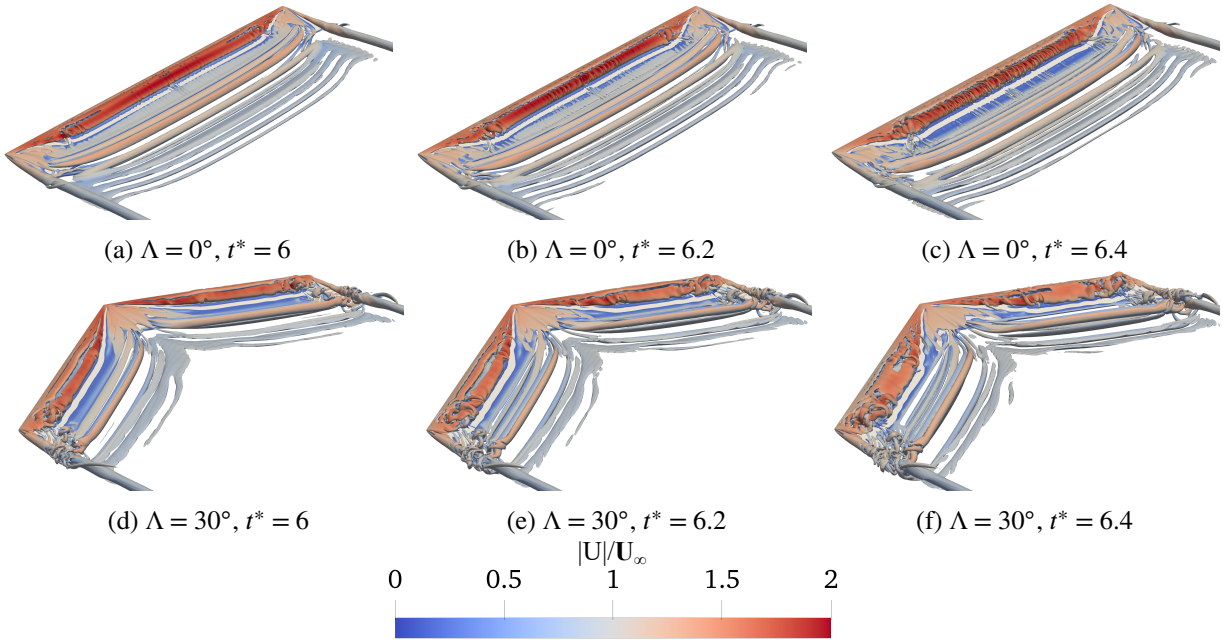

Figure 5.2: Isosurfaces of $Q = 1$ coloured by normalised velocity magnitude for the aspect ratio 6, NACA 0008, $\Lambda = 0°$ and 30° wing geometries at reduced frequency $k = 0.05$ at representative convective times where a coherent LEV exists over the wing.

The flow visualisations at $k = 0.05$ help explain the smooth, quasi-steady lift histories discussed above. In both unswept and swept configurations in Figure 5.2, the LEV remains confined to the fore half of the chord for much of the plunge, exhibiting a long residence time and limited downstream convection prior to breakdown. This weak, slowly evolving LEV structure is consistent with the absence of impulsive lift features in the force response.

For the unswept wing in Figures 5.2a-5.2c, the LEV remains relatively narrow, with a weakly attached leading-edge shear layer near the tip feeding vorticity into the vortex core. In the swept configuration, the inboard shear layer sheds vorticity more continuously into the LEV, leading to gradual vortex thickening and the onset of instability outboard near the tip. However, the LEV remains largely decoupled from the tip-vortex system, limiting its contribution to lift enhancement.

For both wing geometries in Figure 5.2, the LEV ultimately undergoes burst-type breakdown, consistent with the mechanisms described in Chapter 4. However, at this low reduced frequency, the extended residence time and weak LEV development prior to breakdown indicate that quasi-steady separation dynamics dominate the aerodynamic response, rather than strongly unsteady vortex-induced lift.

Figure 5.3 shows the corresponding flow visualisations for the thicker NACA 0018 aerofoil at $k = 0.05$, at times spanning the vicinity of the lift peak for this section. These times were selected to capture the thickness-dependent differences in lift evolution and peak timing shown in Figure 5.1. Compared with the thinner NACA 0008 aerofoil, the NACA 0018 cases exhibit

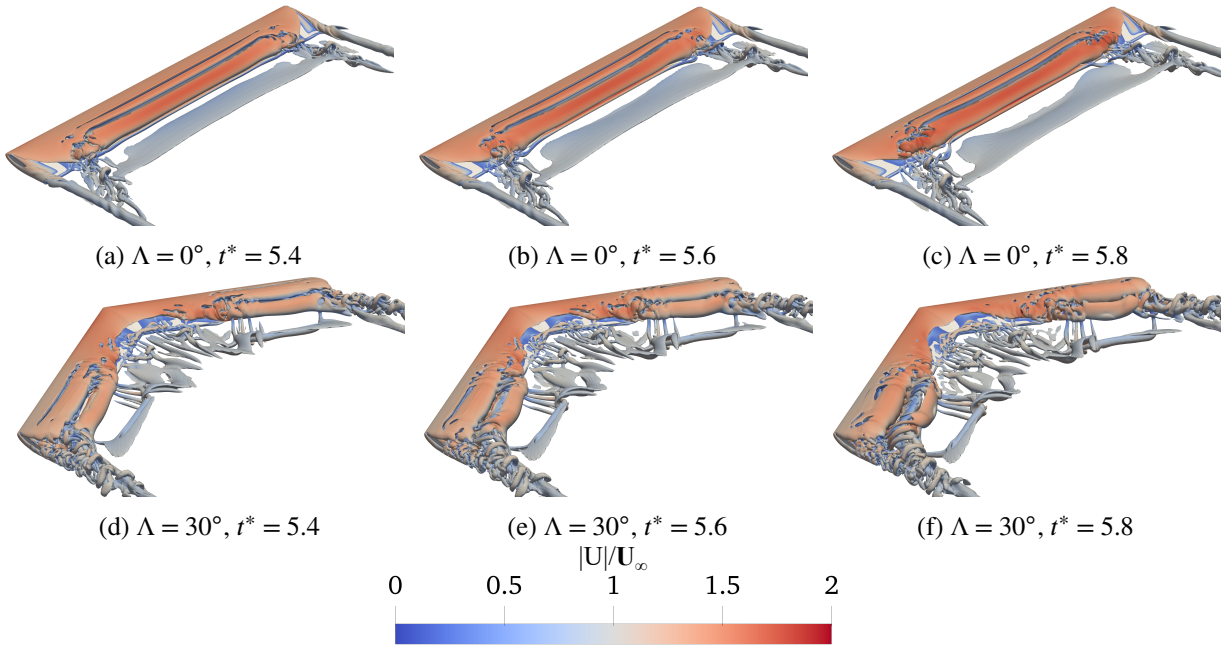

Figure 5.3: Isosurfaces of $Q = 1$ coloured by normalised velocity magnitude for the aspect ratio 6, NACA 0018, $\Lambda = 0°$ and 30° wing geometries at reduced frequency $k = 0.05$ at representative convective times where a coherent LEV exists over the wing.

differences in the separation distribution, with a thicker separated shear layer covering much of the fore half of the chord and LEV roll-up occurring further aft. This more distributed separation and delayed vortex roll-up modify the near-field pressure distribution during the plunge, leading to the non-linear lift evolution observed in the force histories, in contrast to the approximately linear lift growth exhibited by the NACA 0008 section.

For the unswept wing in Figure 5.3, a coherent LEV is present over the aft portion of the chord, but remains relatively weak and only begins to exhibit instability towards the outboard region at later times. In the swept configuration, the LEV core is concentrated over the outboard half of the span and interacts more strongly with the unsteady tip-vortex system, accompanied by increased wake unsteadiness downstream. Relative to the NACA 0008 cases, these features indicate that increased thickness alters the spatial organisation of separation and vortex roll-up, as the thicker leading edge can sustain stronger leading-edge suction before the separated shear layer rolls up into a vortex.

Taken together with the thinner NACA 0008 aerofoil results, the thicker aerofoil observations show that $k = 0.05$ represents a baseline regime in which LEV development is delayed and structurally weak, and lift varies smoothly with the imposed kinematics. At this low reduced frequency, increased aerofoil thickness primarily delays and redistributes separation without producing a stronger or more coherent LEV. Despite the long residence times on each wing observed for both aerofoil profiles, the slow quasi-steady kinematics limit vortex roll-up strength, such that thickness-dependent differences in lift arise from changes in separation behaviour rather

than from enhanced vortex-induced lift. This regime therefore provides a useful reference point against which the increasingly unsteady LEV dynamics and force responses observed at higher reduced frequencies can be assessed.

5.3 Moderate reduced frequencies ($0.1 \leq k \leq 0.2$)

At moderate reduced frequencies, $k = 0.1$ and $k = 0.2$, the flow departs from the quasi-steady behaviour observed at $k = 0.05$ and enters a transitional regime characterised by increasingly unsteady LEV dynamics. Within this reduced frequency range, the initiation timing, coherence, and breakdown mechanism of the LEV change most rapidly with increasing reduced frequency. Across this reduced frequency range, LEV formation occurs progressively earlier in the stroke, its growth rate increases, and inertial effects begin to contribute measurably to the lift response. Consistent with the classification introduced earlier in this chapter, $k = 0.1$ is treated as moderately unsteady, while $k = 0.2$ represents a transitional reduced frequency marking the onset of strongly unsteady behaviour.

5.3.1 Lift response and added-mass effects

The lift coefficient histories at $k = 0.1$ and $k = 0.2$, as shown in Figure 5.4, show a distinct departure from the smooth, quasi-steady response observed at $k = 0.05$. At $k = 0.1$, the lift response becomes weakly non-monotonic during the plunge ramp, with an inflexion appearing near the onset of the motion that is absent at lower reduced frequency. In addition, the lift reduction towards the end of the plunge ramp increases in magnitude and decreases in duration compared with the $k = 0.05$ results. These features indicate the emergence of impulsive, added-mass effects associated with the faster plunge kinematics. The lift continues to increase over much of the stroke separately to the impulsive effects.

Although the peak lift at $k = 0.1$ occurs towards the end of the plunge ramp motion, which is a similar phase to the $k = 0.05$ results, it occurs at an earlier convective time owing to the shorter plunge duration. As a result, the lift no longer tracks the instantaneous kinematics throughout the motion, indicating that LEV growth and convection are no longer sufficiently slow to be approximated by quasi-steady behaviour. This behaviour is evident in Figure 5.4a, where the lift departs from the near-monotonic increase observed at $k = 0.05$ and instead exhibits an early-stroke inflexion and a more abrupt post-peak reduction.

At $k = 0.2$, the effects observed for $k = 0.1$ become more pronounced. The lift no longer increases monotonically during the plunge ramp, instead exhibiting a distinct added-mass peak at the start of the ramp, followed by a reduction in lift. An analogous impulsive response occurs at the end of the ramp motion, producing a negative lift peak. The lift evolution in this regime therefore reflects a combined influence of strong unsteady inertial effects and indicate increasingly dynamic LEV behaviour. This lift behaviour is consistent with earlier LEV formation and the

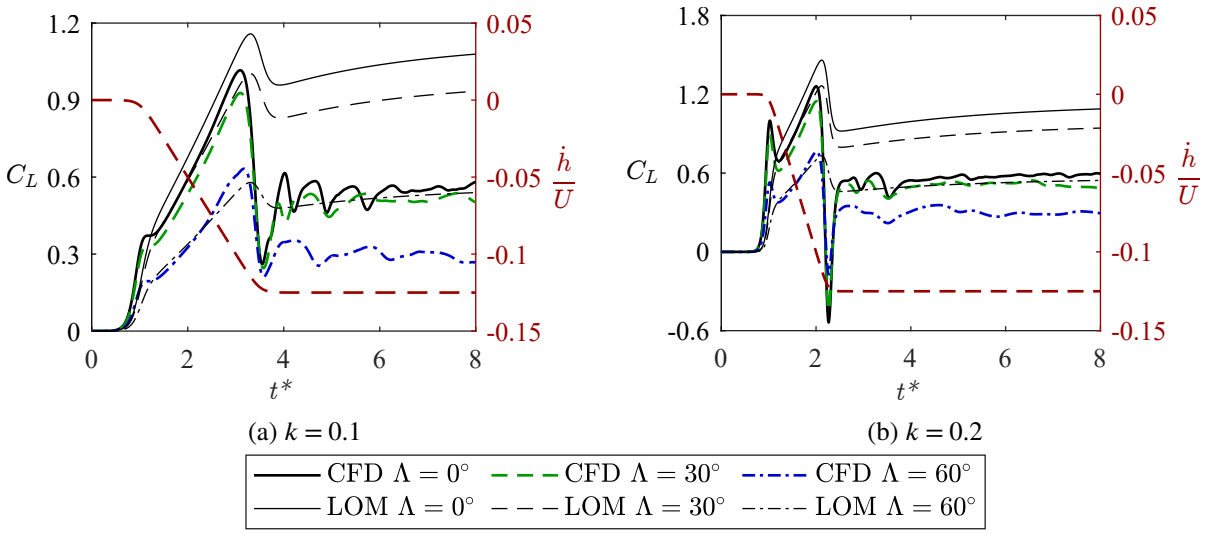

Figure 5.4: Lift coefficient time histories for the aspect ratio 6, NACA 0008 wing geometries at moderate reduced frequencies, with CFD results compared against predictions from the C-LAULLT low-order model. The prescribed plunge velocity kinematics are shown on the right axis.

onset of partial vortex detachment during the stroke, rather than towards the end of the ramp motion.

The increasing impulsive effects at $k = 0.2$ consequently exposes the limitations of low-order unsteady models. While C-LAULLT captures the overall increase in lift with reduced frequency and reproduces the timing of the added-mass peaks, the model cannot represent LEV shedding or partial detachment. As a result, C-LAULLT tends to over-predict lift during the plunge ramp at $k = 0.2$ compared to the CFD results.

5.3.2 LEV initiation and timing (LESP)

The earlier LEV formation at moderate reduced frequencies is quantified using the leading-edge suction parameter (LESP). Figure 5.5 shows the LESP histories at $k = 0.1$ and $k = 0.2$ for each swept wing configuration.

At $k = 0.1$, LESP increases steadily during the plunge ramp, indicating that LEV initiation occurs only towards the later stages of the plunge ramp motion. In contrast, at $k = 0.2$, the LESP rises more rapidly for the unswept and 30° swept wings, consistent with earlier LEV initiation during the plunge ramp. For the 60° swept wing at both reduced frequencies, the LESP remains comparatively low throughout the motion, reflecting the strong influence of spanwise convection in delaying or suppressing LEV roll-up.

Consistent with the theoretical framework outlined in Chapter 3, sweep angle strongly modulates the spanwise distribution and magnitude of LESP. In swept configurations, LESP is highest along the mid-span plane, whereas over the unswept wing, comparable LESP levels are observed at the root and mid-span planes. Increasing sweep angle also reduces the overall LESP magnitude

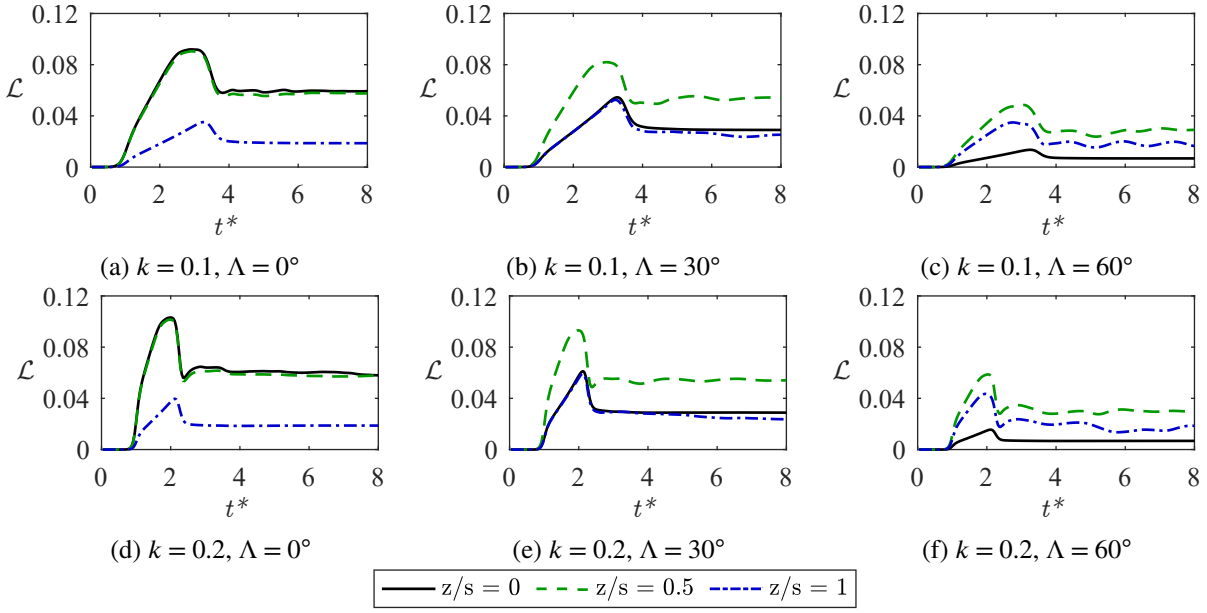

(a) $k = 0.1$, $\Lambda = 0°$ (b) $k = 0.1$, $\Lambda = 30°$ (c) $k = 0.1$, $\Lambda = 60°$

(d) $k = 0.2$, $\Lambda = 0°$ (e) $k = 0.2$, $\Lambda = 30°$ (f) $k = 0.2$, $\Lambda = 60°$

Figure 5.5: Time histories of LESP magnitude for the aspect ratio 6, NACA 0008 geometries, at reduced frequency $k = 0.1$ (*top*) and $k = 0.2$ (*bottom*) along the root, mid-span and tip planes of the wing.

due to the smaller free-stream velocity component normal to the leading edge. Nevertheless, the earlier attainment of peak LESP at $k = 0.2$ persists across all sweep angles, suggesting that reduced frequency, rather than geometry alone, governs the timing of LEV initiation in this transitional regime.

5.3.3 LEV structure and breakdown

The transition in LEV dynamics between $k = 0.1$ and $k = 0.2$ is clearly illustrated by three-dimensional Q-criterion flow visualisations. For all NACA 0008 cases shown here, the convective times are selected shortly after the reduction in lift near the end of the plunge ramp. This ensures that impulsive added-mass transients associated with rapid acceleration and deceleration do not dominate the force response, while retaining the unsteady lift oscillations observed in Figure 5.1 associated with evolving LEV dynamics.

Figure 5.6 shows Q-criterion isosurfaces at $k = 0.1$. Compared with the quasi-steady regime at $k = 0.05$, the LEV is more coherent and stronger, remaining attached over a substantial portion of the chord and span for both the unswept and 30° swept wings. While early signs of unsteadiness are present, particularly in the form of nascent spiral-type structures developing from the outboard LEV legs, the vortex largely retains its coherence throughout the stroke for both wing geometries. In the unswept configuration, localised burst-type vortex thickening is observed near the root in Figure 5.6c, whereas for swept configurations, spanwise convection stabilises the LEV, delaying the onset of instability and suppressing this burst-type behaviour. These features are consistent with a regime in which impulsive kinematic effects begin to influence LEV growth but do not yet

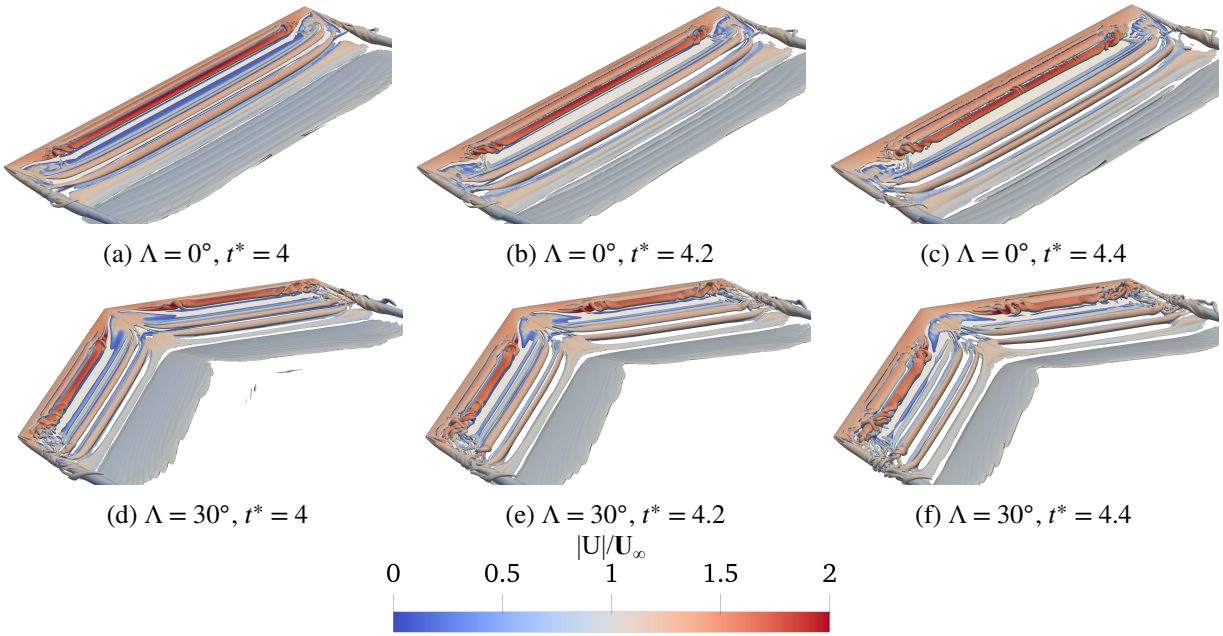

Figure 5.6: Isosurfaces of $Q = 1$ coloured by normalised velocity magnitude for the aspect ratio 6, NACA 0008, $\Lambda = 0°$ and 30°, wing geometries at reduced frequency $k = 0.1$ at representative convective times where a coherent LEV exists over the wing.

control its evolution. The unsteady lift oscillations observed in Figure 5.1 at the convective times shown in Figure 5.6 are consistent with the early development of LEV instability and intermittent vorticity shedding from the outboard LEV legs, rather than with impulsive kinematic forcing. Additionally, the lower magnitude lift oscillations observed for the 30° swept wing compared to the unswept wing are consistent with the qualitative observations in Figure 5.6.

At $k = 0.2$, shown in Figure 5.7, the LEV exhibits qualitatively different behaviour. The vortex forms early in the plunge motion, develops a narrower and more strongly defined core, and undergoes partial detachment and spiral-type instability while still on the wing. Over the unswept wing, this instability initiates from the outboard LEV legs and progresses inboard, consistent with the spiral-type breakdown mechanisms identified in Chapter 4. For the 30° swept wing, although outboard LEV legs exist, inboard progression is limited by the induced spanwise flow convection due to the sweep angle. However, inboard LEV legs form and progress outboard over the 30° swept wing due to the sharp apex geometry. Unlike at $k = 0.1$, burst-type vortex thickening is no longer observed over the unswept wing. Instead, the LEV detaches earlier in the motion due to the more impulsive kinematics, limiting its sustained coupling to the leading edge. As a result, although the lift response in Figure 5.4b remains oscillatory, the oscillations are of reduced amplitude compared with the $k = 0.1$ case, and no single abrupt collapse event is observed following the impulsive peak.

Taken together, these visualisations demonstrate that increasing reduced frequency shifts the governing LEV dynamics from a regime dominated by long residence times and gradual separation to one increasingly influenced by kinematically driven growth and instability. At

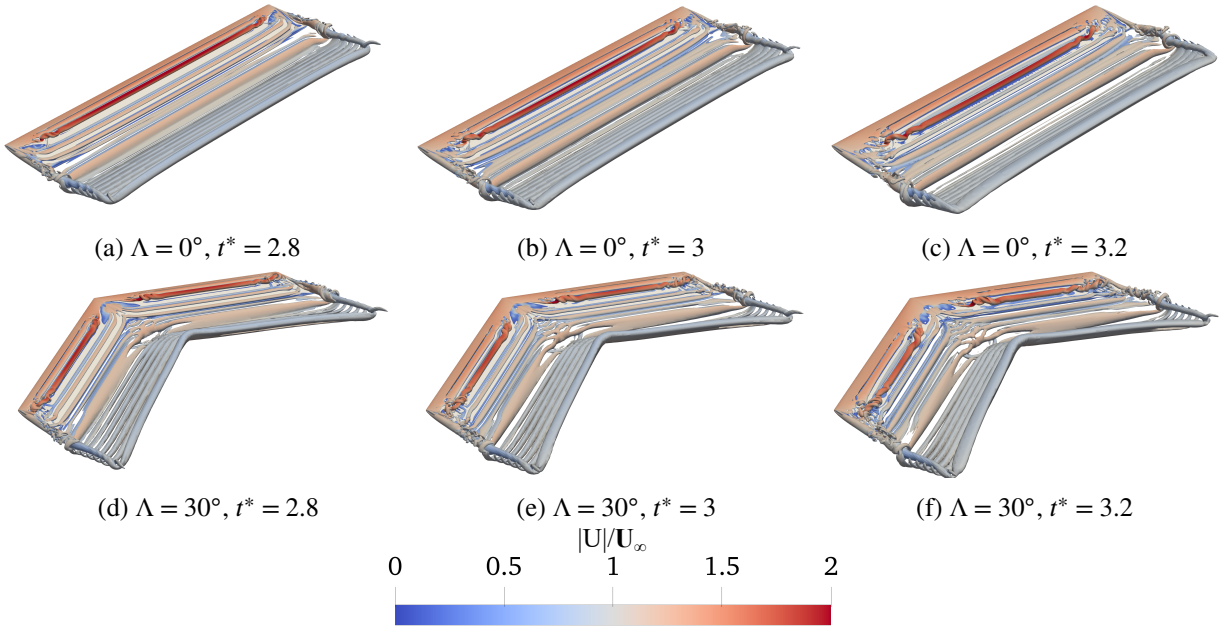

Figure 5.7: Isosurfaces of $Q = 1$ coloured by normalised velocity magnitude for the aspect ratio 6, NACA 0008, $\Lambda = 0°$ and 30° wing geometries at reduced frequency $k = 0.2$ at representative convective times where a coherent LEV exists over the wing.

$k = 0.2$, impulsive effects play a significant role in LEV evolution, leading to spiral-type structures and a corresponding reduction in lift, marking a distinct departure from the $k = 0.05$ regime.

5.3.4 Summary of reduced-frequency transition at $0.1 \leq k \leq 0.2$

In summary, the intermediate reduced-frequency regime, $0.1 \leq k \leq 0.2$, corresponds to a transitional reorganisation of LEV dynamics. As reduced frequency increases, LEV initiation occurs at an earlier convective time, and the influence of kinematic acceleration on vortex growth and stability becomes increasingly significant. The resulting LEV evolution departs from the weakly unsteady behaviour observed at $k = 0.05$, with unsteady LEV development and partial detachment occurring during the plunge ramp motion rather than being confined to its later stages.

The results indicate that $k \approx 0.2$ marks the onset of kinematically driven LEV instability, characterised by spiral-type breakdown developing once the wing has reached the steady-state plunge region of the motion. This reduced frequency regime therefore represents a transitional boundary between behaviour that can be approximated as quasi-steady and the more strongly impulsive vortex dynamics examined in the following section, rather than a fully impulsive limit.

5.4 High reduced frequency regime ($k = 0.4$)

As shown in Figure 5.8, the lift response at $k = 0.4$ is dominated by strongly impulsive behaviour. Large lift peaks occur at the beginning and end of the plunge ramp, corresponding to added-

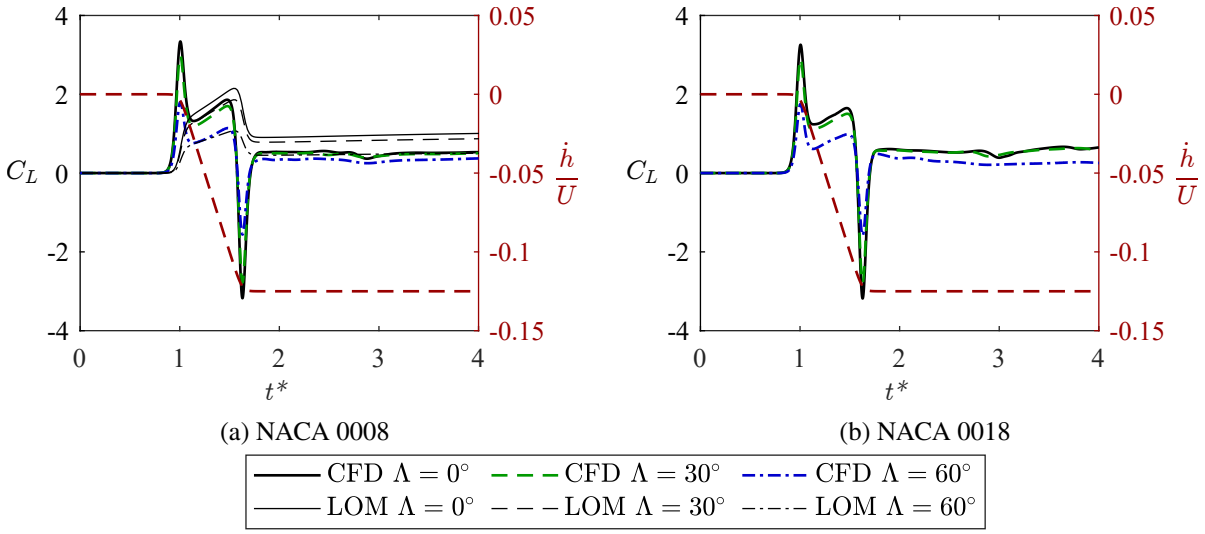

Figure 5.8: Lift coefficient time histories for the aspect ratio 6 wing geometries at reduced frequency $k = 0.4$, with CFD results compared against predictions from the C-LAULLT low-order model. The prescribed plunge velocity kinematics are shown on the right axis.

mass forces generated by the rapid acceleration and deceleration of the wing. These impulsive contributions dominate the force response and are substantially larger than those observed at lower reduced frequencies.

Between these impulsive events, the lift increases approximately linearly during the plunge ramp, similarly to lower reduced frequency cases, but over a much shorter timescale. From the force histories alone, it is not possible to clearly isolate a sustained vortex-induced contribution to lift. This motivates the force partitioning analysis adopted in Chapter 7. The overall lift response is governed primarily by kinematic acceleration rather than by vortex-dominated mechanisms.

C-LAULLT exhibits increasing discrepancies compared to lower reduced frequency cases in this high reduced frequency regime. While the model predicts the overall lift increase with reduced frequency due to unsteady circulation effects, C-LAULLT cannot represent the impulsive added-mass peaks associated with rapid acceleration and deceleration. As a result, the model under-predicts the peak lift at the start and end of the plunge ramp.

In addition, for the unswept configuration, C-LAULLT over-predicts the sustained lift during the plunge ramp and in the subsequent constant-velocity phase due to its inviscid, attached flow assumptions. For swept wing configurations, this over-prediction is less pronounced. These lift prediction discrepancies do not indicate a complete breakdown of the low-order model (LOM), but rather highlight the need for explicit LEV shedding and impulsive-force representations when modelling highly unsteady plunging motions.

The lift response of the thicker NACA 0018 section at $k = 0.4$ follows the same qualitative trends as the thinner NACA 0008 case, with dominant impulsive added-mass peaks, linear lift growth during the plunge ramp and almost constant lift during the steady-state plunge motion after $t^* = 1.6$. While minor differences in peak magnitude and post-peak lift levels are observed,

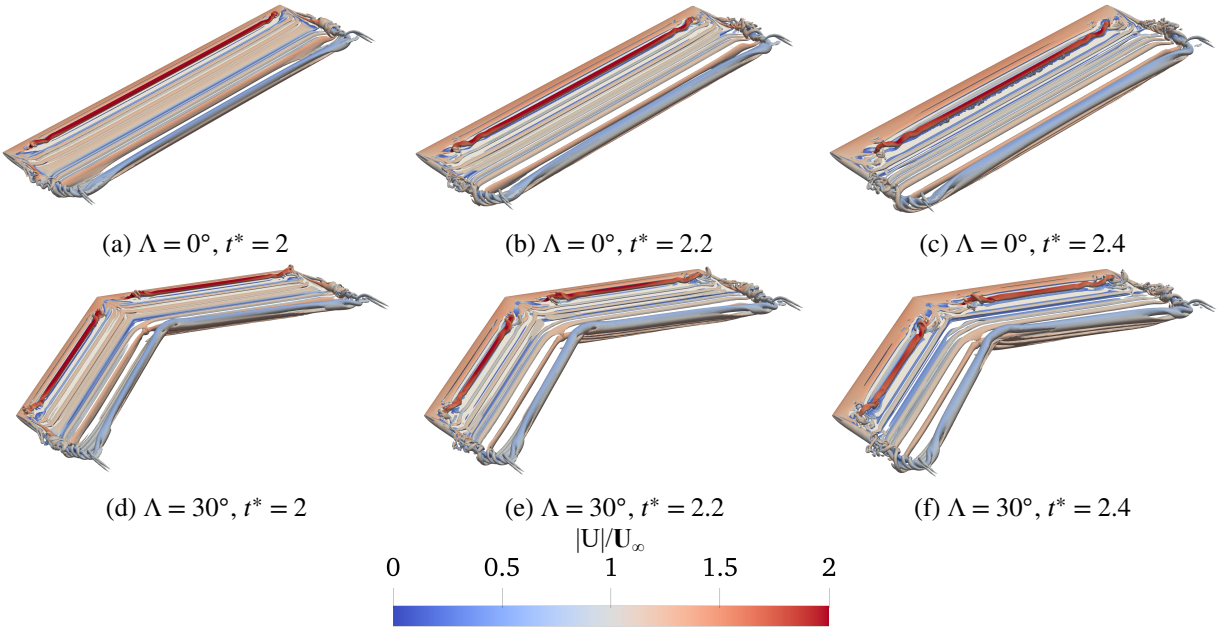

Figure 5.9: Isosurfaces of $Q = 1$ coloured by normalised velocity magnitude for the aspect ratio 6, NACA 0008, $\Lambda = 0°$ and 30° wing geometries at reduced frequency $k = 0.4$ at representative convective times where a coherent LEV exists over the wing.

aerofoil thickness does not fundamentally alter the highly unsteady nature of the response at $k = 0.4$. This aerofoil thickness trend indicates that, at sufficiently high reduced frequency, inertial effects dominate over geometric influences.

The three-dimensional flow field at $k = 0.4$ reflects a highly unsteady response dominated by rapid acceleration and strong inertial effects. Figure 5.9 shows Q-criterion isosurfaces for the unswept and moderately swept wings during the early constant plunge velocity phase of the motion, following completion of the plunge ramp at $t^* = 1.6$. Consistent with the lower reduced frequency cases, this time is selected to enable direct comparison of LEV structure following the initial impulsive acceleration.

For the unswept wing in Figures 5.9a-5.9c, strong leading-edge vorticity is present shortly after completion of the plunge ramp. However, the associated LEV is rapidly convected downstream and remains weakly coupled to the wing surface. The LEV has a narrow core, and its evolution is dominated by downstream convection rather than sustained attachment or growth. At the convective times shown, the lift has settled to an approximately steady level following the impulsive peak, consistent with the downstream shedding of the coherent LEV.

For the moderately swept wing, the overall flow structure shares some similarities to the unswept case, but with stronger spanwise transport along the vortex core. The LEV remains highly three-dimensional and undergoes significant downstream convection, rather than forming a compact attached structure capable of sustaining lift. In both configurations, the flow field closely resembles that observed at $k = 0.2$, but with enhanced vorticity strength and more pronounced three-dimensional effects induced by the impulsive kinematics.

In addition, the highly unsteady motion produces a strongly deflected wake downstream of the wing and a reattachment of the tip-vortex system, reflecting the dominance of inertial effects in organising the flow. These visualisations indicate that, at $k = 0.4$, LEV development occurs within a highly unsteady, impulsively driven flow field. While a LEV is present, the force histories alone do not allow its sustained contribution to lift to be determined beyond the added-mass response associated with rapid acceleration and deceleration. Quantifying the role of the LEV, therefore, warrants further investigation using force partitioning, which is addressed in Chapter 7.

5.5 Conclusions

This chapter has demonstrated that reduced frequency is a primary control parameter governing LEV dynamics on plunging wings. As reduced frequency increases from $k = 0.05$ to $k = 0.4$, the flow transitions from weakly unsteady, quasi-steady-like behaviour to a highly unsteady regime dominated by rapid acceleration and strong inertial effects. Across this range, increasing reduced frequency advances LEV initiation time, due to the earlier end of the plunge ramp motion, and alters both the organisation and stability of the vortex, leading to changes in the dominant breakdown mechanisms.

At low reduced frequency, $k = 0.05$, LEV formation is delayed and weak compared to higher reduced frequencies, and lift follows the imposed kinematics smoothly with minimal unsteady lag. Hence, the C-LAULLT low-order unsteady model performs well. In this regime, aerofoil thickness primarily influences separation behaviour and the consequent lift response. At intermediate reduced frequencies, $0.1 \leq k \leq 0.2$, LEV initiation occurs progressively earlier in convective time, added-mass contributions become increasingly evident in the lift response, and the LEV undergoes partial detachment during the motion. The case $k = 0.2$ marks a critical transitional regime in which impulsive kinematic effects begin to dominate the lift response and have an significant effect on vortex initiation, growth, attachment, and breakdown.

At high reduced frequency ($k = 0.4$), the lift response is dominated by impulsive added-mass effects associated with rapid acceleration and deceleration. Although a LEV is present, its development occurs within a highly unsteady flow field and is accompanied by rapid downstream convection and strong three-dimensional effects. In this regime, LEV evolution primarily influences the post-impulse lift behaviour, while the peak force response is governed by inertial effects. Consistent with this, aerofoil thickness plays only a secondary role relative to reduced frequency effects.

Taken together, these results demonstrate how reduced frequency acts as a primary kinematic control parameter governing the timing, organisation, and stability of LEVs on plunging wings, and how these changes are reflected in the aerodynamic force response. As reduced frequency increases, LEV initiation advances in convective time and vortex evolution becomes increasingly influenced by kinematic acceleration and unsteady inertial effects, leading to distinct changes in

breakdown behaviour, as discussed in Chapter 4. The results also demonstrate the limitations of low-order unsteady models at higher reduced frequencies, where impulsive forces, vortex shedding, and three-dimensional effects play an increasingly important role. Having established the influence of reduced frequency, the following chapter examines how sweep angle further modifies LEV formation and stability through spanwise flow and altered vortex convection mechanisms.

6

Sweep Angle Effects on Vortex Formation and Stability

> *It is far better to foresee even without certainty than not to foresee at all.*
>
> **— Henri Poincaré**
> (Mathematician)

6.1 Introduction

WING sweep angle, Λ, is a fundamental geometric parameter that introduces intrinsic three-dimensionality into the flow over a finite wing. While sweep is classically associated with delaying compressibility effects at high flight speeds, it also plays a critical role in low-Reynolds-number unsteady aerodynamics by inducing spanwise flow across the wing. In flapping and plunging flight, this spanwise flow fundamentally alters the formation, evolution, and stability of leading-edge vortices (LEVs), which are a primary mechanism for lift generation under highly unsteady conditions.

Sweep is a prominent feature in the wings of many natural flyers, including birds, bats, and insects, as well as in bio-inspired micro air vehicles (MAVs). In these applications, sweep is often hypothesised to influence LEV behaviour by promoting spanwise transport of vorticity [2, 4], thereby modifying LEV strength, coherence, and breakdown characteristics. However, despite extensive experimental and numerical investigation, the aerodynamic role of sweep at low Reynolds numbers remains incompletely understood. Some studies report enhanced force production or delayed stall with increasing sweep [47, 116, 118, 122, 124], while others observe weakened LEVs, increased unsteadiness, or little stabilisation at moderate sweep angles up to $\Lambda = 45°$ [48–51, 106]. These findings suggest that sweep does not act as a simple stabilising

mechanism, but instead reorganises the vortex system in a manner that depends strongly on kinematics, aspect ratio, and reduced frequency.

The preceding chapters of this thesis have established two key foundations for understanding unsteady LEV dynamics. Chapter 4 identified and classified distinct LEV breakdown modes on finite plunging wings, demonstrating how breakdown can occur either abruptly or progressively depending on flow conditions and three-dimensional effects. Chapter 5 then examined the role of reduced frequency, showing how increasing unsteadiness alters LEV formation, leading-edge attachment, and stability. Together, these preceding chapters demonstrate that a complex interaction between kinematics and three-dimensional flow physics governs LEV behaviour.

Sweep angle represents the next critical geometric parameter to be analysed. Unlike reduced frequency, which primarily controls temporal unsteadiness, sweep directly modifies the spatial organisation of the flow by introducing a persistent spanwise velocity component. This spanwise flow has the potential to alter not only LEV stability and breakdown behaviour, but also where along the span the LEV first forms, how it evolves in time, and how aerodynamic loads are distributed across the wing.

In this chapter, wing sweep angle is varied between 0° (unswept), 30° (moderately swept), and 60° (highly swept), across a range of aspect ratios and reduced frequencies. Using a combination of IDDES flow visualisations, leading-edge suction parameter (LESP) analysis, and force histories, the effects of sweep are examined from both a flow-physics and an aerodynamic-performance perspective. Particular emphasis is placed on understanding how sweep modifies LEV topology, the spanwise initiation and timing of LEV formation, and the resulting implications for lift generation and vortex stability.

The chapter is organised as follows; Section 6.2 compares the instantaneous LEV flow structures for unswept, moderately swept, and highly swept wings, highlighting how increasing sweep affects the relationship between the LEV, tip vortex, and spanwise flow. Section 6.3 then examines how sweep modifies LEV initiation along the span, drawing on LESP distributions and flow-field observations to explain spanwise variation in LEV initiation. Section 6.4 examines the corresponding lift response for representative cases, highlighting the extent of the sensitivity of global force coefficients to the key flow field structures under unsteady conditions. Finally, Section 6.5 summarises the key effects of sweep angle and discusses their implications for unsteady aerodynamic performance, providing a direct link to the spanwise load distribution analysis presented in Chapter 7.

6.2 Sweep angle effects on LEV flow structures

6.2.1 Unswept wing baseline

The unswept wing provides a baseline configuration in which LEV behaviour is governed primarily by chordwise separation and finite-wing effects, without the additional influence of sweep-induced spanwise flow. In the absence of geometric sweep, there is no imposed spanwise velocity component, hence three-dimensionality primarily arises from pressure gradients associated with the wing-tip and the finite span.

Figure 6.1 shows representative Q-criterion flow visualisations for the unswept wing at $k = 0.4$. The LEV exhibits pronounced spanwise variation and undergoes continuous deformation throughout the convective times shown. A coherent primary LEV forms near the leading edge and subsequently detaches from the wing, remaining a distinct vortical structure aligned parallel to the leading edge towards the wing root as it convects downstream. Further outboard, the LEV does not extend cleanly into the wing-tip. Instead, interactions with tip-induced spanwise flow give rise to distinct outboard vortex legs that interact with LEV, deforming the core flow as time progresses. The inboard progression of the spiralling leg behaviour is visible in Figure 6.1 as a progressive distortion of the outboard LEV region and is consistent with the early stages of spiral-type LEV breakdown at high reduced frequency.

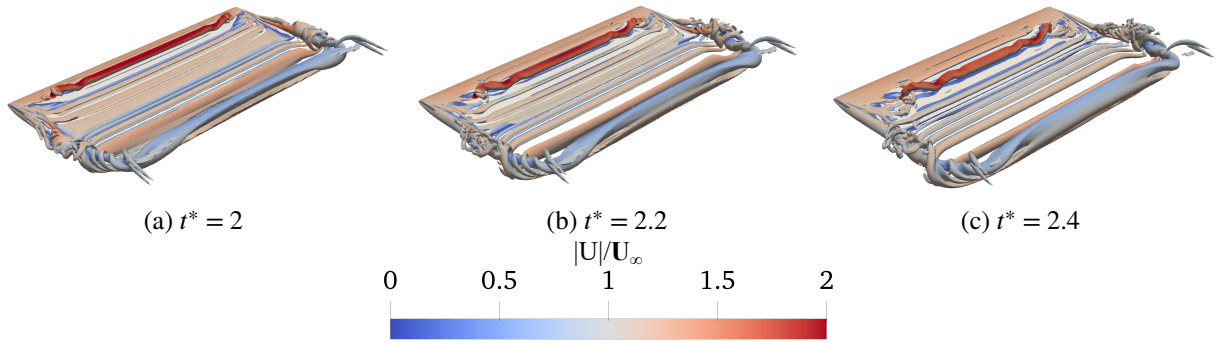

Figure 6.1: Isosurfaces of $Q = 1$ coloured by normalised velocity magnitude for the aspect ratio 3, NACA 0008, $\Lambda = 0°$ wing geometries at reduced frequency $k = 0.4$ at representative convective times where a coherent LEV exists over the wing.

Across the broader set of unswept-wing cases examined in this study, similar tip–LEV interactions are observed, although their manifestation depends on reduced frequency and aspect ratio. Consistent with the reduced frequency trends established in Chapter 5, the LEV on unswept wings remains coherent for longer at lower reduced frequencies, with outboard disturbances developing more gradually. At higher reduced frequencies, as shown here, tip–LEV interactions rapidly introduce spiral instabilities into the LEV. However, in all cases, the unswept wing configuration maintains a clear distinction between the primary LEV and the tip vortex, in contrast to swept wings, where these structures become increasingly coupled.

6.2.2 Moderately swept wing

Figure 6.2 shows representative Q-criterion flow visualisations for the 30° swept wing at $k = 0.4$, which is the same reduced frequency used in Figure 6.1 for the unswept wing reference case. At $k = 0.4$, the vortex system is highly unsteady and is strongly influenced by the impulsive kinematics. In contrast to the unswept configuration, the LEV on the moderately swept wing originates as a symmetric pair associated with the wing apex, with vorticity fed into the primary oblique LEV.

Introducing a moderate sweep angle of 30° fundamentally alters the LEV topology by introducing a persistent spanwise component of the flow along the leading edge. As a result, the primary LEV is no longer aligned parallel to the leading edge, unlike the unswept case. Instead, the LEV core is inclined at an angle greater than the geometric sweep angle, indicating that vorticity is convected in the spanwise direction as the LEV rolls up from the leading-edge shear layer. This oblique orientation reflects the combined influence of leading-edge separation and spanwise transport, rather than purely chordwise LEV development.

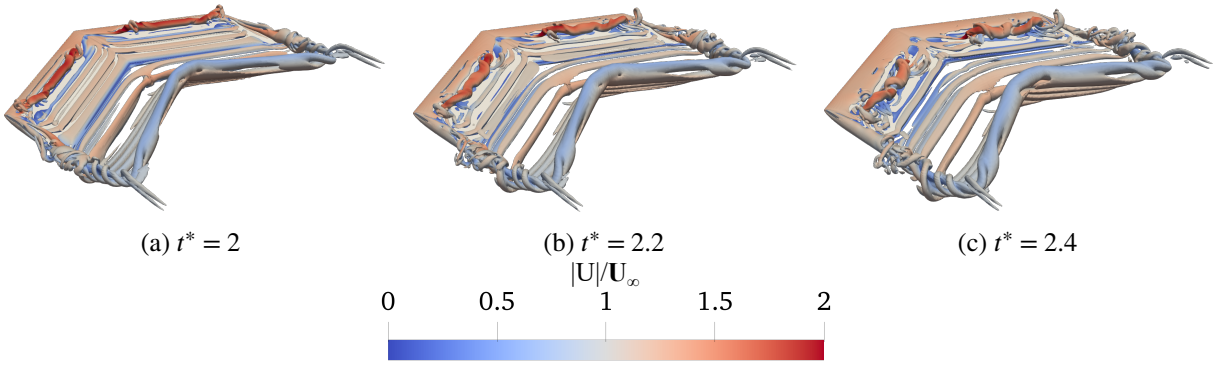

(a) $t^* = 2$ (b) $t^* = 2.2$ (c) $t^* = 2.4$

Figure 6.2: Isosurfaces of $Q = 1$ coloured by normalised velocity magnitude for the aspect ratio 3, NACA 0008, $\Lambda = 30°$ wing geometries at reduced frequency $k = 0.4$ at representative convective times where a coherent LEV exists over the wing.

The LEV core is prone to spiral-type instabilities, which develop first near the apex and tip and then propagate along the full extent of the LEV. By $t^* = 2.4$ (Figure 6.2c), this instability has spread across the span, and the initial LEV structure begins to roll up into a partial arch-like topology. Over the same time period, the tip vortex progressively re-attaches to the wing-tip region, in a comparable manner to the unswept wing. However, unlike the unswept wing, the tip vortex remains dynamically coupled to the evolving LEV structure, due to the sweep-induced spanwise flow. The combined effect is a more apparent breakdown of the LEV than observed for the unswept configuration.

For comparison, Figure 6.3 shows the moderately swept wing at a lower reduced frequency ($k = 0.05$), where the flow evolves more gradually. In this regime, a coherent primary LEV forms along the leading edge and is inclined relative to the leading edge, similarly to Figure 6.2.

The primary LEV is accompanied by a shear layer originating from the apex region (Figures

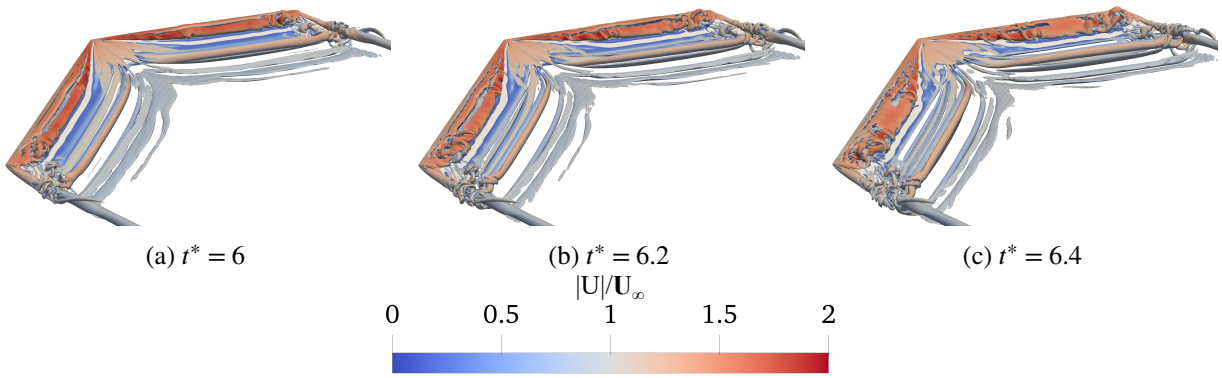

(a) $t^* = 6$ (b) $t^* = 6.2$ (c) $t^* = 6.4$

Figure 6.3: Isosurfaces of $Q = 1$ coloured by normalised velocity magnitude for the aspect ratio 6, NACA 0008, $\Lambda = 30°$ wing geometries at reduced frequency $k = 0.05$ at representative convective times where a coherent LEV exists over the wing.

6.3a–6.3b), which remains attached to the apex and continuously feeds vorticity into the developing LEV core. As a result, the LEV thickens progressively towards mid-span. This is in contrast to the unswept case where a single LEV develops, predominantly through chordwise roll-up, and terminates near the wing-tip. Over the swept wing, the shear layer connected to the wing apex persists over a substantial portion of the downstroke at low reduced frequency, highlighting the sustained influence of sweep on LEV formation even under quasi-steady conditions.

Overall, the moderately swept wing represents an intermediate regime in which sweep introduces an additional instability pathway originating from the wing apex. Vorticity is shed outboard from the apex into the LEV core, promoting spanwise vorticity convection and the LEV is inclined at an oblique angle relative to the leading edge. Additionally, the primary LEV and tip vortex are partially coupled, in contrast to the unswept wing where they exist as separate structures.

6.2.3 Highly swept wing

The flow structures over the 60° swept wing differs markedly from both the unswept and moderately swept configurations, owing to the strong spanwise convection induced by the large sweep angle. Similarly to the moderately swept case, the wing apex at the root acts as a dominant separation point, strongly influencing the organisation of the LEV and its interaction with the outboard flow.

Figure 6.4 shows representative Q-criterion flow visualisations for the highly swept wing at the same reduced frequency as the unswept and moderately swept cases ($k = 0.4$). At $t^* = 2$, the LEV strongly interacts with the outboard flow and displaces the tip vortex away from the leading edge as a result of enhanced spanwise coupling. This behaviour is consistent with observations reported by Visbal and Garmann [125] for highly swept wings under unsteady conditions.

Due to the high wing sweep angle, the inboard shear layer remains attached to the wing apex throughout the motion. The strong spanwise convection associated with the high sweep angle promotes continuous spanwise transport of of leading-edge vorticity, limiting its local accumulation near the apex and thereby preventing the formation of a strongly rolled-up or

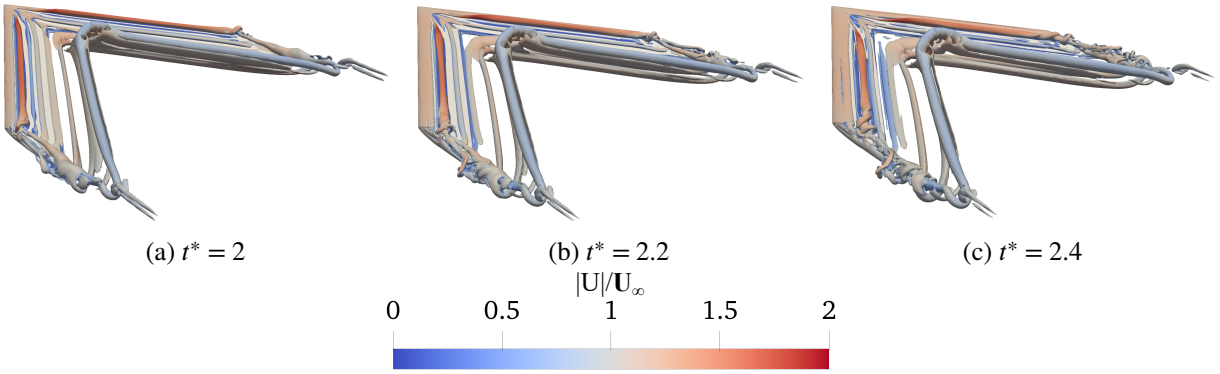

Figure 6.4: Isosurfaces of $Q = 1$ coloured by normalised velocity magnitude for the aspect ratio 3, NACA 0008, $\Lambda = 60°$ wing geometries at reduced frequency $k = 0.4$ at representative convective times where a coherent LEV exists over the wing.

unstable inboard LEV. As the motion progresses, the LEV undergoes spiral-type breakdown in the outboard region, while the tip region becomes characterised by a highly unsteady wake composed of shed vorticity rather than a coherent tip vortex, as evident at $t^* = 2.4$.

For comparison, Figure 6.5 shows the highly swept wing at $k = 0.05$, where the flow evolves more gradually. In this regime, a coherent LEV develops from the wing apex and remains attached along the inboard portion of the leading edge, forming a single, oblique vortex structure inclined relative to the leading edge. Strong spanwise convection associated with the high sweep angle inhibits the accumulation of circulation into a compact chordwise vortex, resulting instead in an LEV core that thickens progressively towards the outboard region. The most apparent reduced-frequency effects between Figures 6.4 and 6.5 are the LEV inclination relative to the leading edge, the size of the LEV core and the breakdown mode observed in the outboard regions.

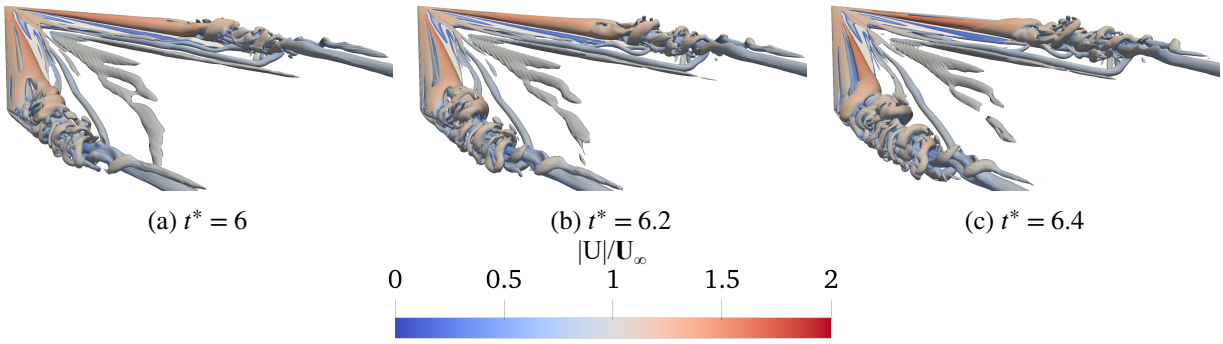

Figure 6.5: Isosurfaces of $Q = 1$ coloured by normalised velocity magnitude for the aspect ratio 3, NACA 0008, $\Lambda = 60°$ wing geometries at reduced frequency $k = 0.05$ at representative convective times where a coherent LEV exists over the wing.

Over the wing surface, the LEV and inboard shear layer appear as a continuous structure rather than as distinct vortical elements. A tip vortex core is not clearly identifiable in the immediate vicinity of the wing at any convective time shown, although the core becomes apparent further downstream in the wake. Towards the outboard portion of the wing, the thickened LEV interacts

with the developing wake, giving rise to a broad region of unsteady vortex shedding rather than a clearly separated LEV and tip vortex system.

At low reduced frequencies, the LEV on the highly swept wing is relatively weak and diffuse. The strong spanwise transport associated with high sweep prevents the accumulation of circulation into a compact LEV, resulting in reduced suction and lower overall lift (Figure 5.1a). Rather than a single global LEV burst, due to the stabilising effect of outboard vorticity shedding from the apex, bursting occurs in the outboard regions.

Taken together, the flow visualisations at $k = 0.4$ and $k = 0.05$ demonstrate that increasing sweep fundamentally redistributes both LEV stability and breakdown along the span. Compared to the unswept and moderately swept configurations, the highly swept wing therefore exhibits a qualitatively different LEV breakdown pathway. Instead of instability being initiated primarily by localised interaction between the LEV and tip vortex, breakdown and bursting occur over a broader outboard region and are accompanied by a highly unsteady tip wake. This behaviour represents the most apparent sweep-induced transition in vortex dynamics and provides a contrast with the unswept and moderately swept wing configurations.

6.3 LEV initiation and spanwise variation with sweep

Beyond altering LEV topology, sweep angle also exerts a strong influence on where along the span the LEV first forms. This behaviour can be examined using LESP, which provides a quantitative indicator of LEV initiation at different spanwise locations.

As shown in Figure 6.6a, for unswept wings, the maximum LESP during the plunging motion typically occurs near the wing root. Inboard sections experience the largest effective angle of attack, owing to weaker downwash effects away from the wing-tip, and therefore reach the critical LESP threshold earliest. As a result, LEV initiation on an unswept wing generally begins near the root and then develops along much of the span over a relatively short time interval.

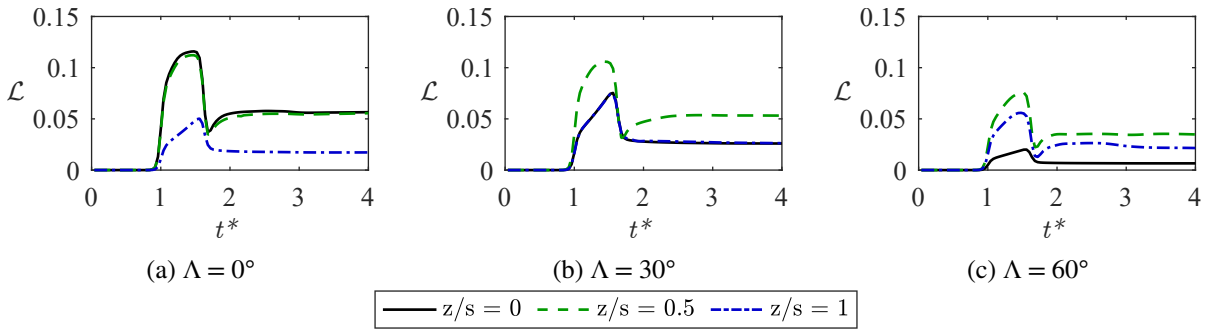

(a) $\Lambda = 0°$ (b) $\Lambda = 30°$ (c) $\Lambda = 60°$

Figure 6.6: Time histories of LESP magnitude for the aspect ratio 3, NACA 0008 wing geometries, at reduced frequency $k = 0.4$ along the root, mid-span and tip planes of the wing.

In contrast, sweep fundamentally redistributes the spanwise suction loading. As shown in Figure 6.6, the peak LESP shifts away from the wing root and is concentrated at the mid-span for

both swept wings. Sweep reduces the effective normal component of the free-stream flow to the leading edge, suppressing leading-edge suction across the wing and promoting spanwise flow, Towards the tip, vorticity is shed more readily due to strong tip effects. Together, these effects suppress sustained suction at both the root and tip, such that the mid-span region becomes the dominant site of suction accumulation for swept wings. Hence the critical LESP threshold is reached earliest at the mid-span, leading to LEV initiation away from the wing root.

Aspect ratio influences how these spanwise initiation patterns manifest. On lower aspect ratio swept wings, the mid-span lies physically closer to the tip, and LEV initiation is therefore influenced by tip effects. On higher aspect ratio wings, the mid-span is more obviously separated from both root and tip effects, hence making the mid-span a distinct location for LEV onset. While these geometric effects are intuitive, they provide useful context for interpreting the sweep trends observed across the different configurations.

The spanwise variation in LEV initiation identified here has important implications for the development of aerodynamic forces and moments on swept wings. However, these consequences cannot be inferred directly from LESP alone and are therefore examined explicitly in Chapter 7 using force and moment partitioning.

6.4 Force response and implications

While the flow visualisations in this chapter reveal pronounced changes in LEV topology with sweep angle, the corresponding influence on the net aerodynamic force is less immediately apparent under highly unsteady conditions at reduced frequency $k = 0.4$. Figure 6.7 presents representative lift coefficient histories for the aspect ratio 3, NACA 0008 wings at reduced frequency $k = 0.4$, corresponding to the Figures 6.1, 6.2 and 6.4 examined throughout this chapter.

At $k = 0.4$, the lift response is strongly influenced by added-mass and kinematic effects associated with the prescribed plunging motion, as previously discussed in Chapter 5. As a result, differences in LEV structure and spanwise flow organisation do not translate directly into clearly separated lift histories. This lack of separation in the global lift response highlights an important limitation of interpreting force coefficients alone when kinematics dominate the lift response.

This apparent disconnect between markedly different vortex dynamics and similar instantaneous lift behaviour motivates the force and moment partitioning analysis presented in Chapter 7, where the vortex-induced contribution is explicitly isolated.

6.5 Concluding remarks on sweep effects

This chapter has examined the influence of sweep angle on LEV dynamics on plunging wings, with particular emphasis on LEV topology, breakdown behaviour, and spanwise initiation. By

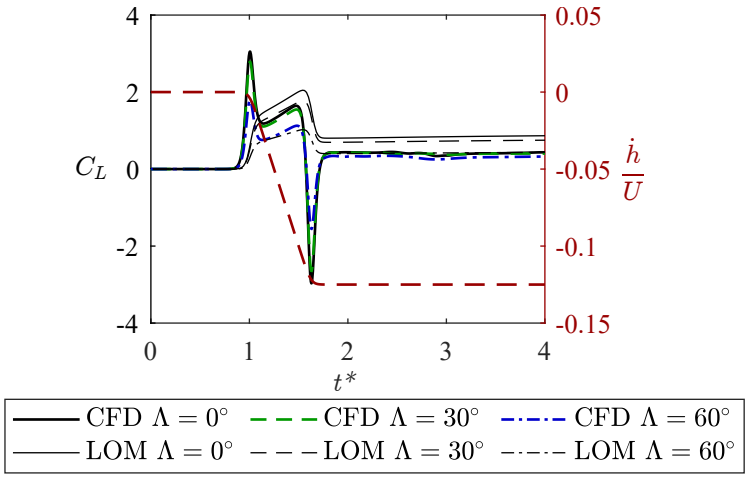

Figure 6.7: Lift coefficient time histories for the aspect ratio 3, NACA 0008 wing geometries, at reduced frequency $k = 0.4$, with CFD results compared against predictions from the C-LAULLT low-order model. The prescribed plunge velocity kinematics are shown on the right axis.

comparing unswept, 30° and 60° swept configurations across a range of reduced frequencies, the role of sweep-induced spanwise flow in shaping unsteady vortex dynamics for wings undergoing unsteady plunge ramp motions has been characterised.

Firstly, the sweep angle was shown to fundamentally alter LEV topology and breakdown pathways. Unswept wings exhibit a predominantly chordwise LEV that remains distinct from the tip vortex, with LEV breakdown typically originating in the outboard region through interaction with the tip-induced flow. Introducing a 30° sweep produces a qualitatively different topology in which separation at the root generates a co-rotating LEV pair, and the primary LEV becomes inclined relative to the leading edge as a result of spanwise vorticity convection. At 60° sweep, strong spanwise transport leads to significant interaction between the LEV and the outboard flow, with LEV breakdown occurring over a broader outboard region and accompanied by a highly unsteady tip wake.

Secondly, sweep was shown to shift the spanwise location of LEV initiation outboard. LESP analysis demonstrated that unswept wings exhibit maximum LESP near the root, whereas swept wings exhibit maximum LESP at the mid-span. This shift arises from the reduction in the effective normal flow component at the leading edge with increasing sweep angle, combined with strong spanwise convection along the leading edge, which limits suction accumulation at both the root and tip. As a result, LEV initiation on swept wings is preferentially associated with the mid-span region rather than the wing root.

Together, these results show that sweep angle acts as a key geometric control parameter that reorganises both the structure of the LEV and the location at which vortex formation first occurs. By introducing strong spanwise transport and reducing the effective normal flow at the leading edge, increasing sweep redistributes suction accumulation and alters the balance between vortex growth, convection, and breakdown across the span.

While the present chapter has focused on flow topology and initiation mechanisms, the implications of these sweep-induced changes for aerodynamic force generation cannot be inferred from global coefficients alone. These consequences are therefore examined explicitly in Chapter 7 using force and moment partitioning, where the relationship between vortex dynamics and unsteady aerodynamic loading is quantified.

7

Vorticity-Induced Lift and Thrust Mechanisms on Swept Wings

> *The whole is more than the sum of its parts.*
>
> **— Aristotle**
> (Philosopher and Polymath)

7.1 Introduction

THE preceding chapters of this thesis established a detailed physical understanding of the vortical structures generated by plunging wings, with particular emphasis on the formation, evolution, and breakdown of the leading-edge vortex (LEV), the influence of wing sweep, and the role of three-dimensional effects associated with finite span and tip vortices. While those analyses focused on identifying and characterising the dominant flow structures, an important question remains: how do these vortical structures translate into aerodynamic force production?

This chapter addresses the above question by applying the force and moment partitioning method (FMPM), originally proposed by Zhang *et al.* [103], to quantify the contributions of individual vortical structures to aerodynamic forces. FMPM provides a framework for decomposing the instantaneous force on a wing into physically interpretable components, allowing the force induced by vorticity in the flow to be examined separately from kinematic and viscous effects. In doing so, the method enables a direct connection to be made between the dominant vortical features examined earlier in the thesis and their associated lift and thrust force contributions.

Although the added-mass and viscous force components can, in principle, be evaluated separately, the present analysis focuses on the contribution of vorticity, in the form of the key three-dimensional vortex structures, to the aerodynamic force response as a function of sweep

angle and reduced frequency. FMPM is therefore used here to interpret how flow topology and spanwise vorticity transport influence lift and thrust, rather than to provide a complete quantitative breakdown of all force components.

Several alternative approaches have been proposed for attributing aerodynamic forces to flow structures, including impulse-based methods [104] and vortex force maps [105]. While these approaches have been applied successfully to a wide range of unsteady flows, their practical implementation often requires additional modelling or interpretive choices, such as the explicit identification of vortex systems, the definition of control volumes, or the specification of regions over which forces are evaluated. FMPM offers a practical alternative, as force contributions are evaluated directly through volume-integral expressions without the need to explicitly define vortex strengths. This simplicity, combined with its applicability to fully three-dimensional, time-dependent flows, has led to its increasingly widespread use in studies of vortex-dominated aerodynamics.

Recent studies have demonstrated the applicability of FMPM to swept wing configurations. Zhu and Breuer [106] applied FMPM to pitching swept wings and showed that, although wing sweep had only a modest influence on the net aerodynamic force, sweep substantially altered the distribution of aerodynamic moments. In particular, they observed that the LEV could contribute negatively to the pitching moment near the wing-tip for highly swept wings, highlighting that changes in vortex topology with sweep can have important consequences for force and moment distribution even when integrated forces are similar. Menon *et al.* [108] further demonstrated that FMPM can distinguish force contributions associated with vortices of different orientations, emphasising the contrasting roles of streamwise and spanwise vortical structures. Related applications to fixed-angle swept wings [109] and delta wings [110] further illustrate the growing use of force-partitioning approaches in vortex-dominated flows.

Despite these advances, the spanwise distribution of vorticity-induced forces on plunging wings has received comparatively little attention. While previous studies have used FMPM to examine moment distributions, the corresponding distributions of lift and thrust force, and their relationship to three-dimensional LEV, tip and wake interactions, have not yet been examined in detail. A key contribution of the present chapter is therefore the explicit quantification of how vorticity-induced lift and thrust vary along the span of varying swept wing geometries, and how these distributions change with reduced frequency and sweep angle.

The force-partitioning analysis is restricted to wings of aspect ratio 3 with a NACA 0008 aerofoil section. This configuration is chosen deliberately. Aspect ratio 3 lies close to the range observed in many natural flyers and bio-inspired micro air vehicles, where unsteady vortex dynamics play a dominant role in force generation. Experimental studies by Han and Breitsamter [47] have also shown that aspect ratios of approximately three can yield strong lift enhancement under unsteady conditions. From a fluid-dynamic perspective, this aspect ratio represents a regime in which the LEV, tip vortex, and wake structures interact strongly, making aspect ratio

3 a particularly informative case for force-partitioning analysis. The use of a thin NACA 0008 aerofoil further minimises thickness-driven separation and pressure-drag effects, ensuring that the force contributions identified here are primarily associated with vortex dynamics rather than aerofoil form effects.

The chapter proceeds as follows; Section 7.2 outlines the theoretical framework of FMPM and defines the force coefficients used in the analysis. Section 7.3 presents the partitioned force results. The influence potential fields are discussed first, with lift contributions of the LEV and tip vortex are examined qualitatively by the instantaneous force-density visualisations, and quantitatively by spanwise force distributions. The same sequence of analysis is then applied to the thrust force to assess the spanwise distribution of thrust and drag-inducing vortical contributions. Finally, Section 7.4 summarises the key findings and discusses their implications for swept-wing configurations operating in unsteady flow.

7.2 Theoretical framework of FMPM

FMPM provides a framework for decomposing the instantaneous aerodynamic force acting on a body into physically interpretable components, derived from the incompressible Navier–Stokes equations. In the present study, the FMPM of Menon and Mittal [172, 173] is used to isolate the contribution of vorticity in the flow to the aerodynamic forces acting on plunging wings.

In FMPM, the total force $\mathbf{F}$ acting on the wing may be written as

$$\mathbf{F} = \mathbf{F}_k + \mathbf{F}_\omega + \mathbf{F}_\sigma + \mathbf{F}_\phi + \mathbf{F}_S, \tag{7.1}$$

where $\mathbf{F}_k$ is the kinematic (added-mass) force associated with the prescribed wing motion, $\mathbf{F}_\omega$ is the vorticity-induced force, $\mathbf{F}_\sigma$ represents viscous stresses, and $\mathbf{F}_\phi$ and $\mathbf{F}_S$ account for irrotational and boundary contributions, respectively.

Under the present simulation conditions of finite free-stream velocity, Reynolds number $Re = 2 \times 10^4$, and a wing starting from rest, the irrotational and boundary terms are small compared to the remaining force components. The total aerodynamic force is therefore well approximated by the sum of the kinematic, vorticity-induced, and viscous contributions, with the vorticity-induced term being the primary focus of the analysis presented in this chapter, as discussed in Section 7.1.

The vorticity-induced force component in a given Cartesian direction i is obtained through a volume integral involving an influence potential ϕ^i, not to be confused with the well-known velocity potential. The influence potential is defined as the solution of Laplace's equation,

$$\nabla^2 \phi^i = 0, \text{ with } \mathbf{n} \cdot \nabla \phi^i = \begin{cases} n_i & \text{on } B \\ 0 & \text{on } \Sigma \end{cases} \text{ for } i = 1, 2, 3. \tag{7.2}$$

Here $\mathbf{n}$ is the outward unit normal vector to the wing surface and n_i is the component of $\mathbf{n}$ in the i^{th} force direction. B represents the wing geometry and Σ is the chosen outer domain boundary for integration of forces. Physically, $\phi^{(i)}$ defines a spatial weighting that relates the location of vorticity in the flow to its force contribution in direction i. By integrating over volumes of interest V the total force due to vorticity F_i^{ω} within the specified volume V_f can be determined as

$$F_i^{\omega} = -2 \int_{V_f} Q\phi^i \, dV \text{ for } i = 1,2,3, \tag{7.3}$$

where $Q = \frac{1}{2}(|\boldsymbol{\omega}|^2 - |\mathbf{S}|^2)$ is the Q-criterion. In the following sections, ϕ^y and ϕ^{-x} are used to evaluate vorticity-induced lift and thrust force contributions, respectively.

7.2.1 Force coefficients

The vorticity-induced force contributions are reported in non-dimensional form using the following coefficients:

$$C_L^{\omega} = \frac{F_y^{\omega}}{0.5\rho {U_{\infty}}^2 S}, \tag{7.4a}$$

$$C_T^{\omega} = \frac{F_{-x}^{\omega}}{0.5\rho {U_{\infty}}^2 S}, \tag{7.4b}$$

where S is the wing planform area and U_{∞} is the free-stream velocity. The thrust coefficient C_T is defined as positive in the $-x$ direction (see Figure 2.4), such that negative values correspond to drag.

7.3 Vorticity-induced force contributions

7.3.1 Vorticity-induced lift

The objective of this section is to quantify the contribution of the key vortical structures, primarily the LEV and tip vortex, identified in previous chapters to aerodynamic lift. This is achieved by considering the lift influence potential, which defines the geometric sensitivity of the wing to vorticity-induced forces, then examining instantaneous lift density fields evaluated at representative convective times where coherent vortical structures are present. The resulting force contributions are then quantified through spanwise distributions of vorticity-induced lift, providing insights into how this distribution is modified by sweep. This spanwise redistribution is particularly relevant for assessing load redistribution and gust sensitivity in MAV applications.

Figure 7.1 shows the lift influence potential ϕ^y evaluated on root, mid-span, and tip planes for the unswept, 30° and 60° swept wings. As the influence potential depends only on the

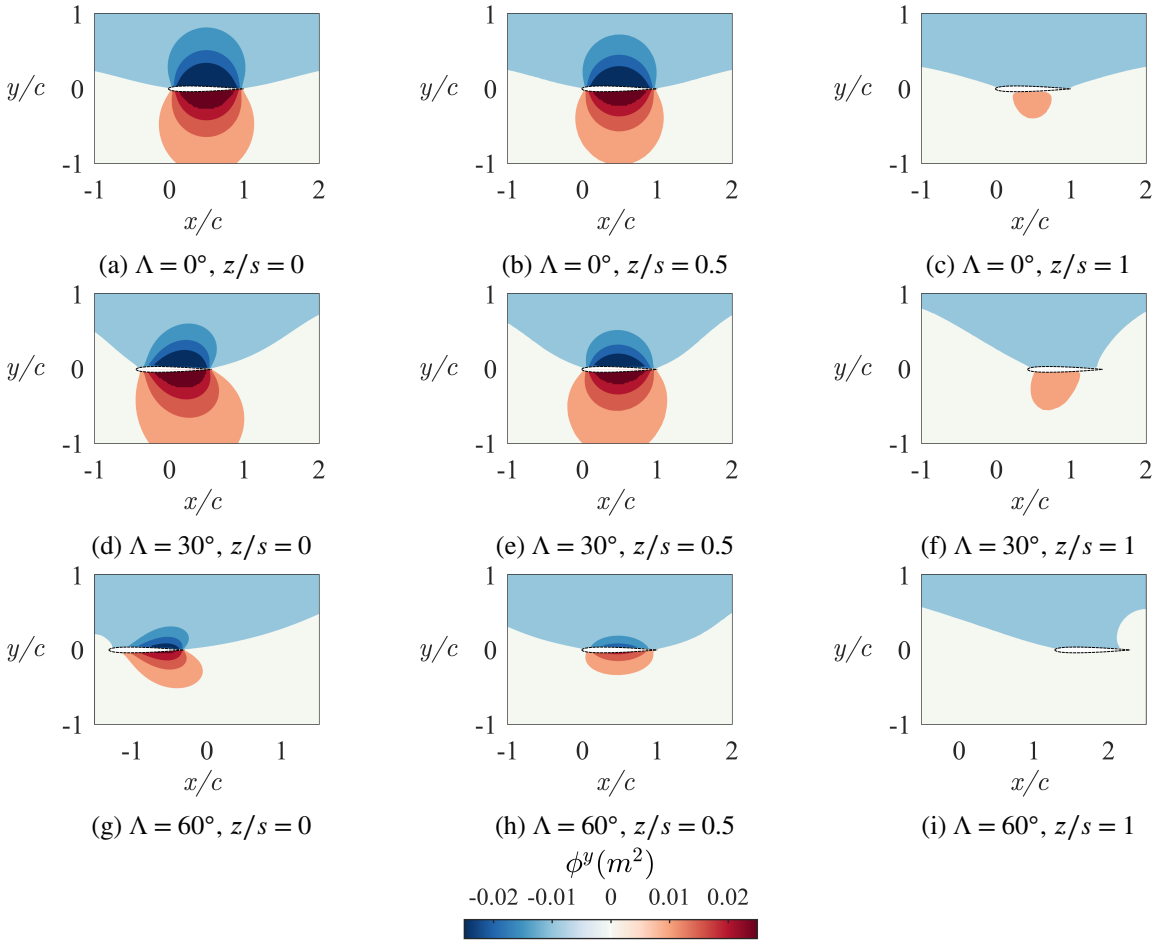

Figure 7.1: Lift influence potentials (ϕ^y) for the aspect ratio 3, NACA 0008 wing geometries along the root, mid-span and tip planes, with the aerofoil boundary indicated by the dashed lines.

instantaneous wing geometry, ϕ^y provides a purely geometric measure of how vorticity at a given spatial location contributes to lift, independent of the flow field.

For all wing configurations, regions of strongly negative ϕ^y are concentrated above the wing surface, centred approximately about the mid-chord region, while regions of positive ϕ^y occur symmetrically below the wing. The magnitude of the negative region is generally higher and occupies a greater area than the corresponding positive region, indicating that vorticity located above the wing has a stronger geometric sensitivity for lift production than vorticity located below the wing. This behaviour is consistent across all spanwise locations.

As the sweep angle is increased, the overall structure of the influence potential remains similar, but its spatial extent relative to the wing changes. In particular, the region of peak negative ϕ^y becomes progressively more confined in the chordwise direction towards the trailing edge and spanwise direction towards the root as sweep increases. While the peak magnitude of ϕ^y does not change substantially, the area over which vorticity can contribute effectively to lift is reduced. As a result, vortical structures must reside closer to the wing surface and further inboard to produce the same lift contribution on more highly swept wings.

From the perspective of swept-wing micro air vehicles, this geometric effect has important implications for operation in disturbed or unsteady environments. As sweep increases, the region over which vorticity can contribute effectively to lift becomes more confined, reducing the sensitivity of lift generation to the precise spatial position of the LEV. While this limits the maximum lift that can be generated for a given vortical structure, sweep also acts to moderate lift fluctuations arising from variations in LEV position or strength. As a result, highly swept wings may exhibit more robust and stable lift behaviour in the presence of atmospheric disturbances, even though their peak lift performance is reduced relative to unswept configurations.

The interaction between this geometric effect and the key vortical flow structures is illustrated in Figure 7.2, which shows isosurfaces of Q-criterion coloured by the lift density distribution $-2Q\phi^y$ for each wing at $k = 0.05$ and $k = 0.4$ at representative convective times where a coherent LEV exists over the wing. These visualisations focus the analysis on coherent, rotation-dominated vortical structures by isolating regions of high Q, rather than distributed regions of weak or shear-dominated vorticity.

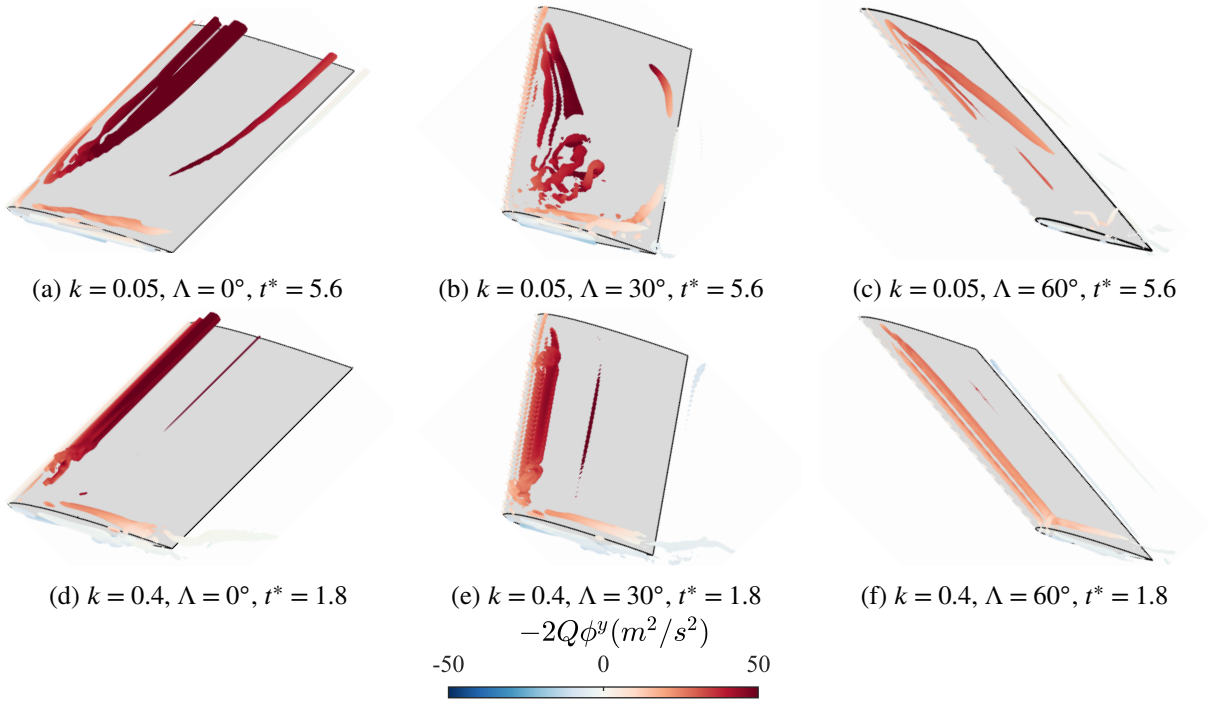

(a) $k = 0.05$, $\Lambda = 0°$, $t^* = 5.6$ (b) $k = 0.05$, $\Lambda = 30°$, $t^* = 5.6$ (c) $k = 0.05$, $\Lambda = 60°$, $t^* = 5.6$

(d) $k = 0.4$, $\Lambda = 0°$, $t^* = 1.8$ (e) $k = 0.4$, $\Lambda = 30°$, $t^* = 1.8$ (f) $k = 0.4$, $\Lambda = 60°$, $t^* = 1.8$

Figure 7.2: Isosurfaces of $Q = 1000$ coloured by lift density distribution ($-2Q\phi^y$) for the aspect ratio 3, NACA 0008 wing geometries, at reduced frequencies $k = 0.05$ and 0.4 at representative convective times where a coherent LEV exists over the wing.

Across all configurations, the LEV is the dominant contributor to lift enhancement. When the LEV resides above the wing surface, it coincides with regions of negative ϕ^y, resulting in positive lift density, as shown by the red colours in Figure 7.2. This behaviour is most clearly observed at lower sweep angles in Figures 7.2a and 7.2d, where the LEV resides within a broader spanwise region of strongly negative ϕ^y, leading to a larger vorticity-induced lift contribution.

Wing sweep modifies the instantaneous lift distribution primarily by altering where the

LEV and associated shear-layer structures reside relative to the influence potential field. At low reduced frequency ($k = 0.05$), increasing sweep confines the LEV more strongly to the inboard region, where the influence potential has a high magnitude, while outboard regions experience a reduced geometric sensitivity to lift production. At higher reduced frequency ($k = 0.4$), the vortical structures have a more consistent structure across sweep angles compared with $k = 0.05$, due to the strong reduced-frequency effects. As a result, instantaneous lift production becomes increasingly concentrated towards the root with increasing sweep.

In contrast to classical aerodynamic theory, where the tip vortex is associated with induced drag and reduced lift effectiveness, the tip vortex does not have a strong detrimental lift contribution in Figure 7.2. This behaviour is influenced by the square wing-tip geometry employed in the present study, which differs from the tapered or rounded tips characteristic of many natural flyers and alters the detailed structure of the tip vortex in unsteady flow. In the present cases, the tip vortex lift contribution is generally weak and often near-neutral, with weakly positive lift density observed in some configurations. This reflects the fact that, although the tip vortex is a strong rotational structure, it primarily resides in regions where the influence potential is relatively low magnitude, thereby limiting its overall contribution to lift.

Similarly, in Figure 7.2b, wake and shear-layer structures shed during LEV breakdown do not produce substantial negative lift contributions in the cases shown. The lift density field shows predominantly positive values of $-2Q\phi^y$, with only small regions of near-zero contribution associated with downstream vortical structures. This indicates that the dominant vortical mechanisms contribute positively to lift at the convective times considered in Figure 7.2.

For MAV applications, these results suggest that sweep does not fundamentally change the lift-enhancing role of the LEV, but it does make lift production more dependent on maintaining a coherent LEV in a smaller, more localised region of the wing.

The effect of the vortex structures on lift is quantified in Figure 7.3, which shows the spanwise distribution of the vorticity-induced lift coefficient C_L^{ω} at the same convective times as shown in Figure 7.2.

At low reduced frequency ($k = 0.05$) in Figure 7.3a, the unswept wing exhibits substantial lift near the root compared to the swept wings, due to the straight geometry without a sharp wing apex, hence the lack of a resulting inboard shear layer. Pronounced local variations are observed along the span, including a peak near $z/c = 1$ associated with the outboard shear layer and a further peak near the tip ($z/c = 1.5$) associated with the tip vortex. Despite this variability, the lift remains predominantly positive along the span.

For both swept wings in Figure 7.3a, the lift distribution differs markedly. At $\Lambda = 30°$, lift increases outboard from the root before remaining elevated over a significant portion of the outer wing. Between these spanwise locations, near $z/c = 0.8$, the lower lift produced corresponds to the region between the inboard coherent LEV and outboard unsteady structures observed in Figure 7.2b. A distinct outboard lift peak is observed for the 30° swept wing near $z/c = 1.1$, associated

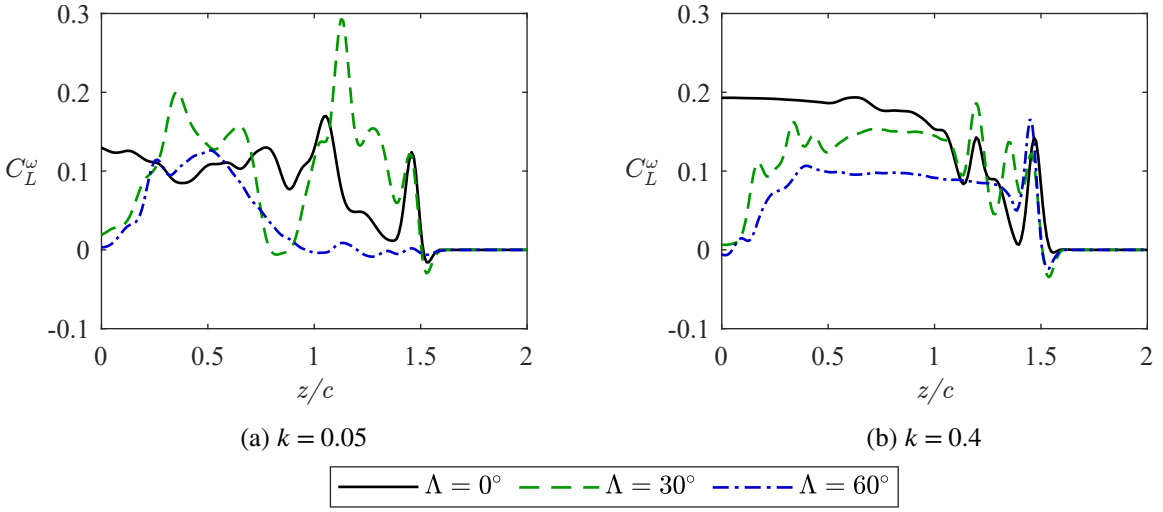

Figure 7.3: Spanwise vorticity-induced lift distributions for the aspect ratio 3, NACA 0008 wing geometries at the convective times shown in Figure 7.2.

with unsteady shedding structures generated during LEV breakdown, such as hairpin-type vortices (see Figure 7.2b). At $\Lambda = 60°$, the lift distribution becomes more strongly inboard-biased, with lift contributions reducing towards the tip as the lift influence potential approaches zero over much of the outboard wing.

At a high reduced frequency ($k = 0.4$) in Figure 7.3b, the unswept wing maintains a relatively stable lift distribution over the inboard two-thirds of the span. Over the swept wings, lift increases from the root to approximately $z/c = 0.4$, after which lift remains relatively stable before gradually decreasing towards the tip. This trend is consistent with the shape of the influence potential, which weights lift production more strongly inboard as sweep increases. Lift production is highly unsteady outboard of $z/c = 1$ for all wings, due to the outboard LEV leg.

Overall, the results indicate that increasing sweep leads to both a redistribution and an overall reduction of vorticity-induced lift. Across all cases, lift production becomes increasingly concentrated towards the inboard region as sweep increases, reflecting the progressive attenuation of the lift influence potential over the outer span. While reduced frequency modifies the detailed structure and unsteadiness of the outboard flow, the qualitative effect of sweep on the spanwise lift distribution remains consistent. Unswept and moderately swept wings sustain significant outboard lift contributions accompanied by greater unsteadiness, whereas the highly swept wing exhibits lower overall lift which is more confined towards the inboard region. At $k = 0.4$, the relationship between increasing sweep angle and reducing vorticity-induced lift is much clearer as the LEV structures produced are more qualitatively similar between sweep angles at the times presented in Figure 7.2.

For increasing wing sweep angle, this redistribution of lift towards the inboard region, together with the less unsteady outboard contribution, highlights a design trade-off for MAV applications. With a 60° sweep angle, the extent of strongly force-producing vortical structures over the

outer span tend to be reduced, which can moderate outboard load fluctuations, but this also confines effective lift production to a more localised inboard region. In contrast, unswept and moderately swept wings can sustain significant outboard lift-producing structures, but these may be accompanied by stronger unsteady interactions, particularly at low reduced frequency for $\Lambda = 30°$ (see Figure 7.3a). This has implications for load variability and stability in disturbed atmospheric conditions.

In summary, the lift influence potential defines a geometric sensitivity that is progressively confined inboard and closer to the wing surface with increasing sweep, while the instantaneous lift density reveals that the LEV remains the primary lift-enhancing structure across all configurations. The combined effect is a redistribution and partial reduction of vorticity-induced lift with increasing sweep, providing a link between the vortex dynamics established earlier in the thesis and their aerodynamic force consequences.

7.3.2 Vorticity-induced thrust

The objective of this section is to examine how the vortical structures identified in earlier chapters contribute to thrust, and how these contributions are modified by wing sweep and reduced frequency. In contrast to lift, thrust generation arises from a balance between thrust-producing and drag-producing vortical mechanisms. As a result, even when the net force remains drag, the spatial distribution of vorticity-induced thrust provides important insight into how unsteady vortex dynamics may be exploited for propulsion in bio-inspired flyers.

In contrast to lift generation, which arises robustly from the formation and persistence of the LEV, the production of thrust in biological and bio-inspired flyers presents a more constrained aerodynamic problem. Biological flyers do not possess a dedicated propulsive system, and thrust must instead be generated through unsteady aerodynamic mechanisms that are intrinsically coupled to lift production. As a result, thrust generation depends sensitively on the spatial arrangement, orientation, and evolution of vortical structures formed during flapping or plunging motion, requiring a more specific organisation of the flow field than is necessary for lift generation.

Understanding how these vortical structures contribute to thrust is therefore of particular importance for bio-inspired micro air vehicles, where propulsion must be achieved without reliance on conventional engines or propellers. Even when the net force remains drag, the presence, magnitude, and redistribution of thrust-producing vortical contributions provide insight into how unsteady kinematics and wing planform geometry influence propulsive effectiveness. The force-partitioning analysis presented here enables these contributions to be identified and quantified directly, revealing how thrust-producing and drag-producing mechanisms coexist and compete within the same unsteady flow field.

The discussion proceeds by first examining the thrust influence potential ϕ^{-x} to establish the geometric effect of sweep on thrust production. Instantaneous thrust density distributions are then used to identify the vortical structures responsible for thrust and drag contributions, followed

by spanwise distributions of the vorticity-induced thrust coefficient to quantify how these effects vary across the wing.

Figure 7.4 shows the thrust influence potential ϕ^{-x} evaluated on the root, mid-span, and tip planes for the unswept, 30° and 60° swept wings considered. As with the lift influence potential, ϕ^{-x} depends only on the instantaneous wing geometry and defines how vorticity at a given spatial location contributes to thrust.

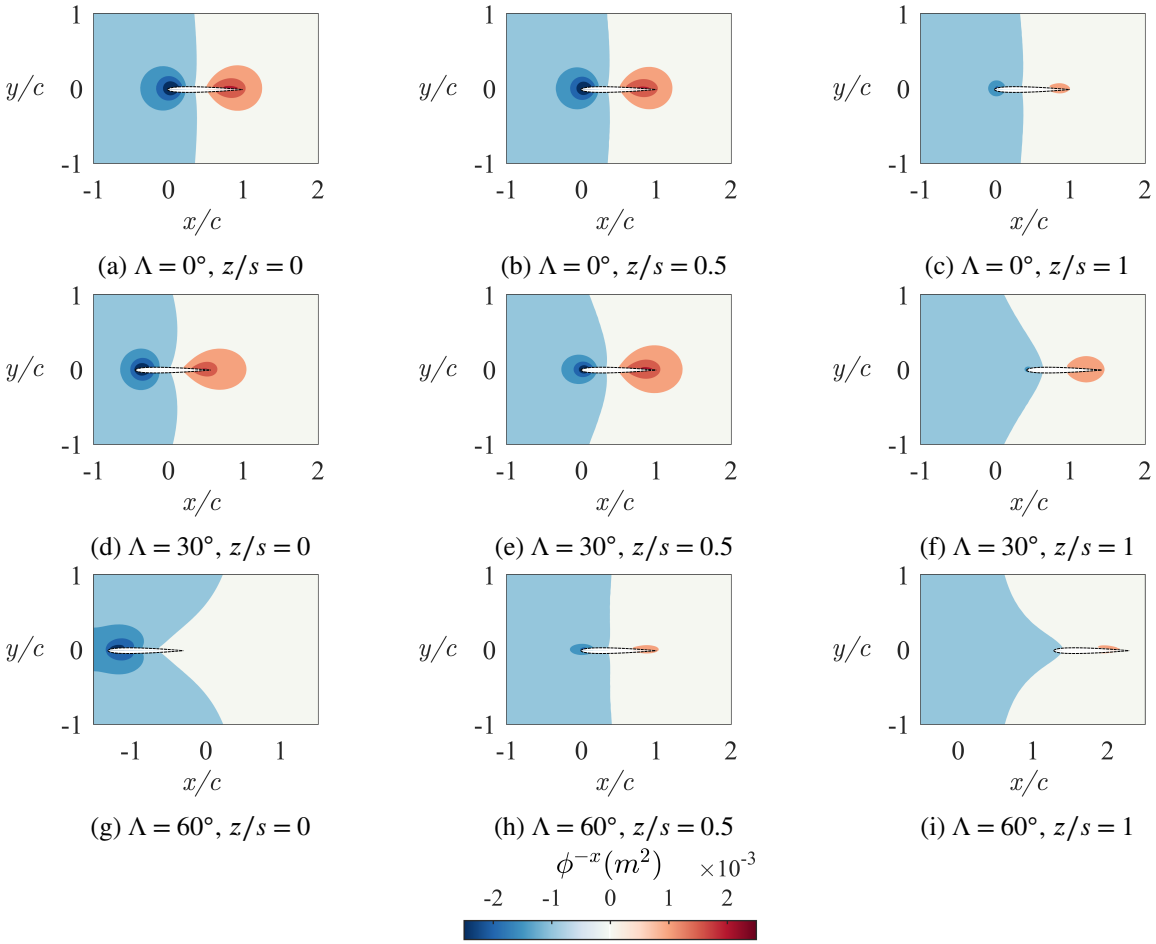

Figure 7.4: Thrust influence potentials (ϕ^{-x}) for the aspect ratio 3, NACA 0008 wing geometries along the root, mid-span and tip planes, with the aerofoil boundary indicated by the dashed lines.

For all configurations, the thrust influence potential exhibits a pronounced asymmetry in the streamwise direction. Regions of negative ϕ^{-x} are generally concentrated upstream of the mid-chord, with the strongest values located near the leading-edge region. Regions of positive ϕ^{-x}, associated with drag-producing contributions, are generally concentrated downstream of the mid-chord and are strongest near the trailing edge. This general structure is observed across most spanwise locations, except for the root plane for the highly swept wing in Figure 7.4g, where the geometry introduces additional distortion of the field.

As sweep increases, the thrust influence potential becomes increasingly asymmetric. The thrust-producing region near the leading edge becomes weaker and more confined with increasing

sweep angle, particularly in the spanwise direction, while its alignment relative to the wing surface changes. For the moderately swept wing, the drag-producing region extends further downstream into the wake. However for the highly swept wing, the downstream drag-producing region is reduced in extent, reflecting the strong geometric reorientation of the wing relative to the freestream.

These differences indicate that sweep does not simply reduce thrust-producing regions uniformly. Instead, increasing sweep redistributes the thrust influence potential, shifting regions of significant thrust-producing capability progressively inboard towards the root and closer to the leading edge. As a result, vortical structures must remain both near the leading edge and inboard to positively contribute to thrust on more highly swept wings.

From a bio-inspired MAV perspective, this geometric effect highlights the sensitivity of unsteady thrust generation to wing planform design. While increasing sweep modifies the spatial constraints on thrust production by confining thrust-favourable regions closer to the root and leading edge, sweep does not preclude thrust-generating contributions. Rather, sweep alters where along the wing such contributions can arise, with important implications for how unsteady kinematics and vortex placement may be exploited to achieve propulsion without dedicated propulsive systems.

The interaction between the thrust influence potential and the flow field is illustrated in Figure 7.5. Isosurfaces of the Q-criterion are shown, coloured by the thrust density distribution $-2Q\phi^{-x}$ for each wing at $k = 0.05$ and $k = 0.4$ at the same convective times as those used in the lift analysis. These visualisations allow the thrust and drag-producing contributions of specific vortical structures to be identified directly.

Across all configurations in Figure 7.5, the thrust density distribution contains both positive, thrust-producing regions and negative, drag-producing regions, in contrast to the predominantly positive lift density observed previously in Figure 7.2. For the unswept wing at low reduced frequency ($k = 0.05$) in Figure 7.5a, the LEV exhibits a neutral contribution near the root, while thrust-producing regions develop progressively towards the outer span. The tip vortex produces a weak drag contribution overall. Away from these localised features, the thrust density remains predominantly positive over much of the outer wing, indicating that unsteady vortical structures can contribute meaningfully to thrust even in the absence of sweep.

In contrast, for the 30° swept wing at $k = 0.05$ in Figure 7.5b, the inboard coherent LEV is predominantly thrust-producing, while the outboard unsteady structures generated during LEV breakdown and the tip vortex contribute strongly to drag. This configuration, therefore, exhibits the strongest coexistence of thrust and drag-producing mechanisms within the same flow field.

For the 60° swept wing at $k = 0.05$ in Figure 7.5c, the inboard LEV contributes only weakly to thrust and transitions towards weakly drag-producing behaviour further outboard. This reflects both the increased inclination of the LEV relative to the leading edge and the altered shape of the thrust influence potential, which reduces the overlap between the LEV and thrust-favourable re-

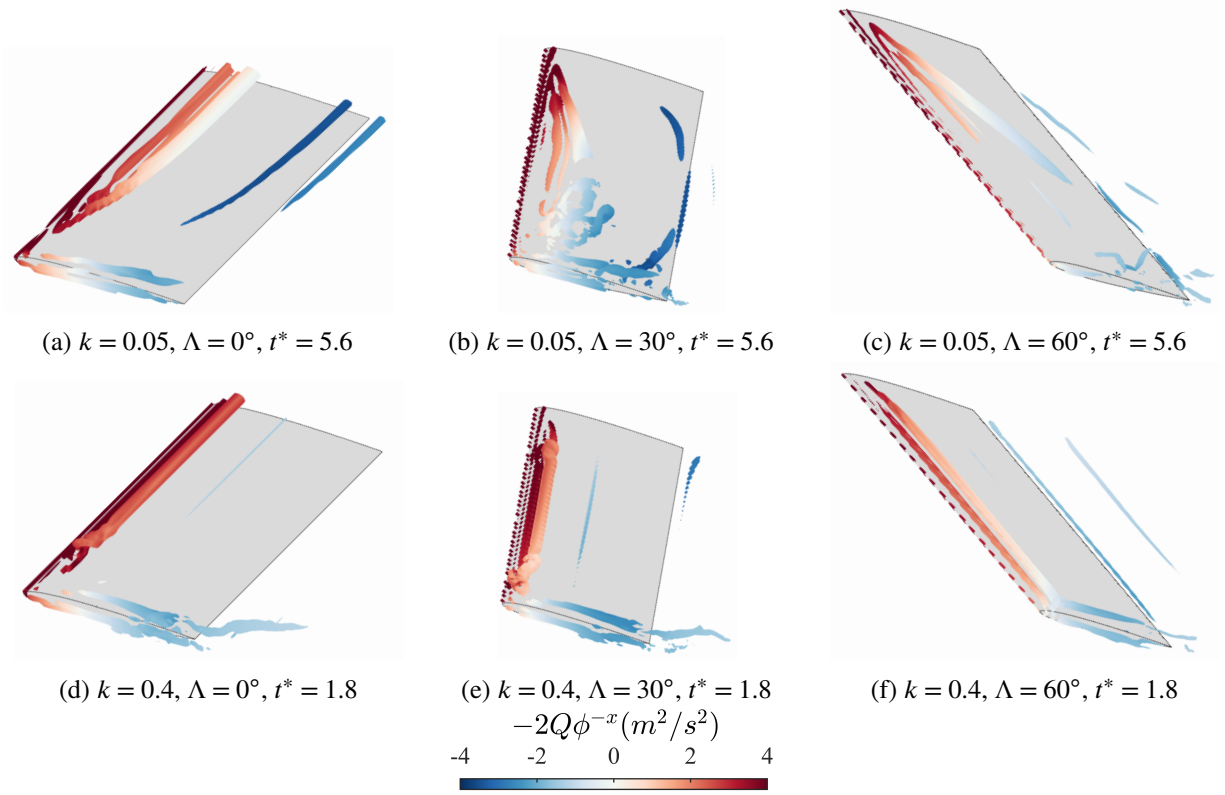

(a) $k = 0.05$, $\Lambda = 0°$, $t^* = 5.6$ (b) $k = 0.05$, $\Lambda = 30°$, $t^* = 5.6$ (c) $k = 0.05$, $\Lambda = 60°$, $t^* = 5.6$

(d) $k = 0.4$, $\Lambda = 0°$, $t^* = 1.8$ (e) $k = 0.4$, $\Lambda = 30°$, $t^* = 1.8$ (f) $k = 0.4$, $\Lambda = 60°$, $t^* = 1.8$

Figure 7.5: Isosurfaces of $Q = 1000$ coloured by thrust density distribution ($-2Q\phi^{-x}$) for the aspect ratio 3, NACA 0008 wing geometries, at reduced frequencies $k = 0.05$ and 0.4 at representative convective times where a coherent LEV exists over the wing.

gions. As a result, thrust production becomes weaker and more sensitive to the precise positioning of the LEV for the 60° swept wing.

At higher reduced frequency ($k = 0.4$), the thrust density fields exhibit stronger spatial separation between thrust and drag-producing regions. The LEV over the unswept wing in Figure 7.5d exhibits sustained thrust-producing contributions associated with the LEV across the majority of the span, while strong drag-producing regions are associated with the tip vortex and downstream wake structures. For both swept wings in Figures 7.5e and 7.5f, thrust-producing contributions are increasingly confined inboard, while drag-producing contributions are associated with the tip vortex and its wake, particularly for the moderately swept case.

The results shown in Figure 7.5 highlight that thrust generation via unsteady vortical structures is inherently intermittent and sensitive to vortex position. While the LEV can contribute positively to thrust, this contribution depends critically on its residence within the negative region of the thrust influence potential identified in Figure 7.4.

The cumulative effect of the vorticity-induced thrust force is quantified in Figure 7.6, which shows the spanwise distribution of the vorticity-induced thrust coefficient C_T^{ω} at the same convective times shown in Figure 7.5.

At low reduced frequency ($k = 0.05$) in Figure 7.6a, the unswept wing exhibits weakly drag-producing contributions near the root, followed by increasing thrust contributions towards the

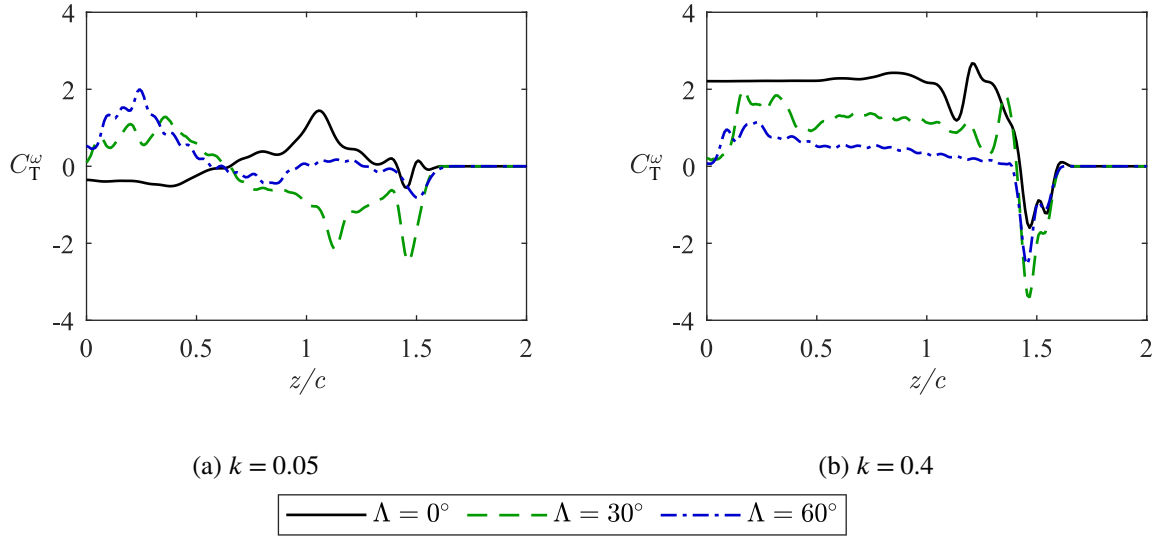

(a) $k = 0.05$ (b) $k = 0.4$

Figure 7.6: Spanwise vorticity-induced thrust distributions for the aspect ratio 3, NACA 0008 wing geometries at the convective times shown in Figure 7.5.

outer span. A pronounced thrust peak near $z/c = 1$ is associated with the outboard shear layer, while the tip vortex produces a weak drag contribution at $z/c = 1.5$. Despite this localised drag contribution, thrust remains positive over much of the outboard half of the span, indicating that unsteady shear-layer dynamics dominate the thrust response in this configuration.

Introducing sweep fundamentally reorganises the spanwise distribution of thrust and drag-producing contributions. For the 30° swept wing at $k = 0.05$, thrust-producing contributions persist over the inboard portion of the span; however, strong drag-producing peaks emerge further outboard.due to both unsteady shedding during LEV breakdown and the tip vortex. These are associated with unsteady shedding during LEV breakdown and with the tip vortex, leading to the largest magnitudes of both thrust- and drag-producing contributions among the configurations considered. This reflects the strong and spatially distributed unsteady vortex activity induced by moderate sweep.

For the 60° swept wing at $k = 0.05$, thrust production becomes confined close to the root, with the majority of the outer span contributing only weakly to drag. The overall magnitude of the thrust coefficient is substantially reduced compared to the other wing configurations, consistent with the low magnitude of the thrust influence potential observed in Figure 7.4i. This indicates that, at high sweep, unsteady thrust generation is increasingly limited to the root region, with diminished effectiveness over the outer span.

At a higher reduced frequency ($k = 0.4$) in Figure 7.6b, the differences between wing sweep angle become more systematic and there is a clear reduced frequency effect. The unswept wing exhibits consistent thrust-producing contributions over most of the span up to $z/c \approx 1$, beyond which the LEV leg causes fluctuations in the thrust produced. At $z/c = 1.5$, there is significant drag associated with the tip vortex. Over both swept wings, thrust increases outboard from the

root due to the attached inboard shear layer. For the moderately swept wing, thrust decreases steadily towards the tip but remains positive over much of the span before the onset of strong drag near the tip vortex. For the highly swept wing, thrust is significantly weaker and approaches zero by $z/c \approx 1$, with minimal thrust contribution from the outboard LEV.

Compared to $k = 0.05$, a higher reduced frequency leads to more persistent thrust-producing regions on the unswept wing. With increasing sweep, thrust production at $k = 0.4$ is progressively suppressed in both magnitude and spanwise extent, whereas at $k = 0.05$ thrust is primarily redistributed towards the root rather than uniformly reduced.

In summary, the thrust influence potential defines a strongly asymmetric geometric field in which thrust and drag-producing regions coexist. The instantaneous thrust density distribution reveals that the LEV can act as a thrust-producing structure under favourable conditions, dependent on the location of vortex structures within the thrust influence potential, while wake and tip vortex structures predominantly contribute to drag. Increasing sweep reshapes and weakens the magnitude of thrust-producing regions in the thrust influence potential, confining the regions inboard, while also moderating the magnitude of thrust fluctuations. These results highlight the fundamental challenge of thrust generation in bio-inspired flyers and underscore the importance of precise control of vortex position and evolution in achieving propulsion without dedicated propulsive devices.

7.4 Conclusions

This chapter applied FMPM to quantify how the vortical structures identified in earlier chapters contribute to aerodynamic force production on plunging wings. By isolating vorticity-induced force components, the analysis provides a direct and quantitative link between three-dimensional vortex dynamics and the resulting lift and thrust forces. This enables the aerodynamic consequences of wing sweep and reduced frequency to be interpreted in terms of flow topology rather than integrated force metrics alone.

The results demonstrate that the LEV is the dominant contributor to vorticity-induced lift across all configurations considered. While wing sweep does not eliminate the lift-enhancing role of the LEV, it modifies the geometric sensitivity of the wing to vorticity-induced lift by progressively confining the region over which lift can be generated effectively. As sweep increases, the lift influence potential becomes increasingly attenuated over the outboard regions of the wing, reducing the contribution in these areas to the total lift. This leads to a redistribution of lift towards the root and closer to the wing surface, which is accompanied by a reduction in overall lift magnitude. Crucially, across all configurations considered, the LEV contributes positively to the vorticity-induced lift, despite substantial changes in its spatial structure and extent with increasing sweep.

In contrast, vorticity-induced thrust was found to arise from a more delicate balance between

thrust and drag-producing vortical contributions that coexist within the same flow field. Unlike lift, thrust generation is highly sensitive to the spatial position, orientation, and evolution of vortical structures relative to the thrust influence potential. Moderate sweep angles can support thrust-producing contributions associated with an inboard coherent LEV. Tip vortex and wake structures predominantly contribute to drag across all sweep angles. At higher sweep angles, thrust-producing regions become increasingly confined near the root and leading edge, resulting in a reduction in overall thrust effectiveness and a stronger dependence on precise vortex placement and coherence.

A key outcome of this analysis is therefore the contrast between the robustness of lift generation and the sensitivity of thrust generation. Lift remains predominantly positive and relatively insensitive to moderate variations in vortex position, with changes in flow structure primarily redistributing lift rather than reversing its sign. Thrust, by contrast, exhibits strong cancellation and intermittency due to the close spatial proximity of thrust and drag-producing regions, making thrust particularly susceptible to vortex convection, breakdown, and shedding. Wing sweep accentuates this distinction by reducing the spatial extent of both lift and thrust-producing regions, thereby moderating force fluctuations while simultaneously limiting peak aerodynamic performance.

From the perspective of bio-inspired MAVs, these findings have important design implications. Unlike conventional aircraft, biological flyers do not possess dedicated propulsion systems and must instead rely on unsteady aerodynamic mechanisms to generate both lift and thrust. The results presented here suggest that swept wing configurations may favour more predictable and robust force generation in the presence of atmospheric disturbances by confining force-producing regions to more insensitive inboard locations. Conversely, unswept wings offer greater potential for unsteady thrust generation through the exploitation of outboard vortex dynamics, but at the cost of increased sensitivity to unsteady flow interactions and load variability. This trade-off between robustness and propulsive effectiveness is likely to be central to the design of bio-inspired flying vehicles operating in gusty, low-Reynolds-number environments.

Overall, the force-partitioning analysis demonstrates that understanding not only which vortical structures form, but also where and how they contribute to aerodynamic forces, is essential for interpreting and designing bio-inspired MAVs. By explicitly linking vortex dynamics to lift and thrust production, this chapter provides a quantitative framework for assessing the aerodynamic consequences of wing sweep in unsteady, three-dimensional flows.

8

Conclusions and Future Work

> *The greatest adventure is what lies ahead.*
>
> **— J.R.R. Tolkien**
> (Writer and Philologist)

This chapter concludes the thesis by answering the research questions proposed in Section 1.3 and synthesising the key findings of the work. Section 8.1 summarises the principal contributions of each chapter and the overarching physical insights obtained, while Section 8.2 outlines potential directions for future research motivated by the results and limitations identified throughout the study.

8.1 Summary and key contributions

This thesis has investigated the unsteady aerodynamics of finite wings undergoing plunge ramp motions at Reynolds number $Re = 2 \times 10^4$, with particular emphasis on the influence of wing sweep on leading-edge vortex (LEV) formation, stability, breakdown and aerodynamic force production. A combination of low-order modelling (LOM), high-fidelity numerical simulation, and the force and moment partitioning method (FMPM) has been used to build a coherent physical picture of swept-wing unsteady aerodynamics, with relevance to micro air vehicle (MAV) design.

Chapter 3 presented a first-order extension of the large-amplitude unsteady lifting line theory (LAULLT) framework of Bird *et al.* [102] to account for wing sweep, based on the unsteady lifting-line formulation of Guermond and Sellier [98]. This resulted in the corrected-LAULLT (C-LAULLT) model, incorporating a cosine-based sweep correction that captures the leading-order reduction in lift with increasing sweep angle. The model performs well for high-aspect-ratio wings at low to moderate reduced frequencies, but does not reproduce the impulsive added-mass lift peaks observed at higher reduced frequencies ($k \geq 0.2$), reflecting the limitations of the uniform outer-solution downwash assumption inherent to lifting-line theory.

Crucially, Chapter 3 also verified the applicability of a variable leading-edge suction parameter (LESP) formulation [164] to finite and swept wings by extending the two-dimensional LESP concept to three dimensions by applying the method on spanwise planes. The results demonstrated that LESP evolution and critical values are not invariant under changes in wing planform geometry, with three-dimensional effects modifying both LESP magnitude and the timing of LEV initiation. This verification established LESP as a physically meaningful indicator of LEV onset for finite wings by comparison to flow field visualisations from high fidelity IDDES simulations.

Chapter 4 examined LEV breakdown modes over finite wings, characterising the simulated flow fields in terms of two established breakdown modes: burst-type and spiral-type breakdown. At low reduced frequency, LEV breakdown occurs via abrupt, burst-type events associated with excessive vortex growth and loss of coherence, whereas at higher reduced frequency, progressive spiral-type breakdown emerges due to three-dimensional instabilities and spanwise transport. These findings clarified the physical origins of LEV coherence loss and provided a framework for interpreting breakdown behaviour across different wing planforms.

Chapter 5 then investigated how reduced frequency influences the development and timing of LEV dynamics within this breakdown framework. Increasing reduced frequency was shown to strengthen LEV formation and advance the onset of vortex initiation, while also shifting the breakdown behaviour towards spiral-type modes previously identified in Chapter 4. Rather than introducing new breakdown mechanisms, these results demonstrated how reduced frequency acts as a key control parameter that modulates the strength, onset, and stability of the LEV.

Chapter 6 isolated the effects of wing sweep, demonstrating that sweep fundamentally alters LEV dynamics through spanwise vorticity transport rather than simple geometric scaling. Swept wings were shown to develop characteristic co-rotating vortex structures about the wing apex, which promote outboard spanwise convection and modify LEV topology. This geometric effect alters the spatial extent of LEVs, with moderate sweep supporting locally stabilised LEVs and higher sweep associated with reduced overall vortex strength. Moderately swept wings exhibited the greatest sensitivity to aspect ratio, displaying substantial changes in LEV topology and stability as spanwise transport competes with tip-induced effects. Collectively, these results provide a mechanistic interpretation for how sweep modifies LEV structure.

Chapter 7 applied force and moment partitioning [172, 173] to quantify the contributions of the key flow structures, primarily the LEV and tip vortex, to both lift and thrust forces. The vorticity-induced force was shown to depend strongly on wing geometry through the influence field, with sweep reducing both the magnitude and persistence of LEV-induced contributions. While unswept wings achieved higher peak lift and thrust at $k = 0.4$, swept wings exhibited reduced sensitivity to reduced-frequency changes and flow disturbances. This contrast highlights a fundamental trade-off between peak aerodynamic performance and robustness, with implications for MAV design and operation in gust-prone environments.

8.2 Limitations and future work

The findings of this thesis and inherent limitations associated with both the CFD modelling approach and LOMs used motivate several promising directions for future research.

While the present study demonstrates that IDDES captures the dominant unsteady separated flow and vortex dynamics mechanisms governing LEV formation, transport, and breakdown at $Re = 2 \times 10^4$, future work could further investigate the role of laminar–turbulent transition in the near-wall boundary layer. In particular, higher-fidelity approaches such as wall-resolved LES or transition-sensitive hybrid methods may provide additional insight into the detailed onset of separation and shear-layer instability. However, the validation results presented in Chapter 2 indicate that the principal large-scale vortex structures and associated force trends are well resolved within the current framework, supporting the conclusions drawn regarding sweep, reduced frequency, and spanwise vortex transport.

A major theoretical extension would be the development of a practical unsteady lifting-line formulation for swept wings, building on the integral ULLT framework of Guermond and Sellier [98]. Such an approach would be particularly relevant for highly swept, high-aspect-ratio wings, where higher-order geometric effects and spanwise separation cannot be treated as small corrections within a first-order framework. Although challenging, a model of this type would provide a powerful low-order tool applicable to swept and curved wings undergoing arbitrary unsteady motion across a wide range of reduced frequencies.

An additional, particularly novel avenue would be to combine LAULLT or C-LAULLT with a variable LESP-based shedding criterion, enabling LEV initiation to be predicted directly within an unsteady lifting-line framework. Embedding a physically motivated LESP criterion into a ULLT model would represent a significant advance in low-order modelling of unsteady separated flows.

The variable LESP formulation employed in this thesis was used as a diagnostic rather than a predictive model, and the limitations identified in Chapter 3 motivate several directions for future development. In its current form, LESP is derived from inviscid theory and infers leading-edge separation indirectly, without explicitly accounting for viscous boundary-layer development, transition, or separation-bubble dynamics. Nor does LESP account for feedback from an LEV developing from the leading-edge shear layer.

Future work should therefore aim to extend LESP-based approaches to incorporate viscous and fully three-dimensional effects, for example by developing a three-dimensional LESP formulation that explicitly includes spanwise and normal velocity components, coupling LESP to reduced-order boundary-layer models, or allowing the critical LESP threshold to vary with local geometry and sweep angle. Such extensions would move LESP beyond a purely diagnostic indicator towards a more physically complete onset model for unsteady separated flows on finite wings, while retaining its computational efficiency.

The present study focused on pure plunging motion at zero fixed angle of attack. Extending the analysis to combined kinematic modes, including pitch–plunge coupling and rotational motion, would provide greater relevance to biological flight and flapping-wing MAVs.

Building on the focus of the present study on natural LEV stability, future work could explore the use of active and passive flow control strategies to deliberately modify LEV formation, stability, and breakdown behaviour. Techniques such as leading-edge actuation, spanwise blowing or suction, and kinematic modulation offer potential routes to stabilising or destabilising the LEV in a controlled manner, informed by the breakdown mechanisms identified in this thesis.

Similarly, future studies should consider more realistic wing geometries, including camber, taper, non-rectangular wing-tips, and flexible or morphing structures. Incorporating fluid–structure interaction effects would allow investigation of passive deformation and its influence on LEV stability, breakdown behaviour, and aerodynamic force production.

Finally, the lift and thrust partitioning results of Chapter 7 suggest opportunities for MAV design and optimisation studies, particularly in balancing peak force production with sensitivity to unsteady motion and external disturbances. Exploring this trade-off systematically could inform design strategies prioritising robustness and controllability over maximum instantaneous performance.

A

Appendix: Operator Definitions for Asymptotic Lifting-Line Theory

THIS appendix provides the formal definitions of the operators used in Guermond and Sellier's [98] asymptotic lifting-line theory, which underpin the first-order sweep correction introduced in Section 3.3. In the main text, only the structure and physical interpretation of the leading-order and first-order terms are required, as the detailed operator expressions are not used directly in the C-LAULLT implementation. The definitions are included here for completeness and to ensure that the equations in Section 3.3 can be interpreted unambiguously. The notation follows the coordinate conventions used in Bird [174], with additional definitions of terms listed below to make the Guermond and Sellier operators self-contained.

A.1 Coordinate system and notation

Following Bird [174], the wing is represented in a body-fixed coordinate system.

- x: chordwise coordinate (positive downstream)
- y: spanwise coordinate (positive outboard)
- z: vertical coordinate (positive upwards)

Each spanwise station y has chord endpoints $c_1(y)$ and $c_2(y)$. The swept lifting-line lies along the quarter-chord location.

Let $[[\psi]](x, y)$ denote the jump in acceleration potential across the lifting surface, proportional to the pressure jump and hence to the bound circulation.

A.2 Zeroth-order 2D operator $\mathcal{K}_0$

The operator $\mathcal{K}_0$ represents the two-dimensional unsteady coupling between the potential jump and the induced downwash at a given spanwise station. $\mathcal{K}_0$ forms the inner (2D) solution in the Guermond and Sellier [98] expansion and is defined as

$$\mathcal{K}_0[[\psi]] = -\frac{1}{2\pi}\mathrm{FP}\int_{c_1(y)}^{c_2(y)}\left[\frac{1}{x-\xi} - ike^{-ik(x-\xi)}\mathrm{FP}\int_{-\infty}^{x-\xi}\frac{e^{ik\tau}}{\tau}d\tau\right][[\psi]](\xi,y)d\xi. \tag{A.1}$$

The finite-part integral reduces to a Cauchy principal value when $k\to 0$.

A.3 First-order 3D operator $\mathcal{K}_1$

The operator $\mathcal{K}_1$ provides the first-order finite-span correction in the asymptotic expansion.

$$\begin{aligned}\mathcal{K}_1[[\psi]] = e^{-ikx}\Bigg\{ &\left[\frac{1}{4\pi r(y)} + \frac{\sin\Lambda}{2\pi}\frac{\partial}{\partial y}\right]\left[G(y)\log\left(\frac{k}{\nu}\right) + H(x,y)\right] \\ &+ \frac{G(y)}{4\pi r(y)}\left[1-\tan^2\Lambda - \log\left(\frac{2}{\cos^2\Lambda}\right)\right] \\ &+ \frac{G'(y)}{2\pi}\left[\log\left(\frac{1+\sin\Lambda}{\cos\Lambda}\right) - \sin\Lambda\log\left(\frac{2}{\cos^2\Lambda}\right)\right] \\ &- i\nu\frac{G(y)}{2\pi\cos\Lambda}\int_{-\infty}^{0}\frac{e^{i\nu v}}{v}dv + w_0(M_0)\Bigg\}\end{aligned} \tag{A.2}$$

Here $r(y)$ is the local half-span radius and ν is a sweep-scaled reduced-frequency parameter.

A.4 Auxiliary definitions

$G(y)$ is the circulation-related integral

$$G(y) = \int_{c_1(y)}^{c_2(y)} e^{ik\xi}[[\psi]](\xi,y)d\xi, \tag{A.3}$$

and $H(y)$ is the geometry-related integral

$$H(x,y) = \int_{c_1(y)}^{c_2(y)}\left[e^{ikx}\log|x-\xi| - ike^{ikx}\int_0^{x-\xi}e^{ik\tau}\log|\tau|d\tau\right][[\psi]](\xi,y)d\xi. \tag{A.4}$$

A.5 The operator $\mathcal{K}_0^{-1}$ and the zeroth-order solution $[[\psi_0]]$

$\mathcal{K}_0^{-1}$ is the functional inverse of $\mathcal{K}_0$. Its application corresponds to solving the two-dimensional lifting-line integral equation at each spanwise station.

The zeroth-order solution $[[\psi_0]]$ is defined as

$$[[\psi_0]] = \mathcal{K}_0^{-1} \cos \Lambda w(M), \tag{A.5}$$

where $w(M)$ is the geometric downwash, for example due to incidence or imposed kinematics. This represents the infinite-aspect-ratio limit and enters the first-order correction $\mathcal{K}_1[[\psi_0]]$ in Equation 3.14.

A.6 Notes on applicability and simplification

- Guermond and Sellier's [98] formulation is derived for moderately swept, large aspect-ratio wings.
- Bird's [174] implementation uses the unswept special case.
- In this thesis, only the leading-order sweep scaling, appearing in Equation 3.14, is used to motivate the C-LAULLT correction.

A.7 Glossary of symbols

The following symbols appear only within Appendix A, hence the definitions are defined here for clarity.

$c_1(y), c_2(y)$	Chordwise limits at spanwise position y
FP	Hadamard finite-part operator
$G(y)$	Circulation-related integral
$H(x, y)$	Geometry-dependent integral
$r(y)$	Local spanwise radius function
ν	Modified reduced-frequency parameter
ξ, τ, υ	Dummy integration variables

A. Appendix: Operator Definitions for Asymptotic Lifting-Line Theory

Appendix: Supplementary Results for the NACA 0008 Aerofoil

This appendix presents supplementary three-dimensional vortex visualisations for the NACA 0008 aerofoil, provided to support the physical interpretation of the flow structures discussed in Chapters 4-6. The figures in this appendix show a Q-criterion isosurfaces to illustrate the topology and coherence of leading-edge vortices under selected combinations of reduced frequency, aspect ratio, and sweep angle.

The cases included in this appendix are representative of those discussed in the main text and are intended to demonstrate the robustness of the observed flow features across the broader parameter space explored in this study. To maintain clarity and avoid repetition, only a limited number of representative configurations are shown, and no new physical interpretations or conclusions are drawn from these visualisations.

Detailed discussion of vortex formation, breakdown, and force response is therefore omitted, and the reader is referred to the corresponding sections of Chapters 4-6 for analysis of the underlying mechanisms.

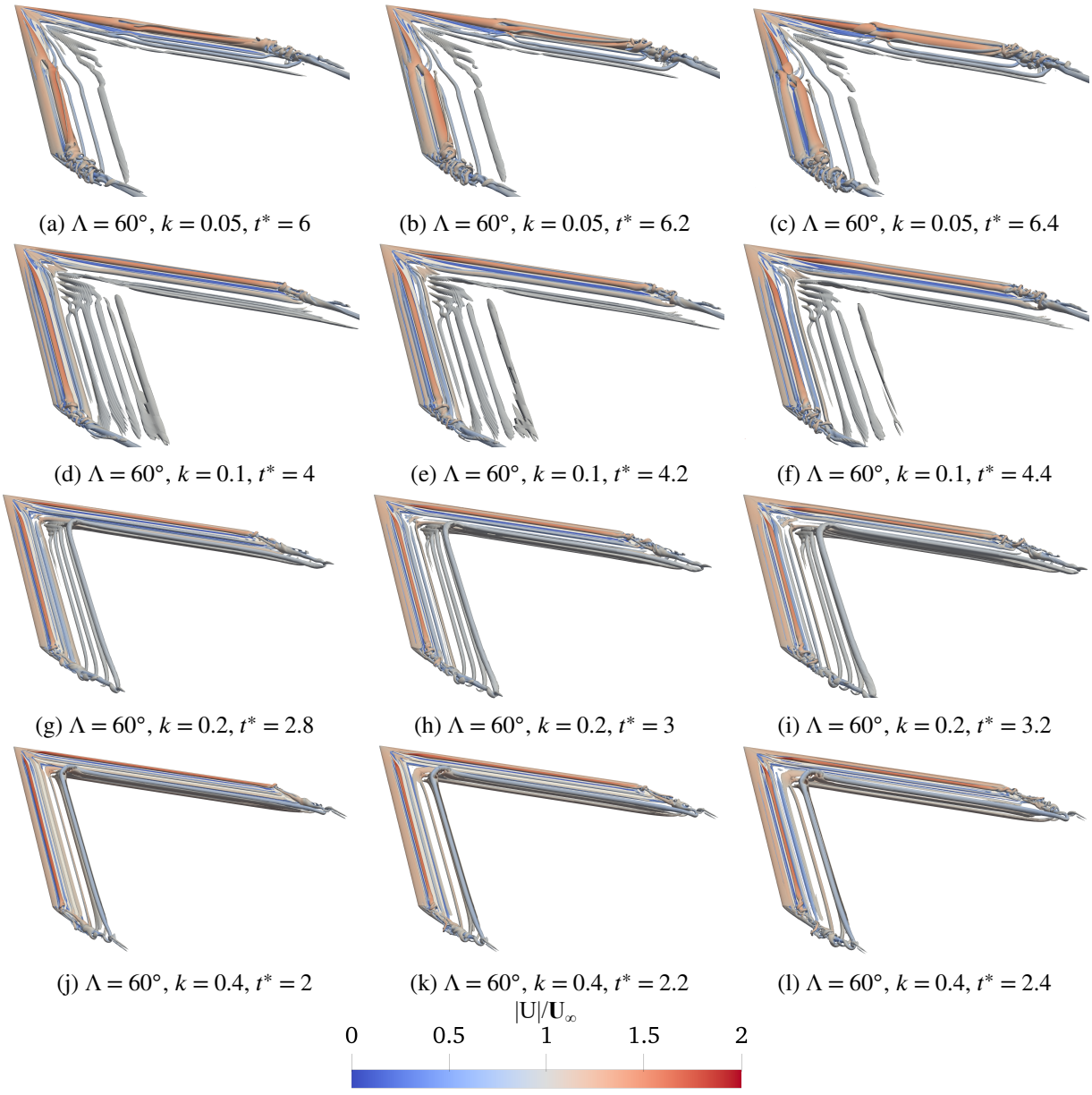

Figure B.1: Isosurfaces of $Q = 1$ coloured by normalised velocity magnitude for the aspect ratio 6, NACA 0008, $\Lambda = 60°$ wing geometries at representative convective times where a coherent LEV exists over the wing.

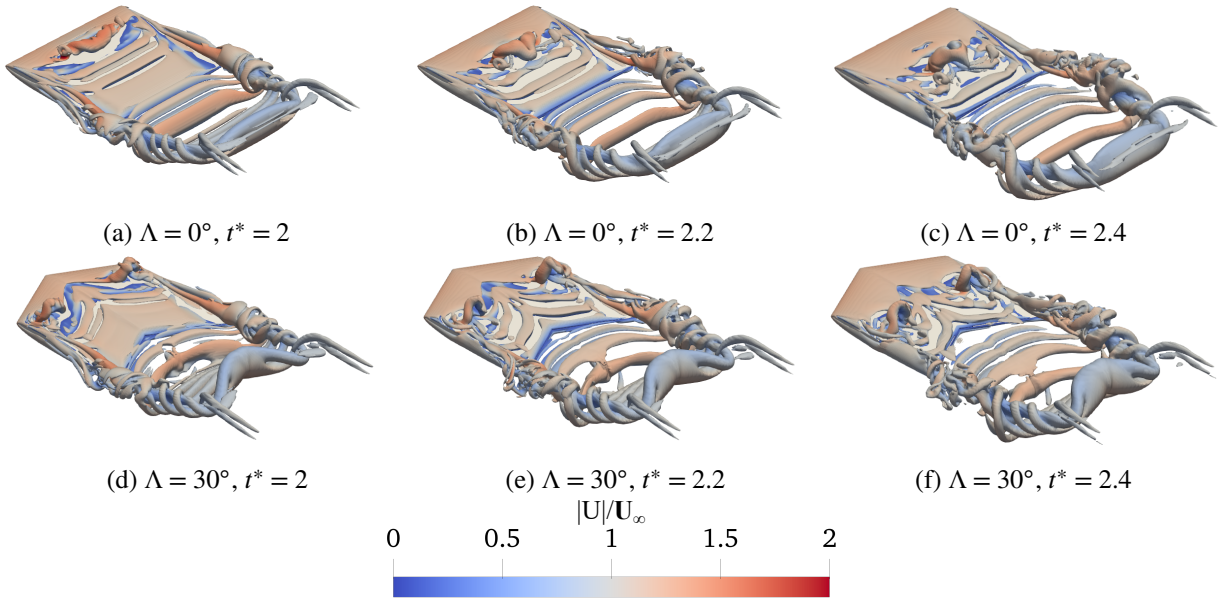

Figure B.2: Isosurfaces of $Q = 1$ coloured by normalised velocity magnitude for the aspect ratio 1, NACA 0008, $\Lambda = 0°$ and 30° wing geometries at reduced frequency $k = 0.4$ at representative convective times where a coherent LEV exists over the wing.

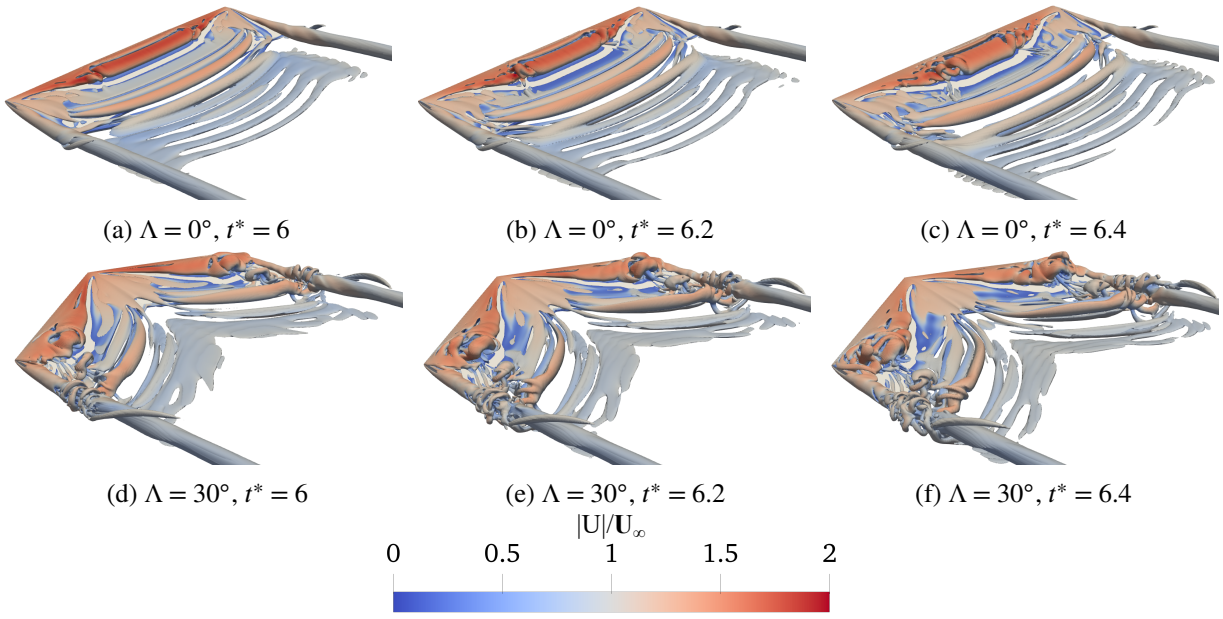

Figure B.3: Isosurfaces of $Q = 1$ coloured by normalised velocity magnitude for the aspect ratio 3, NACA 0008, $\Lambda = 0°$ and 30° wing geometries at reduced frequency $k = 0.05$ at representative convective times where a coherent LEV exists over the wing.

B. Appendix: Supplementary Results for the NACA 0008 Aerofoil

C

Appendix: Supplementary Results for the NACA 0018 Aerofoil

This appendix presents supplementary results for the thicker NACA 0018 aerofoil, included to examine the sensitivity of the reduced-frequency trends discussed in Chapter 5 to aerofoil thickness. The main body of the thesis focuses on the NACA 0008 aerofoil as the baseline configuration. Results for the NACA 0018 aerofoil are therefore included selectively in the main text, with a more complete set of thickness-related cases consolidated here for reference.

The figures in this appendix primarily comprise lift coefficient time histories for the NACA 0018 aerofoil across representative reduced frequencies ($k = 0.05, 0.1, 0.2$ and 0.4) and selected aspect ratios. Where appropriate, corresponding NACA 0008 results are shown alongside NACA 0018 results solely to facilitate direct comparison of thickness effects under otherwise equivalent conditions.

The results are intended to demonstrate that the qualitative influence of reduced frequency on leading-edge vortex development and force response remains consistent with the trends identified for the NACA 0008 aerofoil, while highlighting secondary modifications associated with increased thickness. Detailed interpretation is intentionally omitted in order to maintain focus on the analysis presented in the main text.

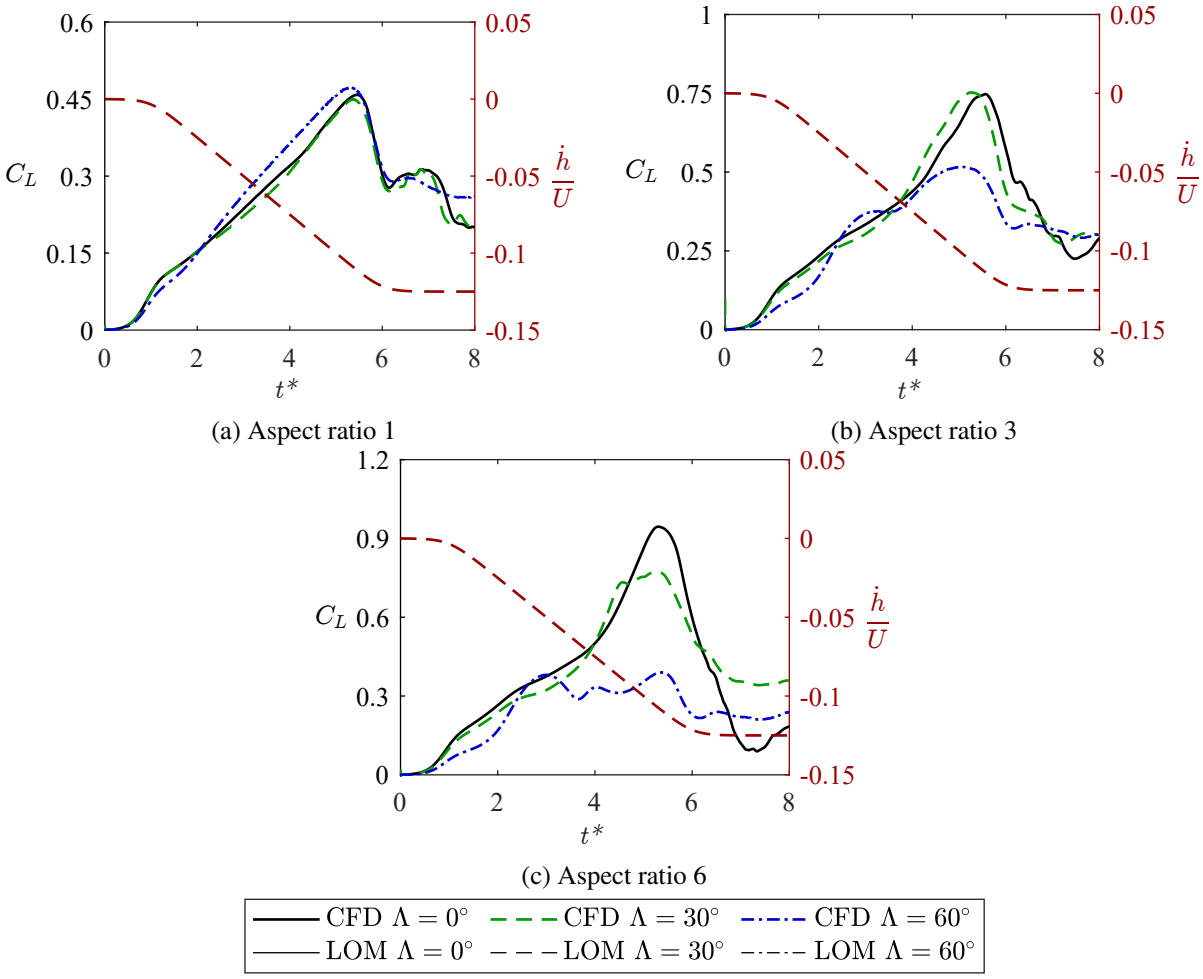

(a) Aspect ratio 1

(b) Aspect ratio 3

(c) Aspect ratio 6

Figure C.1: Lift coefficient time histories for the NACA 0018 wing geometries at reduced frequency $k = 0.05$. The prescribed plunge velocity kinematics are shown on the right axis.

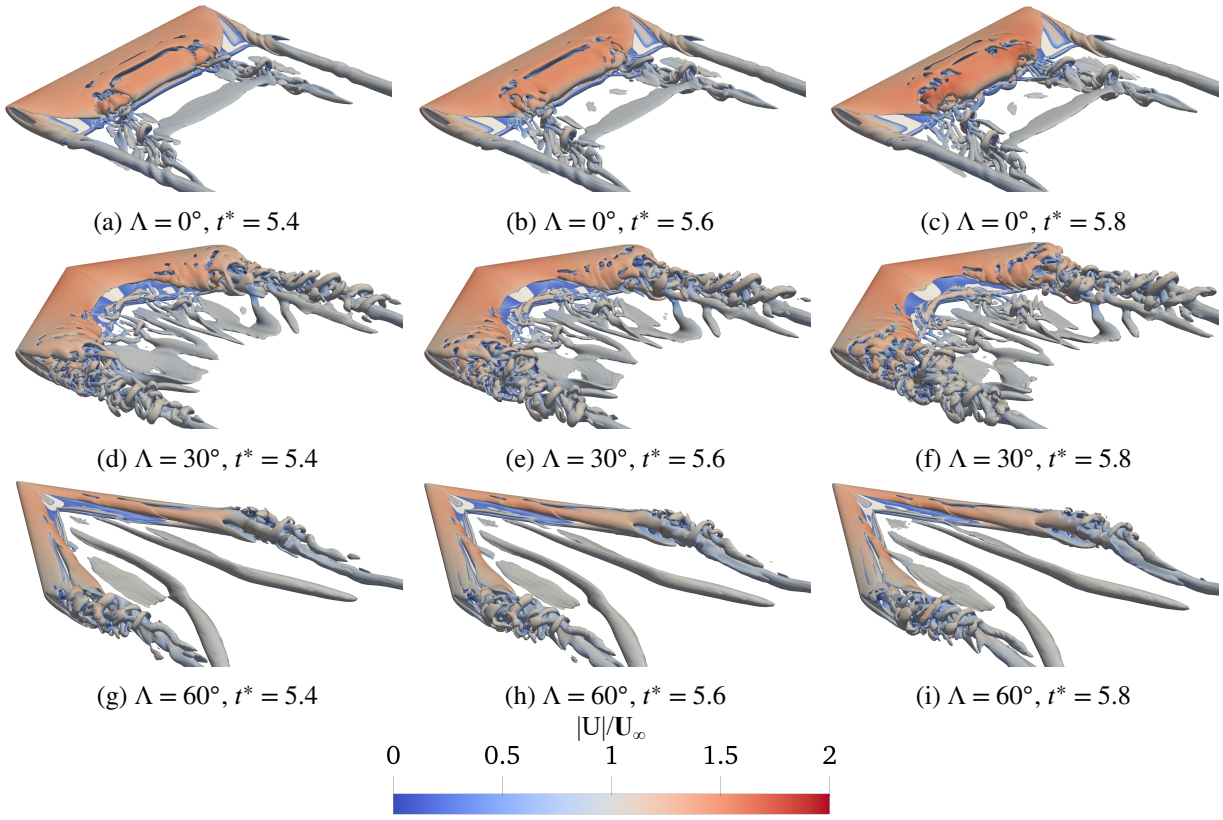

Figure C.2: Isosurfaces of $Q = 1$ coloured by normalised velocity magnitude for the aspect ratio 3, NACA 0018 wing geometries at reduced frequency $k = 0.05$ at representative convective times where a coherent LEV exists over the wing.

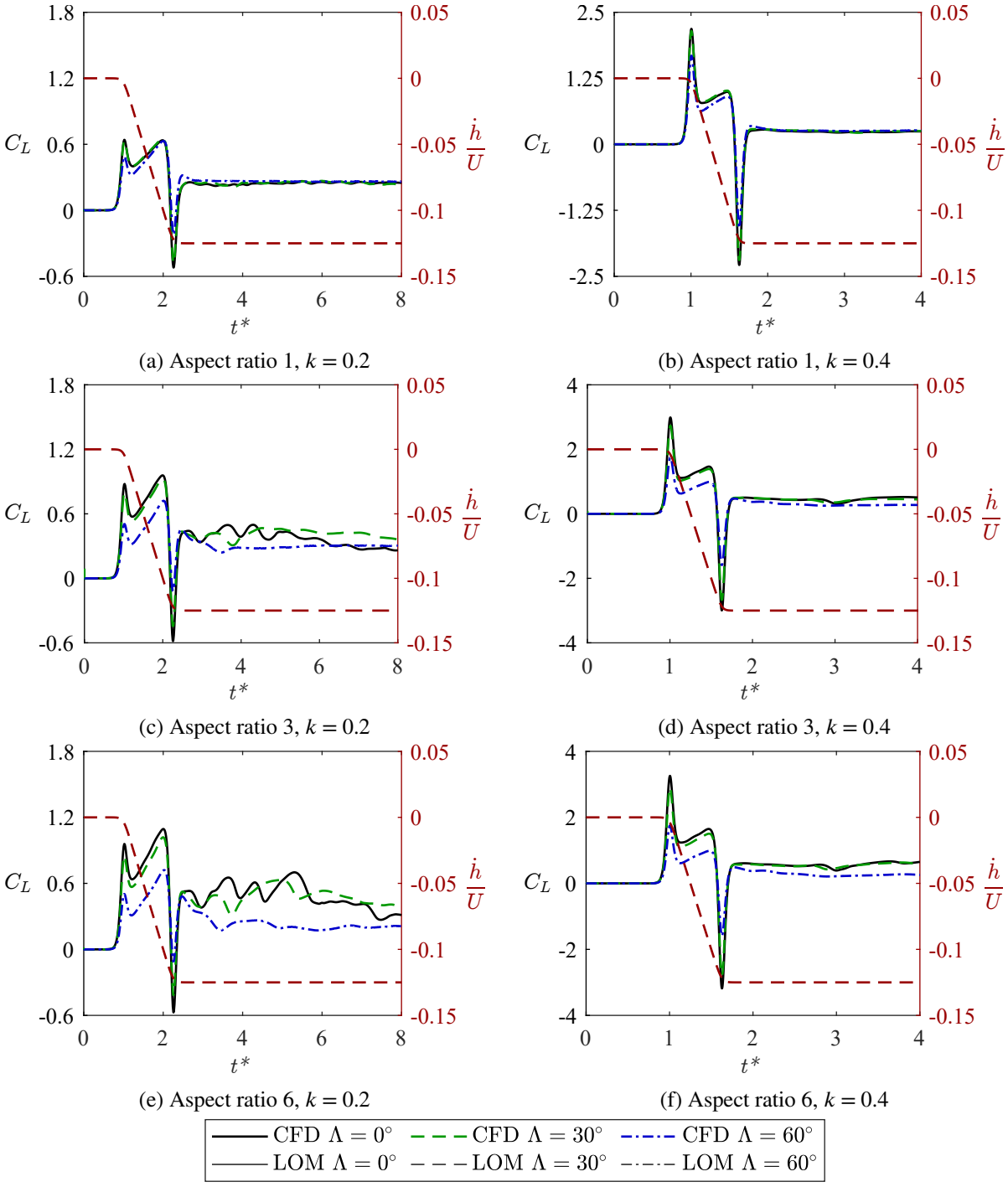

(a) Aspect ratio 1, $k = 0.2$

(b) Aspect ratio 1, $k = 0.4$

(c) Aspect ratio 3, $k = 0.2$

(d) Aspect ratio 3, $k = 0.4$

(e) Aspect ratio 6, $k = 0.2$

(f) Aspect ratio 6, $k = 0.4$

Figure C.3: Lift coefficient time histories for the NACA 0018 wing geometries, at reduced frequencies $k = 0.2$ and $k = 0.4$. The prescribed plunge velocity kinematics are shown on the right axis.

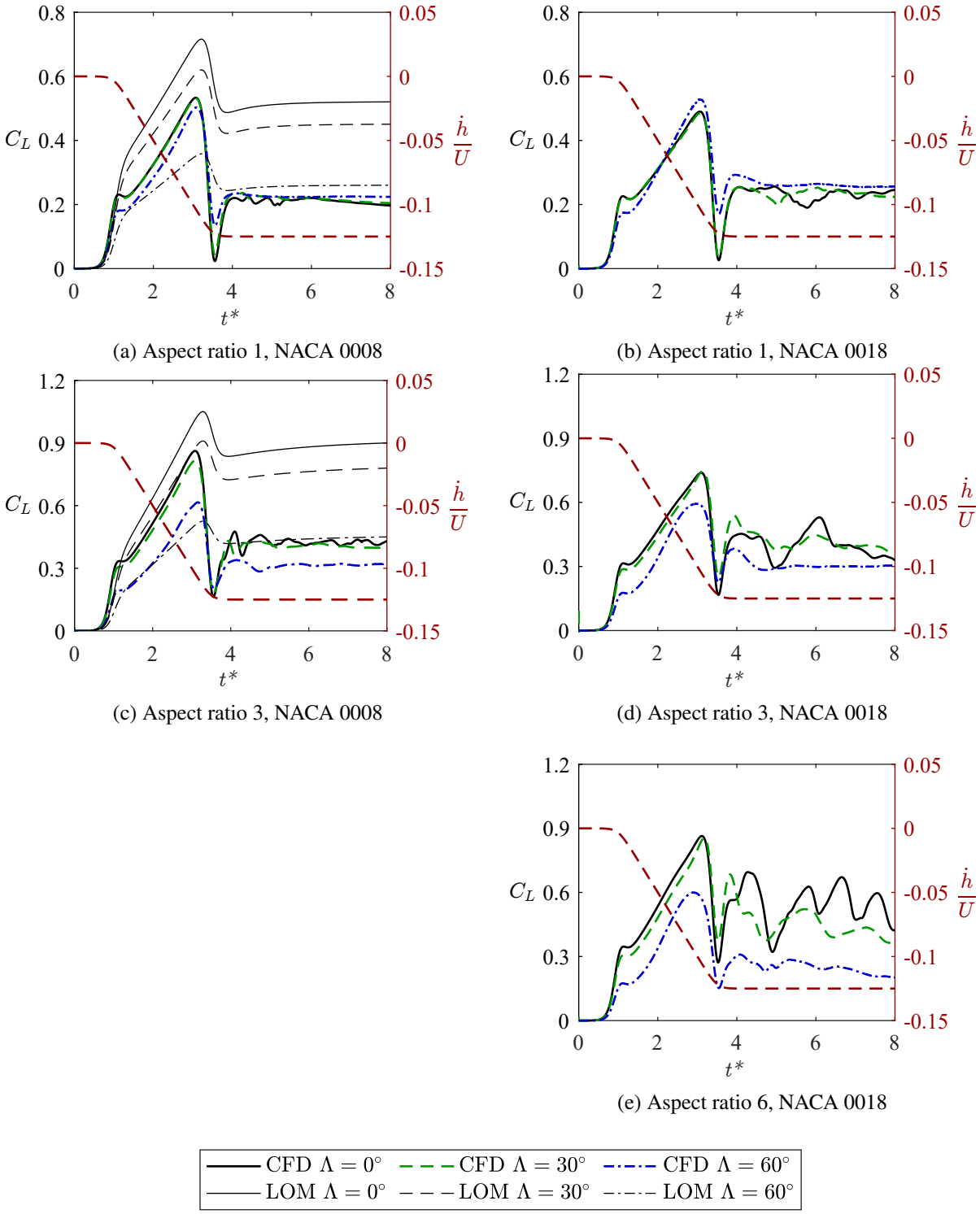

(a) Aspect ratio 1, NACA 0008

(b) Aspect ratio 1, NACA 0018

(c) Aspect ratio 3, NACA 0008

(d) Aspect ratio 3, NACA 0018

(e) Aspect ratio 6, NACA 0018

Figure C.4: Lift coefficient time histories for additional wing geometries at reduced frequency $k = 0.1$, with CFD results compared against predictions from the C-LAULLT low-order model. The prescribed plunge velocity kinematics are shown on the right axis.

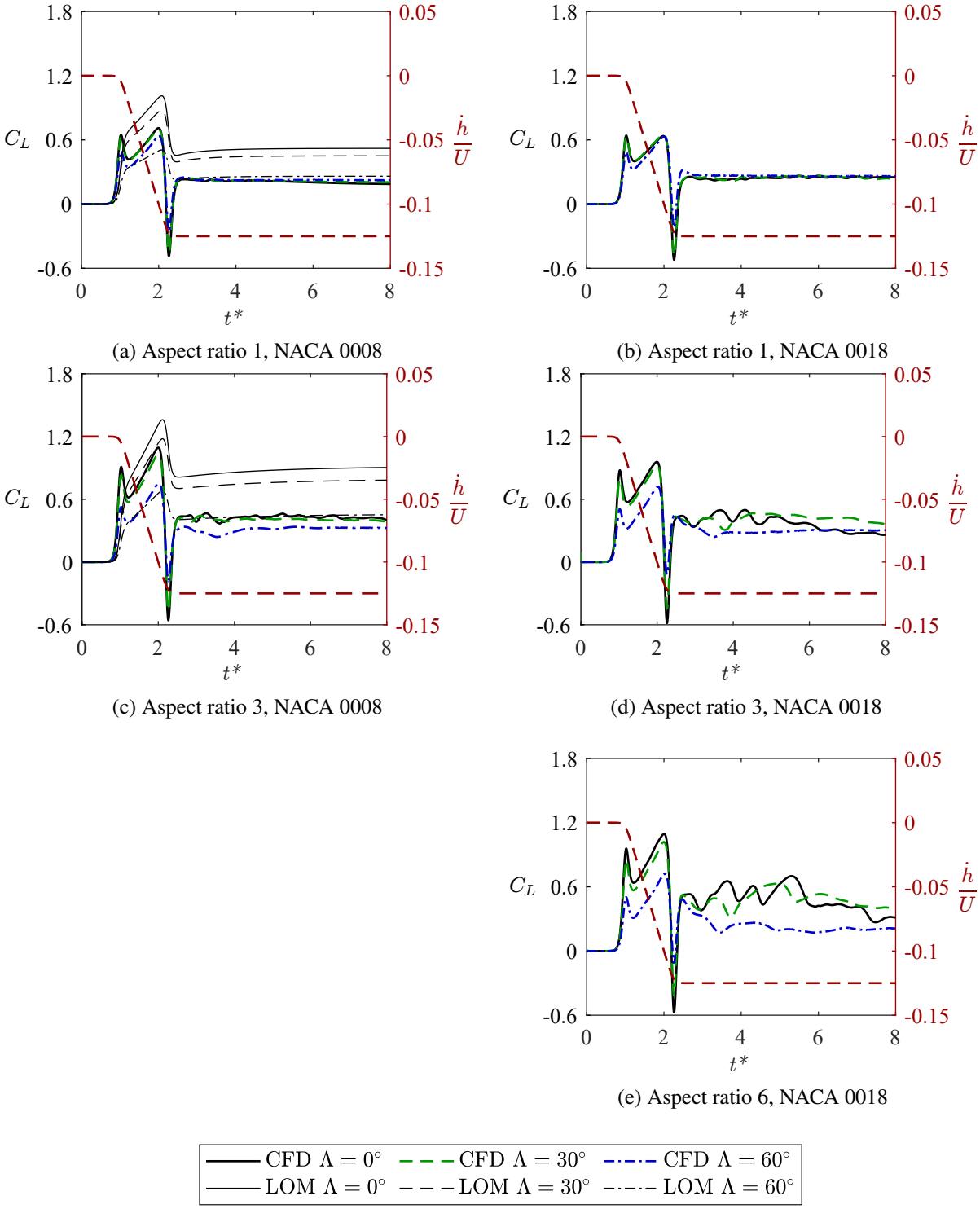

(a) Aspect ratio 1, NACA 0008

(b) Aspect ratio 1, NACA 0018

(c) Aspect ratio 3, NACA 0008

(d) Aspect ratio 3, NACA 0018

(e) Aspect ratio 6, NACA 0018

Figure C.5: Lift coefficient time histories for additional wing geometries at reduced frequency $k = 0.2$, with CFD results compared against predictions from the C-LAULLT low-order model. The prescribed plunge velocity kinematics are shown on the right axis.

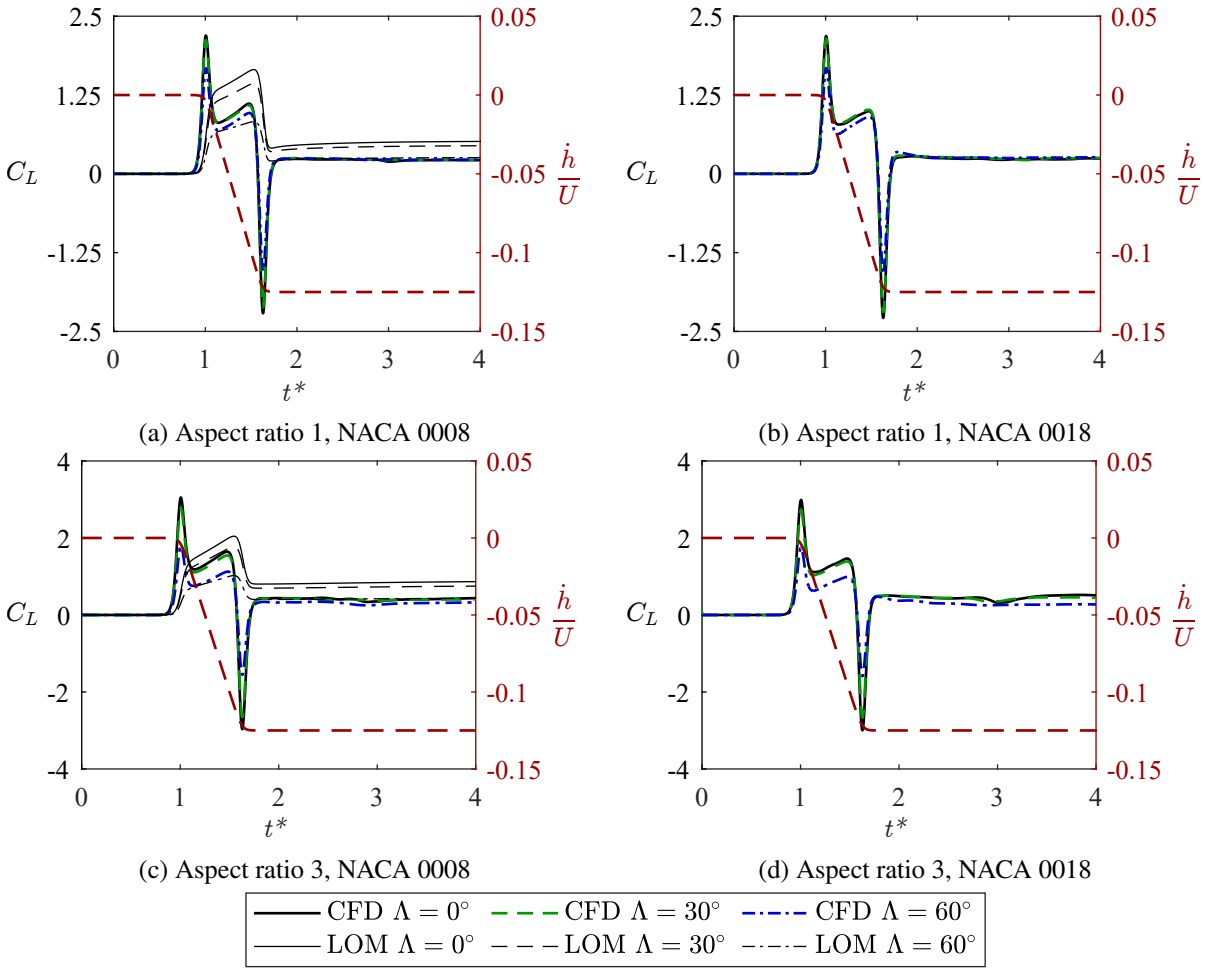

(a) Aspect ratio 1, NACA 0008

(b) Aspect ratio 1, NACA 0018

(c) Aspect ratio 3, NACA 0008

(d) Aspect ratio 3, NACA 0018

Figure C.6: Lift coefficient time histories for the aspect ratio 1 and 3 wing geometries at reduced frequency $k = 0.4$, with CFD results compared against predictions from the C-LAULLT low-order model. The prescribed plunge velocity kinematics are shown on the right axis.

C. Appendix: Supplementary Results for the NACA 0018 Aerofoil

Bibliography

[1] C. P. Ellington, C. van den Berg, A. P. Willmott, and A. L. R. Thomas, "Leading-edge vortices in insect flight," *Nature*, vol. 384, no. 6610, pp. 626–630, 1996.

[2] W. J. McCroskey, "Unsteady airfoils," *Annual Review of Fluid Mechanics*, vol. 14, no. 1, pp. 285–311, 1982.

[3] C. v. d. Berg and C. Ellington, "The three-dimensional leading-edge vortex of a 'hovering' model hawkmoth," *Philosophical Transactions of the Royal Society B: Biological Sciences*, vol. 352, no. 1351, pp. 329–340, 1997.

[4] R. J. Bomphrey, N. J. Lawson, N. J. Harding, G. K. Taylor, and A. L. R. Thomas, "The aerodynamics of *Manduca sexta* : digital particle image velocimetry analysis of the leading-edge vortex," *Journal of Experimental Biology*, vol. 208, no. 6, pp. 1079–1094, 2005.

[5] J. D. Anderson, Jr., *Fundamentals of Aerodynamics*, 2nd ed. New York: McGraw Hill, Inc., 1991.

[6] G. J. Leishman, *Principles of Helicopter Aerodynamics*, 2nd ed. New York: Cambridge University Press, 2006.

[7] W. J. McCroskey, "The phenomenon of dynamic stall," NASA, Technical Memorandum 81264, 1981.

[8] M. Chellapurath, S. Noble, and K. Sreejalekshmi, "Design and kinematic analysis of flapping wing mechanism for common swift inspired micro aerial vehicle," *Proceedings of the Institution of Mechanical Engineers, Part C: Journal of Mechanical Engineering Science*, vol. 235, no. 19, pp. 4026–4036, 2021.

[9] D. Lentink, U. K. Müller, E. J. Stamhuis, R. de Kat, W. van Gestel, L. L. M. Veldhuis, P. Henningsson, A. Hedenström, J. J. Videler, and J. L. van Leeuwen, "How swifts control

their glide performance with morphing wings," *Nature*, vol. 446, no. 7139, pp. 1082–1085, 2007.

[10] P. Weiss, "Wings of change: Shape-shifting aircraft may ply future skyways," *Science News*, vol. 164, no. 23, p. 359, 2003.

[11] J. M. V. Rayner, *Form and Function in Avian Flight*. Boston, MA: Springer, 1988, vol. 5, ch. 1, pp. 1–66.

[12] A. Azuma, *The Biokinetics of Flying and Swimming*, 2nd ed. Reston, VA: American Institute of Aeronautics and Astronautics, Inc., 2006.

[13] J. D. Eldredge and A. R. Jones, "Leading-Edge Vortices: Mechanics and Modeling," *Annual Review of Fluid Mechanics*, vol. 51, no. 1, pp. 75–104, 2019.

[14] S. Frank, "Vortex tilting and the enhancement of spanwise flow in flapping wing flight," Master of Engineering, College of Engineering and Computer Science, 2011.

[15] "Inside Ukraine's drone war against Putin," *The Economist*, 2023. [Online]. Available: https://www.economist.com/europe/2023/08/27/inside-ukraines-drone-war-against-putin

[16] "Russia hits Ukrainian port facilities, Kyiv reports front-line progress," *Reuters*, 2023. [Online]. Available: https://www.reuters.com/world/europe/russian-air-strike-damages-ukraines-izmail-port-injures-two-governor-2023-09-26/

[17] E. Snouffer, "Six places where drones are delivering medicines," *Nature*, 2022. [Online]. Available: https://www.nature.com/articles/d41591-022-00053-9

[18] "NHS launches UK's first COVID test drone delivery service in Scotland," *Skyports*, 2021. [Online]. Available: https://skyportsdroneservices.com/nhs-launches-uks-first-covid-test-drone-delivery-service-in-scotland/

[19] S. Carrell, "Royal Mail uses drones to deliver post in Orkney," *The Guardian*, 2023. [Online]. Available: https://www.theguardian.com/uk-news/2023/aug/01/royal-mail-uses-drones-to-deliver-post-in-the-orkney-islands

[20] "Drones a 'game changer' for rescue teams," *British Broadcasting Corporation*, 2022. [Online]. Available: https://www.bbc.co.uk/news/articles/czqd74e34w9o

[21] "Turkey-Syria earthquake: How drones and a NASA heartbeat detector could transform disaster search," *Sky News*, 2023. [Online]. Available: https://news.sky.com/story/turkey-syria-earthquake-how-technology-can-be-used-to-help-respond-to-natural-disasters-12805170

[22] T. J. Mueller and J. D. DeLaurier, *An Overview of Micro Air Vehicle Aerodynamics*. American Institute of Aeronautics and Astronautics, Inc., 2001, ch. 1, pp. 1–10.

[23] J. Xu and H. Sun, "Experimental studies of passive oscillating hydrofoil for tidal current energy extracting," *Journal of Harbin Engineering University*, vol. 37, no. 2, p. 248 – 253, 2016.

[24] Y. Chen, J. Zhan, J. Wu, and J. Wu, "A fully-activated flapping foil in wind gust: Energy harvesting performance investigation," *Ocean Engineering*, vol. 138, pp. 112–122, 2017.

[25] Q. Xiao and Q. Zhu, "A review on flow energy harvesters based on flapping foils," *Journal of Fluids and Structures*, vol. 46, pp. 174–191, 2014.

[26] X. Wu, X. Zhang, X. Tian, X. Li, and W. Lu, "A review on fluid dynamics of flapping foils," *Ocean Engineering*, vol. 195, p. 106712, 2020.

[27] F. Baarssen, "Wind turbines are already skyscraper-sized – is there any limit to how big they will get?" *The Conversation*, 2023. [Online]. Available: https://theconversation.com/wind-turbines-are-already-skyscraper-sized-is-there-any-limit-to-how-big-they-will-get-196131

[28] M. Hansen, J. Sørensen, S. Voutsinas, N. Sørensen, and H. Madsen, "State of the art in wind turbine aerodynamics and aeroelasticity," *Progress in Aerospace Sciences*, vol. 42, no. 4, pp. 285–330, 2006.

[29] K. Kacprzak, G. Liskiewicz, and K. Sobczak, "Numerical investigation of conventional and modified Savonius wind turbines," *Renewable Energy*, vol. 60, pp. 578–585, 2013.

[30] H. Bai, C. Chan, X. Zhu, and K. Li, "A numerical study on the performance of a Savonius-type vertical-axis wind turbine in a confined long channel," *Renewable Energy*, vol. 139, pp. 102–109, 2019.

[31] J. T. Hansen, M. Mahak, and I. Tzanakis, "Numerical modelling and optimization of vertical axis wind turbine pairs: A scale up approach," *Renewable Energy*, vol. 171, pp. 1371–1381, 2021.

[32] F. W. Lanchester, *Aerodynamics, Constituting the First Volume of a Complete Work on Aerial Flight*. London: Archibald Constable & Co. Ltd., 1907.

[33] L. Prandtl, "Application of modern hydrodynamics to aeronautics," NACA, Technical Report 116, 1923.

[34] R. T. Jones, "Properties of low-aspect-ratio pointed wings at speeds below an above the speed of sound," NACA, Technical Report 835, 1946.

[35] H. A. Wilson, Jr. and J. C. Lovell, "Full-scale investigation of the maximum lift and flow characteristics of an airplane having approximately triangular planform," NACA, Research Memorandum L6K20, 1947.

[36] J. H. B. Smith, "Improved calculations of leading-edge separation from slender, thin, delta wings," *Proceedings of the Royal Society of London. Series A. Mathematical and Physical Sciences*, vol. 306, no. 1484, pp. 67–90, Jul 1968.

[37] K. W. Mangler and J. H. B. Smith, "A theory of the flow past a slender delta wing with leading edge separation," *Proceedings of the Royal Society of London. Series A. Mathematical and Physical Sciences*, vol. 251, no. 1265, pp. 200–217, May 1959.

[38] M. G. Hall, "On the vortex associated with flow separation from a leading edge of a slender wing," Aeronautical Research Council, Technical Report 21, 1959.

[39] M. G. Hall, "A theory for the core of a leading-edge vortex," *Journal of Fluid Mechanics*, vol. 11, no. 2, pp. 209–228, Sep 1961.

[40] K. Stewartson and M. G. Hall, "The inner viscous solution for the core of a leading-edge vortex," *Journal of Fluid Mechanics*, vol. 15, no. 2, pp. 306–318, Feb 1963.

[41] E. C. Polhamus, "A concept of the vortex lift of sharp-edge delta wings based on a leading-edge-suction analogy," NASA, Technical Note D-3767, Dec 1966.

[42] J. E. Lamar, "Some recent applications of the suction analogy to vortex-lift estimates," NASA, Aerodynamic Analyses Requiring Advanced Computers SP-347, Mar 1975.

[43] F. T. Johnson, E. N. Tinoco, P. Lu, and M. A. Epton, "Three-Dimensional Flow over Wings with Leading-Edge Vortex Separation," *AIAA Journal*, vol. 18, no. 4, pp. 367–380, Apr 1980.

[44] S. Leibovich, "The structure of vortex breakdown," *Annual Review of Fluid Mechanics*, vol. 10, no. 1, pp. 221–246, 1978.

[45] J. M. Delery, "Aspects of vortex breakdown," *Progress in Aerospace Sciences*, vol. 30, no. 1, pp. 1–59, 1994.

[46] S. P. Sane and M. H. Dickinson, "The aerodynamic effects of wing rotation and a revised quasi-steady model of flapping flight," *Journal of Experimental Biology*, vol. 205, no. 8, pp. 1087–1096, 2002.

[47] J.-S. Han and C. Breitsamter, "Leading-Edge Vortex Characteristics of Low-Aspect-Ratio Sweptback Plates at Low Reynolds Number," *Applied Sciences*, vol. 11, no. 2450, 2021.

[48] N. Chiereghin, D. Cleaver, and I. Gursul, "Unsteady Force and Flow Measurements for Plunging Finite Wings," in *47th AIAA Fluid Dynamics Conference*, ser. AIAA AVIATION Forum, 2017.

[49] N. Chiereghin, S. Bull, D. J. Cleaver, and I. Gursul, "Three-dimensionality of leading-edge vortices on high aspect ratio plunging wings," *Physical Review Fluids*, vol. 5, no. 6, p. 064701, 2020.

[50] O. Son, A.-K. Gao, I. Gursul, C. Cantwell, Z. Wang, and S. Sherwin, "Leading-edge vortex dynamics on plunging airfoils and wings," *Journal of Fluid Mechanics*, vol. 940, p. A28, 2022.

[51] H. R. Beem, D. E. Rival, and M. S. Triantafyllou, "On the stabilization of leading-edge vortices with spanwise flow," *Experiments in Fluids*, vol. 52, no. 2, pp. 511–517, 2012.

[52] K. Granlund, B. Monnier, M. Ol, and D. Williams, "Airfoil longitudinal gust response in separated vs. attached flows," *Physics of Fluids*, vol. 26, no. 2, p. 027103, 2014.

[53] S. Bull, N. Chiereghin, I. Gursul, and D. Cleaver, "Unsteady aerodynamics of a plunging airfoil in transient motion," *Journal of Fluids and Structures*, vol. 103, p. 103288, 2021.

[54] W. Mallik and D. E. Raveh, "Gust Response at High Angles of Attack," *AIAA Journal*, vol. 57, no. 8, pp. 3250–3260, 2019.

[55] G. Sedky, F. D. Lagor, and A. Jones, "Unsteady aerodynamics of lift regulation during a transverse gust encounter," *Physical Review Fluids*, vol. 5, no. 7, p. 074701, 2020.

[56] S. J. Corkery and H. Babinsky, "An Investigation into Gust Shear Layer Vorticity and the Added Mass Force for a Transverse Wing-Gust Encounter," in *AIAA Scitech 2019 Forum*. American Institute of Aeronautics and Astronautics, 2019.

[57] K. Fukami and K. Taira, "Grasping extreme aerodynamics on a low-dimensional manifold," *Nature Communications*, vol. 14, no. 6480, 2023.

[58] G. Perrotta and A. R. Jones, "Unsteady forcing on a flat-plate wing in large transverse gusts," *Experiments in Fluids*, vol. 58, no. 101, 2017.

[59] S. J. Corkery, H. Babinsky, and J. K. Harvey, "On the development and early observations from a towing tank-based transverse wing–gust encounter test rig," *Experiments in Fluids*, vol. 59, no. 135, 2018.

[60] H. Biler, C. Badrya, and A. R. Jones, "Experimental and computational investigation of transverse gust encounters," in *2018 AIAA Aerospace Sciences Meeting*, ser. AIAA SciTech Forum. American Institute of Aeronautics and Astronautics, 2018.

[61] H. Biler, G. Sedky, A. R. Jones, M. Saritas, and O. Cetiner, "Experimental Investigation of Transverse and Vortex Gust Encounters at Low Reynolds Numbers," *AIAA Journal*, vol. 59, no. 3, pp. 786–799, 2021.

[62] G. Sedky, H. Biler, and A. R. Jones, "Experimental Comparison of a Sinusoidal and Trapezoidal Transverse Gust," *AIAA Journal*, vol. 60, no. 5, pp. 3347–3351, 2022.

[63] S. Watkins, J. Milbank, B. Loxton, and W. Melbourne, "Atmospheric winds and their implications for microair vehicles," *AIAA Journal*, vol. 44, no. 11, pp. 2591–2600, 2006.

[64] A. R. Jones, O. Cetiner, and M. J. Smith, "Physics and Modeling of Large Flow Disturbances: Discrete Gust Encounters for Modern Air Vehicles," *Annual Review of Fluid Mechanics*, vol. 54, no. 1, pp. 469–493, 2022.

[65] A. R. Jones and H. Babinsky, "Reynolds number effects on leading edge vortex development on a waving wing," *Experiments in Fluids*, vol. 51, no. 1, pp. 197–210, 2011.

[66] H. Wagner, "Über die entstehung des dynamischen auftriebes von tragflügeln," *ZAMM - Zeitschrift für Angewandte Mathematik und Mechanik*, vol. 5, no. 1, p. 17–35, Feb 1925.

[67] T. Theodorsen, "General theory of aerodynamic instability and the mechanism of flutter," NACA, Technical Report 496, 1935.

[68] I. E. Garrick, "On some reciprocal relations in the theory of nonstationary flows," NACA, Technical Report 629, 1938.

[69] M. V. Ol, L. Bernal, C.-K. Kang, and W. Shyy, "Shallow and deep dynamic stall for flapping low Reynolds number airfoils," *Experiments in Fluids*, vol. 46, no. 5, pp. 883–901, 2009.

[70] G. Z. McGowan, K. Granlund, M. V. Ol, A. Gopalarathnam, and J. R. Edwards, "Investigations of Lift-Based Pitch-Plunge Equivalence for Airfoils at Low Reynolds Numbers," *AIAA Journal*, vol. 49, no. 7, pp. 1511–1524, 2011.

[71] K. Ramesh, A. Gopalarathnam, J. R. Edwards, M. V. Ol, and K. Granlund, "An unsteady airfoil theory applied to pitching motions validated against experiment and computation," *Theoretical and Computational Fluid Dynamics*, vol. 27, no. 6, pp. 843–864, 2013.

[72] J. Katz, "A discrete vortex method for the non-steady separated flow over an airfoil," *Journal of Fluid Mechanics*, vol. 102, pp. 315–328, Jan 1981.

[73] Y. Hirato, M. Shen, A. Gopalarathnam, and J. R. Edwards, "Vortex-Sheet Representation of Leading-Edge Vortex Shedding from Finite Wings," *Journal of Aircraft*, vol. 56, no. 4, pp. 1626–1640, Jul 2019.

[74] Y. Hirato, M. Shen, A. Gopalarathnam, and J. R. Edwards, "Flow criticality governs leading-edge-vortex initiation on finite wings in unsteady flow," *Journal of Fluid Mechanics*, vol. 910, p. A1, 2021.

[75] S. Aggarwal, "An inviscid numerical method for unsteady flows over airfoils and wings to predict the onset of leading edge vortex formation," Master of Science, Graduate Faculty of North Carolina State University, 2013.

[76] J. Katz and A. Plotkin, *Low-Speed Aerodynamics*, 2nd ed. New York: Cambridge University Press, 2001.

[77] X. Xia and K. Mohseni, "Unsteady aerodynamics and vortex-sheet formation of a two-dimensional airfoil," *Journal of Fluid Mechanics*, vol. 830, pp. 439–478, 2017.

[78] J. Li and Z.-N. Wu, "Unsteady lift for the Wagner problem in the presence of additional leading/trailing edge vortices," *Journal of Fluid Mechanics*, vol. 769, pp. 182–217, 2015.

[79] K. Ramesh, A. Gopalarathnam, K. Granlund, M. V. Ol, and J. R. Edwards, "Discrete-vortex method with novel shedding criterion for unsteady aerofoil flows with intermittent leading-edge vortex shedding," *Journal of Fluid Mechanics*, vol. 751, pp. 500–538, 2014.

[80] K. Ramesh, A. Gopalarathnam, and J. R. Edwards, "Theoretical analysis of perching and hovering maneuvers," in *31st AIAA Applied Aerodynamics Conference*. American Institute of Aeronautics and Astronautics, Jun 2013.

[81] S. Narsipur, K. Ramesh, A. Gopalarathnam, and J. R. Edwards, "Discrete vortex modeling of perching and hovering maneuvers," *Theoretical and Computational Fluid Dynamics*, vol. 37, no. 4, pp. 445–464, 2023.

[82] D. Küchemann, *The Aerodynamic Design of Aircraft*, 1st ed. Oxford: Pergamon Press, 1978.

[83] T. Kinsey and G. Dumas, "Parametric Study of an Oscillating Airfoil in a Power-Extraction Regime," *AIAA Journal*, vol. 46, no. 6, pp. 1318–1330, 2008.

[84] C. Wang and J. D. Eldredge, "Low-order phenomenological modeling of leading-edge vortex formation," *Theoretical and Computational Fluid Dynamics*, vol. 27, no. 5, pp. 577–598, 2013.

[85] H. J. A. Bird, K. Ramesh, S. Ōtomo, and I. Maria Viola, "Usefulness of Inviscid Linear Unsteady Lifting-Line Theory for Viscous Large-Amplitude Problems," *AIAA Journal*, vol. 60, no. 2, pp. 598–609, 2022.

[86] M. Van Dyke, "Lifting-line theory as a singular-perturbation problem," *Journal of Applied Mathematics and Mechanics*, vol. 28, no. 1, pp. 90–102, 1964.

[87] H. J. A. Bird and K. Ramesh, "Unsteady lifting-line theory and the influence of wake vorticity on aerodyanamic loads," *Theoretical and Computational Fluid Mechanics*, vol. 35, pp. 757–758, 2021.

[88] H. K. Cheng, "Lifting-Line Theory of Oblique Wings," *AIAA Journal*, vol. 16, no. 11, pp. 1211–1213, Nov 1978.

[89] J.-L. Guermond, "A generalized lifting-line theory for curved and swept wings," *Journal of Fluid Mechanics*, vol. 211, pp. 497–513, Feb 1990.

[90] J. Hadamard, *Lectures on Cauchy's problem in linear partial differential equations*. New York: Dover, 1923.

[91] J. Hess and A. Smith, "Calculation of potential flow about arbitrary bodies," *Progress in Aerospace Sciences*, vol. 8, pp. 1–138, 1967.

[92] E. C. James, "Lifting-line theory for an unsteady wing as a singular perturbation problem," *Journal of Fluid Mechanics*, vol. 70, no. 4, pp. 753–771, Aug 1975.

[93] T. van Holten, "Some notes on unsteady lifting-line theory," *Journal of Fluid Mechanics*, vol. 77, no. 3, pp. 561–579, Oct 1976.

[94] A. R. Ahmadi and S. E. Widnall, "Unsteady lifting-line theory as a singular perturbation problem," *Journal of Fluid Mechanics*, vol. 153, pp. 59–81, Apr 1985.

[95] H. K. Cheng and L. E. Murillo, "Lunate-tail swimming propulsion as a problem of curved lifting line in unsteady flow. Part 1. Asymptotic theory," *Journal of Fluid Mechanics*, vol. 143, pp. 327–350, Jun 1984.

[96] P. D. Sclavounos, "An unsteady lifting-line theory," *Journal of Engineering Mathematics*, vol. 21, no. 3, pp. 201–226, 1987.

[97] H. J. A. Bird and K. Ramesh, "Theoretical and computational studies of a rectangular finite wing oscillating in pitch and heave," in *6th European Conference on Computational Mechanics ECCM 6 and 7th European Conference on Computational Fluid Dynamics ECFD 7*. European Community on Computational Methods in Applied Sciences ECCOMAS, Jun 2018.

[98] J.-L. Guermond and A. Sellier, "A unified unsteady lifting-line theory," *Journal of Fluid Mechanics*, vol. 229, pp. 427–451, Aug 1991.

[99] P. Devinant, "An approach for unsteady lifting-line time-marching numerical computation," *International Journal for Numerical Methods in Fluids*, vol. 26, pp. 177–197, 1998.

[100] P. Devinant and T. Gallois, "Swept and curved wings: a numerical approach based on generalized lifting-line theory," *Computational Mechanics*, vol. 29, pp. 322–331, 2002.

[101] K. Ramesh, T. P. Monteiro, F. J. Silvestre, G. N. Antonio Bernardo, T. d. S. Siqueira Versiani, and R. Gil Annes da Silva, "Experimental and numerical investigation of post-flutter limit cycle oscillations on a cantilevered flat plate," in *International Forum on Aeroelasticity and Structural Dynamics 2017*. IFASD, Jun 2017.

[102] H. J. Bird, S. Ōtomo, K. K. Ramesh, and I. M. Viola, "A Geometrically Non-Linear Time-Domain Unsteady Lifting-Line Theory," in *AIAA Scitech 2019 Forum*. American Institute of Aeronautics and Astronautics, Jan 2019.

[103] C. Zhang, T. L. Hedrick, and R. Mittal, "Centripetal Acceleration Reaction: An Effective and Robust Mechanism for Flapping Flight in Insects," *PLoS ONE*, vol. 10, no. 8, p. e0132093, 2015.

[104] W. R. Graham, C. W. Pitt Ford, and H. Babinsky, "An impulse-based approach to estimating forces in unsteady flow," *Journal of Fluid Mechanics*, vol. 815, pp. 60–76, 2017.

[105] J. Li and Z.-N. Wu, "Vortex force map method for viscous flows of general airfoils," *Journal of Fluid Mechanics*, vol. 836, pp. 145–166, 2018.

[106] Y. Zhu and K. Breuer, "Flow-induced oscillations of pitching swept wings: Stability boundary, vortex dynamics and force partitioning," *Journal of Fluid Mechanics*, vol. 977, p. A1, 2023.

[107] Y. Zhu, V. Mathai, and K. Breuer, "Nonlinear fluid damping of elastically mounted pitching wings in quiescent water," *Journal of Fluid Mechanics*, vol. 923, p. R2, 2021.

[108] K. Menon, S. Kumar, and R. Mittal, "Contribution of spanwise and cross-span vortices to the lift generation of low-aspect-ratio wings: Insights from force partitioning," *Physical Review Fluids*, vol. 7, no. 11, p. 114102, 2022.

[109] K. Zhang and K. Taira, "Laminar vortex dynamics around forward-swept wings," *Phys. Rev. Fluids*, vol. 7, p. 024704, 2022.

[110] J. Li, X. Zhao, and M. Graham, "Vortex force maps for three-dimensional unsteady flows with application to a delta wing," *Journal of Fluid Mechanics*, vol. 900, p. A36, 2020.

[111] E. Phillips, I. J. Wygnanski, P. M. Menge, and L. Taubert, "Passive and active leading edge devices on a simple swept back wing," in *AIAA Aviation 2019 Forum*, no. 3393, 2019.

[112] M. G. el Hak, A. Pollard, and J.-P. Bonnet, *Flow Control: Fundamentals and Practices*, 1st ed. Berlin: Springer, 1998.

[113] E. K. Oshima, I. J. Wygnanski, and M. Gharib, "Interactions Between the Leading Edge Vortex and Sweeping Jet Actuators on a Simple Swept Wing," in *AIAA SCITECH 2022 Forum*. American Institute of Aeronautics and Astronautics, 2022.

[114] M. Watson, A. J. Jaworski, and N. J. Wood, "Application of synthetic jet actuators for the modification of the characteristics of separated shear layers on slender wings," *The Aeronautical Journal*, vol. 111, no. 1122, p. 519–529, 2007.

[115] D. J. Garmann and M. R. Visbal, "Control of Dynamic Stall on Swept Finite Wings," *AIAA Journal*, vol. 60, no. 9, pp. 5262–5272, 2022.

[116] D. Greenblatt and I. J. Wygnanski, "The control of flow separation by periodic excitation," *Progress in Aerospace Sciences*, vol. 36, no. 1, pp. 487–545, 2000.

[117] M. L. Shur, P. R. Spalart, M. K. Strelets, and A. K. Travin, "A hybrid RANS-LES approach with delayed-DES and wall-modelled LES capabilities," *International Journal of Heat and Fluid Flow*, vol. 29, no. 6, pp. 1638–1649, 2008.

[118] R. Zangeneh, "Investigating sweep effects on the stability of leading-edge vortices over finite-aspect ratio pitch-up wings," *Physics of Fluids*, vol. 33, no. 107104, 2021.

[119] P. R. Hammer, D. J. Garmann, and M. Visbal, "Effect of Aspect Ratio on Finite-Wing Dynamic Stall," *AIAA Journal*, vol. 60, no. 12, pp. 6581–6593, 2021.

[120] J. H. M. Ribeiro, C.-A. Yeh, K. Zhang, and K. Taira, "Wing sweep effects on laminar separated flows," *Journal of Fluid Mechanics*, vol. 950, p. A23, 2022.

[121] K. Zhang, S. Hayostek, M. Amitay, W. He, V. Theofilis, and K. Taira, "On the formation of three-dimensional separated flows over wings under tip effects," *Journal of Fluid Mechanics*, vol. 895, p. A9, 2020.

[122] K. Zhang, S. Hayostek, M. Amitay, A. Burtsev, V. Theofilis, and K. Taira, "Laminar separated flows over finite-aspect-ratio swept wings," *Journal of Fluid Mechanics*, vol. 905, p. R1, 2020.

[123] J. H. M. Ribeiro, J. Neal, A. Burtsev, M. Amitay, V. Theofilis, and K. Taira, "Laminar post-stall wakes of tapered swept wings," *Journal of Fluid Mechanics*, vol. 976, p. A6, 2023.

[124] P. R. Hammer, D. J. Garmann, and M. R. Visbal, "Effect of Aspect Ratio on Swept Wing Dynamic Stall," in *AIAA AVIATION 2021 FORUM*, no. 2948, 2021.

[125] M. R. Visbal and D. J. Garmann, "Effect of Sweep on Dynamic Stall of a Pitching Finite-Aspect-Ratio Wing," *AIAA Journal*, vol. 57, no. 8, pp. 3274–3289, 2019.

[126] W. Lambert, M. Stanek, R. Gurka, and E. Hackett, "Leading-edge vortices over swept-back wings with varying sweep geometries," *Royal Soc. open sci*, vol. 6, no. 7, 2019.

[127] T. Holzmann, *Mathematics, Numerics, Derivations and OpenFOAM: The Basics for Numerical Simulations*, 7th ed. 86825 Bad Wörishofen, Germany: Holzmann CFD, 2019.

[128] O. Reynolds, "IV. On the dynamical theory of incompressible viscous fluids and the determination of the criterion," *Philosophical Transactions of the Royal Society of London. (A.)*, vol. 186, pp. 123–164, 1895.

[129] D. Wilcox, *Turbulence Modelling for CFD*. 5354 Palm Drive, La Cafiada, California 91011, USA: DCW Industries, Inc., 2006.

[130] P. Chou, "On velocity correlations and the solutions of the equations of turbulent fluctuation," *Quarterly of Applied Mathematics*, vol. 3, no. 1, pp. 38–54, 1945.

[131] J. Rotta, "Statistische theorie nichthomogener turbulenz," *Zeitschrift für Physik A*, vol. 129, no. 6, pp. 547–572, 1951.

[132] J. Boussinesq, *Essai sur la théorie des eaux courantes*. Paris, France: No 1. Imprimerie Nationale, Paris, 1877.

[133] P. Spalart and S. Allmaras, "A one-equation turbulence model for aerodynamic flows," in *30th Aerospace Sciences Meeting and Exhibit*, no. 439, 1992.

[134] J. H. Ferziger and M. Perić, *Computational methods for fluid dynamics*, 3rd ed. Berlin Heidelberg New York: Springer, 2002.

[135] J. Smagorinsky, "GENERAL CIRCULATION EXPERIMENTS WITH THE PRIMITIVE EQUATIONS: I. THE BASIC EXPERIMENT*," *Monthly Weather Review*, vol. 91, no. 3, pp. 99–164, 1963.

[136] A. Leonard, "Energy Cascade in Large-Eddy Simulations of Turbulent Fluid Flows," *Advances in Geophysics*, vol. 18A, pp. 237–248, 1975.

[137] P. R. Spalart, W.-H. Jou, M. Strelets, and S. R. Allmaras, "Comments on the feasibility of LES for wings, and on a hybrid RANS/LES approach," in *Proceedings of the First AFOSR International Conference on DNS/LES*, ser. Advances in DNS/LES, Aug 1997.

[138] M. Strelets, "Detached eddy simulation of massively separated flows," in *39th Aerospace Sciences Meeting and Exhibit*. Reno, Nevada, U.S.A.: American Institute of Aeronautics and Astronautics, Jan 2001.

[139] P. R. Spalart, "Detached-eddy simulation," *Annual Review of Fluid Mechanics*, vol. 41, no. 1, pp. 181–202, 2009.

[140] N. Ashton, "Recalibrating delayed detached-eddy simulation to eliminate modelled-stress depletion," in *23rd AIAA Computational Fluid Dynamics Conference*. Denver, Colorado, U.S.A.: American Institute of Aeronautics and Astronautics, June 2017.

[141] P. R. Spalart, S. Deck, M. L. Shur, K. D. Squires, M. K. Strelets, and A. Travin, "A New Version of Detached-eddy Simulation, Resistant to Ambiguous Grid Densities," *Theoretical and Computational Fluid Dynamics*, vol. 20, no. 3, pp. 181–195, 2006.

[142] F. R. Menter and M. Kuntz, "Adaptation of eddy-viscosity turbulence models to unsteady separated flow behind vehicles," in *The Aerodynamics of Heavy Vehicles: Trucks, Buses, and Trains*. Berlin, Heidelberg: Springer, June 2004, pp. 339–352.

[143] M. S. Gritskevich, A. V. Garbaruk, J. Schütze, and F. R. Menter, "Development of DDES and IDDES Formulations for the k-ω Shear Stress Transport Model," *Flow, Turbulence and Combustion*, vol. 88, no. 3, pp. 431–449, 2012.

[144] N. V. Nikitin, F. Nicoud, B. Wasistho, K. D. Squires, and P. R. Spalart, "An approach to wall modeling in large-eddy simulations," *Physics of Fluids*, vol. 12, no. 7, pp. 1629–1632, 2000.

[145] F. Moukalled, L. Mangani, and M. Darwish, *The Finite Volume Method in Computational Fluid Dynamics: An Advanced Introduction with OpenFOAM® and Matlab*, ser. Fluid Mechanics and Its Applications. Cham, Switzerland: Springer International Publishing, 2016, vol. 113.

[146] C. Greenshields and H. Weller, *Notes on Computational Fluid Dynamics: General Principles*. Reading, UK: CFD Direct Ltd, 2022.

[147] H. Jasak, "Error Analysis and Estimation for the Finite Volume Method with Applications to Fluid Flows," Ph.D. dissertation, Department of Mechanical Engineering, June 1996.

[148] R. F. Warming and M. Beam, "Upwind second-order difference schemes and applications in aerodynamic flows," *AIAA Journal*, vol. 14, no. 9, pp. 1241–1249, 1976.

[149] S. V. Patankar and D. B. Spalding, "A calculation procedure for heat, mass and momentum transfer in three-dimensional parabolic flows," *International Journal of Heat and Mass Transfer*, vol. 15, no. 10, pp. 1787–1806, 1972.

[150] S. V. Patankar, *Numerical Heat Transfer and Fluid Flow*, 1st ed., ser. Series in Computational Methods in Mechanics and Thermal Sciences. Washington: Hemisphere Publishing Corporatio, 1980.

[151] R. Issa, "Solution of the implicitly discretised fluid flow equations by operator-splitting," *Journal of Computational Physics*, vol. 62, no. 1, pp. 40–65, 1986.

[152] W. Chen, H. Zheng, Z. Yan, and R. Chen, "Shape design of an artificial pump-lung using high-resolution hemodynamic simulation with high-performance computing," *Physics of Fluids*, vol. 35, no. 3, p. 031909, 2023.

[153] C. Benoit, "Note sur une méthode de résolution des équations normales provenant de l'application de la méthode des moindres carrés a un système d'équations linéaires en nombre inférieur a celui des inconnues. — application de la méthode a la résolution d'un système defini d'équations linéaires," *Bulletin géodésique*, vol. 2, pp. 67–77, 1924.

[154] J. Meijerink and H. A. Van Der Vorst, "An iterative solution method for linear systems of which the coefficient matrix is a symmetric m-matrix," *Mathematics of computation*, vol. 31, no. 137, pp. 148–162, 1977.

[155] D. S. Kershaw, "The incomplete cholesky—conjugate gradient method for the iterative solution of systems of linear equations," *Journal of computational physics*, vol. 26, no. 1, pp. 43–65, 1978.

[156] M. R. Hestenes and E. Stiefel, "Methods of conjugate gradients for solving linear systems," *Journal of Research of the National Bureau of Standards*, vol. 49, no. 6, pp. 409–436, 1952.

[157] V. Faber and T. Manteuffel, "Necessary and Sufficient Conditions for the Existence of a Conjugate Gradient Method," *SIAM Journal on Numerical Analysis*, vol. 21, no. 2, pp. 352–362, 1984.

[158] D. Lentink and M. H. Dickinson, "Rotational accelerations stabilize leading edge vortices on revolving fly wings," *Journal of Experimental Biology*, vol. 212, no. 16, pp. 2705–2719, 2009.

[159] J. D. Eldredge, C. Wang, and M. V. Ol, "A Computational Study of a Canonical Pitch-Up, Pitch-Down Wing Maneuver," in *39th AIAA Fluid Dynamics Conference*, ser. AIAA Meeting Paper, no. 3687, 2009.

[160] R. T. Jantzen, K. Taira, K. O. Granlund, and M. V. Ol, "Vortex dynamics around pitching plates," *Physics of Fluids*, vol. 26, no. 5, 2014.

[161] K. O. Granlund, M. V. Ol, and L. P. Bernal, "Unsteady pitching flat plates," *Journal of Fluid Mechanics*, vol. 733, no. R5, 2013.

[162] P. R. Spalart, "Young-person's guide to detached-eddy simulation grids," NASA, Contractor Report 211032, 2001.

[163] S. Ōtomo, S. Henne, K. Mulleners, K. Ramesh, and I. M. Viola, "Unsteady lift on a high-amplitude pitching aerofoil," *Experiments in Fluids*, vol. 62, no. 6, 2021.

[164] A. Martínez, G. He, K. Mulleners, and K. K. Ramesh, "Modulation of the leading-edge vortex shedding rate in discrete-vortex methods," in *AIAA SCITECH 2022 Forum*, Jan 2022.

[165] K. Ramesh, "On the leading-edge suction and stagnation-point location in unsteady flows past thin aerofoils," *Journal of Fluid Mechanics*, vol. 886, p. A13, 2020.

[166] S. Narsipur, P. Hosangadi, A. Gopalarathnam, and J. R. Edwards, "Variation of leading-edge suction during stall for unsteady aerofoil motions," *Journal of Fluid Mechanics*, vol. 900, p. A25, 2020.

[167] J. Deparday and K. Mulleners, "Modeling the interplay between the shear layer and leading edge suction during dynamic stall," *Physics of Fluids*, vol. 31, no. 10, p. 107104, 2019.

[168] G. He, J. Deparday, L. Siegel, A. Henning, and K. Mulleners, "Stall Delay and Leading-Edge Suction for a Pitching Airfoil with Trailing-Edge Flap," *AIAA Journal*, vol. 58, no. 12, pp. 5146–5155, 2020.

[169] I. Gursul, R. Gordnier, and M. Visbal, "Unsteady aerodynamics of nonslender delta wings," *Progress in Aerospace Sciences*, vol. 41, no. 7, pp. 515–557, 2005.

[170] J. M. Birch and M. H. Dickinson, "Spanwise flow and the attachment of the leading-edge vortex on insect wings," *Nature*, vol. 412, pp. 729–733, 2001.

[171] T. Jardin and T. Colonius, "On the lift-optimal aspect ratio of a revolving wing at low Reynolds number," *Journal of The Royal Society Interface*, vol. 15, no. 143, 2018.

[172] K. Menon and R. Mittal, "On the initiation and sustenance of flow-induced vibration of cylinders: insights from force partitioning," *Journal of Fluid Mechanics*, vol. 907, p. A37, 2021.

[173] K. Menon and R. Mittal, "Quantitative analysis of the kinematics and induced aerodynamic loading of individual vortices in vortex-dominated flows: A computation and data-driven approach," *Journal of Computational Physics*, vol. 443, p. 110515, 2021.

[174] H. J. A. Bird, "Low-order methods for the unsteady aerodynamics of finite wings," Ph.D. dissertation, School of Engineering, June 2021.